Open access • Report • DOI:10.2172/172134

A summary of methods for approximating salt creep and disposal room closure in numerical models of multiphase flow — Source link

G.A. Freeze, K.W. Larson, P.B. Davies

Published on: 01 Oct 1995

Topics: Multiphase flow and Closure (computer programming)

12-20

SANDIA REPORT

SAND94–0251 • UC- 2000
Unlimited Release
Printed October 1995

A Summary of Methods for Approximating Salt Creep and Disposal Room Closure in Numerical Models of Multiphase Flow

G. A. Freeze, K. W. Larson, P. B. Davies

Prepared by
Sandia National Laboratories
Albuquerque, New Mexico 87185 and Livermore, California 94550
for the United States Department of Energy
under Contract DE-AC04-94AL85000

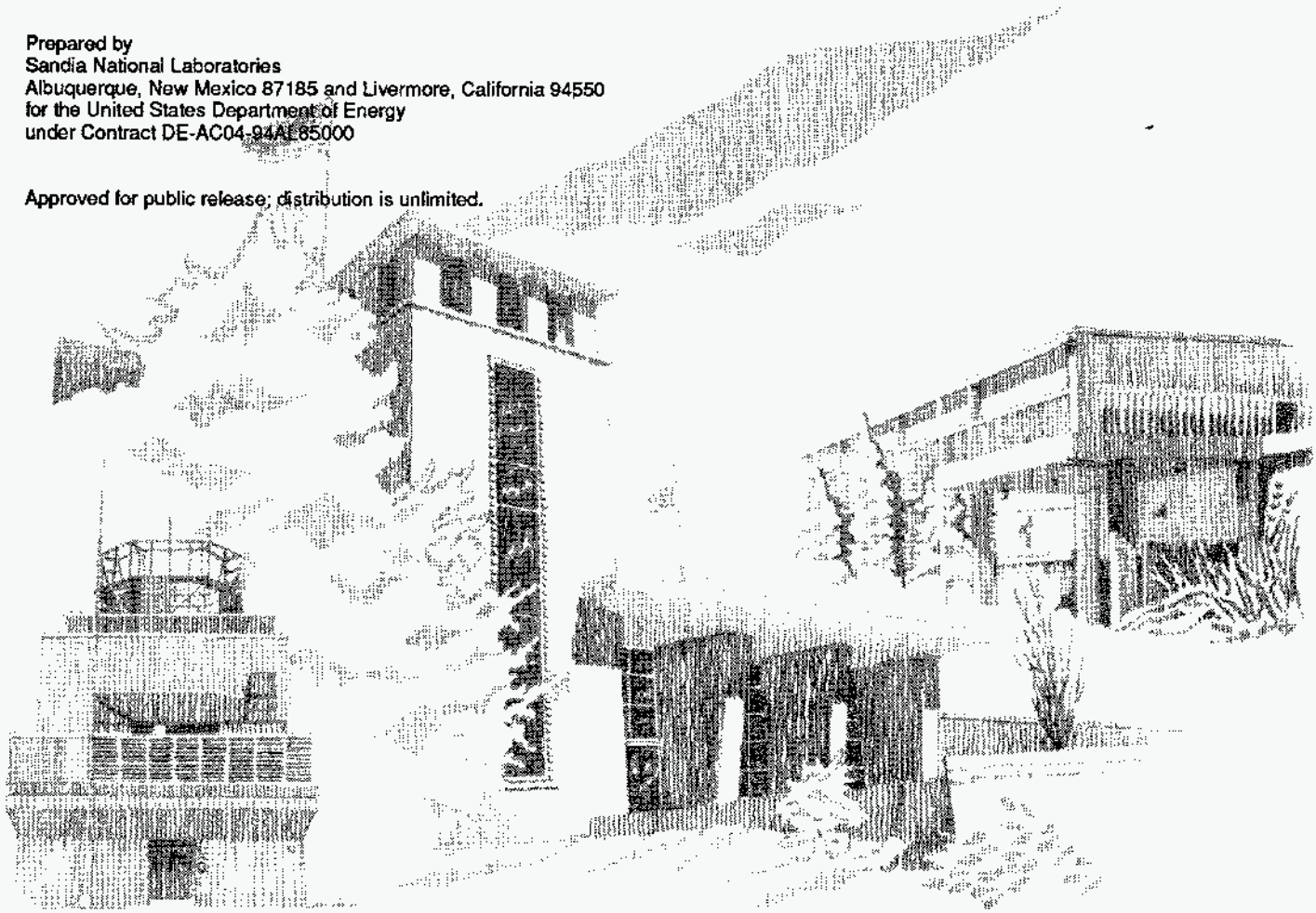

Issued by Sandia National Laboratories, operated for the United States Department of Energy by Sandia Corporation.

Available to DOE and DOE contractors from
Office of Scientific and Technical Information
PO Box 62
Oak Ridge, TN 37831

Prices available from (615) 576-8401, FTS 626-8401

Available to the public from
National Technical Information Service
US Department of Commerce
5285 Port Royal Rd
Springfield, VA 22161

NTIS price codes
Printed copy: A11
Microfiche copy: A01

SAND94-0251
Unlimited Release
Printed October 1995

Distribution
Category UC-2000

A Summary of Methods for Approximating Salt Creep and Disposal Room Closure in Numerical Models of Multiphase Flow

G.A. Freeze and K.W. Larson
INTERA Inc.
Albuquerque, New Mexico

P.B. Davies
Geohydrology Department
Sandia National Laboratories
Albuquerque, New Mexico 87185

ABSTRACT

Eight alternative methods for approximating salt creep and disposal room closure in a multiphase flow model of the Waste Isolation Pilot Plant (WIPP) were implemented and evaluated: three fixed-room geometries (initial, intermediate, fully consolidated); three porosity functions (moles-time-porosity surface, moles-time-porosity lines, pressure-time-porosity lines); and two fluid-phase-salt methods (boundary backstress, capillary backstress). The pressure-time-porosity line interpolation (pressure lines) method is the method used in current WIPP Performance Assessment calculations. The room closure approximation methods were calibrated against a series of room closure simulations performed by Stone (1995a) using a creep closure code, SANCHO.

The fixed-room geometries did not incorporate a direct coupling between room void volume and room pressure. The two porosity function methods that utilized moles of gas as an independent parameter for closure coupling were unable to account for the presence of brine in the room and, therefore, could not capture the dynamic relationship between room pressure, brine volume in the room, and room expansion. The capillary backstress method was unable to accurately simulate conditions of re-closure of the room followed room expansion. Only two methods were

found to be accurate and robust enough to approximate the effects of room closure under most conditions, the boundary backstress method and pressure-time-porosity line interpolation.

The boundary backstress method is thought to be a more reliable indicator of system behavior due to a theoretical basis for modeling salt deformation as a viscous process. It is a complex method and a detailed calibration process is required. The pressure lines method is thought to be less reliable because the results were skewed towards SANCHO results in simulations where the sequence of gas generation was significantly different from the SANCHO gas-generation rate histories used for closure calibration. This limitation in the pressure lines method is most pronounced at higher gas-generation rates (> 0.8 moles per drum per year) and is relatively insignificant at lower gas-generation rates (≤ 0.4 moles per drum per year). Due to its relative simplicity, the pressure lines method is easier to implement in multiphase flow codes and simulations have a shorter execution time (10 to 20 times faster than boundary backstress). The pressure lines method is suggested for continued use in WIPP Performance Assessment calculations as long as simulated gas-generation rate histories are low or are not significantly different from the SANCHO-simulated rates.

ACKNOWLEDGEMENTS

The authors thank Steve Webb, Karsten Pruess, and George Moridis for their support of the TOUGH2 and TOUGH2/EOS8 codes, Mark Reeves for his theoretical insights into fluid flow and salt creep coupling, and Toya Jones for running numerical experiments with various flow and closure coupling schemes. Helpful review comments were provided by Palmer Vaughn, Steve Webb, Karsten Pruess, Al Lappin, and Mike Stone.

CONTENTS

Figures

Figures (continued)

Figures (continued)

Tables

1.0 INTRODUCTION

The Waste Isolation Pilot Plant (WIPP) is a U.S. Department of Energy (DOE) research and development facility designed to demonstrate the safe underground disposal of transuranic (TRU) waste from U.S. defense-related activities. If it can be demonstrated to the U.S. Environmental Protection Agency (EPA) that the WIPP is in compliance with relevant regulatory standards, then disposal of TRU wastes being generated by and stored at various DOE facilities will occur. The WIPP is located 30 miles (50 km) east of Carlsbad in southeastern New Mexico (Figure 1-1). The WIPP repository lies in the lower portion of the Salado Formation at a depth of approximately 655 m below land surface. The Salado Formation is approximately 600 m thick, extending from the contact with the Rustler Formation at about 260 m below land surface to the top of the Castile Formation at about 860 m below land surface. The Salado Formation is comprised of beds of relatively pure halite and impure halite containing interspersed clay and polyhalite. Thin interbeds of anhydrite (Marker Beds) with underlying clay seams are present in laterally contiguous layers. A stratigraphic section of the Salado Formation in the vicinity of the repository is shown in Figure 1-2.

The underground waste storage area is designed to have eight waste disposal panels, each of which will contain seven waste disposal rooms. Each disposal room is approximately 4 m high, 10 m wide, and 91 m long. Each disposal room is to be filled with approximately 6,800 55-gallon drums and/or steel boxes containing contact-handled (CH) transuranic (TRU) waste (U.S. DOE, 1990). In addition, canisters containing remote-handled (RH) TRU waste will be emplaced in large-diameter horizontal boreholes in the room walls. Following waste emplacement, each room will be backfilled above and between the waste drums with crushed salt or a crushed salt and bentonite mixture. With time, the volume of the disposal rooms will change due to salt creep.

Gas generation from post-operational corrosion and microbial degradation of the emplaced waste could produce elevated pressures within the disposal rooms. The elevated pressures could result in gas release from the repository and could enhance contaminant movement towards regulatory boundaries. Gas pressure in the disposal rooms is strongly influenced not only by the gas-generation rate, but also by changes in gas-storage volume caused by creep closure and/or expansion of the rooms and by gas release from the rooms into the surrounding rock. Long-term repository assessment must consider the processes of gas generation, room closure

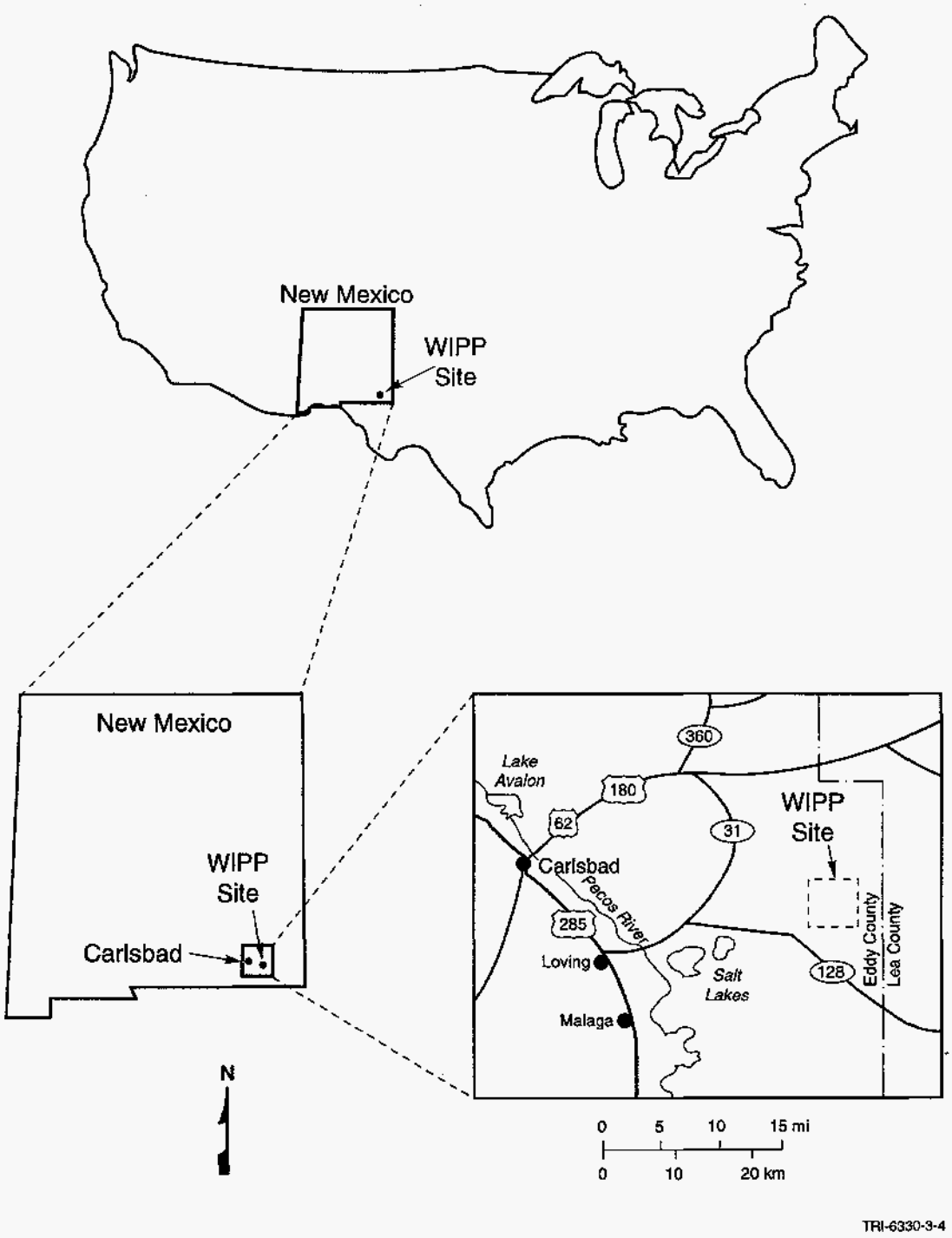

Figure 1-1. Location of the Waste Isolation Pilot Plant (after Beauheim et al., 1991).

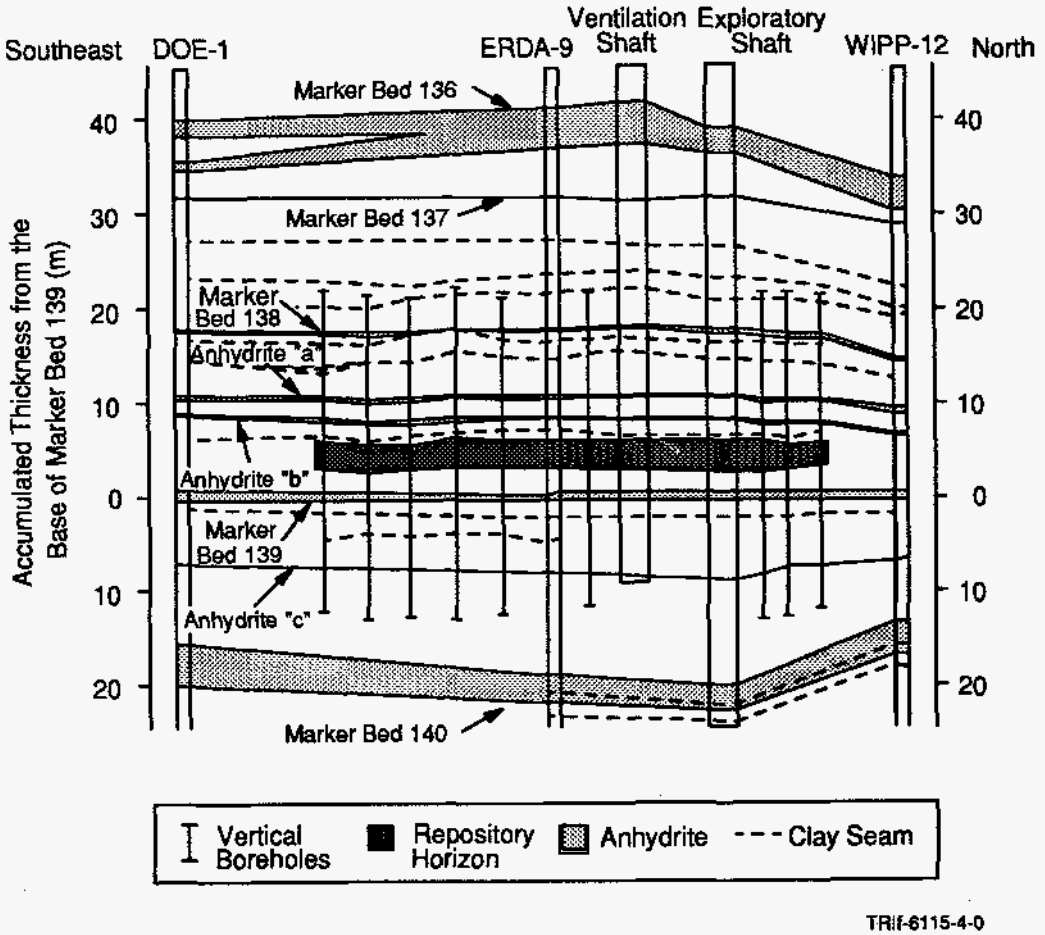

Figure 1-2. Stratigraphic section in the Salado Formation directly above and below the repository horizon (after Davies et al., 1992).

and expansion due to salt creep, and multiphase (brine and gas) fluid flow, as well as the complex coupling between the three processes.

The WIPP Performance Assessment (PA) Department (1992) developed a computer model to evaluate total repository performance which, by necessity, incorporates conceptual models of a large number of physical processes. This report focuses on conceptual models of the processes of gas generation, disposal room closure and expansion, and multiphase fluid flow and on the coupling among them. Several alternative methods for approximating disposal room closure and expansion in a numerical model of multiphase flow are examined, including the method incorporated in the WIPP PA Department (1992) model. The alternative methods are quantitatively evaluated using specific mechanistically-based performance measures.

This report presents: an introductory discussion of the processes of disposal room creep closure and expansion, gas generation, and multiphase fluid flow (Section 1); several alternative methods for approximating room closure and expansion and a multiphase flow model within which the alternative methods can be implemented (Section 2); a comparison of simulation results from each of the alternative methods (Section 3); and conclusions about which methods most accurately predict repository behavior (Section 4). The model development discussed in this report was a collaborative effort between INTERA Inc. and Sandia National Laboratories.

1.1 Disposal Room Closure

Room closure and consolidation is driven by the inward forces resulting from the excavation-related stress redistribution in the Salado Formation surrounding the room. Resistance to room closure is developed by the outward forces (backstress on the room walls) resulting from the stress distribution in the consolidating waste and backfill and from the pressure of waste-generated gas. As room closure occurs, consolidation and compaction of the waste and backfill is expected to produce an increase in the backstress. Over time, gas generation will increase the number of moles of waste-generated gas while room closure due to salt creep will cause a significant reduction in the void volume available for gas storage. In addition, brine that seeps into the room will occupy a portion of the available gas-storage volume. These factors are all likely to contribute to increasing room pressures, which will provide additional resistance to closure. Room pressurization may be mitigated by gas expulsion, brine expulsion, and/or room expansion.

Extensive in-situ and laboratory testing has been performed to determine the constitutive models and parameter values for creep deformation in halite (Krieg, 1984; Munson et al., 1989) and for consolidation of waste and backfill (Sjaardema and Krieg, 1987; Butcher, 1989; Butcher et al., 1991a; Butcher et al., 1991b). These models and parameters were used to perform simulations of room closure using a finite element creep closure code, SANCHO (Stone et al., 1985). With SANCHO, salt creep is simulated by the deformation of the model elements as defined by an elastic-secondary creep constitutive model. The relationships between stress and deformation in the waste and in the backfill are defined by separate constitutive models.

In the absence of waste-generated gas, substantial consolidation of a waste-filled disposal room is expected. Because of the strong contrast in material properties, porosity reduction in consolidating backfill materials is expected to follow a somewhat different path than porosity reduction in the waste. Figure 1-3 illustrates simulated porosity changes over time, representative of consolidation, for waste, for a backfill mixture of salt and bentonite, and an average for the entire disposal room. Also, because of the presence of a variety of different waste forms, porosity reduction in the waste itself is expected to be quite variable (Figure 1-4). Backstress due to consolidation is provided predominantly by the waste. Backfill consolidates more rapidly and with little resistance. Even with high gas-generation rates as under brine-inundated conditions, room closure and consolidation is expected to cause a significant reduction in the void volume available to store waste-generated gas within a disposal room.

1.2 Gas Generation

The potential for significant gas generation from transuranic waste at the WIPP was first examined by Molecke (1979). The steel waste drums, iron, and other metals in the waste will corrode in the presence of brine. The corrosion process has the potential to produce significant quantities of hydrogen gas (H_2). Microbial degradation of cellulosics in the waste (paper, wood, cloth) has the potential to produce significant quantities of various other gases (CO_2, CH_4, H_2S, N_2) in the presence of sufficient microorganisms and nutrients.

Current laboratory experiments focus on quantifying gas-generation rates for the independent processes of anoxic corrosion, microbial activity, and radiolysis (Brush, 1990). Corrosion reactions proposed by Brush (1995) suggest that H_2O (from brine) is necessary for, and is consumed by, the corrosion process. The role of brine in microbial activity is less

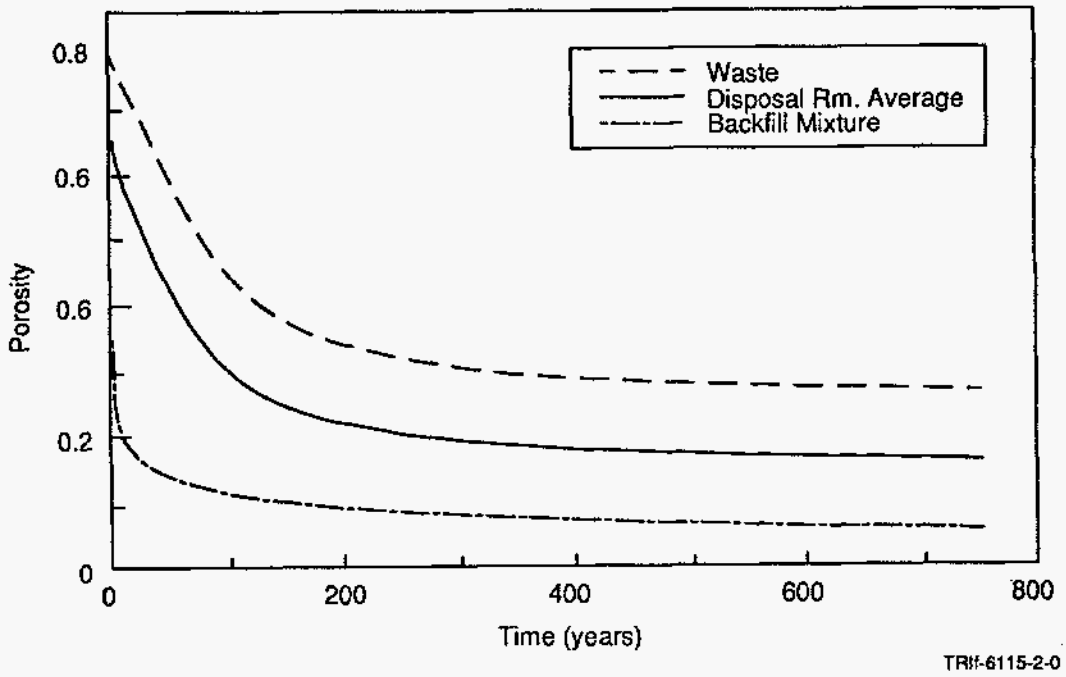

Figure 1-3. Simulation of porosity history of a disposal room filled with TRU waste and a mixture of 70% salt / 30% bentonite backfill and no gas generation (after Butcher et al., 1991a).

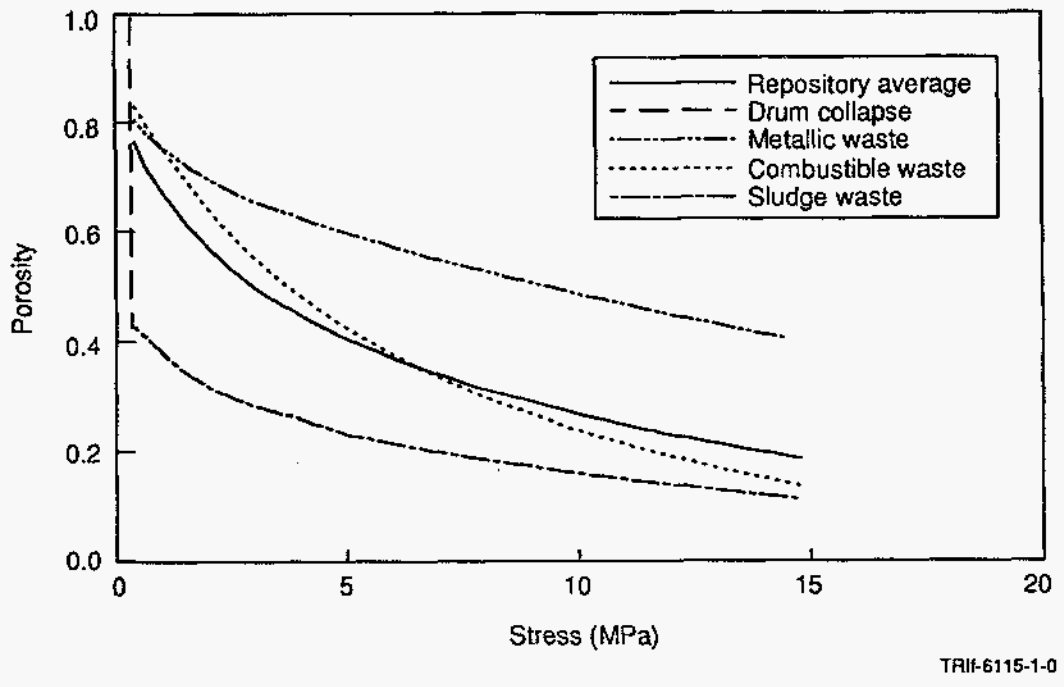

Figure 1-4. Comparison of predicted consolidation curve for repository-averaged waste and the predicted consolidation curves for specific waste types (after Butcher et al., 1991b).

apparent, H_2O may be both produced and consumed. Recognizing the potential importance of H_2O (from brine) on gas-generation rate, the current experiments (Brush, 1991; Brush, 1995) examined gas generation under two scenarios, brine-inundated and vapor-limited (humid) conditions. In the brine-inundated experiments, the steel test specimen was immersed in brine in a closed brine-water vapor system. This corresponds to in-situ fully-brine-saturated conditions or to partially-brine-saturated conditions where the waste is in direct contact (perhaps thinly coated) with brine and has an unlimited H_2O supply. In vapor-limited experiments, the test specimen is suspended in water vapor in equilibrium with brine in a closed brine-water vapor system.

Experimental results (Brush, 1991) suggest a gas-generation rate of approximately 1 mole of gas per drum of CH TRU waste per year for anoxic corrosion under brine-inundated conditions and 0.1 mole per drum per year under vapor-limited conditions. The estimated total gas generation potential for corrosion is 1,050 moles per drum of CH TRU waste (Beráun and Davies, 1992). Brush (1991) also provides an estimate for microbial gas-generation rate of 1 mole per drum per year under brine-inundated conditions and 0.1 mole per drum per year under vapor-limited conditions. The estimated total gas-generation potential for microbial activity is 550 moles per drum (Beráun and Davies, 1992). Radiolysis is expected to make a negligible contribution to the total gas-generation rate.

Given the experimental dependence of gas-generation rate on brine availability, it is likely that the gas-generation processes within a disposal room will be influenced both by brine inflow from the Salado Formation and by brine flow through the waste and backfill within the room. Brine inflow is dependent upon room pressure, which is strongly influenced by the gas-generation rate. This coupling between gas-generation rate and brine flow is examined in more detail by Freeze et al. (1995).

1.3 Multiphase Fluid Flow

It is anticipated that the pore space in the disposal room will be filled with both aqueous and gaseous phases, and that both phases may flow between the room and the Salado Formation. This study considers both a waste-generated gas phase and brine phase comprised of brine initially in the room and brine flowing into the room from the Salado Formation. A pressure difference between the brine and gas phases can exist in the pores. This difference is the gas-

brine capillary pressure. The capillary pressure is function of pore size, relative fluid (gas and brine) properties, and degree of saturation. Brine will flow out of the repository in response to an outward brine pressure gradient. Similarly, gas will flow out of the repository in response to gas pressure gradients. An outward gas pressure gradient cannot be achieved until the disposal room gas pressure exceeds the capillary resistance (quantified by the gas-brine capillary pressure plus the brine pore pressure) within the surrounding Salado Formation, at which time gas is able to displace brine from the pores. The anhydrite interbeds provide the preferred path for gas release from the room because of a low gas-brine threshold capillary pressure relative to halite (Davies, 1991).

For this study, fluid movement through the Salado Formation was modeled as potential-flow through a porous medium that did not deform in response to salt creep. A deforming rock matrix would alter intrinsic rock properties and would likely produce some deformation and or fracturing in the interbeds. These effects were not included in this study but were examined in sensitivity simulations by Freeze et al. (1995).

1.4 Process Coupling

An evaluation of the impact of waste-generated gas on repository performance requires analysis of complex, interrelated chemical, hydrologic, and geomechanical processes. Figure 1-5 is a schematic diagram illustrating the primary relationships between these processes. Some discussion of these relationships was presented by Davies et al. (1992). Many of the processes are coupled through room pressure. Gas generation, driven by chemical processes, increases the quantity of gas in a room, thereby increasing room pressure. The geomechanical processes of room closure and expansion cause direct changes in the void volume available to store gas within the room, thereby directly impacting room pressure. The hydrologic process of fluid flow in and out of the room changes the quantity of brine and gas in the room, thereby impacting room pressure. One must also consider how changing room pressure impacts each of these processes. Increasing room pressure provides backstress on the room walls which tends to resist room closure, inhibit consolidation of the room contents, and may produce room expansion.

While these process couplings are all very important for evaluating repository behavior, this study focuses on the coupling between room pressure and room closure/consolidation and

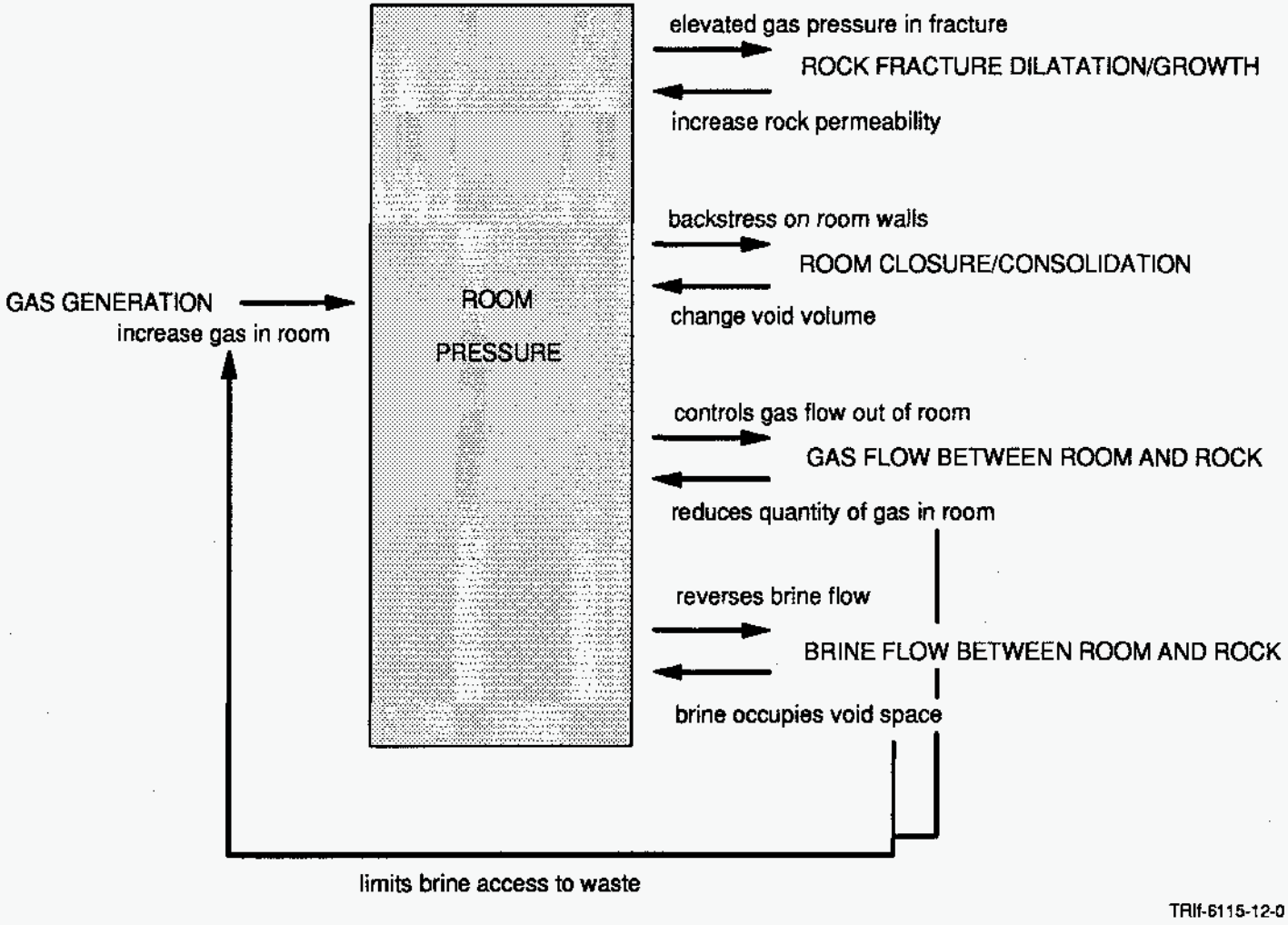

Figure 1-5. Schematic illustration of the chemical, hydrologic, and mechanical coupling that control repository response to waste-generated gas (after Davies et al., 1992).

how it can be used to approximate salt creep and room closure in a numerical model of multiphase flow. Stone (1995a) used the mechanical creep closure code SANCHO to characterize the coupling between gas generation, room pressure, and room closure. Stone (1995a) simulated the closure of a single, perfectly sealed disposal room filled with waste and backfill under five different gas-generation rate histories. The five rate histories were identified by a rate history multiplier, f, which ranged from 0.0 to 1.0. In addition to constitutive models describing salt creep, waste consolidation, and backfill consolidation, the resistance to closure provided by the pressure of waste-generated gas, calculated from the ideal gas law, was simulated. These SANCHO simulations will be referred to as the SANCHO f-series.

The simulated gas-generation rates for the f=1.0 case were: 2 moles per drum per year for the first 550 years (anoxic corrosion and microbial activity); 1 mole per drum per year from 550 years to 1,050 years (anoxic corrosion only); and 0 moles per drum per year from 1,050 years to the end of the simulation at 2,000 years. The f=1.0 rate history corresponds to the best estimate of rates derived from the gas-generation experiments performed under brine-inundated conditions (Brush, 1991). For the other cases (f=0.0, 0.2, 0.4, and 0.6), the simulated gas-generation rates for each time period were obtained by multiplying the f=1.0 rate by the rate multiplier, f. The total gas-generation potential for the f=1.0 case was 1600 moles per drum. For the other cases, because the gas-generation time periods remained the same, the gas potentials were proportionally reduced by the rate multiplier. Note that the f=0.0 case corresponds to no gas generation.

SANCHO f-series simulation results for closure of a perfectly sealed room, quantified by room porosity and room gas pressure, are shown in Figures 1-6a and 1-6b, respectively. At higher gas-generation rates ($f \geq 0.4$), room pressurization occurred quickly, and room closure was moderate. The resulting compression of the waste was insignificant, so most of the resistance to room closure was provided by the gas pressure. At elevated gas pressures, room closure was actually reversed, producing room expansion with corresponding increases in void volume. This expansion had a moderating effect on room pressurization. At lower gas-generation rates ($f \leq 0.2$) room closure was greater. The resulting compression of the waste was significant and the resistance to room closure was provided by both the gas pressure and the stresses in the waste. At the lower gas-generation rates, the backstress was large enough to stop room closure prior to reaching a fully compacted state, but gas pressures were not high enough to produce room expansion. With no gas generation (f=0.0) the room achieved a relatively stable porosity of 0.22 after 2,000 years of closure.

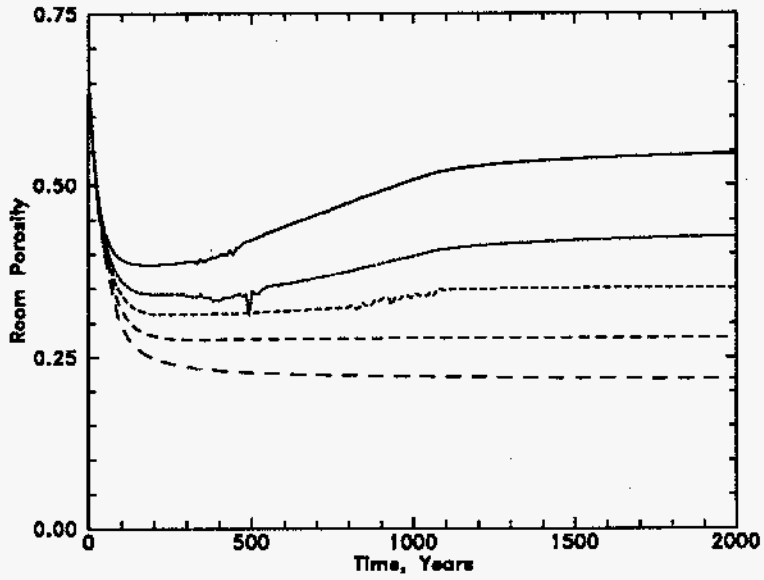

(a) Room Porosity

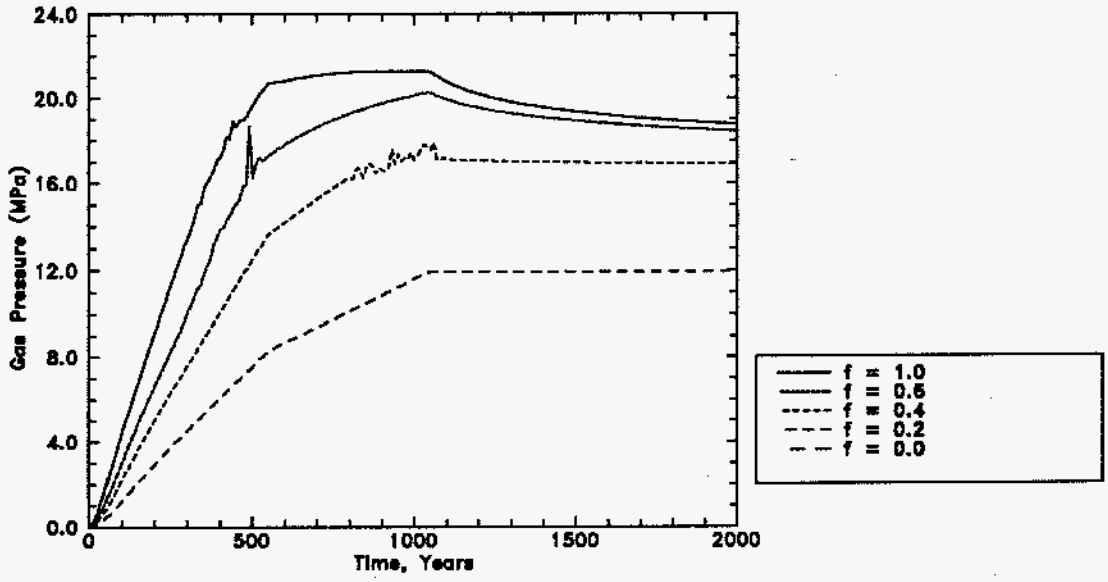

(b) Room Pressure

Figure 1-6. SANCHO simulation results for the closure of a perfectly sealed disposal room under five gas-generation rate histories, differentiated by a rate multiplier f (after Stone, 1995a).

The results of the SANCHO f-series simulations (Figure 1-6) provide a relationship between gas generation and room closure for a perfectly sealed room. Several methods for incorporating this relationship into a coupled multiphase flow and closure model are described in Section 2.

2.0 MODEL DEVELOPMENT

A numerical model was created to simulate the coupled processes of gas generation, room closure, and multiphase brine and gas flow in a single, isolated disposal room and in the surrounding halite and interbeds of the Salado Formation. A multiphase flow code, TOUGH2 (Pruess, 1987; Pruess, 1991), provided the basis for implementing the process coupling. Room closure simulations performed by Stone (1995a) using the mechanical creep closure code SANCHO provided guidance for room void volume changes representative of room closure. Gas generation was implemented by situating a number of gas sources within the modeled disposal room. Simulated gas-generation rates were specified to be consistent with experimentally determined gas-generation rates and were not dependent on brine availability. Brine-dependent gas-generation was examined by Freeze et al. (1995).

A fixed-room geometry conceptualization (i.e., no room closure) was developed in which the room void volume remained constant during a simulation. The effects of room closure on fluid flow were demonstrated indirectly by comparing simulation results from three different fixed-room geometries (fixed void volumes). Two empirically-based approaches for approximating salt creep and room closure were implemented in TOUGH2: the porosity function technique and the fluid-phase-salt technique. Both approaches utilized links to the SANCHO f-series simulation results of Stone (1995a) to calculate room void volume changes with time during a simulation.

This section describes the development of the enhanced code, TOUGH2/EOS8 (Section 2.1), the fixed-room geometry conceptualization (Section 2.2), and several porosity-function-based and fluid-phase-salt-based methods for coupling room closure with multiphase fluid flow (Section 2.3).

2.1 TOUGH2/EOS8 Code

TOUGH2/EOS8, used to couple multiphase flow, gas generation, and room closure, was adapted from TOUGH2 (Pruess, 1987; Pruess, 1991). TOUGH2 is a numerical simulator for multi-dimensional, coupled fluid and heat flow of multiphase, multicomponent mixtures in porous and fractured (dual porosity/dual permeability) media. The heat flow and dual

porosity/permeability capabilities were not used for this application. A detailed description of the capabilities of TOUGH2 can be found in Pruess (1991); a short summary is presented here.

TOUGH2 assumes that fluid flow follows Darcy's Law, with relative permeability and capillary pressure relationships used to describe interference between different fluid phases. Spatial discretization follows the integral finite difference method. Time stepping follows a fully-implicit backward finite difference scheme. The resulting set of coupled non-linear equations are solved using a Newton-Raphson iteration technique. The linear equations at each iteration are solved using sparse LU-decomposition and back-substitution.

TOUGH2 is comprised of five modules, with the fluid properties contained primarily within an equation-of-state (EOS) module. A three-phase, three-component equation-of-state module, EOS8 (water, air, "dead" oil) was adapted specifically for this application from the two-phase, two-component EOS3 (water, air) module by Karsten Pruess at Lawrence Berkeley Laboratories. The third "dead" oil phase is used with the fluid-phase-salt technique to represent "fluid" salt. A test version of the preconditioned conjugate gradient linear equation solver, developed by Karsten Pruess and George Moridis at Lawrence Berkeley Laboratories, was incorporated into TOUGH2/EOS8.

Enhancements were made to the EOS8 module by Stephen Webb at Sandia National Laboratories and by the report authors. The enhanced EOS8H (brine, hydrogen, salt) module includes: fluid properties representative of WIPP brine rather than water; and hydrogen properties as in EOS5 (water, hydrogen) rather than air properties. Additional enhancements made to the code include: the capability to adjust region (room) porosity based on pressure-porosity-time and moles-porosity-time relationships; and an exponential relationship to calculate gas-salt capillary pressure in the room as a function of room void volume. The porosity-time relationships are used with the porosity function technique to adjust the room void volume. The exponential gas-salt capillary pressure relationship is used with the fluid-phase-salt-based capillary backstress method.

2.2 Multiphase Brine and Gas Flow With Fixed-Room Geometry

The fixed-room geometry conceptualization examined three different room geometries (initial room, intermediate room, and fully consolidated room), which were representative of the range of room closure states predicted by Stone (1995a). The room void volume was held constant during each simulation (i.e., there was no explicit room closure). The effects of room closure on fluid flow were demonstrated indirectly by comparing the simulation results from different fixed-room geometries for an identical gas-generation rate history. A similar approach was used by Davies et al. (1992) and Webb (1992).

The fixed-room conceptualization used a two-dimensional fluid-flow continuum representative of a disposal room surrounded by the halite and the anhydrite interbeds of the Salado Formation. The fluid-flow continuum was used to model multiphase brine and gas flowing through halite with anhydrite interbeds. The Salado Formation was conceptualized as a homogeneous halite containing single anhydrite interbeds above and below the disposal room (Figure 2-1). A single, isolated, half-width disposal room (with symmetry across the centerline assumed) was simulated. Each of the four regions (disposal room, halite, upper interbed, and lower interbed) in the fluid-flow continuum was defined by a different set of physical properties.

The near-field discretization of the fluid-flow continuum is shown in Figure 2-2. To reduce effects from the model boundaries, a relatively extensive section of the Salado Formation around the disposal room was modeled. The far-field extent of the fluid-flow continuum is shown in Figure 2-3. The total vertical dimension of the model was 262.5 m and the total horizontal model dimension was 2,285.0 m. The third model dimension was assumed to be 1.0 m. As shown in Figure 2-3, the interbeds had a finer horizontal discretization to better capture migration distances. Changes in fluid pressures at the external no-flow boundaries were monitored during simulations. It was found that pressure changes of 1 MPa or less at the model boundaries had little effect on room void volume or room pressures. Model boundaries were extended where necessary to ensure less than 1 MPa pressure changes. Only extremely minor changes in other physical measures such as saturations were tolerated at the boundaries.

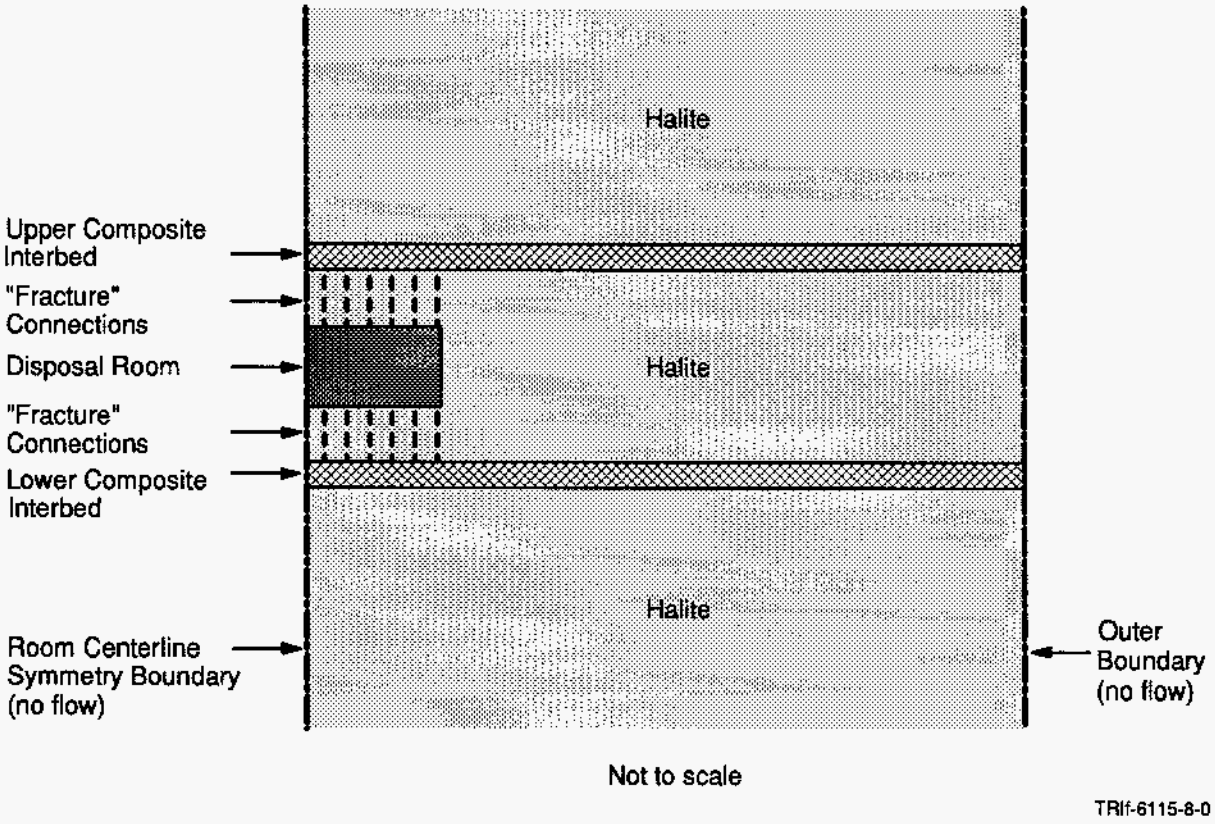

Figure 2-1. Schematic representation of the fluid-flow continuum (after Davies et al., 1992).

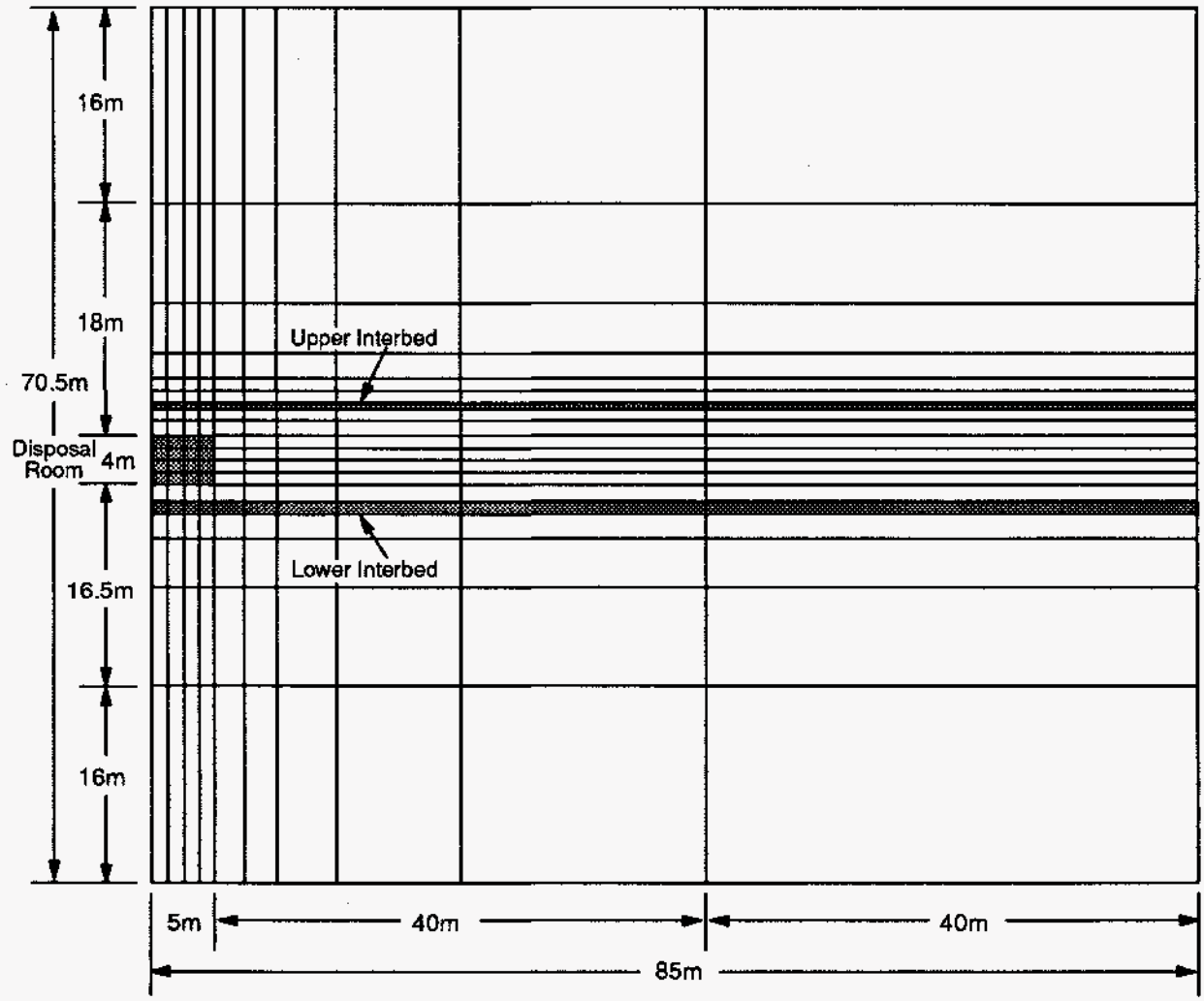

Figure 2-2. TOUGH2/EOS8 discretization of the fluid-flow continuum in the vicinity of the disposal room.

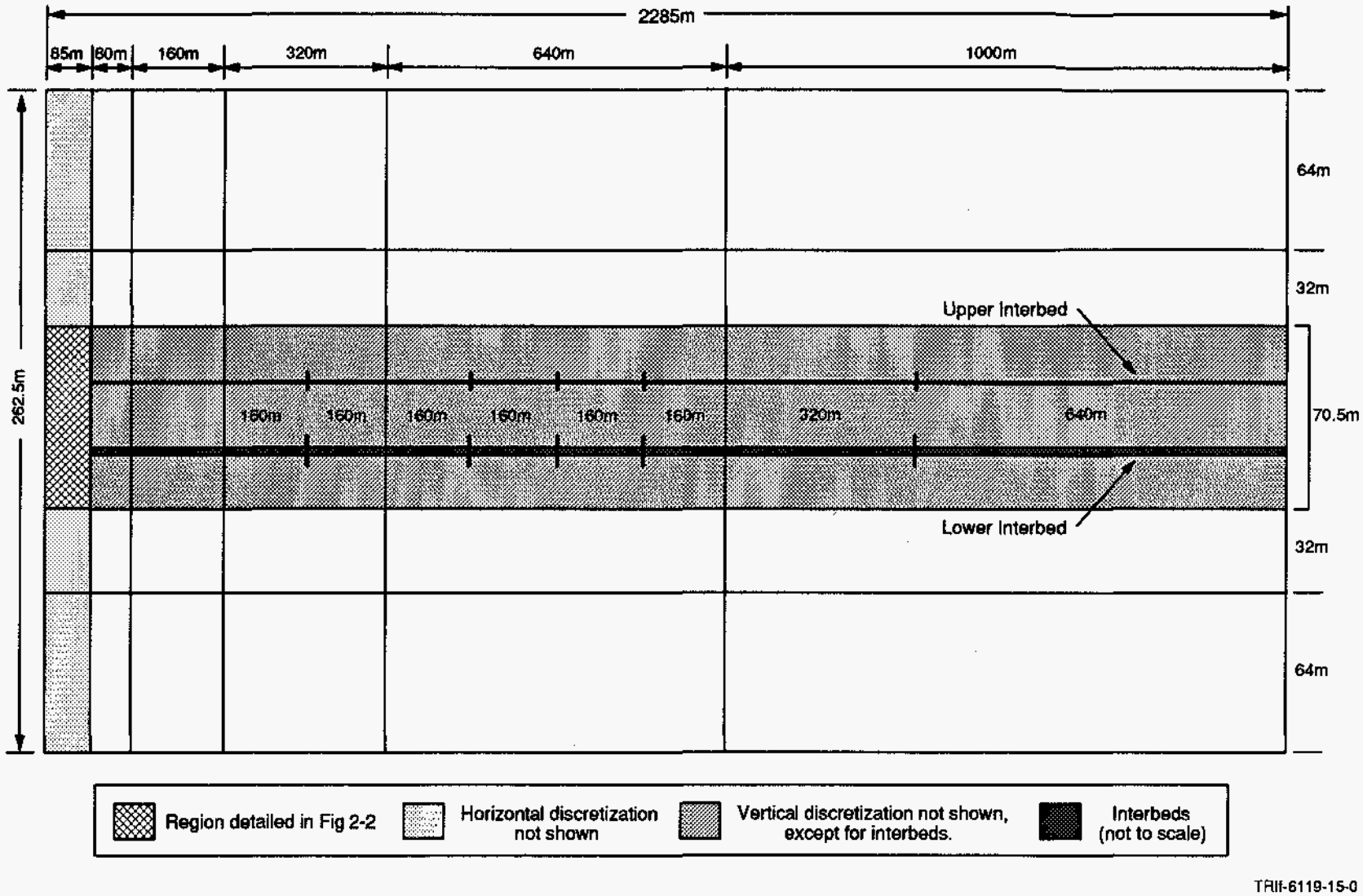

Figure 2-3. Far-field extent of the fluid-flow continuum.

The U.S. DOE (1986) design document specifies excavated room dimensions of 3.96 m (13 ft) high by 10.06 m (33 ft) wide by 91.44 m (300 ft) long. The modeled two-dimensional disposal room had a height of 4.0 m, a half-width of 5.0 m, and a unit length of 1.0 m. The volume of the modeled disposal room, scaled to full width and length, was 3,658 m^3. An initial porosity of 0.66 was assumed based on a room-averaged value of the initial waste and backfill porosities (Beráun and Davies, 1992). The initial room void volume was 2,415 m^2.

For the initial room geometry, room dimensions and porosity consistent with the initial (excavated) conditions were assumed. The initial room had a height of 4.0 m, a half-width of 5.0 m, and a corresponding scaled volume of 3,658 m^3.

For the intermediate room geometry, room dimensions were determined from the f=1.0 room closure simulation conducted by Stone (1995a). The volume of the intermediate room was defined as the minimum void volume (766 m^3) reached in the f=1.0 simulation (Figure 1-6a). The room closure simulations of Stone (1995a) assumed a constant solids volume of 1,229 m^3 for a disposal room. The sum of void and solids volumes corresponds to an intermediate room total volume of 1,995 m^3. Vertical and horizontal closure distances for the room wall mid-points (representative of maximum closure) were also predicted by Stone (1995a). The intermediate room dimensions were selected by estimating vertical and horizontal closure distances that produced approximately the intermediate room volume of 1995 m^3 while maintaining the ratio of mid-point vertical to horizontal closure. The estimated vertical closure was 1.44 m and the estimated horizontal closure was 1.41 m, resulting in an intermediate room with a height of 2.52 m (3.96 m minus 1.44 m), a half-width of 4.32 m (5.03 m minus 0.71 m), and a corresponding scaled volume of 1,991 m^3. The intermediate room porosity, calculated from the void volume and total volume, was 0.38.

For the fully consolidated room geometry, room dimensions were determined from the no gas generation (f=0.0) room closure simulation conducted by Stone (1995a). The volume of the fully consolidated room was defined by the final (2,000 year) void volume (343 m^3) reached in the f=0.0 simulation. This void volume corresponds approximately to the void volume of a disposal room compacted under lithostatic pressure. The sum of void volume and the constant solids volume corresponds to a fully consolidated room total volume of 1,572 m^3. The dimensions of the fully consolidated room were estimated from the vertical and horizontal closure distances for the room wall mid-points in a manner analogous to the intermediate room. The estimated vertical closure was 1.88 m and the estimated horizontal closure was 1.81 m,

resulting in a fully consolidated room with a height of 2.08 m, a half-width of 4.12 m, and a corresponding scaled volume of 1,567 m^3. The fully consolidated room porosity, calculated from the void volume and total volume, was 0.22.

With the integral finite difference discretization method, the intermediate and fully consolidated rooms were implemented by simply adjusting porosities and connection areas for the room elements. No changes to the fluid-flow continuum elements were necessary. This implementation produced a slight flow area discrepancy at the room boundary, however, scoping simulations indicated that the discrepancy did not have an observable effect on results. For all three fixed-room geometries the disposal room was discretized into 16 equal-sized elements (Figure 2-2) with gas sources located in the 6 elements in the interior of the room.

The fluid-flow continuum includes a 0.3 m thick upper interbed, located 2.1 m above the room. The thickness of the upper composite interbed is equal to the sum of the thicknesses of anhydrite "a" and anhydrite "b". A 0.9 m thick lower interbed, equal to the thickness of Marker Bed 139, was included 1.6 m below the room. Composite interbeds were utilized to simplify the problem for computational efficiency. Direct connections between interbed elements and elements on the edge of the disposal room were specified. These connections were specified to have large transmissivities, representative of fracture-like connections. The connection transmissivities were constant throughout each simulation.

The advantage of the fixed-room geometry is a relatively fast execution time because of the two-phase, single-continuum conceptualization. The disadvantage of the fixed-room geometry is the inability to simulate the time-varying effects of room closure on room pressure. This is particularly evident at early time, when there is rapid closure, and at late time, when room expansion may have a mitigating effect on increasing room pressure.

2.3 Multiphase Brine and Gas Flow Coupled With Room Closure

Two different approaches, porosity functions and fluid-phase-salt, were developed to model the impact of room closure on multiphase brine and gas flow in the Salado Formation. Both techniques assumed the initial room geometry (Section 2.2) as an initial condition but simulated a disposal room with changing porosity and void volume over time. These two approaches are

distinguished by the manner in which the room void volumes predicted by Stone (1995a) with SANCHO were used to calculate time-varying room void volumes in TOUGH2/EOS8.

2.3.1 Porosity Function Approach

The porosity function approach was used to simulate multiphase brine and gas flow in the same two-dimensional fluid-flow continuum (Figures 2-2 and 2-3) that was used with the fixed-room geometry conceptualization. The difference is that, with the porosity function technique, the disposal room porosity (void volume) was recalculated at each time step as a function of quantity of gas in the room and time. Gas quantity in the room was represented by either the number of moles of gas or the gas pressure. By correlating simulated pressure-time or moles-time conditions in the disposal room with a specified porosity function, a corresponding porosity for the simulated room was determined. The original concept for a moles-time-porosity function based on the SANCHO f-series room closure results was developed by Butcher and Mendenhall (1993). Three different porosity functions were investigated for this application: moles-time-porosity surface interpolation (Section 2.3.1.1), moles-time-porosity line interpolation (Section 2.3.1.2), and pressure-time-porosity line interpolation (Section 2.3.1.3).

Simulations using the porosity function method require more execution time than fixed-room geometry simulations because of the room porosity adjustments, but are still significantly faster than fluid-phase-salt simulations due to the two-phase, single-continuum conceptualization. Because of the time-dependent room void volume, the most obvious disadvantage of the fixed-room method was overcome.

2.3.1.1 MOLES-TIME-POROSITY SURFACE INTERPOLATION

The moles-time-porosity surface is a three-dimensional data set, calculated from the room porosity vs. time and moles of gas in the room vs. time results from the five SANCHO f-series simulations performed by Stone (1995a). The SANCHO results were mapped to a regularly-spaced three-dimensional surface of porosity versus time and moles of gas in the room (Figure 2-4). Translation from the SANCHO results representing the five rate histories to the regularly-spaced surface was done with the surface mapping package SURFER, Version 4 (Golden Software, 1994). The mapping procedure follows the formulation described in Butcher and Mendenhall (1993). Because the translation to the regularly-spaced surface involved

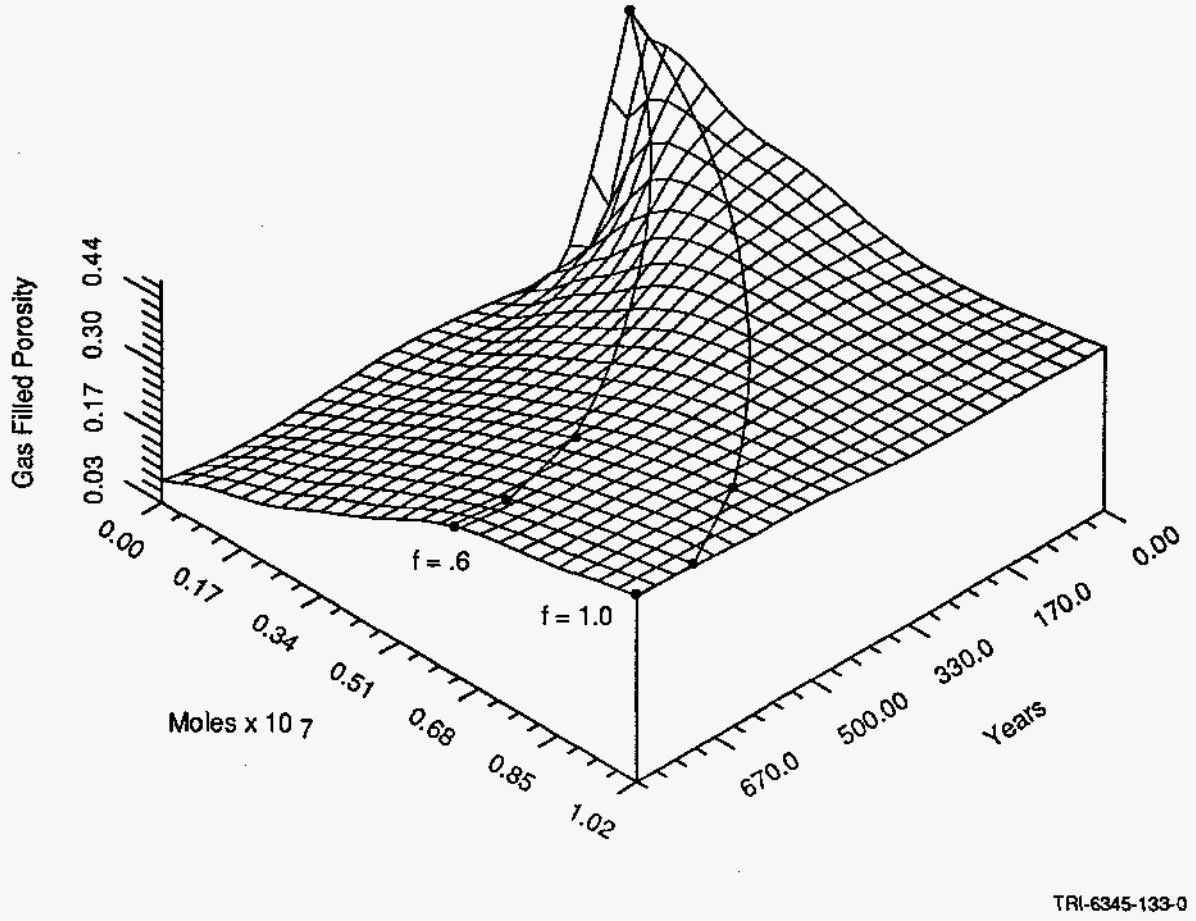

Figure 2-4. Moles-time-porosity surface created from SANCHO simulation results (after Butcher and Mendenhall, 1993).

interpolation, there is some uncertainty associated with all points on the mapped surface. The uncertainties (mapping errors) are largest for points on the surface furthest removed from the points defining the five SANCHO simulations.

At each TOUGH2/EOS8 time step, the simulated time and moles of gas in the room are correlated with a unique room porosity value from the surface. The room porosity value is obtained by linear interpolation between the four points on the porosity surface data set which bound the current time and moles of gas in the room conditions of a TOUGH2/EOS8 simulation. The simulated room porosity is then adjusted to the value determined from the porosity surface. With this process, the SANCHO-simulated relationship between room porosity, moles of gas in the room, and time resulting from room closure, was transferred to TOUGH2/EOS8 where it was simulated in conjunction with multiphase fluid flow.

The room porosity values assigned in TOUGH2/EOS8 simulations represent porosity which can be occupied by both the brine and gas phases. When the saturation of brine in the room becomes large, the void volume available for gas becomes small, and gas pressures will rise. Under most circumstances, rising gas pressure will force the room to expand, increasing the porosity. However, the moles-time-porosity technique uses moles of gas to set the porosity of the room, ignoring the void volume occupied by brine. As a result, room porosity determined from the moles-time-porosity surface does not account for the presence of brine in the room.

2.3.1.2 MOLES-TIME-POROSITY LINE INTERPOLATION

The line interpolation technique was developed to eliminate the uncertainty introduced by mapping the SANCHO data onto a regularly-spaced surface (Section 2.3.1.1). The TOUGH2/EOS8 room porosities are set at each time step by interpolation among the four moles-time-porosity line data points which bound the TOUGH2/EOS8 simulated times and moles of gas in the room. An interpolation algorithm was added to TOUGH2/EOS8 for this purpose. In cases where the TOUGH2/EOS8 simulated time and moles conditions were not bounded by four SANCHO data points, extrapolation was used to obtain a room porosity value. Because the room porosities are calculated directly from the SANCHO results, surface mapping errors are eliminated.

To mitigate possible adverse effects of numerical oscillations apparent in the original SANCHO results (Figure 1-6), sections of the data were smoothed. The sections of SANCHO room porosity versus time exhibiting numerical oscillations data were replaced by straight line segments. The time and porosity at the ends of each line segment were taken directly from SANCHO results. The original SANCHO data lines were then replaced along the straight line segments with values interpolated between the endpoints.

As with the moles-time-porosity surface (Section 2.3.1.1), the moles-time-porosity line interpolation method does not account for the volume of brine in the room because room porosity is set as a function of moles of gas in the room.

2.3.1.3 PRESSURE-TIME-POROSITY LINE INTERPOLATION

The pressure-time-porosity line interpolation technique is similar in implementation to the moles-time-porosity line interpolation except that room pressure replaced moles of gas in the room as one of the dependent variables. The use of gas pressure rather than moles of gas to represent the gas conditions allowed the influence of brine on room pressure to impact room porosity changes.

As in the moles-time-porosity line interpolation technique, the pressure-time-porosity line interpolation utilizes results from the five SANCHO f-series simulations directly to calculate porosity. Appendix B lists pressure and porosity as a function of time from each of the five SANCHO simulations. The TOUGH2/EOS8 simulations utilized a smoothed data set in which room porosities were calculated by the method described in Section 2.3.1.2. Smoothed pressures were calculated from the ideal gas law, with room void volume set by the smoothed porosity values. The result was a smoothed pressure-time-porosity data set internally consistent with respect to time, moles of gas in the room, room porosity, and room pressure (Figure 2-5).

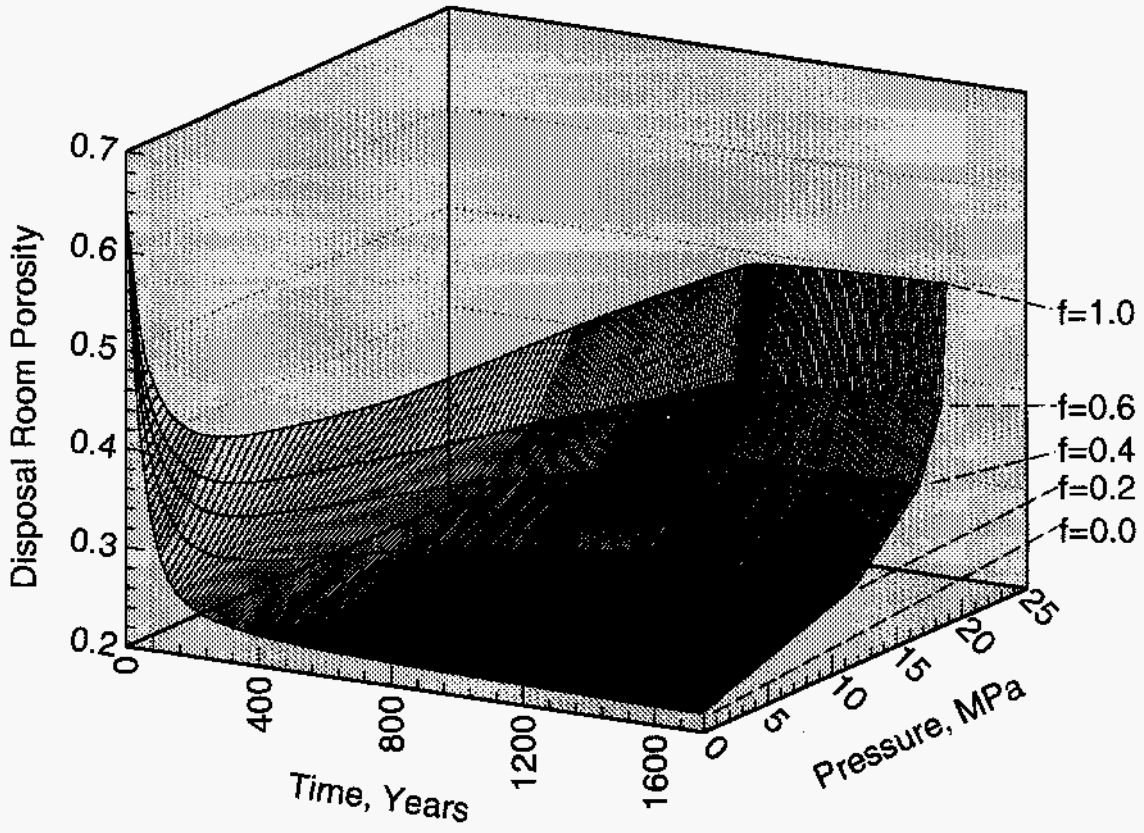

Figure 2-5. Pressure-time-porosity lines created from SANCHO simulation results.

2.3.2 Fluid-Phase-Salt Approach

Because salt deformation can be approximated as a viscous deformation process (Nettleton, 1934; Biot and Ode, 1965; Berner et al., 1972; Ramberg, 1981; Davies, 1984), salt creep can be modeled using a highly-viscous fluid. A theoretical relationship between potential-driven salt flow and mechanical salt creep was derived by Reeves (1995). This relationship is summarized in Appendix A. The fluid-phase-salt approach uses a Darcy flow approximation to represent salt creep. Using TOUGH2/EOS8, salt was modeled as a fluid phase having high viscosity, increasing the number of simulated phases to three (gas, brine, and salt). Room closure was represented by the salt phase flowing into the disposal room. The fluid-phase-salt approach used a dual continuum conceptualization. Multiphase brine and gas flow was confined to the same fluid-flow continuum (Figures 2-2 and 2-3) that was used with the fixed-room geometry and porosity function methods. Flow of the salt phase was confined to a separate salt-flow continuum.

The salt-flow continuum was used to model single-phase flow of fluid salt through a fixed matrix with an assumed porosity of 1.0. The flow properties of fluid salt were selected such that the flow of salt into the disposal room would simulate room closure. The salt-flow continuum contained only two regions, disposal room and fluid halite. The discretization is shown in Figure 2-6. The vertical model dimension was 94.0 m and the horizontal model dimension was 50.0 m. The interbeds were not included in the salt-flow continuum because they were not considered to have a significant impact on the physical process of room closure due to salt creep. The process of room closure using fluid-phase-salt is partially dependent on the discretization of the salt-flow continuum. For this application, the selected discretization and overall dimensions were sufficient to mitigate boundary effects.

As described in Section 1.4, the SANCHO f-series room closure simulations explicitly modeled the resistance to closure (backstress) offered by both the gas pressure in the room and the consolidation of the room contents (waste and backfill). However, the theoretical relationship between potential-driven salt flow and mechanical salt creep is confined to a pressure-controlled backstress. Because of the additional backstress caused by the consolidation of the room contents, the theoretical relationship could not be used to predict room closure. Instead, a calibration process was employed to derive empirical relationships (based on the theoretical relationship) between the salt-phase flow parameters (i.e., viscosity) and mechanical salt creep parameters that could be used in combination with backstress approximation

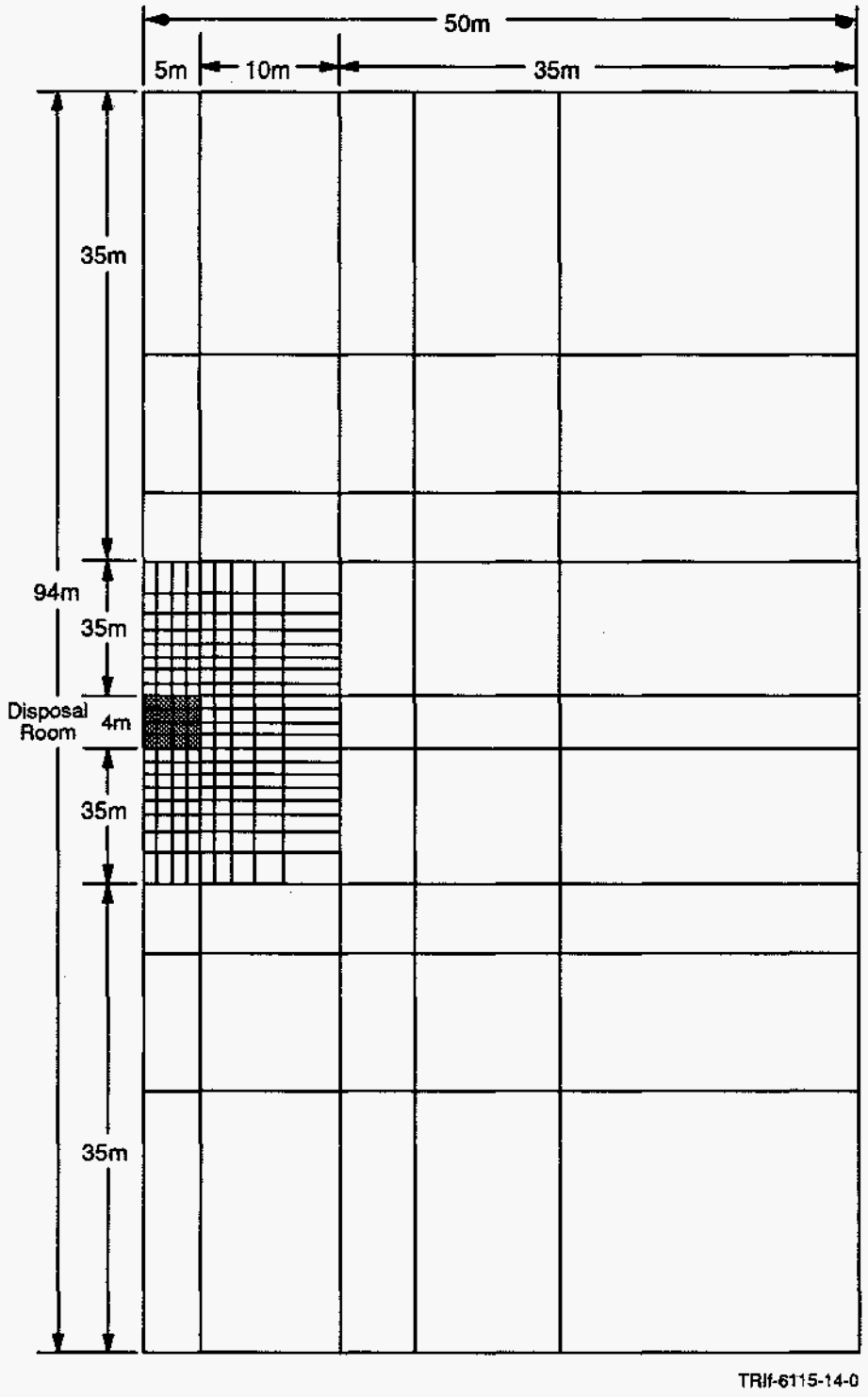

Figure 2-6. TOUGH2/EOS8 discretization of the salt-flow continuum.

methods to reproduce the room closures and pressures from the SANCHO f-series simulations. The calibration process is described in Section 3.1.

Two different fluid-phase-salt methods, boundary backstress (Section 2.3.2.1) and capillary backstress (Section 2.3.2.2), were implemented in TOUGH2/EOS8 to approximate the effects of the backstress caused by compression of the room contents. Both methods connect the salt-flow continuum to the fluid-flow continuum via the disposal room, with no other connections between the two continuums. Each approach adopts a different disposal room conceptualization to connect the two continuums.

2.3.2.1 BOUNDARY BACKSTRESS METHOD

In the boundary backstress method, the effect of the consolidation of the room contents on room closure was accounted for by the presence of an artificial boundary within the disposal room. The disposal room was effectively split into two regions, connected across the artificial boundary (Figure 2-7). Connections between the disposal room and the salt-flow continuum were limited to the region of the disposal room defined as the salt-accessible region. Connections between the disposal room and the fluid-flow continuum were limited to the region of the disposal room defined as the salt-inaccessible region. Connections specified across the artificial boundary were used to control flow between the salt-accessible and salt-inaccessible regions. Salt flow was not permitted across the artificial boundary thereby restricting salt to the salt-accessible portion of the room. Brine and gas were permitted to flow across the artificial boundary, making the entire room void volume available to brine and gas, however brine and gas were not permitted to flow into the salt-flow continuum. Capillary pressure relationships were used to create artificially high phase pressures which prevented the flow of phases into regions where they were not permitted.

Conceptually, as room closure proceeds, the waste drums are compacted irreversibly until some minimum void volume remains within the waste. That void volume is assumed to be inaccessible to salt. Accordingly, the location of the artificial boundary was selected such that the salt-inaccessible region had a void volume (343 m^3) equivalent to the void volume of the fully consolidated room. The salt-accessible region contained the remainder of the initial room void volume.

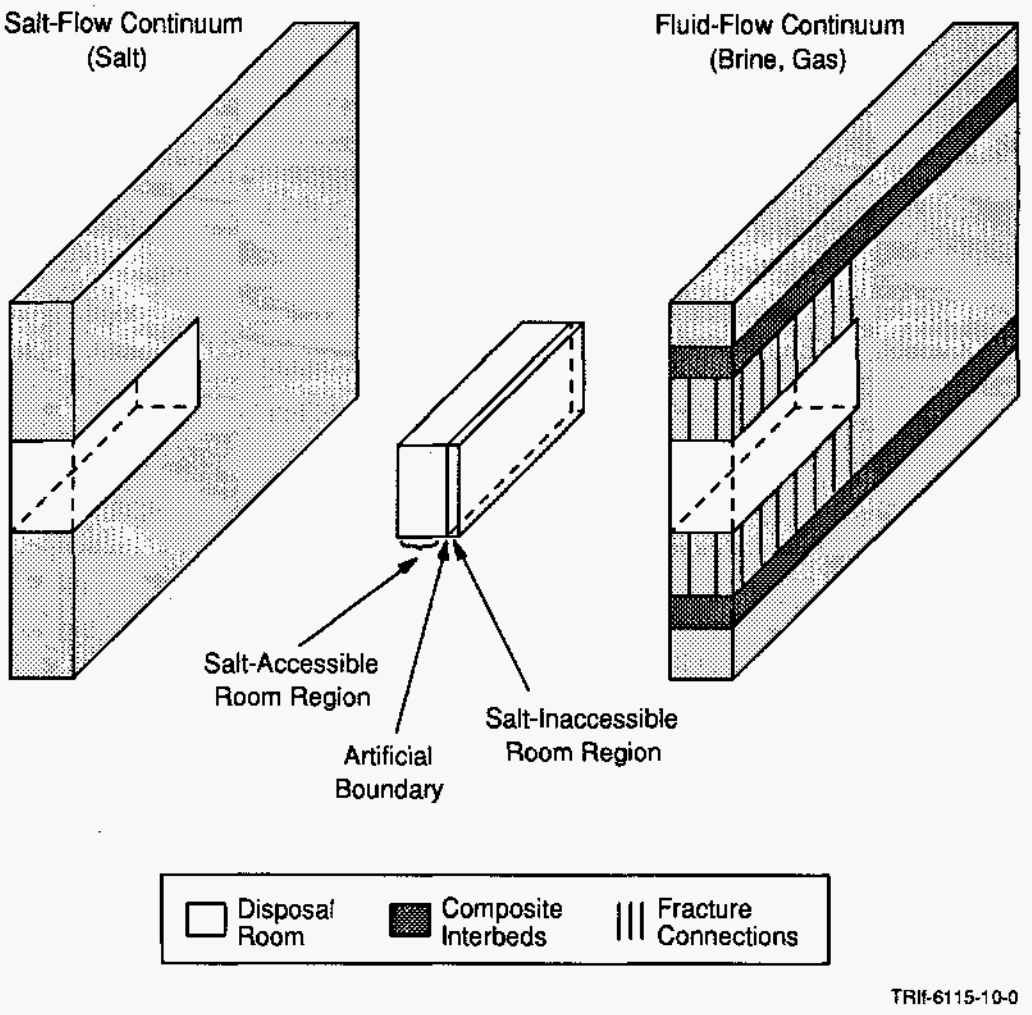

Figure 2-7. System conceptualization with the boundary backstress coupling method.

Waste-generated gas was introduced into both room regions simultaneously. The allocation of the waste-generated gas between the salt-accessible room (with a changing void volume available to gas due to salt inflow) and salt-inaccessible room (with a constant void volume available to gas) was continually adjusted based on the continually changing ratio of void volume in the salt-accessible room to void volume in the salt-inaccessible room.

The model geometry, initial conditions, and gas generation scheme were such that a pressure gradient from the salt-accessible room region (containing gas and salt) to the salt-inaccessible room region (containing gas and brine) was maintained during room closure. Therefore, by constraining the flow of gas from the salt-accessible region across the artificial boundary to the salt-inaccessible region, additional pressurization of the salt-accessible region was achieved. The additional pressurization produced additional resistance to salt inflow which was analogous to the additional backstress caused by consolidation of the waste and backfill. The flow of gas across the artificial boundary was controlled by the gas-phase pressure gradient, the transmissivity of the flow connections, and the relative permeability to gas in the salt-accessible region. An empirical calibration process (Section 3.1.1) was used to determine the parameters controlling the gas-phase pressures and transmissivity in combination with the parameters controlling salt-phase flow. The selected parameters produce the desired additional backstress over the range of SANCHO f-series gas-generation rate histories.

The gas-phase pressure in the salt-accessible room region was directly dependent on the void volume available to gas (changing due to salt flow to and from the salt creep continuum) and the gas mass (changing due to gas generation and flow to the salt-inaccessible region). It was also influenced by the presence of salt through capillary relationships. The gas-phase pressure in the salt-inaccessible room region was also directly dependent on the void volume available to gas (changing due to brine flow to and from the fluid flow continuum) and the gas mass (changing due to gas generation and flow from the salt-accessible region).

Equilibration of gas-phase pressures across the artificial boundary was governed by the flow of gas, which was controlled by the connection transmissivity. By selecting an upstream weighing scheme for mobility, the connection transmissivity was directly controlled by the combination of the intrinsic permeability and the relative permeability to gas (k_{rg}) in the salt-accessible (upstream) room region. Additional control on the transmissivity was exerted by adjusting the area of the connections between the room regions. With integral finite difference

discretization, the connection area can be adjusted without changing the volumes of the two room regions.

In the case of large room closure (as with low gas generation rates), there will be significant salt inflow, and the porosity of the salt-accessible room region will contain a large volume of salt and a relatively small volume of gas (quantified by a low gas saturation, S_g). For a typical k_{rg} versus S_g relationship, the low S_g corresponds to a low (near-zero) k_{rg} value, which results in a significant reduction in gas flow across the artificial boundary. The additional gas mass retained in the salt-accessible room due to the reduced flow causes additional pressurization which provides additional resistance to closure. Because of the restricted flow across the artificial boundary, the salt-inaccessible room is slow to equilibrate with the salt-accessible room and is somewhat buffered from the additional pressurization. In the case of more moderate room closure (as with high gas generation rates), the salt-accessible room region will contain a moderate volume of salt and a relatively large volume of gas. For a high S_g, the corresponding k_{rg} value will be non-zero and may approach one, and will not significantly reduce gas flow across the artificial boundary. As a result there is no additional pressurization of the salt-accessible region. Qualitatively, the additional resistance to closure is similar to the resistance to closure provided by the compression of the waste in that it is more significant when there is greater room closure.

In summary, the boundary backstress method provided additional resistance to closure analogous to waste and backfill consolidation by combining: (1) a flow-restricting boundary which divided the disposal room into two regions; (2) a scheme to partition injected gas between the two room regions; (3) upstream weighing of phase mobilities; and (4) the gas relative permeability relationships. The parameters controlling these processes were determined empirically, in combination with the calibration parameters governing salt-phase flow (Section 3.1.1), to reproduce SANCHO room closure. A single set of parameters was selected that produced a close match with closure results for the entire range of gas generation rates ($f=0.0$ through $f=1.0$) simulated by Stone (1995a).

2.3.2.2 CAPILLARY BACKSTRESS METHOD

In the capillary backstress method, an exponential gas-salt capillary relationship was specified in the room which increased salt-phase pressure and reduced salt inflow as room closure proceeded (i.e., as room void volume decreased). When calibrated (Section 3.1.2), the

exponential capillary pressure relationship can be used to mimic the effects of consolidation of the room contents on room closure. The capillary backstress method utilized a dual-continuum approach (Figure 2-7), however, the disposal room was modeled as a single region within which the movement of gas, brine, and salt was unrestricted by artificial boundaries.

In a three phase system, two capillary pressure relationships, gas-brine and gas-salt, are required to define the differences in pressure between the three phases. TOUGH2/EOS8 uses gas pressure as a primary variable and calculates the pressures of the other two phases from the appropriate capillary pressure relationships.

Because the salt is confined under a lithostatic load, both the initial and long-term pressures of the salt should be approximately equal to lithostatic pressure (15 MPa). However, the near-room salt experiences significant pressure changes as room closure and expansion occurs. In both fluid-phase-salt methods salt-phase flow occurs between the salt-flow continuum and the disposal room in response to a salt-phase pressure gradient. The salt-phase pressure gradient changes due to the changing room gas pressure (through the gas-salt capillary pressure) and the near-room transient salt pressure. The capillary backstress method replaces the default TOUGH2/EOS8 gas-salt capillary pressure relationship in the room with a calibrated exponential relationship in which the gas-salt capillary pressure increases rapidly as room void volume decreases below about 600 m^3 (Figure 2-8).

The capillary backstress method was developed out of concern that the split-room conceptualization used in the boundary backstress method might adversely impact brine and gas flow within the room. Because the capillary backstress method utilized a single region to simulate the disposal room, it was expected that brine and gas flow within, to, and from the room might be different than with the boundary backstress method.

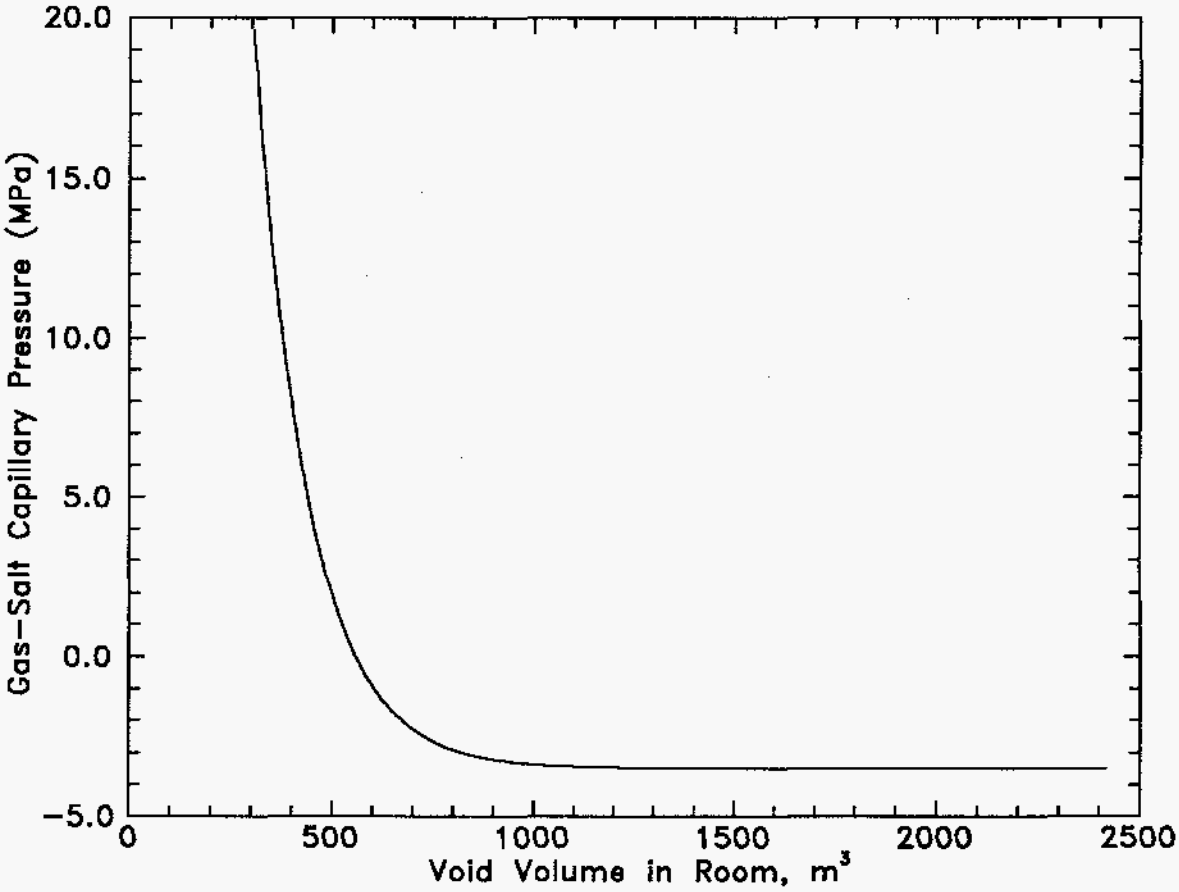

Figure 2-8. Exponential gas-salt capillary pressure relationship used with the capillary backstress coupling method.

3.0 SIMULATION RESULTS

Section 2 described the following approaches for examining the effects of coupled gas generation, multiphase flow, and room closure on repository performance:

Fixed-Room Conceptualizations (Section 2.2)
- Initial Room Geometry
- Intermediate Room Geometry
- Fully Consolidated Room Geometry

Porosity Function Approaches (Section 2.3.1)
- Moles-Time-Porosity Surface Interpolation
- Moles-Time-Porosity Line Interpolation
- Pressure-Time-Porosity Line Interpolation

Fluid-Phase-Salt Approaches (Section 2.3.2)
- Boundary Backstress Method
- Capillary Backstress Method

To evaluate which method or methods provide realistic approximations of process coupling, the following TOUGH2/EOS8 simulations were performed: room closure calibration; sealed room closure (no fluid flow between the room and the Salado Formation); and coupled flow and closure.

Room closure calibration (Section 3.1) simulated the closure and consolidation of a sealed disposal room under each of the five gas-generation rate histories used by Stone (1995a). These simulations were analogous to the SANCHO f-series simulations (Stone, 1995a), with waste-generated gas confined to the room and no brine present. These simulations provided an indication of how well each of the methods could reproduce the coupled gas generation and room closure results from SANCHO. For the fluid-phase-salt methods, these simulations were used to calibrate the salt flow and backstress approximation parameters to reproduce the SANCHO results.

Sealed room closure (Section 3.2) used the same conceptualization as room closure calibration. Simulations were performed with (1) a gas-generation rate history different in both

magnitude and duration than the SANCHO rate histories, and (2) a constant brine source within the room.

Coupled flow and closure (Section 3.3) simulated the closure and consolidation of a disposal room coupled with brine and gas flow between the room and the surrounding Salado Formation. Several different gas-generation rate histories were simulated. These simulations examined the performance of each method under coupled flow and closure conditions.

All simulations used best estimates of the hydrologic and fluid properties for the disposal room and the Salado Formation. A detailed summary of all hydrologic and fluid properties, including rationales and comments concerning the determination of the best estimate values, is presented in Freeze et al. (1995). The best estimate represents a most likely value, but has no statistical significance (i.e., it is not a calculated mean, median, average, or expected value).

Hydrologic parameters include all physical properties, multiphase flow properties, and initial conditions controlling multiphase brine and gas flow within the fluid-flow continuum (disposal room, halite, and interbeds). Best estimate hydrologic parameters are summarized in Table 3-1.

Table 3-1. Simulated Hydrologic Parameters

Parameter	Units	Disposal Room	Halite	Anhydrite Interbeds
Intrinsic Permeability (k)	m^2	$1x10^{-17}$	$1x10^{-21}$	$1x10^{-19}$
Porosity (ϕ)		0.66[a]	0.01	0.01
Rock Compressibility (α)	Pa^{-1}	0.0	$2.7x10^{-11}$	$8.3x10^{-12}$
Residual Brine Saturation (S_{br})		0.276	0.20	0.20
Residual Gas Saturation (S_{gr})		0.02	0.20	0.20
Pore-Size Lambda (λ)		2.89	0.70	0.70
Threshold Pressure (p_t)	MPa	0.0	10.3	0.3
Initial Brine Pressure (p_o)	MPa	0.1[a]	12.0	12.0
Initial Brine Saturation (S_{bo})		0.01[a]	1.0	1.0

[a] These parameters vary with room closure and fixed-room geometry.

In porosity function and fluid-phase-salt simulations, the initial room porosity was 0.66 and room porosity changed with room closure and expansion. With the fixed-room conceptualization, room porosity, initial brine pressure, and initial brine saturation were different for each geometry. For initial room geometry simulations, the values were as shown in Table 3-1. For intermediate room geometry simulations, the room porosity was 0.38, the initial room pressure was 0.32 MPa, and the initial brine saturation was 0.03. With the fully consolidated room geometry, the room porosity was 0.22, the initial room pressure was 0.70 MPa, and the initial brine saturation was 0.07. Multiphase flow properties were determined from measured data on analogue materials using a model modified from Brooks and Corey (1964). The methodology is described in Freeze et al. (1995). Simulated relative permeability relationships for the disposal room are shown in Figure 3-1. The simulated gas-brine capillary pressure in the disposal room was zero. The simulated relative permeability and capillary pressure relationships for the Salado Formation halite and interbeds are shown in Figures 3-2 and 3-3.

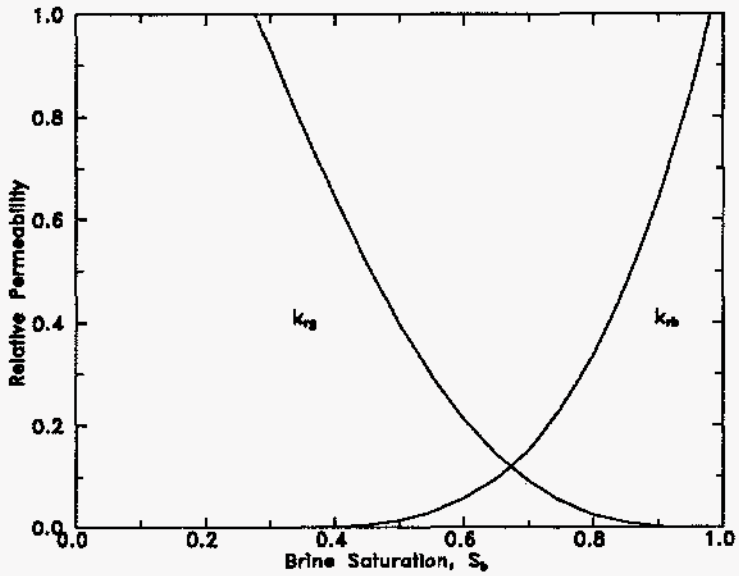

Figure 3-1. Simulated relative permeability relationships for the disposal room.

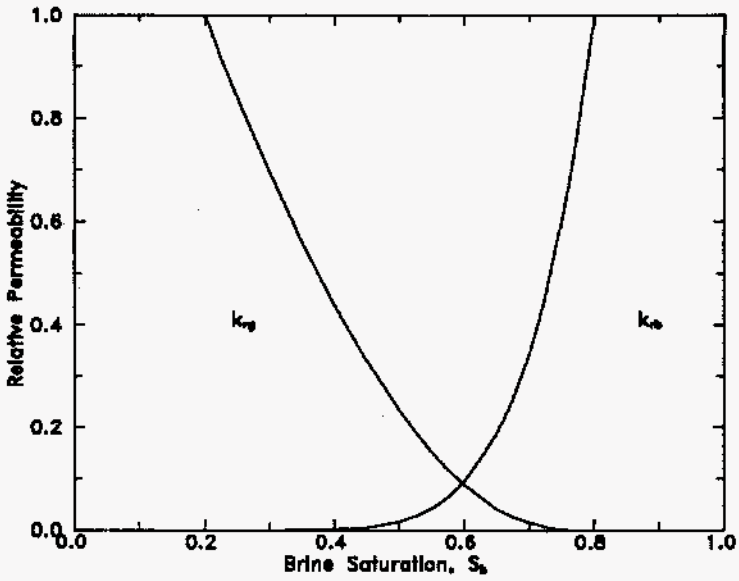

Figure 3-2. Simulated relative permeability relationships for the Salado Formation halite and interbeds.

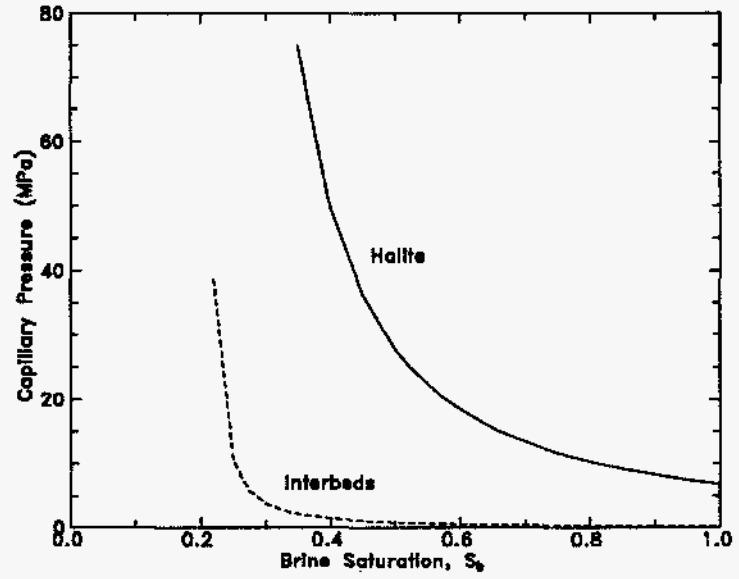

Figure 3-3. Simulated gas-brine capillary pressure relationships for the Salado Formation halite and interbeds.

Fluid properties were determined internally by TOUGH2/EOS8 from equation of state relationships. With the modified EOS8H module, the gas is assumed to be hydrogen, behaving as an ideal gas with a viscosity of 9×10^{-6} Pa•s. The brine has a density of 1,200 kg/m^3, a viscosity of 1.6×10^{-3} Pa•s, and a compressibility of 2.4×10^{-10} Pa^{-1}. The solubility of hydrogen in brine is described by a Henry's Law Constant, K_H, of 2.9×10^{10} Pa. The fluid properties presented here are approximate values. Actual values, which vary as a function of temperature and pressure, are given in Freeze et al. (1995).

The simulated gas-generation rate histories are summarized in Table 3-2 in terms of moles per drum per year.

Table 3-2. Simulated Gas-Generation Rate Histories (moles/drum/yr)

1. Room Closure Calibration			
	0-550 yrs	550-1050 yrs	> 1050 yrs
f=1.0	2.0	1.0	0.0
f=0.6	1.2	0.6	0.0
f=0.4	0.8	0.4	0.0
f=0.2	0.4	0.2	0.0
f=0.0	0.0	0.0	0.0

2. Sealed Room Closure				
		0-550 yrs	550-1050 yrs	> 1050 yrs
f=0.2 with 0.175 m^3/yr brine		0.4	0.2	0.0
	0-250 yrs	250-750 yrs	750-1200 yrs	1200-1825
Non f-series	0.4	2.0	0.0	0.8

3. Coupled Flow and Closure			
	0-550 yrs	550-1050 yrs	> 1050 yrs
2 / 1 (brine-inundated)	2	1	0
	0-5500 yrs	5500-10500 yrs	> 10500 yrs
0.2/0.1 (vapor-limited)	0.2	0.1	0
0 / 0 (no gas generation)	0	0	0

With TOUGH2/EOS8, gas generation wa ılated with gas sources in the disposal room. Source rates were specified in units of kg he conversion from moles per drum per year makes the following assumptions: 6,804 per room; 365.25 days per year; and 2.016 x 10^{-3} kg per mole of H_2. Furthermore, each had six gas sources, located in the six elements (grid blocks) nearest the room center. Ga ration was scaled down to account for the half-width and unit length of the simulated rc However, simulation results were re-scaled to represent a full room (full width, 91.44 r th).

All simulations assumed a total eration potential of 1,600 moles per drum (1.09×10^7 moles per room), which is comprised of 1,050 moles per drum for anoxic corrosion and 550 moles per drum for microbial degradation (Beráun and Davies, 1992). This gas potential corresponds to a gas mass of about 22,000 kg. In each simulation, gas-generation rates were specified for the duration of the simulation, changing from an early time rate to a late time rate when the microbial potential was exhausted, and changing to zero when the corrosion potential was exhausted. In some lower gas-generation rate simulations the total gas potential was not exhausted by the end of the simulation.

3.1 Room Closure Calibration

TOUGH2/EOS8 is a fluid and heat flow code and does not directly simulate mechanical deformation. The geomechanics of salt creep and room closure and consolidation are approximated in the flow and closure coupling methods, all of which are based on results from the SANCHO mechanical deformation code. Room closure calibration was performed for each of the coupling methods by comparing TOUGH2/EOS8 simulation results of gas generation in a sealed room (i.e., no brine inflow and no gas release) with results from the SANCHO f-series simulations.

With the fixed-room geometry conceptualization, room closure was not explicitly modeled and room closure calibration was not required. A comparison of the fixed-room void volumes with the SANCHO f-series room closure results are shown in Figure 3-4. The fixed-room void volumes approximate the range of expected room closure with the intermediate room most representative of high gas-generation rates ($f \geq 0.6$) and the fully consolidated room most representative of low rates ($f \leq 0.2$).

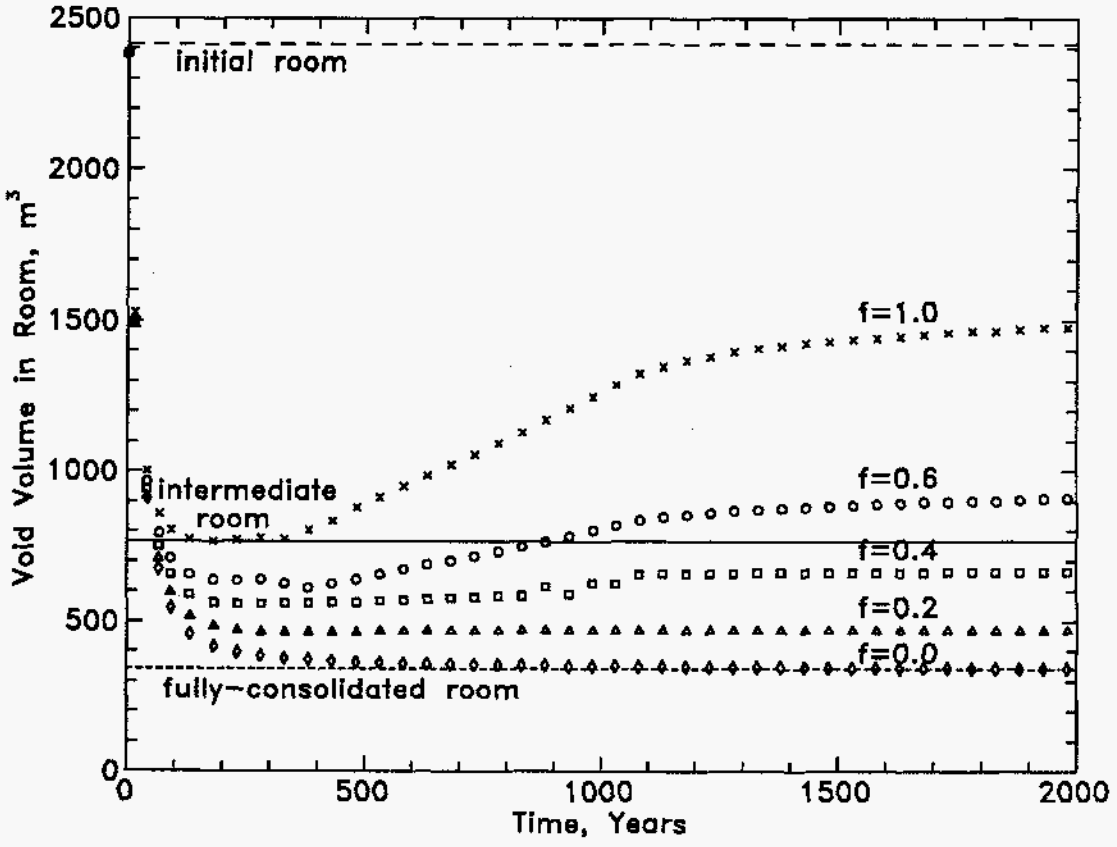

Figure 3-4. Comparison of fixed room geometry void volumes with SANCHO results (Stone, 1995a) for the closure of a sealed room under five different gas-generation rate histories.

With the porosity function approach, room closure was determined by interpolating between SANCHO-produced gas-time-porosity relationships. A comparison of the TOUGH2/EOS8 porosity function results with SANCHO f-series results was somewhat redundant, as the porosity functions were able to exactly reproduce the room closure and room pressure data from which they were derived. TOUGH2/EOS8 calibration results are shown for moles-time-porosity surface interpolation, moles-time-porosity line interpolation, and pressure-time-porosity line interpolation in Figures 3-5, 3-6, and 3-7, respectively.

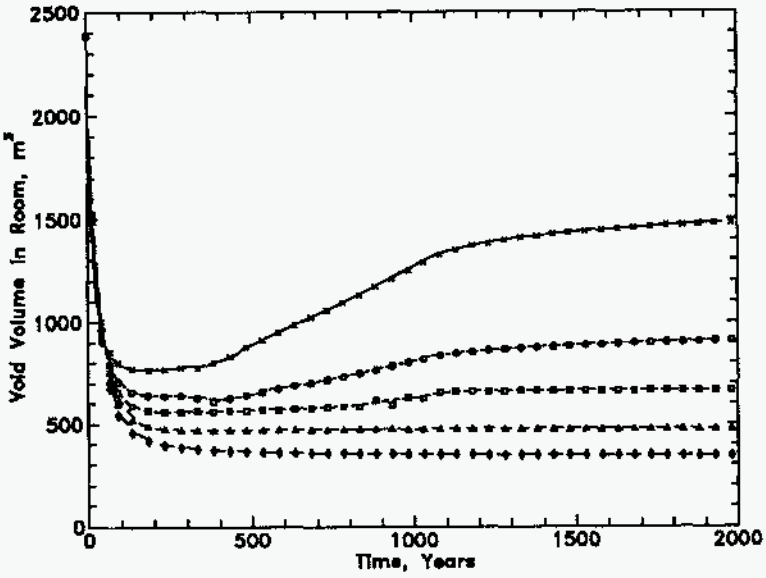

(a) Void Volume

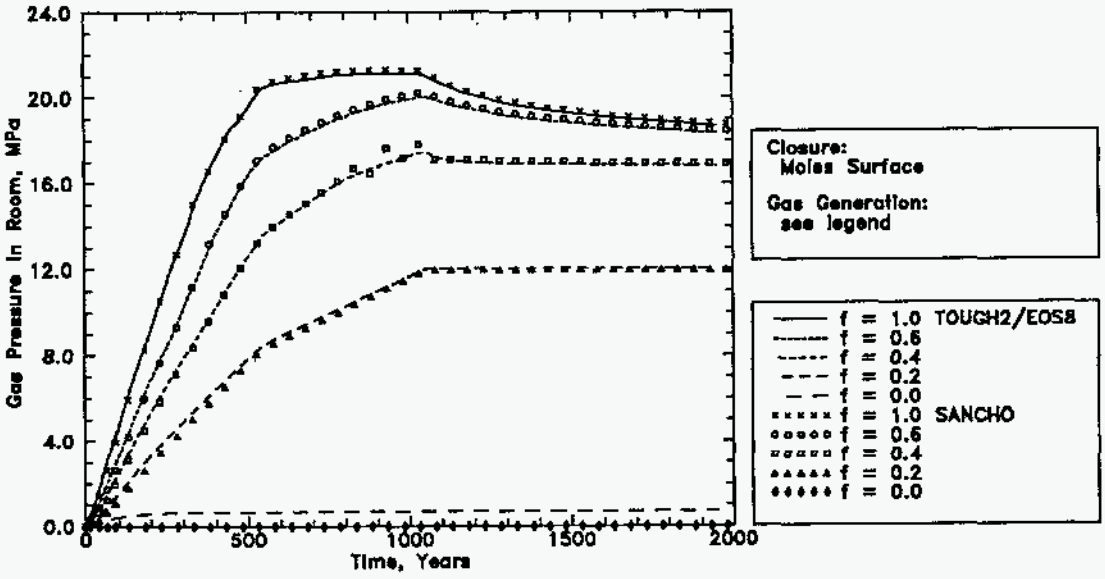

(b) Room Pressure

Figure 3-5. Comparison of TOUGH2/EOS8 moles-time-porosity surface results with SANCHO results (Stone, 1995a) for the closure of a sealed room under five different gas-generation rate histories.

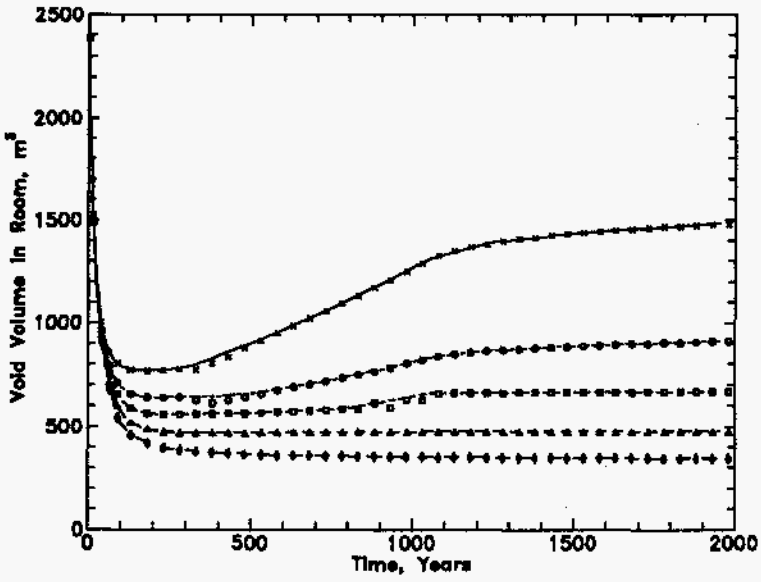

(a) Void Volume

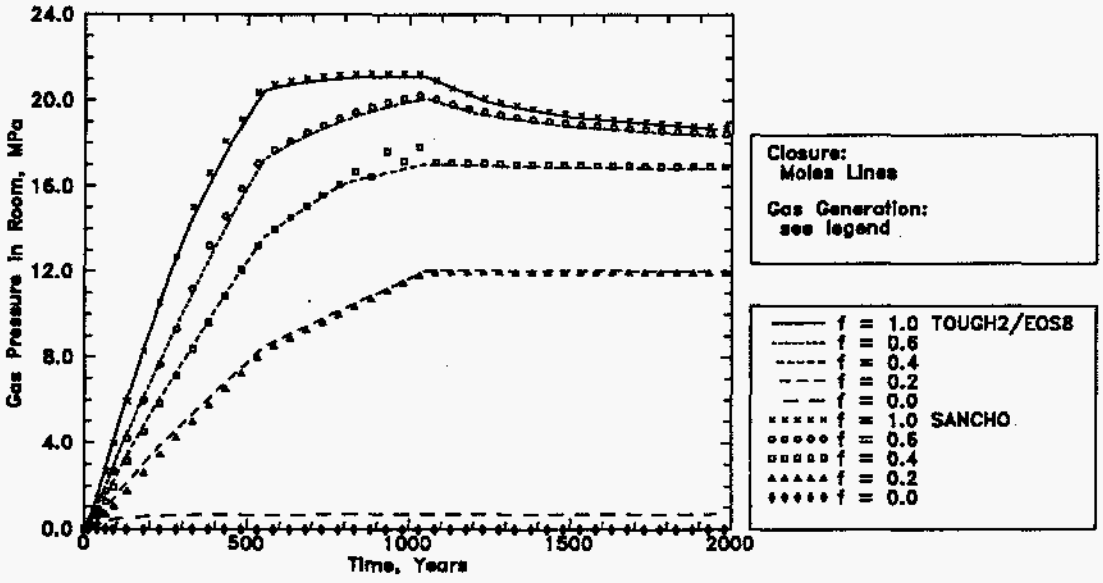

(b) Room Pressure

Figure 3-6. Comparison of TOUGH2/EOS8 moles-time-porosity line results with SANCHO results (Stone, 1995a) for the closure of a sealed room under five different gas-generation rate histories.

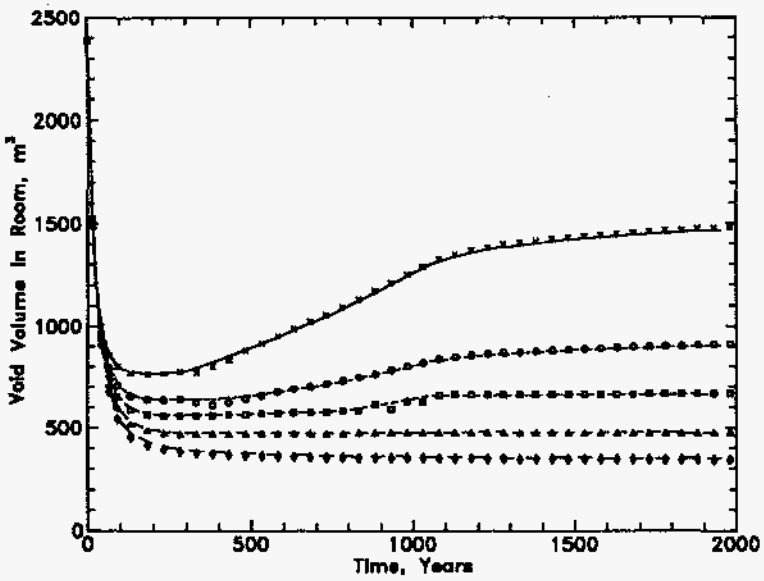

(a) Void Volume

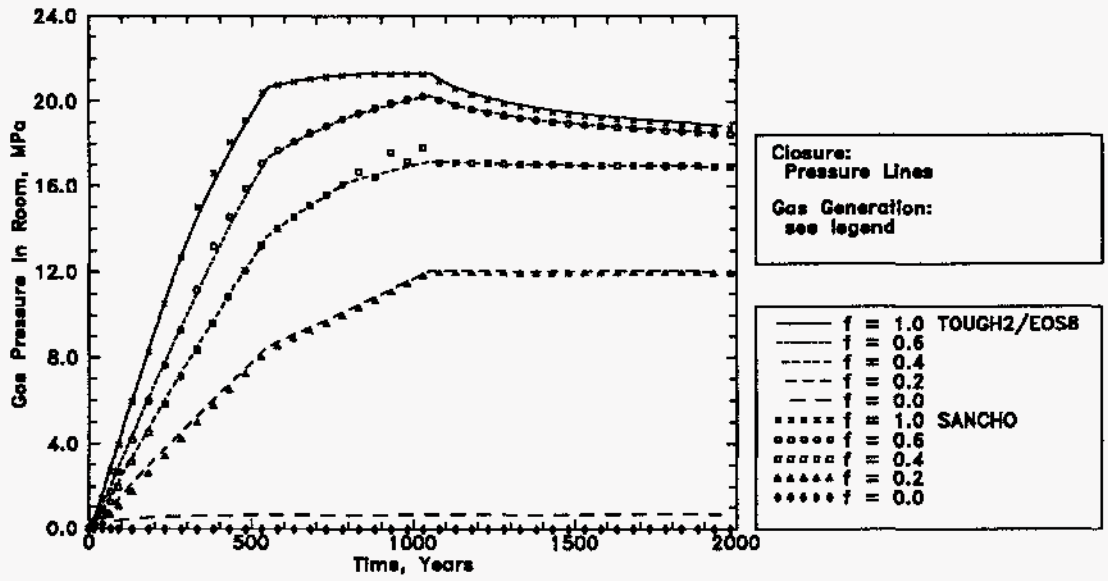

(b) Room Pressure

Figure 3-7. Comparison of TOUGH2/EOS8 pressure-time-porosity line results with SANCHO results (Stone, 1995a) for the closure of a sealed room under five different gas-generation rate histories.

With the fluid-phase-salt approach, calibration of TOUGH2/EOS8 room closure was an iterative process to determine the combination of salt-phase flow properties and backstress control parameters that most closely reproduced the entire suite of SANCHO f-series results. Salt creep was represented by potential-driven flow of fluid salt. The flow of salt was controlled by the pressure gradient between the salt-flow continuum and the disposal room, by the salt-phase flow properties, and by the backstress approximation scheme. The initial salt-phase pressures of 15.0 MPa in salt-flow continuum and 0.1 MPa in the disposal room, which were selected to be consistent with the initial conditions used by Stone (1995a), produced a flow of salt-phase fluid from the salt-flow continuum into the room that was representative of room closure. For each method (boundary backstress and capillary backstress) a set of salt-phase flow parameters was selected which produced TOUGH2/EOS8 results that closely matched the room closure and room pressure results from the SANCHO f-series. Where practical, the physical properties of salt and the theoretical relationships between potential flow parameters and mechanical salt creep parameters (Appendix A) were preserved. However, because the theoretical relationship could not account for the backstress caused by the consolidation of the room contents, the salt-phase flow properties and backstress control parameters were determined through an empirical calibration process for both the boundary backstress method (Section 3.1.1) and the capillary backstress method (Section 3.1.2).

3.1.1 Boundary Backstress Method

The boundary backstress method (Section 2.3.2.1) utilized an artificial boundary to divide the disposal room into a salt-accessible and a salt-inaccessible region. A scheme to partition injected gas between the two room regions maintained a pressure gradient from the salt-accessible room to the salt-inaccessible room. The area (available for flow) of the connection between the two room regions (boundary connection area) was selected to restrict gas flow across the artificial boundary, resulting in artificially high pressures in the salt-accessible region. The high pressure provided additional resistance to salt inflow (closure) analogous to waste and backfill compression.

Salt-phase viscosity and salt-phase relative permeability were used to control salt flow into the room. The boundary connection area was used in combination with upstream weighting of phase mobilities and the gas relative permeability relationships to control gas flow across the artificial boundary and thereby regulate room gas pressures. The gas-salt capillary pressure was

used to modify room gas and salt pressures and therefore influenced both salt flow into the room and gas flow across the boundary. Salt-phase viscosity, μ_s, and salt-phase relative permeability, k_{rs}, were specified to have the following functional form:

$$\mu_s = A_\mu + B_\mu (p_s - p_{s\,ref})^2 \qquad (3\text{-}1)$$

where:

μ_s	=	salt-phase viscosity (Pa-s),
p_s	=	salt-phase pressure (Pa), and
$p_{s\,ref}$	=	reference salt-phase pressure (-3.4×10^6 Pa).

$$k_{rs} = C_{rs} * (S_s - S_{sr}) / (1 - S_{sr}) \qquad (3\text{-}2)$$

where:

k_{rs}	=	salt-phase relative permeability,
S_s	=	salt-phase saturation, and
S_{sr}	=	irreducible salt-phase saturation (0.01).

A_μ, B_μ, and C_{rs} are fitting parameters. The reference salt pressure was selected to be equal to the initial salt pressure in the room. The initial salt pressure was determined as the sum of the initial gas pressure (0.1 MPa) and the gas-salt capillary pressure (-3.5 MPa, see below). Five calibration parameters, the salt-phase viscosity coefficients (A_μ and B_μ), the salt-phase permeability multiplier (C_{rs}), the boundary connection area (A_{bound}), and the gas-salt capillary pressure (p_{cgs}), were determined empirically (and non-uniquely) to reproduce SANCHO room closure. The following set of calibration parameters, valid over the entire range of f-series gas-generation rate histories, was determined by iterative calibration:

A_μ	=	3.0×10^{-8} Pa-s
B_μ	=	2.5×10^{-21} s/Pa
C_{rs}	=	0.01
A_{bound}	=	7.5 m^2
p_{cgs}	=	-3.5 MPa

Boundary backstress calibration results are shown in Figure 3-8. The boundary backstress method slightly underestimates room pressure at high gas-generation rates ($f \geq 0.6$) and slightly overestimates room pressure at low rates ($f \leq 0.2$). Implications of these calibration results on coupled flow and closure simulations are discussed in Section 3.3. The salt-phase viscosity coefficients, A_μ and B_μ, define the viscosity-pressure relationship for salt (Figure 3-9). The salt-

phase viscosity acts in conjunction with the intrinsic and relative permeabilities to control salt mobility, which is the potential flow equivalent to salt creep.

The selection of the gas-salt capillary pressure requires some discussion. Rapid room closure resulted in equilibration between pressures in the salt-accessible room region and in the near-field salt-flow continuum within the first few years of simulation. Because salt-phase flow provided the mechanism for pressure equilibration, the pressures were strongly influenced by the far-field salt-phase pressure of 15.0 MPa, representative of lithostatic pressure. The gas-phase pressure in the salt-accessible room region was dependent on the mass of gas present and the void volume available to gas. It was also influenced by the near-15.0 MPa pressure of the salt phase sharing the void space through the gas-salt capillary pressure relationship.

In the case of large room closure (corresponding to f=0.2 and lower), the influence of the salt phase on the salt-accessible region gas-phase pressures was not transferred to the salt-inaccessible region due to restricted gas flow that resulted in slow pressure equilibration between the room regions. The gas pressures in the salt-inaccessible room were more directly comparable with SANCHO room gas pressures than were the near-15.0 MPa gas pressures in the salt-accessible room. In the case of low to moderate room closure (corresponding to f=0.4 and higher), the influence of the salt phase on the salt-accessible region gas-phase pressures was readily transferred to the salt-inaccessible region due to relatively unrestricted gas flow that resulted in rapid pressure equilibration between the room regions. The gas-phase pressures in the salt-inaccessible room region were somewhat skewed towards 15.0 MPa and were lower than the corresponding SANCHO room pressures, but were still more directly comparable with SANCHO than were the gas pressures in the salt-accessible room.

To compensate for the fact that the TOUGH2/EOS8 room gas pressures were slightly lower than the corresponding SANCHO room gas pressures at the higher gas generation rates ($f \geq 0.4$), a constant gas-salt capillary pressure was specified in the salt-accessible room. The gas-salt capillary pressure increased gas-phase pressures in the salt-accessible room by a constant value. At high gas generation rates, the gas-phase pressure increase was transferred to the salt-inaccessible room, increasing gas pressures there towards the SANCHO values. At low gas generation rates, the gas-phase pressure increase was not transferred to the salt-inaccessible room and gas-phase pressures there, already similar to the SANCHO values, were not affected.

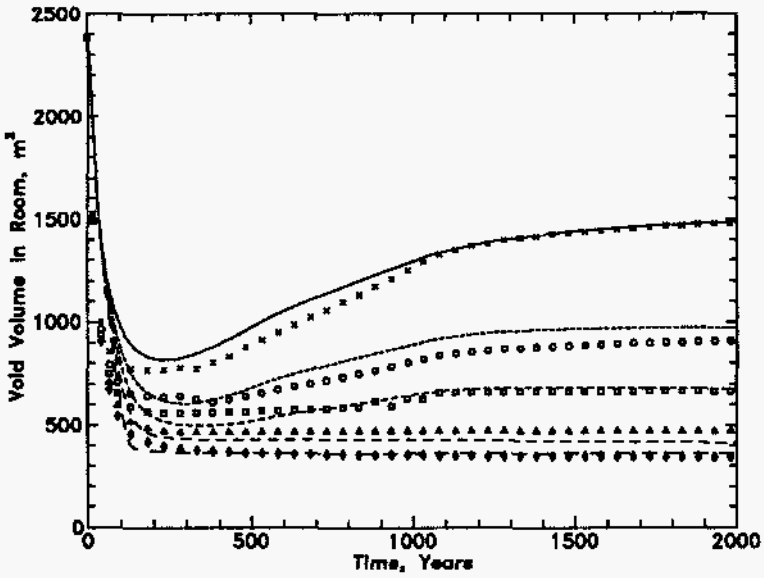

(a) Void Volume

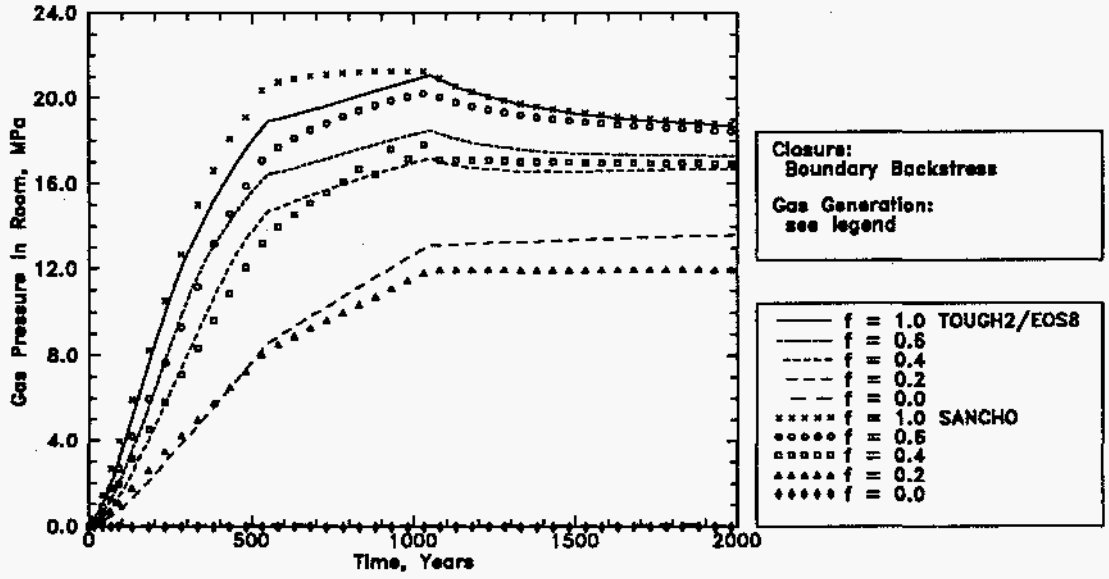

(b) Room Pressure

Figure 3-8. Room closure calibration of TOUGH2/EOS8 boundary backstress method to SANCHO simulated closure of a sealed room (Stone, 1995a) under five different gas-generation rate histories.

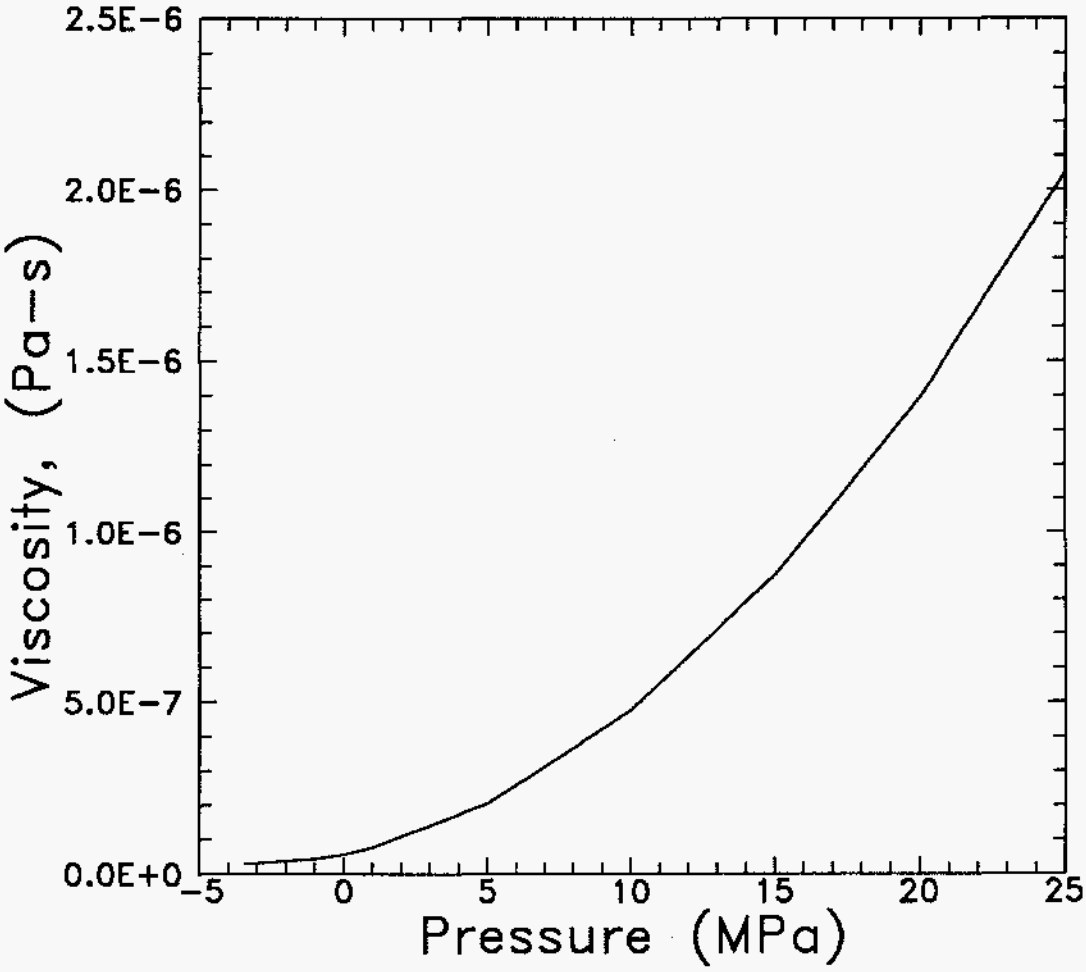

Figure 3-9. Salt phase viscosity relationship used in TOUGH2/EOS8 with the boundary backstress method.

The constant gas-salt capillary pressure also produced better agreement between long-term SANCHO and TOUGH2/EOS8 simulated room pressures. In SANCHO, the rate of salt creep was very slow for high gas-generation rate simulations and the system approached lithostatic equilibrium very slowly. Rapid pressurization from the high gas-generation rates produced gas-phase pressures in the room that remained greater than lithostatic for a long period of time. In TOUGH2/EOS8, salt flow in response to pressure gradients resulted in the system approaching equilibrium (at lithostatic salt-phase pressure) more quickly. With zero gas-salt capillary pressure, the late-time room gas-phase pressures were approximately lithostatic. However, with a constant, non-zero gas-salt capillary pressure, late-time room gas-phase pressures were greater than lithostatic, consistent with the SANCHO results.

The boundary backstress method captures a wide range of room closure and pressure behavior (f=0.0 to 1.0) with a single set of calibrated parameters. For this reason, it is expected that the method can predict essential room behavior under a similarly wide range of gas generation and closure conditions.

3.1.2 Capillary Backstress Method

The capillary backstress method (Section 2.3.2.2) provided resistance to room closure analogous to waste and backfill compression with an exponential gas-salt capillary pressure relationship that reduced salt inflow as closure proceeded. The changing capillary pressure modified room salt pressures and thereby affected salt flow into the room. Salt flow was also influenced by the salt-phase viscosity (Equation 3-1) and relative permeability (Equation 3-2). The gas-salt capillary pressure, p_{cgs}, was calculated from:

$$p_{cgs} = D_{pc}\, e^{-(E_{pc})(V_m)} + F_{pc} \qquad (3\text{-}3)$$

where:

V_m = TOUGH2/EOS8 room void volume (m).

D_{pc}, E_{pc}, and F_{pc} are fitting parameters. Equation 3-3 was calibrated such that the room void volume was 342 m^3 when the gas pressure in the room was 0.7 MPa (representative of long-term conditions for f=0.0) and 480 m^3 when the gas pressure was 12.0 MPa (long-term conditions for f=0.2). The calibration also required that the capillary pressure exponentially

approach a lower limit of -3.5 MPa as void volume increases. The -3.5 MPa lower limit was selected so that TOUGH2/EOS8 would better reproduce the SANCHO room pressure as discussed in Section 3.1.1.

The exponential capillary pressure function (Figure 2-8) was calibrated using Equation 3-3 with:

$$D_{pc} = 2.22 \times 10^{8} \text{ Pa}$$
$$E_{pc} = 1.36 \text{ 1/m}^3$$
$$F_{pc} = -3.5 \times 10^{6} \text{ Pa}$$

The void volumes in Figure 2-8 were scaled to represent a full-size room. Equation 3-3 uses the void volume of a unit length, half-width model room. The sharp increase in gas-salt capillary pressure at low void volume corresponds to the increased backstress from room consolidation as closure proceeds.

In addition to the three gas-salt capillary pressure coefficients (D_{pc}, E_{pc}, and F_{pc}), three other calibration parameters, the salt-phase viscosity coefficients (A_μ and B_μ) and the salt-phase relative permeability multiplier (C_{rs}), were determined empirically (and non-uniquely) to reproduce SANCHO room closure. The following set of calibration parameters, valid over the entire range of f-series gas-generation rates, was determined by iterative calibration:

$$A_\mu = 8.0 \times 10^{-5} \text{ Pa-s}$$
$$B_\mu = 3.5 \times 10^{-18} \text{ s/Pa}$$
$$C_{rs} = 20.0$$

Capillary backstress calibration results are shown in Figure 3-10. The capillary backstress method underestimates room pressure at high gas-generation rates ($f >= 0.6$). Implications of these calibration results on coupled flow and closure simulations are discussed in Section 3.3. The viscosity-pressure relationship for salt is shown in Figure 3-11. The salt-phase viscosities were approximately three orders of magnitude higher than for the boundary backstress method. However, because C_{rs} was also about three orders of magnitude higher, salt mobilities were approximately the same under both methods.

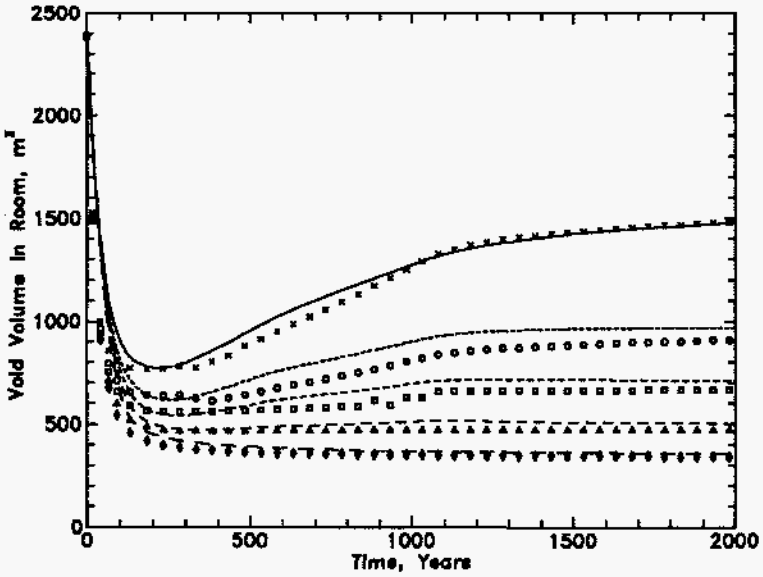

(a) Void Volume

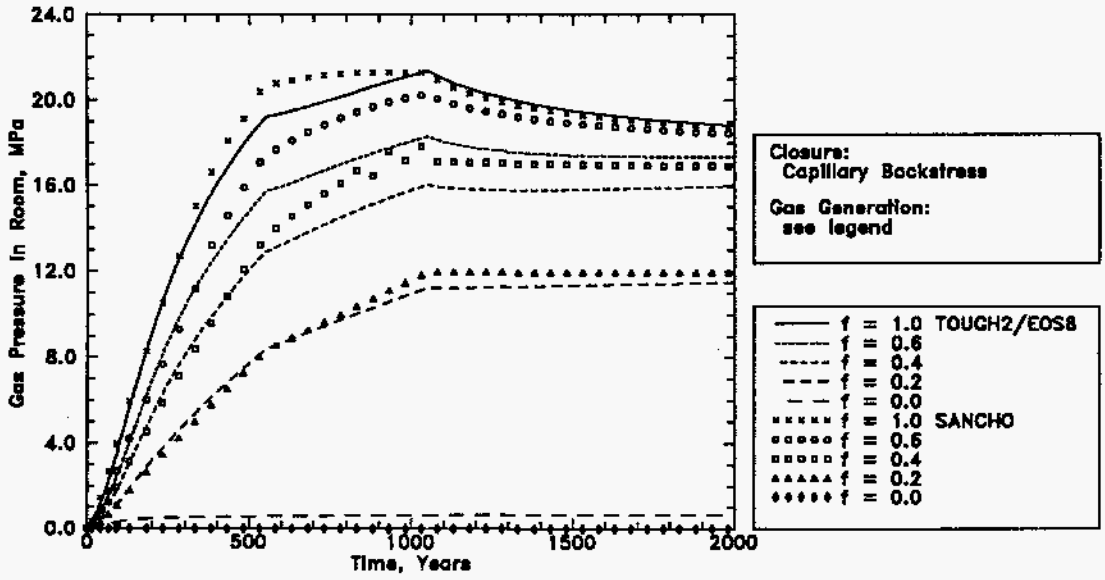

(b) Room Pressure

Figure 3-10. Room closure calibration of TOUGH2/EOS8 capillary backstress method to SANCHO simulated closure of a sealed room (Stone, 1995a) under five different gas-generation rate histories.

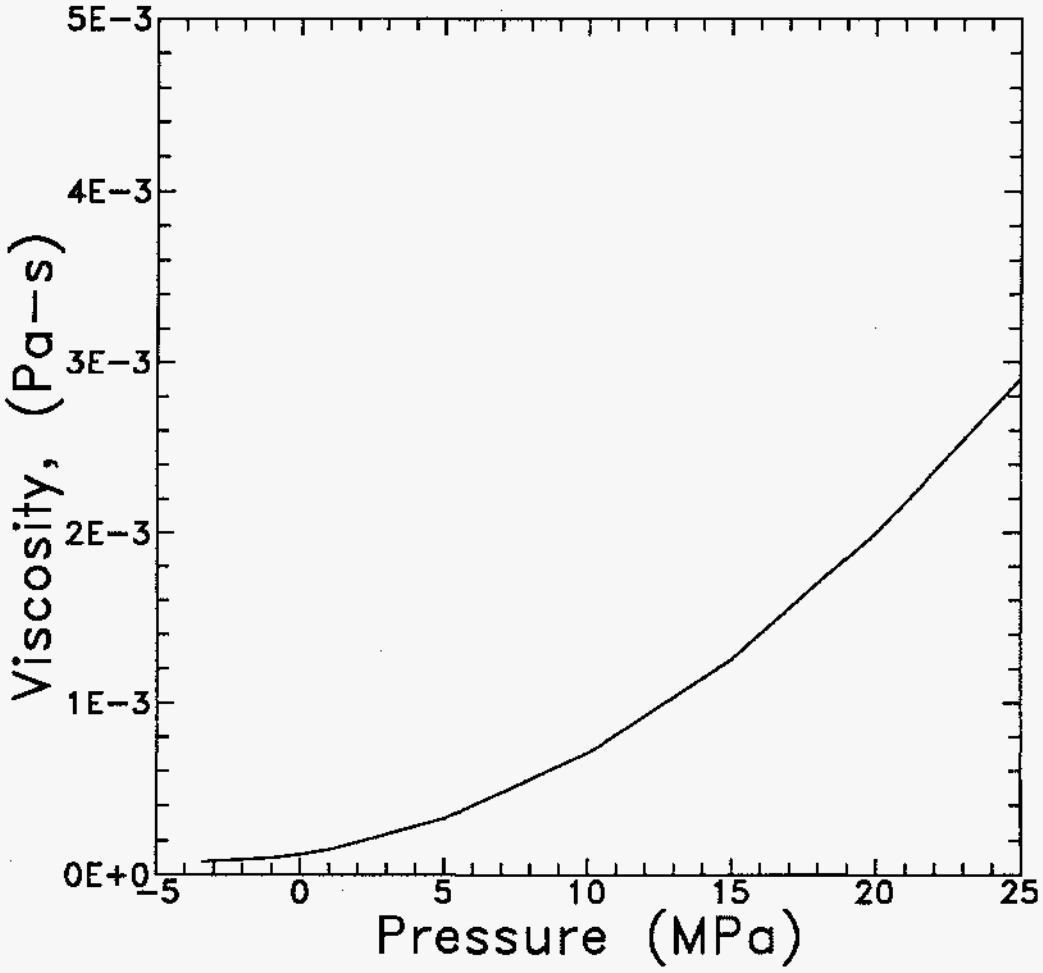

Figure 3-11. Salt phase viscosity relationship used in TOUGH2/EOS8 with the capillary backstress method.

3.2 Sealed Room Closure

Two sets of sealed room closure simulations were performed in addition to the room closure calibration simulations (Section 3.1). Room closure calibration showed that both the porosity function and fluid-phase-salt coupling methods could predict room closure under each of the five f-series gas-generation rate histories when gas was confined to the room and no brine was present. The additional simulations examined the effects of brine in the room and of a non-f-series rate history on the behavior of the various coupling methods.

To examine the impact of brine in the room, a sealed room was simulated having the f=0.2 gas-generation rate history and a constant brine source within the room. Brine sources were located in each of the six elements containing a gas source. The total brine injection rate, scaled to represent a full room, was 210 kg/yr (approximately 0.175 m^3/yr) corresponding to brine volume in the room the end of 2,000 years of approximately 350 m^3. Simulation results for disposal room void volume and gas pressure are shown in Figures 3-12a and 3-12b, respectively.

As discussed in Sections 2.3.1.1 and 2.3.1.2, the presence of brine in the room does not impact room closure in the moles-based porosity function methods. Results from these brine source simulations confirm that observation. For the boundary backstress, capillary backstress, and pressure-time-line methods, an increase in room void volume (Figure 3-12a) partially mitigated the increase in room gas pressure (Figure 3-12b) resulting from the constant brine generation. However, Figure 3-12a shows that, for the moles-time-surface and moles-time-line interpolation methods (which overlay each other in Figures 3-12a and 3-12b), there was no change in room void volume beyond the end of gas generation at 1,050 years (Figure 3-12a) because the number of moles of gas in the room did not change beyond that time. Figure 3-12b shows that, in the absence of room expansion for the moles-based methods, gas pressures in the room increased significantly as brine generation continued. With the two moles-based porosity function methods, brine generation did not impact the room porosity through the porosity functions but it did reduce the void volume available for gas, resulting in the high room pressures.

To examine the impact of a non-f-series rate history on the behavior of the various coupling methods, a sealed room was simulated with a gas generation rate of 0.4 moles per drum per year for the first 250 years, 2.0 moles per drum per year from 250 years to 750 years; 0 moles per drum per year from 750 years to 1,200 years, 0.8 moles per drum per year from 1,200 years

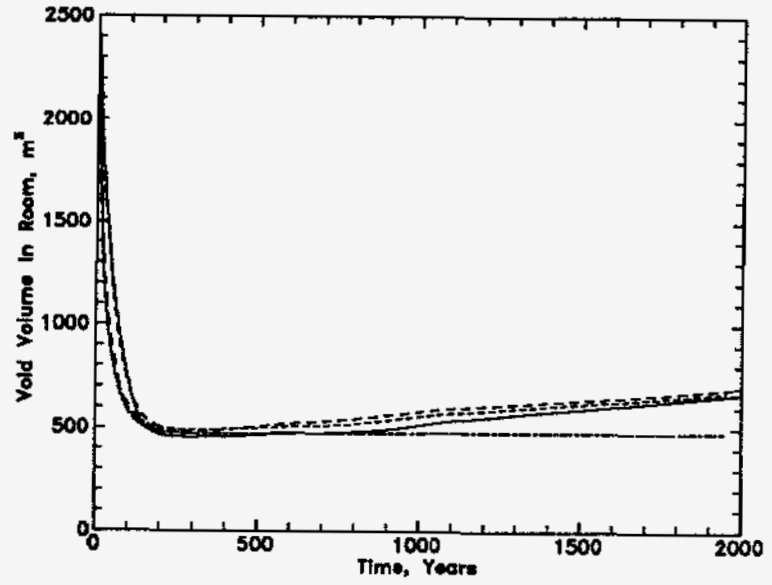

(a) Void Volume

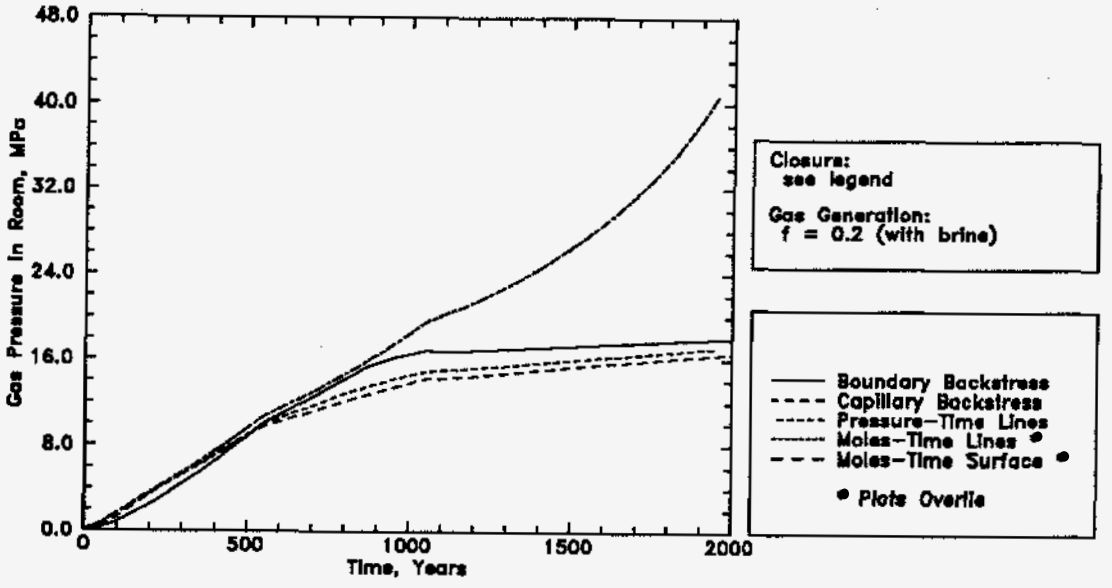

(b) Room Pressure

Figure 3-12. Comparison of flow and closure coupling methods for a sealed room with a constant brine source (note deviatory behavior of moles-based methods beyond 1,050 years).

to 1,825 years; and 0 moles per drum per year from 1,825 years to the end of the simulation at 2,000 years. This rate history is quite different from the f-series in that the gas-generation rate did not decrease with time. The initial low rate was followed by a high rate and a zero gas-generation rate was followed by a non-zero rate. The specified times for rate switches were also different from the f-series simulations. The total gas-generation potential of 1,600 moles per drum was the same as for the f=1.0 case.

Simulations results for disposal room void volume and gas pressure are shown in Figures 3-13a and 3-13b, respectively. The two fluid-phase-salt methods, boundary backstress and capillary backstress, produced similar results. The pressure-time-porosity line interpolation method produced results different from the fluid-phase-salt methods. With the two fluid-phase-salt methods, the room gas pressure responded instantaneously to changes in the gas-generation rate, while the rate of room expansion, which had a mitigating effect on room pressure, responded more gradually. With the pressure lines method, both the room gas pressure and void volume responded instantaneously to changes in the gas-generation rate. Differences in the response to changes in the gas-generation rate between the fluid-phase-salt methods and the pressure lines method were particularly evident at 750 years, 1,050 years, and 1,200 years.

At 750 years, following a decrease to zero gas generation, the rate of room expansion slowed for the two fluid-phase-salt methods and actually reversed for the pressure lines method. The room gas pressures responded to the room void volume, decreasing in response to the continued room expansion with the fluid-phase-salt methods, and increasing slightly with the pressure lines method. It is reasonable to assume that the stress state would change gradually as it approached equilibrium with the room pressure and the room void volume and that the 20 MPa room pressure would decline in response to continued, but slower, room expansion during the equilibration period. This type of response was correctly predicted by the fluid-phase-salt methods.

However, the pressure lines method predicted an immediate reversal from room expansion to room closure at 750 years. It is unlikely that the cessation of gas generation in the room would result in an instantaneous change in the stresses in the halite, and that such a change would create an inward force able to overcome the 20 MPa room pressure (backstress) necessary to initiate closure. It is more likely that the pressure lines response at 750 years was impacted by the structure of the pressure lines, specifically the f=1.0 line (Figure 3-7) which most closely approximates the simulated pressure-time conditions. In the SANCHO f=1.0 simulation,

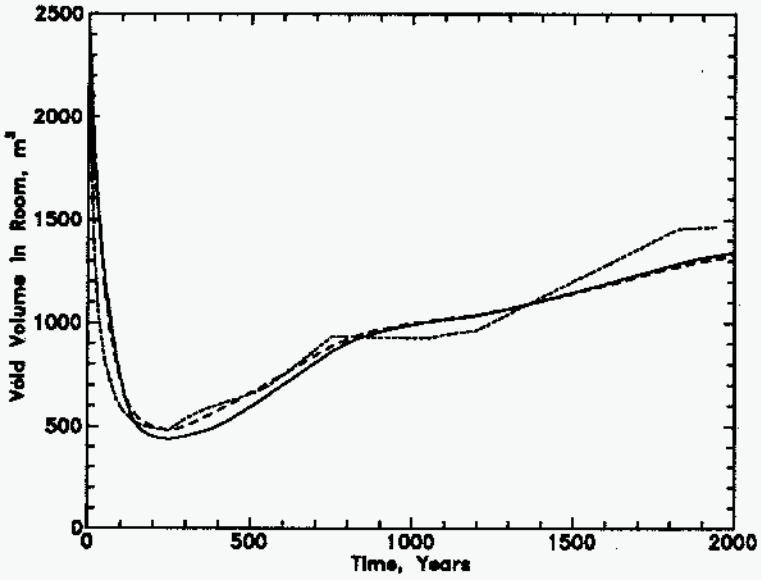

(a) Void Volume

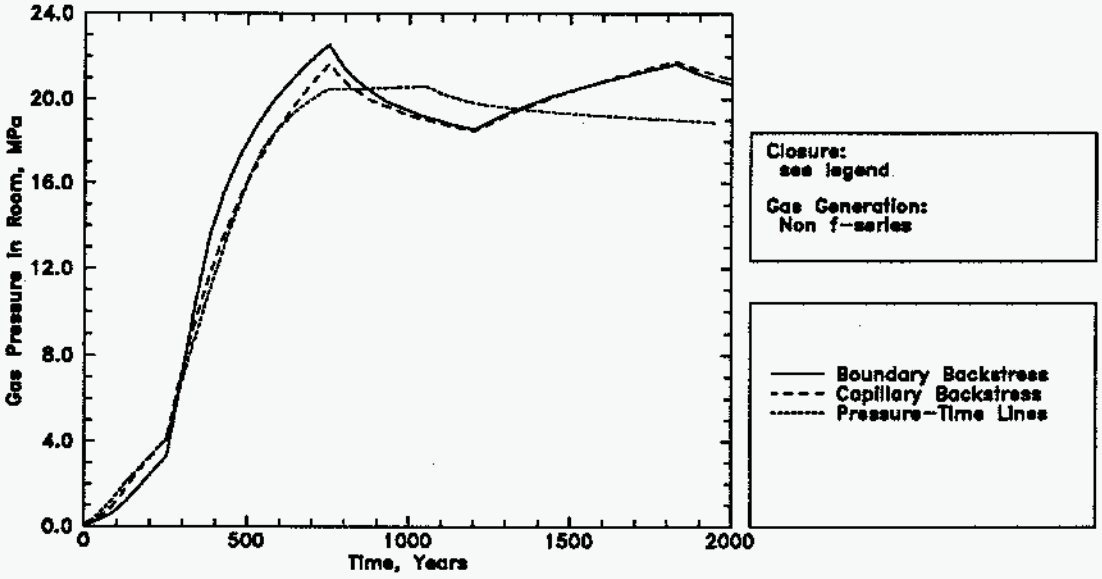

(b) Room Pressure

3-13. Comparison of flow and closure coupling methods for a gas-generation rate history different from the SANCHO f-series.

room pressure was relatively constant at about 20 MPa between 550 and 1,050 years (Figure 3-7b) and this pressure trend seems to be evident in the pressure lines response between 750 and 1,050 years in Figure 3-13b.

At 1,050 years the pressure lines method predicted a change in room closure and room pressure response despite the fact that there was no change in gas-generation rate. The declining room pressure appears to be an artifact of the SANCHO f=1.0 simulation, in which room pressure declined after 1,050 years (Figure 3-7b).

At 1,200 years, following an increase in gas-generation rate, the rate of room expansion increased with all three methods. However, the room gas pressure increased for the fluid-phase-salt methods and decreased for the pressure lines method. It is reasonable to assume that the resumption of gas-generation would increase room pressure which would, in turn, increase the rate of room expansion. However, with the pressure lines method, the room expansion was not driven by gas generation because the room pressure continued to decline. This pressure lines method response again appears to be strongly influenced by the structure of the SANCHO-generated pressure lines, specifically the f=1.0 simulation.

These non f-series rate history simulations demonstrate that the use of the pressure-time-porosity line interpolation method skews results towards the SANCHO f-series results because time is used as one of the interpolation axes. The time axis indirectly contains information about the history of salt creep and backstress on the room walls. Therefore, the backstress and room closure history described by the porosity function are specific to the SANCHO-simulated gas-generation rate history. When TOUGH2/EOS8 simulations are run using gas-generation rate histories significantly different from rate histories used to create the porosity function, errors can be introduced, especially at higher ($f > 0.4$) gas-generation rates.

In the lower gas-generation rate ($f < 0.4$) SANCHO simulations there was little change in room void volume following the initial period of room closure (Figure 3-7a). Because the room void volume is less sensitive to changes in room pressure at low rates, the pressure lines method may be better able to simulate non f-series rate histories that maintain low gas-generation rates (i.e., as when vapor-limited conditions produce relatively low gas-generation rates).

Results from these sealed room simulations suggest that (1) moles-based porosity functions are not accurate if the volume of brine in the room is significant, (2) pressure-time-porosity line

interpolation may introduce errors when the simulated gas-generation rate history is significantly different from the SANCHO f-series rate histories, particularly at high ($f > 0.4$) gas-generation rates, and (3) fluid-phase-salt methods work reasonably well under both f-series and non f-series gas-generation rate histories.

3.3 Coupled Flow and Closure

To examine the behavior of the boundary backstress, capillary backstress, and pressure-time-porosity line methods under coupled flow and closure conditions, simulations were performed assuming three different specified gas-generation rate (moles per drum per year) histories as listed in Table 3-2: 2/1; 0.2/0.1; and 0/0. The rate histories are denoted by the gas-generation rates during specified first and second gas-generation periods. In each simulation, gas-generation rates were specified for the duration of the simulation, changing from the first period rate to the second period rate when the microbial potential was exhausted, and changing to zero when the corrosion potential was exhausted. The specified 2/1 rate history corresponds to the best estimate of gas-generation rates under brine-inundated conditions and is equivalent to the $f=1.0$ rate history used by Stone (1992) in SANCHO simulations. The specified 0.2/0.1 rate history corresponds to the best estimate of gas-generation rates under vapor-limited conditions. The specified 0/0 rate history has no gas generation and is equivalent to the $f=0.0$ rate history. These simulated gas-generation rates were independent of the volume of brine actually present in the disposal room.

For the moderate room closure observed with the 2/1 rate history, the intermediate room void volume most closely approximated the void volume (closure) history of the room over the duration of the simulation and was the only fixed-room geometry included in the comparison. For the relatively large closure observed with the 0.2/0.1 and 0/0 rate histories, the fully consolidated room void volume more closely approximated the void volume history of the room and was the only fixed-room geometry included in the comparison. The moles-based porosity functions were not included in the comparison because of their inability to account for the impact of brine in the room.

For these gas-generation rate histories, gas was still being released from the room after 2,000 years, which was the duration of the SANCHO room closure simulations. In fact, the 0.2/0.1 rate history generates gas until 10,500 years. Although regulatory compliance is

evaluated at 10,000 years, the coupled flow and closure simulations were extended to 12,000 years, at which time gas release had nearly ceased, room pressures had stabilized, and gas generation was complete. The extension to 12,000 years allowed for the comparison of flow and closure coupling methods to encompass the complete period of gas generation, release, and migration.

To examine the applicability of the assumed salt creep and room closure behavior beyond 2,000 years, 12,000-year TOUGH2/EOS8 simulations of closure of a sealed room for the 2/1 ($f=1.0$) rate history were performed using both the boundary backstress and pressure lines methods. Simulation results are shown in Figure 3-14. These TOUGH2/EOS8 results were compared with results from a 10,000 year SANTOS room closure simulation with the $f=1.0$ rate history performed by Stone (1995b). SANTOS is a recently enhanced version of SANCHO and is described in Stone (1995b). The TOUGH2/EOS8 void volume history (particularly using boundary backstress) compared favorably with the SANTOS results. Because of differences in the simulated problem geometry, SANTOS void volumes for the $f=1.0$ case were slightly different from the SANCHO void volumes during the first 2,000 years. SANTOS room pressures were not available, but given the direct relationship between room pressure and void volume, comparisons with TOUGH2/EOS8 pressures should also be favorable.

The extension of salt creep and room closure processes in TOUGH2/EOS8 beyond the 2,000-year SANCHO calibration time requires some discussion. Time extension in the fixed-room geometry simulations was trivial because they were not directly coupled to room closure. The pressure-time-porosity lines were extrapolated to 12,000 years. Because conditions changed little in the final years of the SANCHO simulations (Figure 3-14), the 12,000 year conditions of the pressure-time-porosity lines were set identically to the 2,000 year conditions (see Appendix B). For the fluid-phase-salt methods, no adjustments were made to the empirically calibrated salt-phase properties to extend the model to 12,000 years. This approach assumes that trends extrapolated from the salt creep and room closure response in the first 2,000 years adequately characterize the response beyond 2,000 years. Given the good agreement between TOUGH2/EOS8 results and SANTOS results over 10,000 years, it appears that the assumptions made in extending the TOUGH2/EOS8 room closure processes beyond 2,000 years were reasonable. New porosity functions and new calibrated fluid-phase-salt properties can be determined if a sufficient suite of 10,000 year SANTOS simulations is performed. Until then, the 2,000 year closure calibrations provide an adequate approximation for flow and closure coupling.

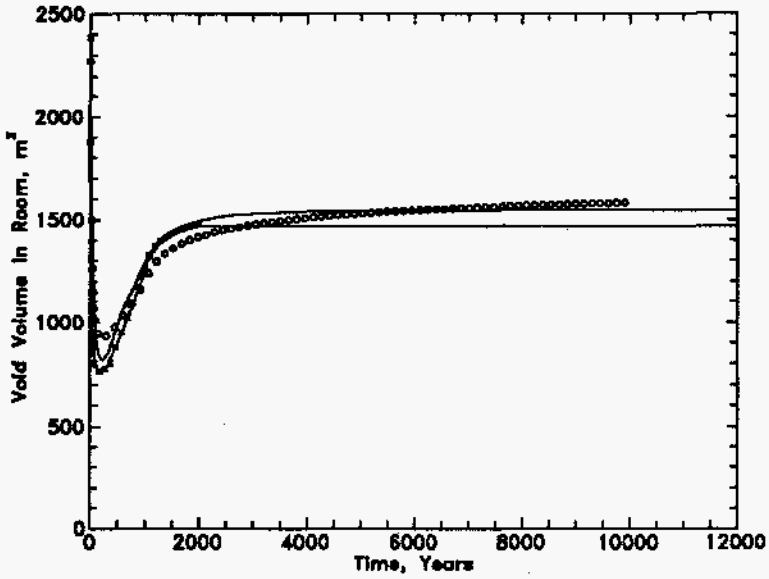

(a) Void Volume

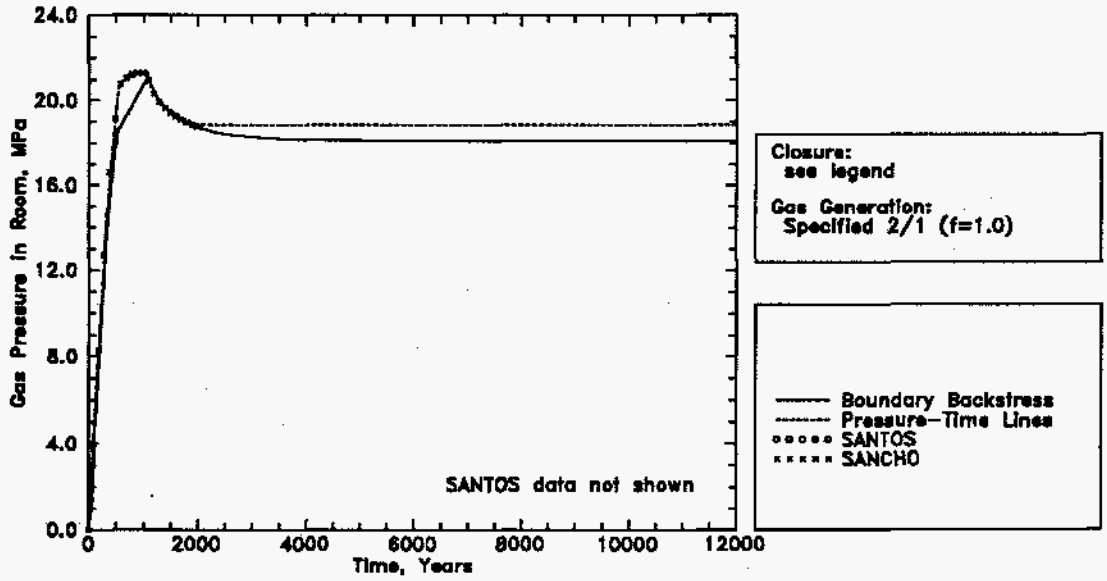

(b) Room Pressure

Figure 3-14. Comparison of TOUGH2/EOS8 (boundary backstress and pressure lines methods) results with SANCHO and SANTOS results for a 12,000 year simulation of closure of a sealed room.

A comparison of sealed room closure and coupled flow and closure with the 2/1 (f=1.0) rate history using the boundary backstress method is shown in Figure 3-15. The comparison illustrates the differences in room closure and room pressure behavior between a sealed room simulation and a simulation where there is brine inflow from and gas release to the Salado Formation. In the coupled flow and closure simulation, cumulative brine inflow peaked at about 200 years at 35 m^3 (Figure 3-15c). The presence of brine in the room reduced the void volume available to gas, leading to slightly elevated room pressures at early time. These elevated pressures in the coupled flow and closure simulation cannot be seen in Figure 3-15b because of the sharply increasing room pressure at early time. The coupled flow and closure simulation also showed reduced room closure (Figure 3-15a) due to the elevated room pressure and brine occupying void volume in the room. The volume of brine in the room (35 m^3) approximately corresponds to the difference in room closure at 200 years between the sealed room simulation and the coupled flow and closure simulation. Gas release, which began at about 500 years (Figure 3-15d), caused room expansion to slow relative to the sealed room case and eventually resulted in re-closure of the room (Figure 3-15a). Gas release also resulted in lower room pressures relative to the sealed room case (Figure 3-15b).

Coupled flow and closure results from the 2/1 gas-generation rate history simulations using each coupling method are shown in Figure 3-16, results from the 0.2/0.1 rate history simulations are shown in Figure 3-17, and the 0/0 rate history results are shown in Figure 3-18. Differences between the coupling methods produced differences in the simulation results. Different gas-generation rate histories accentuated certain characteristics of each of the coupling methods. For the 2/1 rate history, initial room closure was followed by room expansion (Figure 3-16a). At the end of gas generation at 1,050 years, continued gas expulsion (Figure 3-16d) resulted in re-closure of the room (Figure 3-16a). For the first 5,500 years, the two fluid-phase-salt methods, boundary backstress and capillary backstress, produced similar system behavior, but the pressure-time-porosity line interpolation results were notably different (Figures 3-16a, 3-16b, and 3-16d). At about 5,500 years, the capillary backstress results showed a radical change in behavior and started to deviate significantly from the boundary backstress results (Figures 3-16a, 3-16b, and 3-16d). For the two lower gas-generation rate histories, 0.2/0.1 and 0/0, initial room closure (Figures 3-17a and 3-18a) was greater and room expansion was less than with the 2/1 rate history (Figure 3-16a) and there was no re-closure of the room. For the lower rate cases, the capillary backstress and pressure-time-porosity function results were similar to each other but were different from the boundary backstress results.

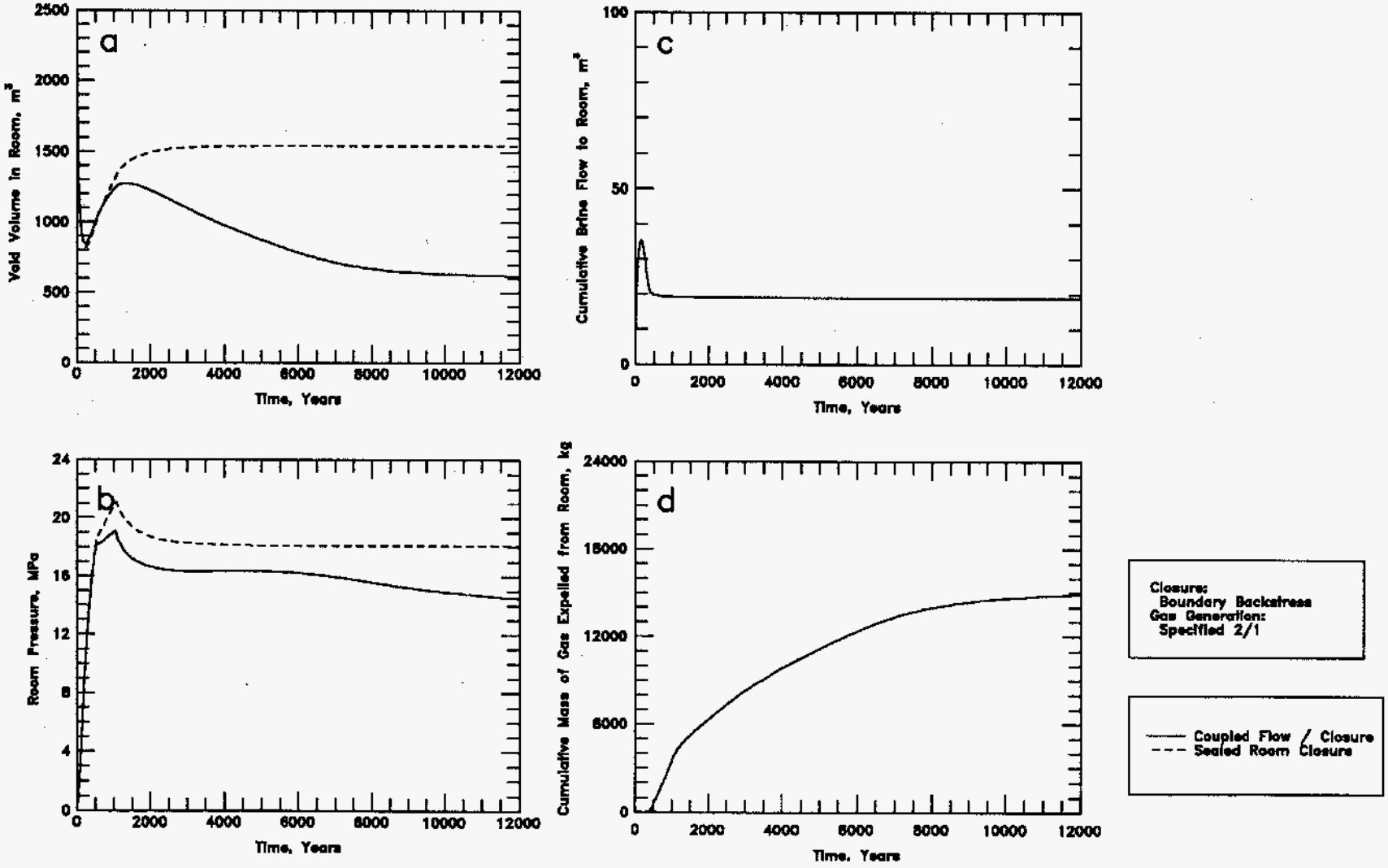

Figure 3-15. Comparison of TOUGH2/EOS8 (boundary backstress method) results for closure of a sealed room and coupled flow and closure under the specified 2/1 gas-generation rate history.

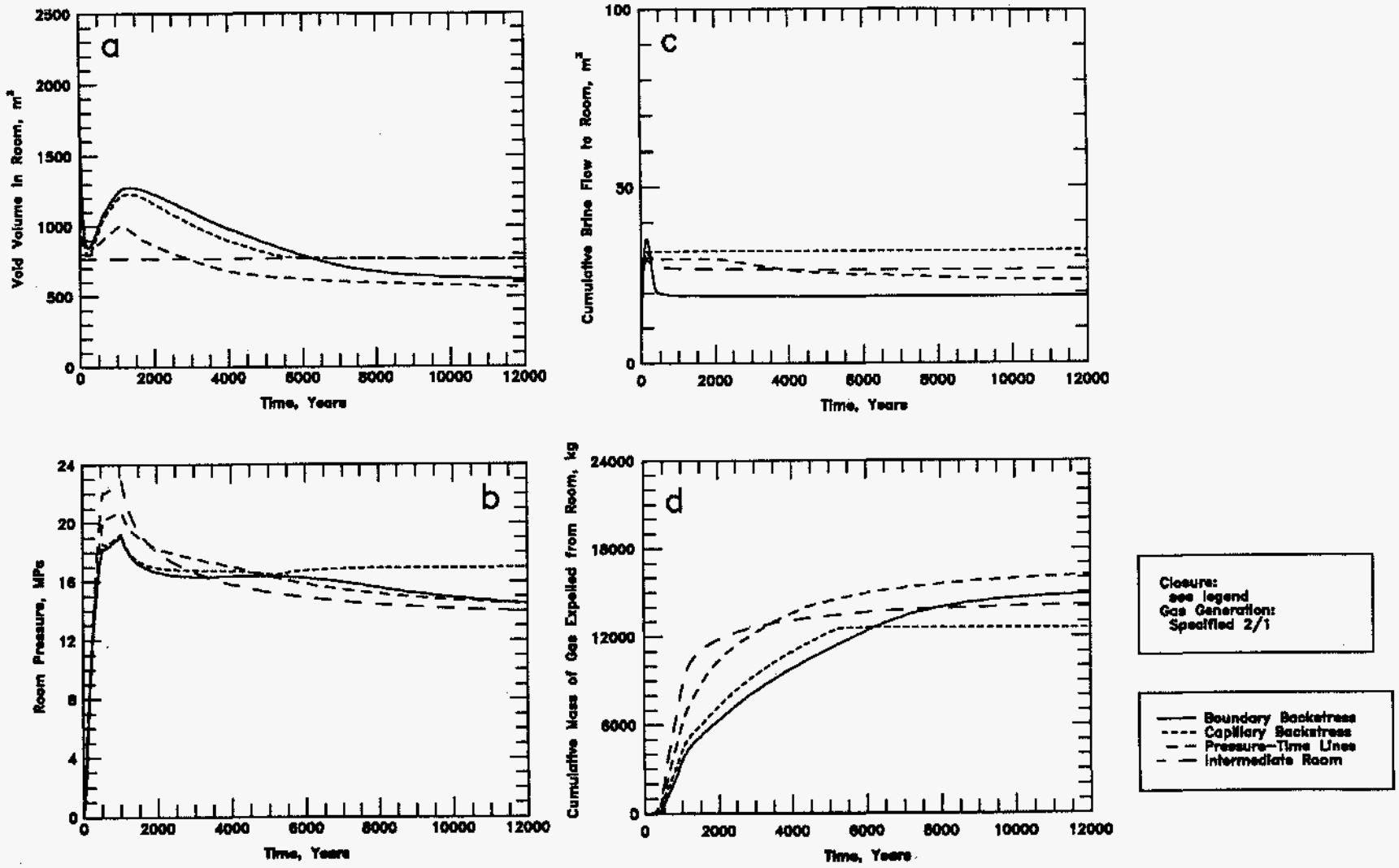

Figure 3-16. Comparison of TOUGH2/EOS8 flow and closure coupling methods under the specified 2/1 gas-generation rate history (note deviotory behavior of capillary backstress method beyond 5,500 years).

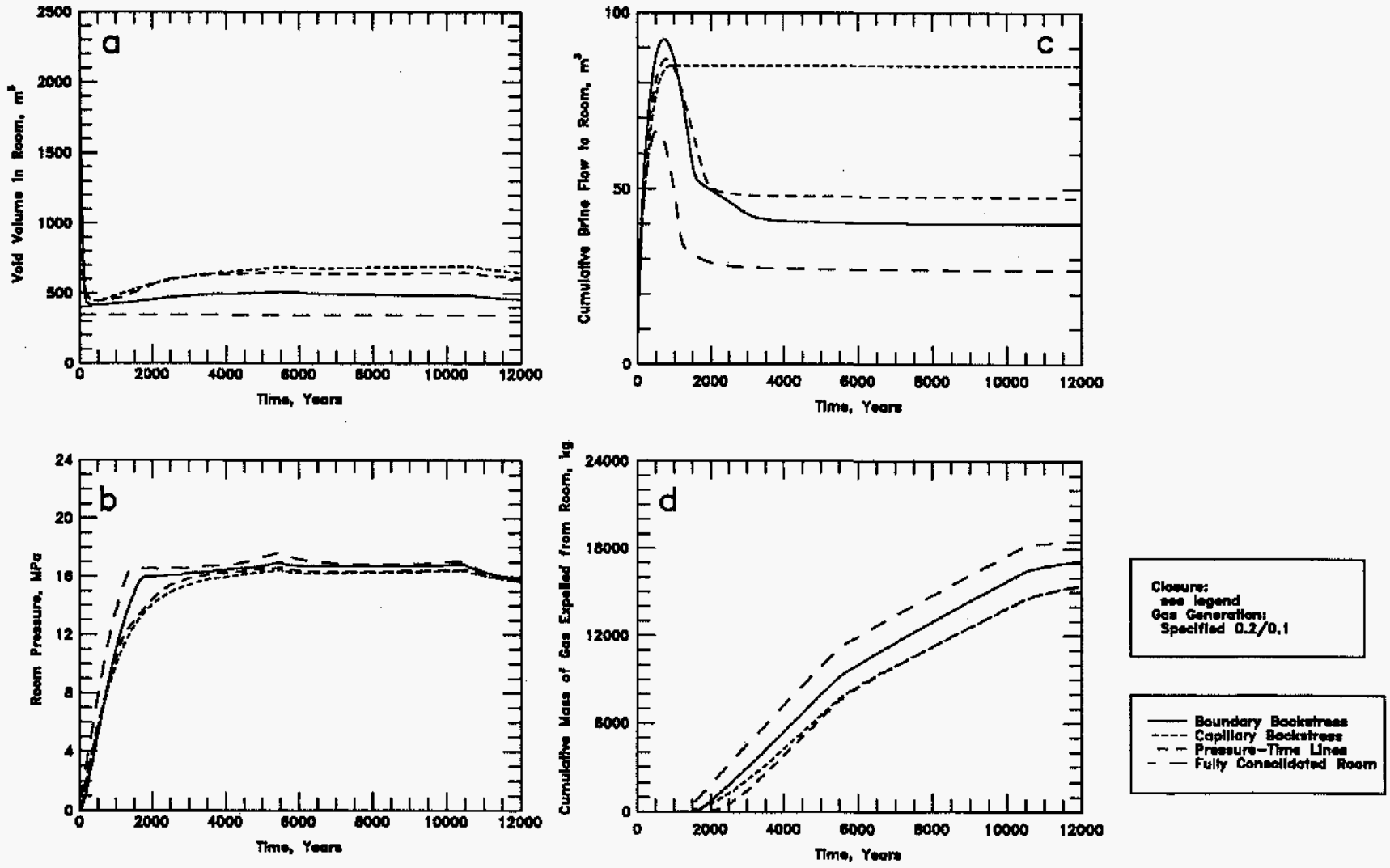

Figure 3-17. Comparison of TOUGH2/EOS8 flow and closure coupling methods under the specified 0.2/0.1 gas-generation rate history.

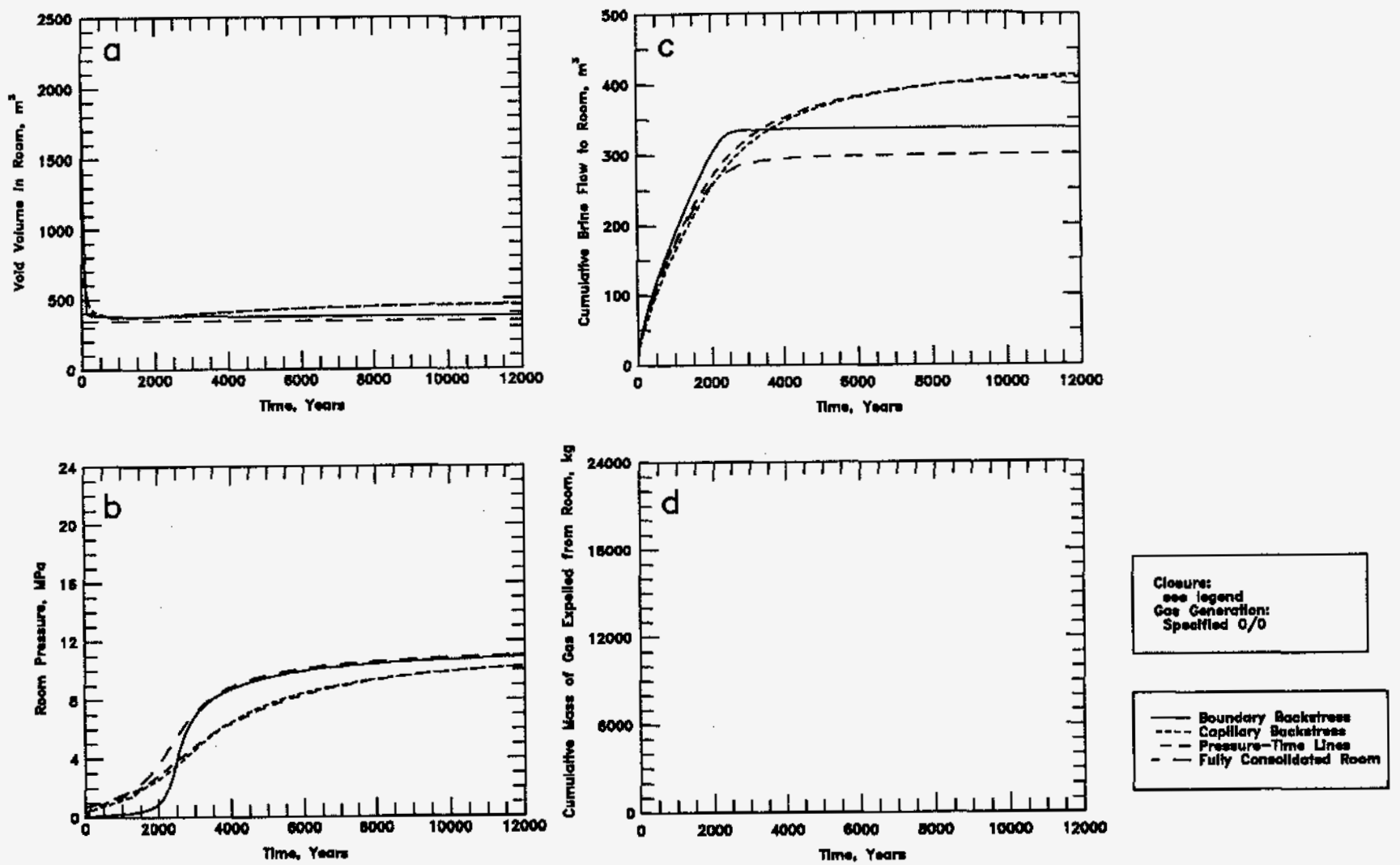

Figure 3-18. Comparison of TOUGH2/EOS8 flow and closure coupling methods under the specified 0/0 (no gas generation) rate history.

The differences between the simulation results from each of the coupling methods are attributable to: (1) differences in the room closure calibration for each of the methods; (2) differences in the coupling of room closure with multiphase flow for each of the methods; and (3) the inability of the capillary backstress method to accurately simulate re-closure of the room. These three causes of differences in simulation results are discussed in the following paragraphs.

The differences in the room closure calibration for each of the methods varied with the gas-generation rate history. For the 2/1 (f=1.0) rate history, the calibrated room pressure was higher for the pressure lines method (Figure 3-7b) than for the boundary backstress method (Figure 3-8b). This comparison is also shown in Figure 3-14b. The calibrated pressure for the capillary backstress method (Figure 3-10b) was similar to the boundary backstress calibrated pressure. The higher room pressure for the pressure lines method translated to greater early time gas expulsion (Figure 3-16d) and less room expansion (Figure 3-16a) than for the two fluid-phase-salt methods. For the 0.2/0.1 rate history (approximated by f=0.1 at early time), the calibrated room pressure was higher for the boundary backstress method (Figure 3-8b) than for the other two methods. The higher room pressure translated to greater early time gas expulsion (Figure 3-17d) and less room expansion (Figure 3-17a) for the boundary backstress method.

The differences in the coupling of room closure with multiphase flow for each of the methods was due to differences in the conceptualization of the disposal room. Multiphase flow was controlled by the gas and brine-phase saturations within the disposal room. These phase saturations impact both brine and gas expulsion through relative permeability relationships. Brine expulsion (Figures 3-16c and 3-17c) is indicated by a decrease in cumulative brine inflow. In simulations using the fluid-phase-salt methods, the presence of the salt phase in the room (from closure) resulted in lower gas and brine saturations and correspondingly lower relative permeabilities for gas and brine. With the capillary backstress method, the reduced relative permeabilities resulted in less brine expulsion than the other methods. However, with the boundary backstress method, brine inflow was typically confined to the small salt-inaccessible room region, producing high brine saturations and increased relative permeability with no salt-phase-induced reduction in relative permeability. As a result, the boundary backstress method produced more brine expulsion than any other method. With the pressure lines and fixed-room methods, brine flowed into the entire room volume and relative permeabilities were not reduced by the presence of a salt phase. Brine saturations and brine expulsion were typically lower than for boundary backstress but higher than for capillary backstress. These differences in brine expulsion were observed under both the 2/1 and 0.2/0.1 rate histories (Figures 3-16c and 3-17c,

respectively). Note that brine expulsion typically continued for a few thousand years and then ceased as the volume of brine in room decreased to residual saturation.

Because the fixed-room conceptualization does not couple multiphase flow with closure, fixed-room results were useful for comparing the behavior of multiphase flow with and without closure coupling. Brine expulsion from a fixed room was similar to both boundary backstress and pressure lines brine expulsion with the 2/1 (Figure 3-16c) and 0.2/0.1 (Figure 3-17c) rate histories. The lack of brine expulsion in the capillary backstress simulations appears to be a method-dependent problem, caused by the reduced relative permeabilities due to the presence of the third (salt) phase. With no gas generation (Figure 3-18c), brine inflow continued until the room void volume was almost entirely filled with brine, at which time room pressures started to rise due to the relative incompressibility of brine in the room. Fixed-room brine inflow and room pressure results were most closely approximated by the boundary backstress results. These comparisons suggest that the dual room region conceptualization used in the boundary backstress method does not adversely affect brine flow.

Gas expulsion from a fixed room was most similar to the pressure lines method under the 2/1 rate history (Figure 3-16d) and most similar to the boundary backstress method under the 0.2/0.1 rate history (Figure 3-17d). These similarities appear to result from similarities in the room pressure history, suggesting that gas expulsion is much more dependent on the driving (room) pressure than on small method-dependent discrepancies in relative permeability.

For the 2/1 rate history, the capillary backstress results beyond 5,500 years were in error due to re-closure of the room. The initial room closure and subsequent room expansion was strongly influenced by backstress that was rapidly increasing with closure and by room pressure that was rapidly increasing due to gas generation. Because the exponential gas-salt capillary pressure relationship (Equation 3-3) was calibrated to the initial room closure and expansion (Section 3.1.2), it inherently included the effects of increasing backstress (on closure) and increasing room pressure (on expansion). Following the end of gas generation at 1,050 years, continued gas expulsion resulted in re-closure of the room. However, the rate of re-closure were not the same as during initial closure and could not be accurately simulated using the exponential gas-salt capillary pressure relationship. As the room void volume approached 700 m^3 during re-closure, a rapid increase in gas-salt capillary pressure occurred which effectively stopped further room re-closure. This result appears to be unrealistic when compared to the results of the boundary backstress and pressure-time-porosity simulations (Figure 3-16).

For the other rate histories, re-closure did not occur and the capillary backstress method yielded acceptable results.

In summary, differences between the coupling methods produced differences in the simulation results. Different gas-generation rate histories accentuated certain characteristics of each of the coupling methods. Three causes for the differences between the simulation results were identified. Most important were differences in the room closure calibration for each of the methods.

The boundary backstress method is considered the most robust and accurate method for coupling multiphase flow and room closure. Possible adverse effects of the dual room conceptualization were demonstrated not to be significant by a comparison with the capillary backstress and pressure lines methods for closure and with fixed-room geometries for multiphase flow. The pressure lines method is useful for simulations with low gas-generation rates ($f \leq 0.2$) or with gas-generation rate histories similar to the SANCHO f-series. This method should be used with caution if simulated gas-generation rate histories involve high rates ($f > 0.4$) in a significantly different sequence than the f-series rate histories to which the method was calibrated. The capillary backstress method is useful for low gas-generation rate simulations in which room re-closure does not occur. The fixed-room geometry method is useful for performing simple multiphase flow scoping calculations.

4.0 CONCLUSIONS

Eight alternative methods for approximating salt creep and room closure in a multiphase flow model were implemented and evaluated: three fixed-room geometries (Section 2.2); three porosity functions (Section 2.3.1); and two fluid-phase-salt methods (Section 2.3.2).

The fixed-room geometry approach did not incorporate the important feedback between room pressure and room void volume and was therefore of little utility for coupled flow and closure simulations. However, the three fixed-room geometries provided bounding calculations for flow between the room and the Salado Formation and in some cases this approach could be useful for scoping calculations.

For the three porosity function methods, simulated pressure-time or moles-time conditions that deviated significantly from the SANCHO f-series conditions (used to produce the porosity functions) resulted in simulated porosity behavior that was skewed towards the SANCHO results (Section 3.2). These effects were particularly evident at higher gas-generation rates (consistent with estimated brine-inundated rates). Therefore, the porosity function methods were only reliable when gas-generation rate histories were similar to the f-series rate histories or when rates were low (consistent with estimated vapor-limited rates). The two moles-driven porosity functions were unable to account for the presence of brine in the room and therefore could not accurately capture the dynamic relationship between room pressure, brine volume in the room, and room expansion.

The two fluid-phase-salt methods overcame the deficiencies of the porosity function methods in that any gas-generation rate history could be simulated and the room closure coupling was not adversely affected by the presence of brine. However, the capillary backstress method was unable to simulate conditions where re-closure of the room followed room expansion. The capillary backstress method also produced high salt-phase saturations in the room, which reduced the relative permeability to brine within the room and impeded brine expulsion. With the boundary backstress method, the dual room region conceptualization appeared not to adversely impact brine flow or gas release to the Salado Formation. The fluid-phase-salt methods were calibrated to be accurate over the range of SANCHO f-series rate histories. It is uncertain whether the empirical calibration relationships are valid for gas-generation and room closure conditions which are significantly outside the SANCHO f-series conditions.

In summary, only two methods were found to be accurate and robust enough to approximate the effects of room closure under most conditions, the boundary backstress method and the pressure-time-porosity line interpolation method. Comparisons of these two coupling methods under different gas-generation rate histories are presented in Figures 3-16 through 3-18. Minor differences in brine and gas flow between pressure lines results and boundary backstress results were primarily due to differences between the room closure calibration of the two methods. The boundary backstress method is thought to be a more reliable indicator of system behavior due to the theoretical basis for modeling salt deformation as a viscous process. However, it is a complex method and a detailed calibration process is required. The pressure lines method is thought to be less reliable due to the potential skewing of results towards SANCHO f-series results. This limitation in the pressure lines method is most pronounced if gas-generation rate histories involve high rates ($>$ 0.8 moles per drum per year) in a significantly different sequence than the f-series rate histories to which the method was calibrated. Due to its relative simplicity, the pressure lines method is easier to implement in multiphase flow codes and simulations have significantly shorter execution times (10 to 20 times faster than boundary backstress). The pressure lines method is suggested for continued use in WIPP Performance Assessment calculations as long as simulated gas-generation rate histories are low ($\leq$ 0.4 moles per drum per year) or are not significantly different from the SANCHO f-series rate histories.

5.0 REFERENCES

Beauheim, R.L., G.J. Saulnier, Jr., and J.D. Avis. 1991. *Interpretation of Brine-Permeability Tests of the Salado Formation at the Waste Isolation Pilot Plant Site: First Interim Report.* SAND90-0083. Albuquerque, NM: Sandia National Laboratories.

Beráun, R., and P.B. Davies. 1992. "Baseline Design Input Data Base to be Used During Calculations Effort to be Performed by Division 1514 in Determining the Mechanical Creep Closure Behavior of Waste Disposal Rooms in Bedded Salt," *Preliminary Performance Assessment for the Waste Isolation Pilot Plant, December 1992. Volume 3: Model Parameters.* Sandia WIPP Project. SAND92-0700/3. Albuquerque, NM: Sandia National Laboratories. A-5 through A-13.

Berner, H., H. Ramberg, and O. Stephansson. 1972. "Diapirism in Theory and Experiment," *Tectonophysics.* Vol. 15, no. 3, 197-218.

Biot, M.A., and H. Ode. 1965. "Theory of Gravity and Instability with Variable Overburden and Compaction," *Geophysics.* Vol. 30, no. 2, 213-227.

Brooks, R.H., and A.T. Corey. 1964. *Hydraulic Properties of Porous Media.* Hydrology Papers No. 3. Fort Collins, CO: Colorado State University.

Brush, L.H. 1990. *Test Plan for Laboratory and Modeling Studies of Repository and Radionuclide Chemistry for the Waste Isolation Pilot Plant.* SAND90-0266. Albuquerque, NM: Sandia National Laboratories.

Brush, L.H. 1991. "Appendix A: Current Estimates of Gas Production Rates, Gas Production Potentials, and Expected Chemical Conditions Relevant to Radionuclide Chemistry for the Long-Term WIPP Performance Assessment," *Preliminary Comparison with 40 CFR Part 191, Subpart B for the Waste Isolation Pilot Plant, December 1991, Volume 3: Reference Data.* Eds. R.P. Rechard, A.C. Peterson, J.D. Schreiber, H.J. Iuzzolino, M.S. Tierney, and J.S. Sandha. SAND91-0893/3. Albuquerque, NM: Sandia National Laboratories. A-25 through A-36.

Brush, L.H. 1995. "Likely Gas-Generation Reactions and Current Estimates of Gas-Generation Rates for the Long-Term WIPP Performance Assessment," *A Summary of Methods for Approximating Salt Creep and Disposal Room Closure in Numerical Models of Multiphase Flow.* G.A. Freeze, K.W. Larson, and P.B. Davies. SAND94-0251. Albuquerque, NM: Sandia National Laboratories. C-5 through C-45.

Butcher, B.M. 1989. *Waste Isolation Pilot Plant Simulated Waste Compositions and Mechanical Properties.* SAND89-0372. Albuquerque, NM: Sandia National Laboratories.

Butcher, B.M., and F.T. Mendenhall. 1993. *A Summary of the Models Used for the Mechanical Response of Disposal Rooms in the Waste Isolation Pilot Plant with Regard to Compliance with 40 CFR 191, Subpart B.* SAND92-0427. Albuquerque, NM: Sandia National Laboratories.

Butcher, B.M., C.F. Novak, and M. Jercinovic. 1991a. *The Advantages of a Salt/Bentonite Backfill for Waste Isolation Pilot Plant Disposal Rooms.* SAND90-3074. Albuquerque, NM: Sandia National Laboratories.

Butcher, B.M., T.W. Thompson, R.G. Van Buskirk, and N.C. Patti. 1991b. *Mechanical Compaction of Waste Isolation Pilot Plant Simulated Waste.* SAND90-1206. Albuquerque, NM: Sandia National Laboratories.

Davies, P.B. 1984. "Deep-Seated Dissolution and Subsidence in Bedded Salt Deposits," PhD dissertation. Stanford, CA: Applied Earth Sciences Department, Stanford University.

Davies, P.B. 1991. *Evaluation of the Role of Threshold Pressure in Controlling Flow of Waste-Generated Gas into Bedded Salt at the Waste Isolation Pilot Plant Repository.* SAND90-3246. Albuquerque, NM: Sandia National Laboratories.

Davies, P.B., L.H. Brush, and F.T. Mendenhall. 1991. "Assessing the Impact of Waste-Generated Gas from the Degradation of Transuranic Waste at the Waste Isolation Pilot Plant: An Overview of Strongly Coupled Chemical, Hydrologic, and Structural Processes," *Gas Generation and Release from Radioactive Repositories, 3rd Organisation for Economic Co-Operation and Development/Nuclear Energy Agency (OECD/NEA) Gas Workshop, Aix-en-Provence, France, September 23-26, 1991.* SAND90-0707C. Paris, France: Organisation for Economic Co-Operation and Development. 54-74.

Freeze, G.A., Larson, K.W., and P.B. Davies. 1995. *Coupled Multiphase Flow and Closure Analysis of Repository Response to Waste-Generated Gas at the Waste Isolation Pilot Plant (WIPP).* SAND93-1986. Albuquerque, NM: Sandia National Laboratories.

Golden Software, Inc. 1994. *SURFER for Windows User's Guide.* Golden, CO: Golden Software Inc. (Available from Golden Software, Inc., 809 14th St., Golden, CO (303) 279-1021.)

Krieg, R.D. 1984. *Reference Stratigraphy and Rock Properties for the Waste Isolation Pilot Plant (WIPP) Project.* SAND83-1908. Albuquerque, NM: Sandia National Laboratories.

Molecke, M.A. 1979. *Gas Generation from Transuranic Waste Degradation: Data Summary and Interpretation.* SAND79-1245. Albuquerque, NM: Sandia National Laboratories.

Munson, D.E., A.F. Fossum, and P.E. Senseny. 1989. "Approach to First Principles Model Prediction of Measured WIPP In Situ Room Closure in Salt," *Rock Mechanics as a Guide for Efficient Utilization of National Resources: Proceedings of the 30th U.S. Symposium, West Virginia University, Morgantown, WV, June 19-22, 1989.* Ed. A.W. Khair. Brookfield, VT: A.A. Balkema. 673-680.

Nettleton, L.L. 1934. "Fluid Mechanics of Salt Domes," *Bulletin of the American Association of Petroleum Geologists.* Vol. 18, no. 9, 1175-1204.

Pruess, K. 1987. *TOUGH User's Guide.* NUREG/CR-4645, SAND86-7104, LBL-20700. Berkeley, CA: Lawrence Berkeley Laboratory.

Pruess, K. 1991. *TOUGH2 - A General-Purpose Numerical Simulator for Multiphase Fluid and Heat Flow.* LBL-29400. Berkeley, CA: Lawrence Berkeley Laboratory.

Ramberg, H. 1981. *Gravity, Deformation and the Earth's Crust. 2nd ed.* New York, NY: Academic Press.

Reeves, M. 1995. "Potential-Flow Analysis of Transient Salt Creep Into a Circular Cavity," *A Summary of Methods for Approximating Salt Creep and Disposal Room Closure in Numerical Models of Multiphase Flow.* G.A. Freeze, K.W. Larson, and P.B. Davies. SAND94-0251. Albuquerque, NM: Sandia National Laboratories. C-47 through C-84.

Sjaardema, G.D., and R.D. Krieg. 1987. *A Constitutive Model for the Consolidation of WIPP Crushed Salt and Its Use in Analyses of Backfilled Shaft and Drift Configurations.* SAND87-1977. Albuquerque, NM: Sandia National Laboratories.

Stone, C.M. 1995a. "Creep Closure Behavior of Waste Disposal Rooms in Bedded Salt Due to Gas Generation Produced by Several Alternatives of the Engineered Alternatives Task Force," *A Summary of Methods for Approximating Salt Creep and Disposal Room Closure in Numerical Models of Multiphase Flow.* G.A. Freeze, K.W. Larson, and P.B. Davies. SAND94-0251. Albuquerque, NM: Sandia National Laboratories. C-85 through C-105.

Stone, C.M. 1995b. "Application of SANTOS to Waste Disposal Room Problems Including a Demonstration of Coupled Structural/Porous Flow Capability," *A Summary of Methods for Approximating Salt Creep and Disposal Room Closure in Numerical Models of Multiphase Flow.* G.A. Freeze, K.W. Larson, and P.B. Davies. SAND94-0251. Albuquerque, NM: Sandia National Laboratories. C-107 through C-133.

Stone, C.M., R.D. Krieg, and Z.E. Beisinger. 1985. *SANCHO, A Finite Element Computer Program for the Quasistatic, Large Deformation, Inelastic Response of Two-Dimensional Solids.* SAND84-2618. Albuquerque, NM: Sandia National Laboratories.

U.S. Department of Energy. 1986. *Design Validation Final Report.* DOE/WIPP 86-010. San Francisco, CA: Bechtel National, Inc.

U.S. Department of Energy. 1990. *Final Supplement Environmental Impact Statement, Waste Isolation Pilot Plant.* DOE/EIS-0026-FS. Washington, D.C.: U.S. Department of Energy, Office of Environmental Restoration and Waste Management.

Webb, S.W. 1992. "Sensitivity Studies for Gas Release From the Waste Isolation Pilot Plant (WIPP)," *Gas Generation and Release from Radioactive Repositories, 3rd Organisation for Economic Co-Operation and Development/Nuclear Energy Agency (OECD/NEA) Gas Workshop, Aix-en-Provence, France, September 23-26, 1991.* SAND91-1872c. Paris, France: Organisation for Economic Co-Operation and Development. 309-326.

WIPP PA (Performance Assessment) Department. 1992. *Preliminary Performance Assessment for the Waste Isolation Pilot Plant, December 1992 - Volume 2: Technical Basis.* SAND92-0700/2. Albuquerque, NM: Sandia National Laboratories.

APPENDIX A: THEORETICAL RELATIONSHIP BETWEEN POTENTIAL FLOW AND VISCOELASTIC DEFORMATION

Appendix A: Theoretical Relationship Between Potential Flow and Viscoelastic Deformation

Both Davies (1984) and Reeves (1995) used a radial geometry to compare viscoelastic deformation with Darcy fluid flow. The radial model consisted of a circular repository (with radius r=a) having a pressure P_o, surrounded by an infinite intact salt region having a boundary ($r=\infty$) pressure of P_∞.

Viscoelastic deformation can be described by the Maxwell relationship (Reeves, 1995):

$$\dot{\varepsilon} = \frac{\dot{\tau}}{2G} + \frac{\tau}{\eta} \qquad \text{(A-1)}$$

where:

- $\dot{\varepsilon}$ = shear strain rate,
- $\dot{\tau}$ = shear stress rate,
- τ = shear stress,
- G = elastic shear modulus, and
- η = Maxwell-flow viscosity.

The first term on the right-hand side of the equation represents elastic deformation and the second term represents viscous deformation. In SANCHO, the elastic-secondary creep constitutive model which simulates salt creep, also has a strain rate comprised of elastic and inelastic components.

Davies (1984) showed that, under steady-state conditions, the Maxwell-flow viscosity (η) is proportional to shear stress (τ):

$$\eta = \frac{\tau^{(1-n)}}{A} \qquad \text{(A-2)}$$

and that the maximum shear stress (τ_{max}), representative of the deviatoric stress, is:

$$\tau_{max} = - \left[\frac{P_\infty - P_o}{n} \right] \left[\frac{a}{r} \right]^{\frac{2}{n}} \qquad \text{(A-3)}$$

where A and n are material constants (n is equal to 1 for a linear rheology, greater than 1 for a non-linear rheology, and is estimated to be 4.9 in the WIPP salt).

Reeves (1995) showed that, for a given intrinsic permeability (k), salt viscosity (μ_s) could be used to control salt fluid mobility, and was proportional to η. Combining this relationship with Equations A-2 and A-3, Reeves (1995) derived the following theoretical expression for steady-state potential-flow salt viscosity (μ_s):

$$\mu_s \propto (P_\infty - P_o)^{-(n-1)} \qquad \text{(A-4)}$$

This relationship provides the theoretical basis for the fluid phase salt flow and closure coupling method. In TOUGH2/EOS8 simulations with the boundary backstress coupling method, the following empirically determined salt viscosity was used:

$$\mu_s = 3.0E{-}8 + 2.5E{-}21 \ (p_s - p_{s\,ref})^2 \qquad \text{(A-5)}$$

where:

p_s = salt phase pressure (Pa), and
$p_{s\,ref}$ = reference salt phase pressure (-3.4×10^6 Pa).

Although the functional forms of Equations A-4 and A-5 are not identical, both define salt viscosity using a pressure difference term that changes as pressure (either P_o or p_s) changes. The pressure difference is the potential-flow analogy to the deviatoric stress. In the TOUGH2/EOS8 simulations the near-field salt pressure equilibrated with the room pressure very quickly. Therefore, P_o in Equation A-4 can be equated with p_s in Equation A-5. Figure A-1 shows that the empirical salt viscosity is greater than the theoretical salt viscosity at low pressures, up to about 6 MPa. At room pressures greater than 6 MPa, empirical viscosities much lower than the theoretical values were required to produce the proper behavior. Viscosities in Figure A-1 are normalized to μ_o at $P_o = 0.1$ MPa and $p_s = -3.4$ MPa.

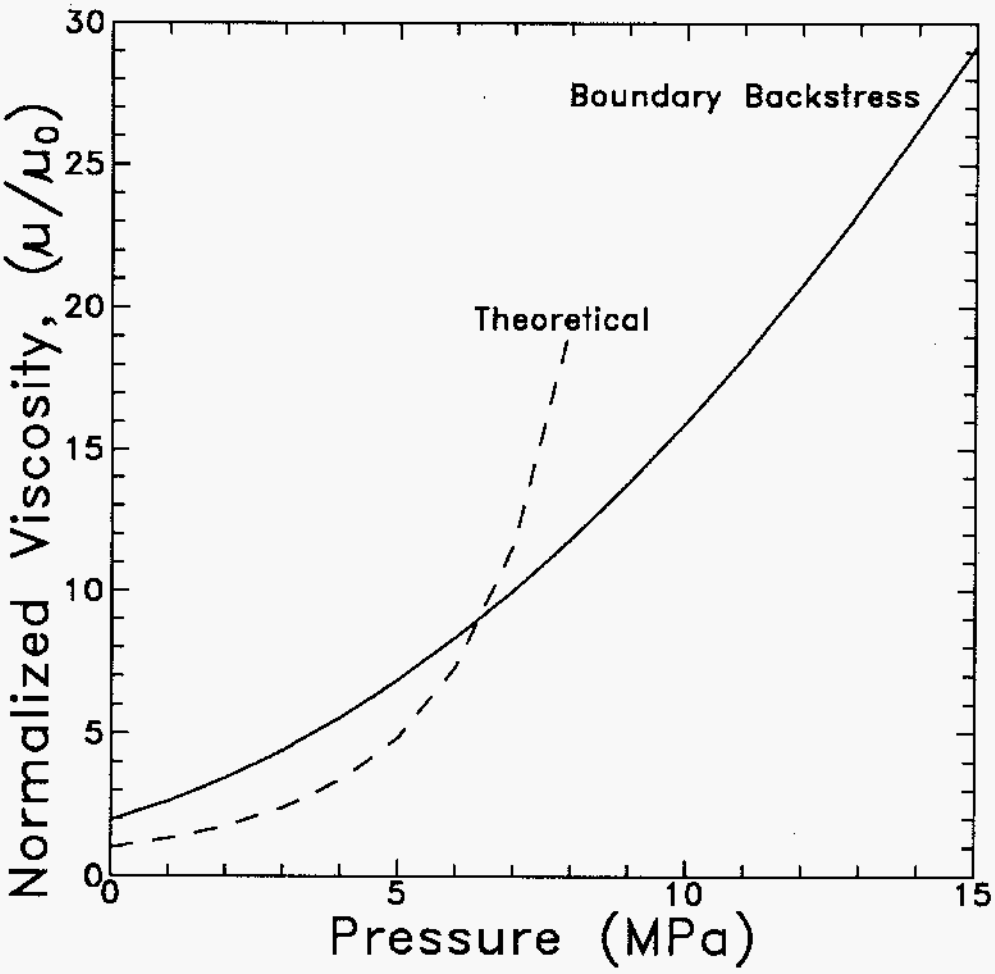

Figure A-1. Comparison of empirical and theoretical salt viscosity relationships.

The theoretical potential-flow salt viscosity (Equation A-4) represents steady-state viscous flow. The empirically determined TOUGH2/EOS8 salt viscosity (Equation A-5), in conjunction with the boundary backstress methodology, implicitly represents all processes inherent in SANCHO (viscous flow, elastic shear, and room backstress) with an equivalent viscous flow. The difference between the empirical and theoretical salt viscosities is primarily caused by two processes: the increased effects of room backstress as maximum closure is reached and expansion begins, and the increased effects of elastic shear as the viscosity increases. Differences due the room geometry, circular versus rectangular, may also be present but are not discussed here.

At low pressures, when maximum room closure is occurring, the effects of backstress due to consolidation of the room are greatest. During this period, the empirical salt viscosity is greater than the theoretical viscosity to account for the reduction in closure rate due to backstress. At high pressures, salt viscosity increases and the effects of elastic shear are increased. The empirical viscosity is less than the theoretical viscosity to produce additional salt flow representative of elastic flow.

Reeves (1995) provides the basis for the following theoretical treatment of elastic shear effects. Reeves (1995) derived the following equation, for a linear rheology, describing the incremental salt velocity (Δv) resulting from a change in pressure at the room boundary (ΔP_o):

$$\Delta v = -\frac{a^2}{\eta}\left[\Delta P_o(t_{\eta G}) + \Delta P_o(t)\right]\frac{1}{r} \qquad \text{(A-6)}$$

where:

$\Delta P_o(t) = \alpha_1 t$, and
$t_{\eta G} = \eta / 2G$.

Equation A-6 identifies a constant elastic shear component (first right-hand-side term) and a time-varying viscous flow component (second right-hand-side term) to the salt deformation. A low η corresponds to a small $t_{\eta G}$ ($\sim$50 days for η corresponding to the lower end of the range for WIPP salt). Because the time constant $t_{\eta G}$ is small for a low η, the elastic shear term is insignificant relative to the viscous flow term as t becomes greater than $t_{\eta G}$ (i.e. $t > 50$ days). A higher η corresponds to a larger $t_{\eta G}$ ($\sim$6000 years for η corresponding to the upper end of the range for WIPP salt). The resulting elastic shear effects are much more significant and it takes longer ($t > 6000$ years) to achieve steady-state viscous flow. Recalling that μ_s is proportional to η, Figure A-1 indicates that at low salt viscosities (corresponding to pressures less than

6 MPa) viscous flow was the dominant process. At higher salt viscosities (corresponding to pressures greater than 6 MPa) an empirical salt viscosity below the steady-state theoretical value was required to account for the additional elastic flow. Reeves (1995) also determined that elastic shear effects, represented by a change in shear stress $\Delta\tau = \Delta P_o(a/r)^2$, decreased with distance away from the repository.

To incorporate the effects of elastic shear into the theoretical potential-flow viscosity, Reeves (1995) presents a Darcy-Flow Viscosity Submodel, which adjusts near-field salt viscosities. The following is a discussion of general methodology of the submodel. A pressure, $P_o(t_o)$, is defined that corresponds to a time t_o at which elastic shear effects are negligible and steady-state viscous flow conditions exist. Based on Figure A-1, $P_o(t_o)$ is about 3 MPa. A steady-state viscous or "relic" component of salt viscosity is calculated from Equation A-4 with $P_o = P_o(t_o)$. An elastic shear component is added to the "relic" component in the near-field ($r < 10a$ for WIPP salt) when $t > t_o$ by defining $\Delta P_o = P_o(t) - P_o(t_o)$. To calculate the additional elastic shear component of salt viscosity, Equation A-4 is re-evaluated from Equations A-2 and A-3, recognizing that $\tau = \tau_{max} + \Delta\tau$ where $\Delta\tau = \Delta P_o(a/r)^2$.

In the SANCHO simulations of Stone (1995), room expansion (increasing room volume) began at room pressures less than lithostatic (P_∞). Room backstresses (room pressure plus backstress associated with the waste and backfill) were not reported but may also have been less than P_∞ . Brown and Weatherby (1993) reported that room expansion began at backstresses of about 10 MPa. It appears that the backstress on the room walls may be responsible for producing room expansion at less-than-lithostatic pressure due to the altered near-field stress distribution. A theoretical basis for the inclusion of room backstress into the potential-flow model has not been developed. Reeves (1995) attributes the less-than-lithostatic room expansion to near-field elastic shear effects and presents a Repository Boundary-Condition Submodel, which adjusts boundary viscosities to produce flow reversal. This submodel indirectly accounts for room backstress by altering the viscosity at the room boundary.

The empirical TOUGH2/EOS8 salt viscosity (Equation A-5) implicitly accounts for the effects of viscous flow, elastic shear, and room backstress. Qualitative methods to adjust the theoretical steady-state salt viscosity (Equation A-4) to account for elastic shear and room backstress have been presented. With a more quantitative treatment, it is hoped that these methods can be used to theoretically predict the salt viscosity required to reproduce mechanical salt creep, thus removing the need for empirical determination.

References for Appendix A

Brown, W.T., and J.R. Weatherby. 1993. "Appendix A: Influence of Gas Generation Potential and Gas Generation Rate on the Performance of CH-TRU Disposal Rooms," *A Summary of the Models Used for the Mechanical Response of Disposal Rooms in the Waste Isolation Pilot Plant with Regard to Compliance to 40 CFR 191, Subpart B.* B.M. Butcher and F.T. Mendenhall. SAND92-0427. Albuquerque, NM: Sandia National Laboratories. A-5 through A-25.

Davies, P.B. 1984. "Deep-Seated Dissolution and Subsidence in Bedded Salt Deposits." PhD dissertation. Stanford, CA: Applied Earth Sciences Department, Stanford University.

Reeves, M. 1995. "Potential-Flow Analysis of Transient Salt Creep Into a Circular Cavity," *A Summary of Methods for Approximating Salt Creep and Disposal Room Closure in Numerical Models of Multiphase Flow.* G.A. Freeze, K.W. Larson, and P.B. Davies. SAND94-0251. Albuquerque, NM: Sandia National Laboratories. C-47 through C-84.

Stone, C.M. 1995. "Creep Closure Behavior of Waste Disposal Rooms in Bedded Salt Due to Gas Generation Produced by Several Alternatives of the Engineered Alternatives Task Force," *A Summary of Methods for Approximating Salt Creep and Disposal Room Closure in Numerical Models of Multiphase Flow.* G.A. Freeze, K.W. Larson, and P.B. Davies. SAND94-0251. Albuquerque, NM: Sandia National Laboratories. C-85 through C-105.

APPENDIX B: PRESSURE-TIME-POROSITY LINES DATA

Pressure-Time-Porosity Dataset: Room Pressure (Pa) and Room Porosity vs. Time (Years) for f-series data

	f=1.0		f=0.6		f=0.4		f=0.2		f=0.0	
Time	P, Pa	Porosity	P, Pa	Porosity	P, Pa	Porosity	P, Pa	Porosity	P, Pa	Porosity
0	0	0.66018	0	0.66018	0	0.66018	0	0.66018	0	0.66018
0.50048	7611	0.64914	4566.6	0.64915	3044.6	0.64913	1522.3	0.64913	0	0.64912
1.001	15565	0.64409	9339.3	0.64408	6226.4	0.64407	3113.5	0.64405	0	0.64399
6.0057	105930	0.61491	63766	0.61416	42489	0.61427	21197	0.6148	0	0.61568
11.01	216780	0.58879	131150	0.58679	87884	0.58556	43807	0.5863	0	0.58752
16.015	364650	0.55352	221690	0.5503	148950	0.54839	74539	0.54817	0	0.54859
21.02	542420	0.52274	331540	0.51817	223690	0.51521	112280	0.51424	0	0.51386
26.025	747470	0.4963	453160	0.49374	309200	0.48801	155380	0.48676	0	0.4873
31.03	963470	0.47707	588140	0.47282	402910	0.46614	203220	0.464	0	0.46526
36.034	1191100	0.46171	733840	0.45522	503750	0.44808	255280	0.44481	0	0.44408
41.039	1428300	0.44911	888210	0.44039	611630	0.43255	311550	0.42807	0	0.42536
46.044	1673400	0.43857	1050300	0.42769	725510	0.41916	371360	0.41356	0	0.40901
51.049	1924500	0.42971	1218000	0.4169	844270	0.40762	435040	0.4005	0	0.39404
56.053	2178200	0.42243	1390300	0.40767	968700	0.39724	502870	0.38846	0	0.37998
61.058	2434200	0.4163	1568100	0.39944	1098200	0.38789	574640	0.37736	0	0.36666
66.063	2692000	0.41108	1750000	0.39217	1232600	0.37939	650530	0.367	0	0.3541
71.068	2950700	0.40663	1935200	0.38573	1371500	0.37164	730100	0.35742	0	0.3427
76.072	3209100	0.40287	2123500	0.37999	1514200	0.36459	812340	0.34878	0	0.33241
81.077	3466800	0.39967	2314000	0.37488	1660000	0.35821	896390	0.34111	0	0.32309
86.082	3723700	0.39695	2505800	0.37036	1807900	0.35251	981990	0.33427	0	0.31464

Pressure-Time-Porosity Dataset: Room Pressure (Pa) and Room Porosity vs. Time (Years) for f-series data

	f=1.0		f=0.6		f=0.4		f=0.2		f=0.0	
Time	P, Pa	Porosity	P, Pa	Porosity	P, Pa	Porosity	P, Pa	Porosity	P, Pa	Porosity
91.087	3979200	0.39464	2698300	0.36637	1956500	0.3475	1069000	0.32815	0	0.30708
96.091	4232800	0.39269	2891000	0.36285	2105600	0.3431	1157000	0.32264	0	0.30034
101.1	4484600	0.39106	3083500	0.35976	2254800	0.33921	1246000	0.3177	0	0.29436
111.11	4981500	0.38856	3466600	0.35467	2552900	0.33273	1425400	0.3093	0	0.28437
121.12	5469500	0.38689	3845300	0.35078	2849200	0.32766	1604900	0.30262	0	0.27667
131.12	5949300	0.3858	4218300	0.34785	3142400	0.32368	1781800	0.29749	0	0.27059
141.13	6422700	0.3851	4585100	0.34567	3431800	0.32059	1956200	0.29347	0	0.26563
151.14	6891700	0.38465	4945500	0.3441	3716300	0.31824	2129000	0.29024	0	0.26153
161.15	7357100	0.38436	5299900	0.34298	3995800	0.31646	2300400	0.28759	0	0.25808
171.16	7819600	0.3842	5648900	0.3422	4271100	0.31512	2470300	0.2854	0	0.25512
181.17	8279400	0.38413	5993100	0.34169	4542500	0.31412	2638900	0.28359	0	0.25254
191.18	8737200	0.38412	6333500	0.34137	4810200	0.31339	2806100	0.28208	0	0.25024
201.19	9192800	0.38417	6670000	0.34121	5074600	0.31287	2971900	0.28083	0	0.24819
211.2	9646100	0.38426	7002900	0.34118	5335900	0.31252	3136300	0.2798	0	0.24633
221.21	10089000	0.38458	7334100	0.3412	5594500	0.31231	3299300	0.27895	0	0.24469
231.22	10537000	0.38477	7664500	0.34124	5850600	0.3122	3461000	0.27825	0	0.24323
241.23	10977000	0.38513	7994000	0.3413	6104900	0.31217	3621400	0.27768	0	0.24192
251.24	11409000	0.3856	8322800	0.34138	6358300	0.31217	3780700	0.27722	0	0.24074
261.25	11841000	0.38604	8651100	0.34146	6610900	0.31219	3938900	0.27684	0	0.23966
271.26	12270000	0.38651	8978800	0.34155	6862900	0.31223	4096000	0.27655	0	0.23867

Pressure-Time-Porosity Dataset: Room Pressure (Pa) and Room Porosity vs. Time (Years) for f-series data

	f=1.0		f=0.6		f=0.4		f=0.2		f=0.0	
Time	P, Pa	Porosity	P, Pa	Porosity	P, Pa	Porosity	P, Pa	Porosity	P, Pa	Porosity
281.27	12691000	0.38708	9306000	0.34165	7114500	0.31228	4252100	0.27633	0	0.23777
291.28	13116000	0.38756	9632600	0.34176	7365600	0.31234	4407200	0.27616	0	0.23694
301.29	13505000	0.38862	9950100	0.34185	7616300	0.3124	4561500	0.27604	0	0.23617
311.3	13894000	0.38962	10277000	0.34194	7866700	0.31247	4714800	0.27596	0	0.23546
321.31	14213000	0.39134	10603000	0.34203	8116700	0.31255	4867600	0.27592	0	0.23481
331.32	14551000	0.39306	10929000	0.34212	8366300	0.31263	5019800	0.2759	0	0.23419
341.32	14883000	0.39478	11254000	0.34221	8615600	0.31271	5171700	0.27589	0	0.23362
351.33	15209000	0.3965	11580000	0.3423	8864600	0.3128	5323300	0.27589	0	0.23308
361.34	15531000	0.39822	11905000	0.34239	9113300	0.31289	5474600	0.2759	0	0.23258
371.35	15847000	0.39994	12230000	0.34248	9361600	0.31298	5625600	0.27592	0	0.23211
381.36	16158000	0.40165	12554000	0.34257	9609600	0.31308	5776500	0.27595	0	0.23166
391.37	16464000	0.40337	12879000	0.34266	9857400	0.31317	5927200	0.27598	0	0.23125
401.38	16765000	0.40509	13203000	0.34275	10105000	0.31327	6077600	0.27602	0	0.23085
411.39	17061000	0.40681	13502000	0.34325	10352000	0.31337	6228000	0.27606	0	0.23048
421.4	17352000	0.40853	13800000	0.34375	10599000	0.31347	6378100	0.2761	0	0.23012
431.41	17638000	0.41025	14096000	0.34425	10845000	0.31357	6528100	0.27614	0	0.22978
441.42	17920000	0.41197	14391000	0.34476	11091000	0.31367	6678000	0.27619	0	0.22946
451.43	18196000	0.41369	14685000	0.34526	11337000	0.31377	6827700	0.27624	0	0.22916
461.44	18468000	0.41541	14977000	0.34576	11583000	0.31388	6977300	0.27629	0	0.22887
471.45	18736000	0.41713	15268000	0.34626	11826000	0.31402	7126800	0.27634	0	0.22859

Pressure-Time-Porosity Dataset: Room Pressure (Pa) and Room Porosity vs. Time (Years) for f-series data

	f=1.0		f=0.6		f=0.4		f=0.2		f=0.0	
Time	P, Pa	Porosity	P, Pa	Porosity	P, Pa	Porosity	P, Pa	Porosity	P, Pa	Porosity
481.46	18999000	0.41885	15558000	0.34676	12064000	0.31425	7276100	0.27639	0	0.22833
491.47	19257000	0.42057	15846000	0.34726	12301000	0.31448	7425300	0.27644	0	0.22807
501.48	19512000	0.42229	16133000	0.34776	12537000	0.31474	7574400	0.2765	0	0.22783
511.49	19761000	0.42401	16393000	0.34863	12768000	0.31505	7723300	0.27656	0	0.2276
521.5	20007000	0.42573	16650000	0.34949	12998000	0.31537	7872100	0.27661	0	0.22738
531.51	20248000	0.42745	16905000	0.35036	13226000	0.31571	8020800	0.27667	0	0.22717
541.52	20485000	0.42917	17158000	0.35122	13455000	0.31602	8169300	0.27673	0	0.22696
551.52	20689000	0.43089	17385000	0.35209	13657000	0.31641	8305300	0.27679	0	0.22677
561.53	20731000	0.43261	17477000	0.35295	13776000	0.3165	8379500	0.27681	0	0.22658
571.54	20738000	0.43433	17568000	0.35382	13885000	0.31673	8453800	0.27684	0	0.2264
581.55	20774000	0.43605	17657000	0.35468	13996000	0.31692	8528000	0.27687	0	0.22623
591.56	20795000	0.43795	17746000	0.35555	14106000	0.31712	8602200	0.2769	0	0.22606
601.57	20825000	0.43971	17835000	0.35641	14216000	0.31732	8676300	0.27693	0	0.22589
611.58	20860000	0.4414	17922000	0.35728	14326000	0.31753	8750400	0.27696	0	0.22573
621.59	20883000	0.44322	17993000	0.35815	14436000	0.31773	8824500	0.27699	0	0.22558
631.6	20916000	0.44491	18096000	0.35878	14544000	0.31795	8898600	0.27701	0	0.22543
641.61	20947000	0.44661	18180000	0.35964	14651000	0.31818	8972700	0.27704	0	0.22529
651.62	20969000	0.44838	18264000	0.36049	14757000	0.31842	9046700	0.27707	0	0.22515
661.63	21000000	0.45005	18342000	0.3614	14865000	0.31863	9120600	0.2771	0	0.22501
671.64	21025000	0.45177	18419000	0.36231	14970000	0.3189	9194500	0.27713	0	0.22488

Pressure-Time-Porosity Dataset: Room Pressure (Pa) and Room Porosity vs. Time (Years) for f-series data

	f=1.0		f=0.6		f=0.4		f=0.2		f=0.0	
Time	P, Pa	Porosity	P, Pa	Porosity	P, Pa	Porosity	P, Pa	Porosity	P, Pa	Porosity
681.65	21046000	0.45352	18503000	0.36313	15076000	0.31912	9268400	0.27716	0	0.22475
691.66	21072000	0.45519	18574000	0.3641	15182000	0.31936	9342300	0.27719	0	0.22462
701.67	21092000	0.45692	18643000	0.36507	15286000	0.31962	9416200	0.27722	0	0.2245
711.68	21110000	0.45866	18719000	0.36596	15390000	0.31986	9490100	0.27725	0	0.22438
721.69	21131000	0.46035	18789000	0.36691	15492000	0.32013	9563900	0.27728	0	0.22426
731.7	21147000	0.46209	18852000	0.36792	15594000	0.3204	9637600	0.27732	0	0.22415
741.71	21163000	0.46381	18919000	0.36889	15697000	0.32067	9711300	0.27735	0	0.22404
751.72	21179000	0.46552	18986000	0.36985	15796000	0.32097	9784900	0.27738	0	0.22393
761.72	21191000	0.46726	19046000	0.37088	15897000	0.32125	9858600	0.27741	0	0.22382
771.73	21204000	0.46898	19106000	0.3719	15995000	0.32155	9932300	0.27744	0	0.22372
781.74	21216000	0.47069	19168000	0.37289	16092000	0.32187	10006000	0.27747	0	0.22362
791.75	21225000	0.47242	19225000	0.37392	16190000	0.32217	10080000	0.2775	0	0.22352
801.76	21235000	0.47414	19281000	0.37496	16213000	0.32317	10153000	0.27753	0	0.22342
811.77	21244000	0.47585	19336000	0.376	16259000	0.32417	10226000	0.27757	0	0.22332
821.78	21251000	0.47757	19390000	0.37704	16304000	0.32517	10300000	0.2776	0	0.22323
831.79	21258000	0.47928	19442000	0.3781	16348000	0.32616	10373000	0.27763	0	0.22314
841.8	21264000	0.48099	19492000	0.37917	16392000	0.32716	10447000	0.27766	0	0.22305
851.81	21269000	0.4827	19542000	0.38023	16435000	0.32816	10520000	0.2777	0	0.22296
861.82	21274000	0.4844	19591000	0.3813	16477000	0.32916	10594000	0.27773	0	0.22287
871.83	21278000	0.48609	19637000	0.38239	16519000	0.33016	10667000	0.27776	0	0.22279

Pressure-Time-Porosity Dataset: Room Pressure (Pa) and Room Porosity vs. Time (Years) for f-series data

	f=1.0		f=0.6		f=0.4		f=0.2		f=0.0	
Time	P, Pa	Porosity	P, Pa	Porosity	P, Pa	Porosity	P, Pa	Porosity	P, Pa	Porosity
881.84	21281000	0.48779	19683000	0.38347	16561000	0.33116	10740000	0.2778	0	0.22271
891.85	21284000	0.48947	19729000	0.38456	16601000	0.33216	10813000	0.27783	0	0.22262
901.86	21286000	0.49115	19772000	0.38566	16642000	0.33316	10887000	0.27786	0	0.22254
911.87	21288000	0.49283	19814000	0.38676	16681000	0.33416	10960000	0.27789	0	0.22247
921.88	21290000	0.49449	19856000	0.38786	16720000	0.33516	11033000	0.27793	0	0.22239
931.89	21291000	0.49615	19895000	0.38897	16759000	0.33616	11106000	0.27796	0	0.22231
941.9	21292000	0.49781	19935000	0.39008	16797000	0.33716	11179000	0.27799	0	0.22224
951.91	21292000	0.49945	19972000	0.3912	16834000	0.33816	11252000	0.27803	0	0.22216
961.92	21292000	0.5011	20009000	0.39233	16871000	0.33916	11325000	0.27806	0	0.22209
971.93	21292000	0.50273	20045000	0.39345	16907000	0.34016	11398000	0.2781	0	0.22202
981.93	21291000	0.50435	20080000	0.39458	16942000	0.34116	11471000	0.27813	0	0.22195
991.94	21291000	0.50597	20113000	0.39572	16978000	0.34215	11544000	0.27816	0	0.22188
1002	21290000	0.50758	20146000	0.39686	17012000	0.34315	11617000	0.2782	0	0.22181
1012	21289000	0.50918	20177000	0.398	17046000	0.34415	11690000	0.27823	0	0.22175
1022	21287000	0.51078	20208000	0.39915	17080000	0.34515	11763000	0.27827	0	0.22168
1032	21286000	0.51236	20238000	0.4003	17113000	0.34615	11836000	0.2783	0	0.22161
1042	21284000	0.51394	20266000	0.40146	17145000	0.34715	11908000	0.27833	0	0.22155
1052	21255000	0.51549	20269000	0.40259	17156000	0.34815	11966000	0.27836	0	0.22149
1062	21144000	0.51679	20194000	0.40346	17152000	0.3482	11966000	0.27836	0	0.22143
1072	21043000	0.51797	20125000	0.40427	17149000	0.34824	11965000	0.27837	0	0.22136

Pressure-Time-Porosity Dataset: Room Pressure (Pa) and Room Porosity vs. Time (Years) for f-series data

	f=1.0		f=0.6		f=0.4		f=0.2		f=0.0	
Time	P, Pa	Porosity	P, Pa	Porosity	P, Pa	Porosity	P, Pa	Porosity	P, Pa	Porosity
1082	20950000	0.51906	20062000	0.40501	17145000	0.34829	11965000	0.27837	0	0.2213
1092	20865000	0.52006	20005000	0.40569	17142000	0.34833	11965000	0.27838	0	0.22124
1102	20786000	0.521	19951000	0.40632	17138000	0.34838	11965000	0.27838	0	0.22118
1112.1	20713000	0.52187	19901000	0.40692	17135000	0.34842	11965000	0.27838	0	0.22113
1122.1	20644000	0.5227	19854000	0.40748	17131000	0.34847	11965000	0.27838	0	0.22107
1132.1	20579000	0.52347	19810000	0.40801	17128000	0.34851	11965000	0.27838	0	0.22101
1142.1	20518000	0.52421	19768000	0.40851	17125000	0.34856	11965000	0.27838	0	0.22096
1152.1	20460000	0.5249	19728000	0.40899	17121000	0.34861	11964000	0.27838	0	0.2209
1162.1	20405000	0.52557	19691000	0.40945	17118000	0.34865	11964000	0.27839	0	0.22085
1172.1	20353000	0.5262	19654000	0.40988	17114000	0.3487	11964000	0.27839	0	0.22079
1182.1	20303000	0.5268	19620000	0.4103	17111000	0.34874	11964000	0.27839	0	0.22074
1192.1	20256000	0.52738	19587000	0.41071	17108000	0.34879	11964000	0.27838	0	0.22069
1202.1	20210000	0.52793	19555000	0.41109	17104000	0.34883	11964000	0.27838	0	0.22063
1212.2	20167000	0.52846	19524000	0.41147	17101000	0.34888	11964000	0.27838	0	0.22058
1222.2	20125000	0.52897	19495000	0.41183	17097000	0.34892	11964000	0.27839	0	0.22053
1232.2	20085000	0.52946	19466000	0.41218	17069000	0.34895	11964000	0.27839	0	0.22048
1242.2	20047000	0.52993	19439000	0.41251	17063000	0.34903	11964000	0.27839	0	0.22043
1252.2	20010000	0.53039	19412000	0.41284	17056000	0.34912	11964000	0.27839	0	0.22038
1262.2	19974000	0.53083	19386000	0.41315	17051000	0.34918	11964000	0.27839	0	0.22034
1272.2	19940000	0.53125	19361000	0.41346	17046000	0.34925	11964000	0.27839	0	0.22029

Pressure-Time-Porosity Dataset: Room Pressure (Pa) and Room Porosity vs. Time (Years) for f-series data

	f=1.0		f=0.6		f=0.4		f=0.2		f=0.0	
Time	P, Pa	Porosity	P, Pa	Porosity	P, Pa	Porosity	P, Pa	Porosity	P, Pa	Porosity
1282.2	19906000	0.53167	19337000	0.41376	17040000	0.34932	11964000	0.27839	0	0.22024
1292.2	19874000	0.53207	19314000	0.41405	17036000	0.34939	11964000	0.27839	0	0.22019
1302.2	19843000	0.53245	19291000	0.41433	17027000	0.3495	11964000	0.27839	0	0.22015
1312.2	19813000	0.53283	19269000	0.4146	17022000	0.34956	11964000	0.27839	0	0.2201
1322.3	19783000	0.53319	19247000	0.41487	17024000	0.34954	11964000	0.27839	0	0.22006
1332.3	19755000	0.53355	19226000	0.41513	17020000	0.34959	11964000	0.27839	0	0.22001
1342.3	19727000	0.53389	19206000	0.41539	17018000	0.34962	11964000	0.27839	0	0.21997
1352.3	19701000	0.53422	19186000	0.41563	17014000	0.34967	11964000	0.27839	0	0.21992
1362.3	19675000	0.53455	19166000	0.41588	17012000	0.3497	11964000	0.27839	0	0.21988
1372.3	19649000	0.53487	19147000	0.41611	17018000	0.34961	11964000	0.27839	0	0.21984
1382.3	19625000	0.53518	19129000	0.41634	17013000	0.34969	11964000	0.27839	0	0.21979
1392.3	19600000	0.53548	19111000	0.41657	17012000	0.3497	11964000	0.27839	0	0.21975
1402.3	19577000	0.53577	19093000	0.41679	17013000	0.34968	11964000	0.27839	0	0.21971
1412.3	19554000	0.53606	19076000	0.41701	17009000	0.34974	11964000	0.27838	0	0.21967
1422.4	19532000	0.53634	19059000	0.41722	17014000	0.34967	11964000	0.27838	0	0.21963
1432.4	19510000	0.53662	19042000	0.41743	17010000	0.34972	11964000	0.27839	0	0.21959
1442.4	19489000	0.53688	19026000	0.41763	17004000	0.34979	11964000	0.27839	0	0.21955
1452.4	19468000	0.53715	19010000	0.41783	17005000	0.34978	11964000	0.27839	0	0.21951
1462.4	19448000	0.5374	18995000	0.41803	16999000	0.34986	11964000	0.27839	0	0.21947
1472.4	19428000	0.53765	18979000	0.41822	17001000	0.34983	11964000	0.27838	0	0.21943

Pressure-Time-Porosity Dataset: Room Pressure (Pa) and Room Porosity vs. Time (Years) for f-series data

	f=1.0		f=0.6		f=0.4		f=0.2		f=0.0	
Time	P, Pa	Porosity	P, Pa	Porosity	P, Pa	Porosity	P, Pa	Porosity	P, Pa	Porosity
1482.4	19409000	0.5379	18964000	0.41841	16999000	0.34987	11964000	0.27838	0	0.21939
1492.4	19390000	0.53814	18950000	0.41859	16988000	0.35	11964000	0.27838	0	0.21935
1502.4	19371000	0.53838	18935000	0.41877	16991000	0.34997	11964000	0.27838	0	0.21931
1512.4	19353000	0.53861	18921000	0.41895	16985000	0.35005	11964000	0.27838	0	0.21928
1522.4	19335000	0.53883	18907000	0.41913	16982000	0.35009	11964000	0.27838	0	0.21924
1532.5	19318000	0.53906	18894000	0.4193	16981000	0.3501	11964000	0.27838	0	0.2192
1542.5	19300000	0.53927	18880000	0.41947	16972000	0.35022	11965000	0.27838	0	0.21917
1552.5	19284000	0.53949	18867000	0.41964	16974000	0.3502	11965000	0.27838	0	0.21913
1562.5	19267000	0.5397	18854000	0.4198	16973000	0.35021	11965000	0.27838	0	0.21909
1572.5	19251000	0.5399	18841000	0.41996	16970000	0.35025	11965000	0.27838	0	0.21906
1582.5	19235000	0.54011	18829000	0.42012	16972000	0.35021	11965000	0.27838	0	0.21902
1592.5	19220000	0.54031	18817000	0.42028	16967000	0.35029	11965000	0.27838	0	0.21899
1602.5	19204000	0.5405	18805000	0.42043	16966000	0.35029	11965000	0.27838	0	0.21895
1612.5	19189000	0.5407	18793000	0.42058	16970000	0.35024	11965000	0.27838	0	0.21892
1622.5	19174000	0.54088	18781000	0.42073	16966000	0.35029	11965000	0.27837	0	0.21888
1632.6	19160000	0.54107	18769000	0.42088	16968000	0.35027	11965000	0.27837	0	0.21885
1642.6	19146000	0.54125	18758000	0.42103	16966000	0.35029	11965000	0.27837	0	0.21882
1652.6	19132000	0.54143	18747000	0.42117	16963000	0.35034	11965000	0.27838	0	0.21878
1662.6	19118000	0.54161	18736000	0.42131	16966000	0.3503	11965000	0.27838	0	0.21875
1672.6	19104000	0.54179	18725000	0.42145	16963000	0.35033	11965000	0.27838	0	0.21872

Pressure-Time-Porosity Dataset: Room Pressure (Pa) and Room Porosity vs. Time (Years) for f-series data

	f=1.0		f=0.6		f=0.4		f=0.2		f=0.0	
Time	P, Pa	Porosity	P, Pa	Porosity	P, Pa	Porosity	P, Pa	Porosity	P, Pa	Porosity
1682.6	19091000	0.54196	18714000	0.42159	16959000	0.35039	11965000	0.27837	0	0.21868
1692.6	19078000	0.54213	18704000	0.42172	16958000	0.35041	11965000	0.27837	0	0.21865
1702.6	19065000	0.54229	18693000	0.42186	16954000	0.35046	11965000	0.27837	0	0.21862
1712.6	19052000	0.54246	18683000	0.42199	16954000	0.35045	11965000	0.27837	0	0.21859
1722.6	19039000	0.54262	18673000	0.42212	16954000	0.35046	11965000	0.27837	0	0.21856
1732.6	19027000	0.54278	18663000	0.42224	16946000	0.35056	11965000	0.27837	0	0.21853
1742.7	19015000	0.54294	18653000	0.42237	16946000	0.35057	11965000	0.27837	0	0.21849
1752.7	19003000	0.54309	18644000	0.4225	16945000	0.35057	11965000	0.27837	0	0.21846
1762.7	18991000	0.54324	18634000	0.42262	16941000	0.35063	11965000	0.27837	0	0.21843
1772.7	18979000	0.5434	18625000	0.42274	16941000	0.35062	11965000	0.27837	0	0.2184
1782.7	18968000	0.54354	18615000	0.42286	16937000	0.35068	11965000	0.27837	0	0.21837
1792.7	18957000	0.54369	18606000	0.42298	16935000	0.35071	11965000	0.27837	0	0.21834
1802.7	18946000	0.54384	18597000	0.4231	16937000	0.35068	11965000	0.27837	0	0.21831
1812.7	18934000	0.54398	18588000	0.42321	16934000	0.35071	11965000	0.27837	0	0.21828
1822.7	18924000	0.54412	18579000	0.42333	16935000	0.3507	11966000	0.27836	0	0.21825
1832.7	18913000	0.54426	18570000	0.42344	16934000	0.35071	11966000	0.27836	0	0.21823
1842.8	18902000	0.5444	18562000	0.42355	16930000	0.35076	11966000	0.27836	0	0.2182
1852.8	18892000	0.54453	18553000	0.42366	16933000	0.35072	11966000	0.27836	0	0.21817
1862.8	18882000	0.54466	18545000	0.42377	16933000	0.35073	11966000	0.27836	0	0.21814
1872.8	18871000	0.5448	18536000	0.42388	16930000	0.35077	11966000	0.27836	0	0.21811

Pressure-Time-Porosity Dataset: Room Pressure (Pa) and Room Porosity vs. Time (Years) for f-series data

	f=1.0		f=0.6		f=0.4		f=0.2		f=0.0	
Time	P, Pa	Porosity	P, Pa	Porosity	P, Pa	Porosity	P, Pa	Porosity	P, Pa	Porosity
1882.8	18861000	0.54493	18528000	0.42399	16931000	0.35076	11966000	0.27836	0	0.21808
1892.8	18851000	0.54506	18520000	0.42409	16928000	0.3508	11966000	0.27836	0	0.21806
1902.8	18842000	0.54518	18512000	0.4242	16928000	0.3508	11966000	0.27836	0	0.21803
1912.8	18832000	0.54531	18504000	0.4243	16927000	0.35081	11966000	0.27836	0	0.218
1922.8	18822000	0.54543	18496000	0.4244	16922000	0.35087	11966000	0.27836	0	0.21797
1932.8	18813000	0.54556	18488000	0.42451	16922000	0.35088	11966000	0.27836	0	0.21795
1942.8	18804000	0.54568	18480000	0.42461	16919000	0.35092	11966000	0.27836	0	0.21792
1952.9	18795000	0.5458	18473000	0.4247	16917000	0.35095	11966000	0.27836	0	0.21789
1962.9	18785000	0.54592	18465000	0.4248	16918000	0.35093	11966000	0.27836	0	0.21787
1972.9	18776000	0.54604	18458000	0.4249	16913000	0.35099	11966000	0.27835	0	0.21784
1982.9	18768000	0.54615	18450000	0.425	16911000	0.35101	11966000	0.27835	0	0.21781
1992.9	18759000	0.54627	18443000	0.42509	16911000	0.35102	11966000	0.27835	0	0.21779
12001	18759000	0.54627	18443000	0.42509	16911000	0.35102	11966000	0.27835	0	0.21779

APPENDIX C: REFERENCED MEMORANDA

Appendix C: Referenced Memoranda

Sandia National Laboratories

Albuquerque, New Mexico 87185

date: June 18, 1993

to: M. S. Tierney, 6342

L. H. Brush

from: L. H. Brush, 6348

subject: **Likely Gas-Generation Reactions and Current Estimates of Gas-Generation Rates for the Long-Term WIPP Performance Assessment**

INTRODUCTION

This memorandum identifies likely gas-generation reactions (Table 1), provides current estimates of humid and inundated gas-generation rates (Tables 2 and 3), and calculates the gas-generation potential for radiolysis of H_2O in brine by ^{239}Pu for the 1993 long-term WIPP performance-assessment (PA) calculations. A. R. Lappin, 6305, has provided estimates of gas-generation potentials for other processes.

I understand that because of severe time constraints and the higher priorities assigned to other changes in the models to be used for the 1993 PA calculations, you will not have time to incorporate the current version of the gas-generation model J. W. Garner and I provided to P. Vaughn in February 1993. Therefore, I understand you will use the same gas-generation model used in the 1991 and 1992 calculations. This approach consists of listing likely gas-generation reactions, calculating the average stoichiometric gas-production ratio of these reactions, estimating average gas-production rates, and allowing gas production to proceed until the total quantity of gas expected (the gas-generation potential) is attained for a given set of assumptions. I refer to this model as the "average-stoichiometry model." The assumptions include (but are not necessarily limited to): (1) the inventory of reactants (steels and other Fe-base alloys, Al and Al-base alloys, and, perhaps, other metals; cellulosics, plastics, and rubbers); (2) the extent to which these materials are convertible to gas (this is especially important in the case of plastics and rubbers); (3) whether sufficient H_2O will be available (this is especially significant in the case of reactions that occur only in the presence of brine, such as anoxic corrosion of steels). Of course, assumptions such as these are also necessary for the gas-generation model Garner and I are developing.

Given the severe time constraints and the higher priorities assigned to other improvements in the PA models, I concur with your

decision to retain the average-stoichiometry model used in the 1991 and 1992 PA calculations. However, I recommend using additional gas-generation reactions, if possible, and current estimates of gas-generation rates. I describe these reactions and rates below. Of course, I realize that there may not be time to make any changes in the average-stoichiometry model at this point.

Garner and I will continue to develop a thermodynamic and kinetic reaction-path gas-generation model. The current version of this model includes the following processes: (1) corrosion of steels and other Fe-base materials by O_2, H_2O, H_2O and CO_2, or H_2S; (2) passivation of steels by CO_2; (3) depassivation of steels by destabilization of $FeCO_3$; (4) microbial degradation of cellulosics with O_2, NO_3^-, Fe(III) hydroxide, or SO_4^{2-} as the electron acceptor; (5) consumption of CO_2 by $Ca(OH)_2$ (in cementitious materials) and CaO (a potential backfill additive). The main differences between the reaction-path model and the average-stoichiometry model used in the 1991 and 1992 PA calculations are that: (1) the reaction-path model includes more gas-producing reactions than the average-stoichiometry model; (2) the reaction-path model includes gas-consuming reactions; (3) the reaction-path model includes interactions among gas-producing and gas-consuming processes, such as passivation of steels by microbially-produced CO_2 and depassivation of steels due to consumption of CO_2 by $Ca(OH)_2$ and CaO. We will provide you with the latest version of this model as soon as you are ready to incorporate it in the PA models.

CORROSION

Oxic corrosion of steel waste containers (drums and boxes), Fe-base alloys in the waste, and, perhaps, other metals would consume O_2 in mine air trapped in WIPP disposal rooms at the time of filling and sealing. Oxic corrosion would also consume O_2 produced by radiolysis of H_2O in brine. After depletion of the O_2 initially present, anoxic corrosion of Fe-base and other metals could produce significant quantities of H_2, at least in microenvironments without radiolytically produced O_2. Other metals that could consume O_2 and produce H_2 include (but are not necessarily limited to) Al, Al-base alloys, Pb, and Pu. Oxic and anoxic corrosion could also consume significant quantities of brine and H_2O vapor.

Oxic Corrosion

Brush (1990) concluded that oxic corrosion of steels, other Fe-base alloys, and, perhaps, other metals would not have a significant, direct effect on the gas and H_2O budget of WIPP disposal rooms. However, this process could be important from the standpoint of the O_2 budget of the repository. The O_2 budget will in turn affect how soon the repository becomes anoxic after filling and sealing, the extent to which microenvironments dominated by brine radiolysis remain oxic, whether gas is consumed or produced, and which gases are consumed and

produced. The O_2 budget will also affect the oxidation state of radionuclides and hence their chemical behavior. Therefore, Garner and I have added the following reaction to the reaction-path gas-generation model to simulate oxic corrosion:

$$2Fe + H_2O + 1.5O_2 = 2\gamma FeO(OH) \qquad (1)$$

We are using this reaction because N. R. Sorensen, 1832, observed that $\gamma FeO(OH)$ (lepidocrocite) was the most abundant corrosion product in oxic, inundated experiments carried out for the Strategic Petroleum Reserve Project. Sorensen also observed Fe_3O_4 as a major corrosion product and $\beta FeO(OH)$ as a minor corrosion product. Therefore, Garner and I may also add an equation simulating the formation of Fe_3O_4. (Addition of an equation for $\beta FeO(OH)$ would not change the stoichiometry of Reaction 1).

For my best estimate of the O_2-consumption rate for oxic corrosion, I recommend 5 moles per m^2 of steel per year, the value (rounded off to one significant figure) reported by Molecke (1979). Lappin et al. (1989) estimated that there are 6 m^2 of steels and other Fe-base alloys per drum of CH TRU waste, 4 m^2 for CH TRU waste containers and an estimated 2 m^2 for the Fe-base alloys in CH TRU waste. (These values do not include steel or other Fe-base alloys in canisters or plugs to be used for RH TRU waste, any steels or other Fe-base alloys contained in RH TRU waste, or steels or other Fe-base alloys used for ground support in the WIPP underground workings.) Therefore, this rate is equivalent to 30 moles of O_2 per drum of CH TRU waste per year. I computed the oxic-corrosion rate as follows.

The rate at which Fe is consumed by Reaction 1 is:

$$((2 \text{ moles Fe}) / (1.5 \text{ moles } O_2)) \cdot 5 \text{ moles } O_2/(m^2 \cdot \text{yr})$$

$$= 6.67 \text{ moles Fe}/(m^2 \cdot \text{yr}). \qquad (2)$$

(Only one of the figures in this and the following equations are significant, but I did not round off until the end of these calculations.) This rate is equivalent to:

$$6.67 \text{ moles}/(m^2 \cdot \text{yr}) \cdot 5.5847 \cdot 10^{-2} \text{ kg/mole}$$

$$= 3.7231 \cdot 10^{-1} \text{ kg}/(m^2 \cdot \text{yr}). \qquad (3)$$

In Equation 2, "$5.5847 \cdot 10^{-2}$ kg" is the mass of a mole of metallic Fe. The thickness of the layer of Fe removed from the surface per year is:

$$3.7231 \cdot 10^{-1}\ \text{kg}/(\text{m}^2 \cdot \text{yr}) \,/\, 7.86 \cdot 10^{3}\ \text{kg}/\text{m}^3$$

$$= 5 \cdot 10^{-5}\ \text{m/yr}. \qquad (4)$$

In Equation 4, "$7.86 \cdot 10^3$ kg/m^3" is the density of metallic Fe. This rate is equivalent to about 50 μm of steel per year (Table 2). I cannot compare these estimates of O_2-consumption or corrosion rates with previous estimates because I did not estimate these rates for oxic corrosion of steels for the 1991 and 1992 PA calculations (see Brush, 1991).

My minimum estimates of O_2-consumption and corrosion rates for oxic corrosion of steels and other Fe-base alloys under inundated conditions, 0 moles per per m^2 of steel per year or 0 moles of O_2 per drum of CH TRU waste per year and 0 μm of steel per year (Table 2), are based on the possibility of passivation by formation of an adherent corrosion product (see Anoxic Corrosion below), or by precipitation of salts on the surfaces of corroding metals due to the consumption of H_2O during oxic corrosion of steels, other Fe-base alloys, and, perhaps, other metals. Although laboratory studies have not demonstrated these mechanisms yet, they are possible, especially (in the case of the latter mechanism) if microbial degradation of cellulosics and brine radiolysis also consume significant quantities of H_2O.

My maximum estimates of O_2-consumption and corrosion rates for oxic corrosion of steels and other Fe-base alloys under inundated conditions (Table 2) are based on estimates of the effects of pH on these rates. I have not yet considered the effects of total pressure, the partial pressures of gases expected in WIPP disposal rooms, or temperature on oxic corrosion. However, I have considered the effects of these factors on anoxic corrosion (see below); the analysis for anoxic corrosion suggests that pH is the most important of these factors. In the case of oxic corrosion, O_2-consumption and corrosion rates are inversely proportional to pH. I used the inverse relationship between pH and oxic-corrosion rates observed experimentally for applications other than the WIPP Project and estimates of the range of pH expected in WIPP disposal rooms after filling and sealing to estimate the maximum values of these rates.

I assume that the O_2-consumption rate of 5 moles per m^2 of steel per year (Molecke, 1979), which I used for my best estimate of this and other rates under inundated conditions (Table 2), pertains to Reaction 1 at a neutral or nearly neutral pH. Furthermore, I expect that the pH in WIPP disposal rooms will vary between about 3 and 12. Although obtained with deionized H_2O, the results of Uhlig and Revie (1963) suggest that the O_2-consumption and corrosion rates for oxic corrosion of steels are constant or essentially constant between a pH of about 4 and 10, that these rates are higher by about a factor of 1.5 at a pH of 3, and that they are lower by a factor of 0.6 at a pH of 11 and by a factor of 0.4 at a pH of 12. Therefore, the possibility of pH values as low as 3 in WIPP disposal rooms necessitates multiplying my

best estimates in Table 2 by a factor of 1.5:

$$1.5 \cdot 5 \text{ moles/m}^2 = 8 \text{ moles/(m}^2 \cdot \text{yr)}; \quad (5a)$$

$$1.5 \cdot 30 \text{ moles/(drum} \cdot \text{yr)} = 50 \text{ moles/(drum} \cdot \text{yr)}; \quad (5b)$$

$$1.5 \cdot 50 \ \mu\text{m/yr} = 80 \ \mu\text{m/yr}. \quad (5c)$$

These are my maximum estimates, rounded to one significant figure, of these rates under inundated conditions (Table 2). Because they are maximum estimates, I have rounded them up in all three cases. The effects of basic conditions on oxic corrosion need not be considered at this point because, although they decrease these rates, my minimum estimates are already 0 moles of O_2 per m^2 of steel per year, 0 moles of O_2 per drum of CH TRU waste per year, and 0 μm of steel per year because of possible passivation (see above).

My best estimates of O_2-consumption and corrosion rates for oxic corrosion of steels and other Fe-base alloys under humid conditions are 0.5 moles of O_2 per m^2 of steel per year, 3 moles of O_2 per drum of CH TRU waste per year, and 5 μm of steel per year (Table 3). I arbitrarily assume that these rates are one tenth of my current best estimates for oxic corrosion under inundated conditions (Table 2). I did not estimate these rates for oxic corrosion of steels for the 1991 and 1992 PA calculations (Brush, 1991).

My arbitrary minimum estimates of O_2-consumption and corrosion rates for oxic corrosion of steels and other Fe-base alloys under humid conditions are also 0 moles of O_2 per m^2 of steel per year, 0 moles of O_2 per drum of CH TRU waste per year, and 0 μm of steel per year (Table 3).

My maximum estimates of O_2-consumption and corrosion rates for oxic corrosion of steel and other Fe-base alloys under humid conditions are 5 moles of O_2 per m^2 of steel per year, 30 moles of O_2 per drum of CH TRU waste per year, and 50 μm of steel per year (Table 2). I arbitrarily assume that these rates are identical to my current best estimates for oxic corrosion under inundated conditions (Table 2).

If oxic-corrosion rates under humid conditions affect the overall performance of the repository significantly, laboratory studies will be necessary to replace these arbitrary estimates with experimentally-based results.

Anoxic Corrosion

Anoxic corrosion of steels, other Fe-base alloys, and, perhaps, other metals may, if brine is present, produce significant quantities

of H_2 and consume significant qu ities of H_2O (Lappin et al., 1989; Brush, 1990).

I used thermodynamic calcul ons and laboratory studies carried out for applications other t the WIPP Project to predict the behavior of steels and other Fe-base alloys under expected WIPP conditions (see Brush, 1990). I am extending these thermodynamic calculations to support of the development of the reaction-path gas-generation model (see INTRODUCTION above).

R. E. Westerman and M. R. Telander of Pacific Northwest Laboratory (PNL) are carrying out laboratory studies of anoxic corrosion for the WIPP Project. So far, they have studied two heats each of the low-C steels ASTM A 366 and ASTM A 570 under inundated conditions (specimens immersed in Brine A) and humid conditions (specimens suspended above Brine A) with initially pure atmospheres of N_2, CO_2, and H_2S at low pressures (about 1 to 15 atm) at 30 ± 5°C. ASTM A 366 simulates the waste drums to be emplaced in the repository; ASTM A 570 simulates the boxes. Brine A is a synthetic brine that, although developed to simulate fluids equilibrated with K^+- and Mg^{2+}-bearing minerals in overlying potash-rich zones prior to entering the repository (Molecke, 1983), is coincidentally similar in composition to intergranular brines from the Salado Fm. at or near the stratigraphic horizon of the WIPP underground workings. Westerman and Telander have also conducted experiments with these steels under inundated conditions with initially pure N_2, CO_2, and H_2 at high pressures (about 35 or 70 atm). Finally, they have performed preliminary experiments with these steels in simulated backfill materials (crushed salt and a mixture of 70 wt % crushed salt and 30 wt % bentonite) at low pressures. Westerman and Telander also plan to study anoxic corrosion of Al and Al-base materials.

Telander and Westerman (in prep.) have identified three likely anoxic-corrosion reactions. At low fugacities (similar to partial pressures) of CO_2 and H_2S, the reaction observed in 3-, 6-, 12-, and 24-month experiments appears to be:

$$Fe + 2H_2O = Fe(OH)_2 + H_2. \qquad (6a)$$

However, Brush (1990) calculated that $Fe(OH)_2$ is unstable with respect to Fe_3O_4. Therefore, significant quantities of steels and other Fe-base alloys could eventually corrode via the reaction:

$$3Fe + 4H_2O = Fe_3O_4 + 4H_2. \qquad (6b)$$

At relatively high CO_2 fugacities, the experimentally observed reaction is:

$$Fe + H_2O + CO_2 = FeCO_3 + H_2. \quad (7)$$

Formation of the adherent corrosion product $FeCO_3$ (siderite) by this reaction will passivate steels and, presumably, other Fe-base alloys after the consumption of various quantities of CO_2. Currently, laboratory studies at PNL suggest a range of 0.33 to 2.2 moles of CO_2 per m^2 of steel for the amount of CO_2 required for passivation, depending on the CO_2 partial pressure and the pH of the brine. However, I do not recommend revision of the average-stoichiometry gas-generation model to include passivation. To avoid potential criticism, inclusion of this process would also necessitate the inclusion of depassivation, the simulation of which would require a reaction-path model such as the one Garner and I are developing.

Finally, at relatively high H_2S fugacities, the experimentally observed reaction appears to be:

$$Fe + 2H_2S = FeS_2 + 2H_2. \quad (8a)$$

Laboratory studies at PNL suggest that this reaction also passivates steels and other Fe-base alloys. However, I do not recommend revision of the average-stoichiometry model to include passivation by this reaction for the reasons given in connection with Equation 3 (above).

A literature review by Telander and Westerman (in prep.) and thermodynamic calculations for the reaction-path model have identified another possible reaction involving H_2S:

$$Fe + H_2S = FeS + H_2. \quad (8b)$$

The literature reviewed by Telander and Westerman (in prep.) suggests that this reaction does not passivate steels and other Fe-base alloys. Table 1 summarizes these anoxic-corrosion reactions.

In addition to these corrosion reactions, there exist numerous likely reactions among Fe-bearing corrosion products such as $Fe(OH)_2$, Fe_3O_4, $FeCO_3$, FeS, and FeS_2. Garner and I are incorporating these reactions in the reaction-path model to predict, among other things, if and when depassivation of steels will occur. I do not recommend revising the average-stoichiometry model to include reactions among corrosion products.

My best estimates of H_2-production and corrosion rates for anoxic corrosion of steels and other Fe-base alloys under inundated conditions are based on data reported by Telander and Westerman (in prep.) They obtained average H_2-production rates of 0.19, 0.21, 0.16, and 0.10 moles per m^2 of steel per year in experiments carried out under

inundated conditions with initially pure N_2 at low pressures (about 10 to 15 atm) for 3, 6, 12, and 24 months, respectively. Because there are 6 m^2 of steels and other Fe-base alloys per drum of CH TRU waste (Lappin et al., 1989), these rates are equivalent to 1.14, 1.26, 0.96, and 0.60 moles of H_2 per drum of CH TRU waste per year. The average corrosion rates in the 3-, 6-, 12-, and 24-month runs were 1.97, 1.72, 1.23, and 0.99 μm of steel per year. For my best estimates, I prefer values of 0.1 moles of H_2 per m^2 of steel per year or 0.6 moles of H_2 per drum of CH TRU waste per year and 1 μm of steel per year (see Table 2). These rates, from the 24-month experiments at PNL, are less by as much as about a factor of two than the rates observed in the 3-, 6-, and 12-month runs. Therefore, my best estimates are now half or about half those provided for the 1991 and 1992 PA calculations (Brush, 1991), 0.2 moles of H_2 per m^2 of steel per year, 1 mole of H_2 per drum of CH TRU waste per year, and 2 μm of steel per year, for which I used the 6-month results.

Strictly speaking, my best estimates of H_2-production and corrosion rates for anoxic corrosion of steels and other Fe-base alloys under inundated conditions (Table 2) pertain only to Reaction 6a, the reaction which apparently occurs with initially pure N_2 at low and high pressures. However, I arbitrarily assume that, at any given pH, Reactions 6b, 7, 8a, and 8b occur at the same rate as Reaction 6a. Therefore, my best estimates also apply to these reactions. Clearly, Reaction 7 proceeded much faster than Reaction 6a in low-pressure, inundated experiments at PNL, at least prior to passivation (below). However, this was probably because the pH of Brine A was much lower in runs with initially pure CO_2 at low pressures than in runs with initially pure N_2 at low pressures. I describe the effects of pH in the discussion of my maximum estimates for anoxic corrosion under inundated conditions (below).

My minimum estimates of H_2-production and corrosion rates for anoxic corrosion of steels and other Fe-base alloys under inundated conditions (Table 2) are based on passivation observed by Telander and Westerman (in prep.) in 6-, 12-, and 24-month, low-pressure (about 12 to 15 atm) experiments with initially pure CO_2. In these runs, the H_2-production and corrosion rates were high initially but decreased to 0 moles of H_2 per m^2 of steel per year or, 0 moles of H_2 per drum of CH TRU waste per year and 0 μm of steel per year after about 3 or 4 months due to passivation by Reaction 7 (above). Passivation at these pressures apparently required 0.33 moles of CO_2 per m^2 of steel, a very small quantity relative to the total microbial CO_2 production potential. My minimum estimates of these rates are identical to those provided for the 1991 and 1992 PA calculations (Brush, 1991). However, Telander and Westerman (in prep.) have now completed 12- and 24-month experiments, which confirm the results of the 6-month runs. Furthermore, since preparing their report, Westerman and Telander have also observed passivation in 6- and 12-month, high-pressure (about 36 to 40 atm) runs. These high-pressure tests partially address the concerns of those who claimed that high CO_2 partial pressures and concomitant acidification of brine would destabilize the passivating

film of $FeCO_3$ and restart anoxic corrosion and H_2 production. Experiments carried out to date suggest that these high CO_2 partial pressures increase the quantity of CO_2 required to passivate steels somewhat, from 0.33 to 2.2 moles per m^2 of steel. However, this requirement is still very small relative to the total microbial CO_2 production potential. On the other hand, these high CO_2 partial pressures apparently decrease the time required for passivation somewhat, from about 3 or 4 months to 2 months.

At least two other passivation mechanisms are possible. First, after a few days of H_2 production, Telander and Westerman (in prep.) have observed passivation of steels under inundated conditions with initially pure H_2S at low pressures (about 5 to 6 atm) for up to about 200 days. This is probably due to formation of the adherent corrosion product FeS_2 (pyrite) by Reaction 8a (above). Based on preliminary results obtained with the reaction-path model, Garner and I think that FeS_2 formation may be unlikely in WIPP disposal rooms. This is because H_2S fugacities high enough and CO_2 and H_2 fugacities low enough to stabilize FeS_2 may be unlikely, given expected stoichiometries for microbial gas-production reactions. Therefore, passivation by $FeCO_3$ appears more likely than passivation by FeS_2. However, the latter is still possible.

A second passivation mechanism is precipitation of salts on the surfaces of corroding metals due to the consumption of H_2O during anoxic corrosion (see Oxic Corrosion above).

The results of laboratory studies of anoxic corrosion at PNL demonstrate that passivation of steels, at least by $FeCO_3$, is a real phenomenon under at least some combinations of conditions expected in WIPP disposal rooms. However, based on preliminary results of modeling studies, Garner and I believe that depassivation of steels is also possible, especially if consumption of CO_2 by $Ca(OH)_2$ (in hydrated cementitious materials) and CaO (a potential backfill additive) decrease the fugacity of CO_2 below values required to stabilize $FeCO_3$. Nevertheless, minimum estimates of 0 moles of H_2 per m^2 of steel per year or 0 moles of H_2 per drum of CH TRU waste per year and 0 μm of steel per year seem justified at this time.

For my maximum estimates of H_2-production and corrosion rates for anoxic corrosion of steels and other Fe-base alloys under inundated conditions (Table 2), I estimated the effects of pH, pressure, and temperature on these rates. These H_2-production and corrosion rates are: (1) inversely proportional to pH; (2) proportional to the partial pressures of CO_2 and, probably, H_2S (both of these gases decrease the pH of any brine they are in contact with as their partial pressures increase); (3) proportional to the partial pressure of N_2 and hence the total pressure; (4) inversely proportional to the partial pressure of H_2; (5) probably proportional to temperature. I used estimated or experimentally measured relationships between these parameters and the H_2-production and corrosion rates, and estimates of the extreme values of these parameters in the repository after filling and sealing to

estimate the maximum values of these rates.

Telander and Westerman (in prep.) reported that the pH of Brine A, initially 6.7, increased to values of 8.3, 8.3, and 8.4 after the 6-, 12-, and 24-month, low-pressure experiments with initially pure N_2. (They did not report the pH of Brine A after the 3-month runs.) Therefore, the best estimates of these rates (Table 2) pertain to Reaction 6a at a neutral or nearly neutral pH. I expect that the pH in WIPP disposal rooms will vary between about 3 and 12. Although obtained for applications other than the WIPP Project, the results of Uhlig and Revie (1963) and Grauer et al. (1991) suggest that the H_2-production and corrosion rates for anoxic corrosion of steels are constant or essentially constant between a pH of about 4 and 10, that these rates are higher by about a factor of 50 at a pH of 3, and that they are lower by a factor of 0.05 at a pH of 11 and by a factor of 0.005 at a pH of 12. Therefore, the possibility of pH values as low as 3 in WIPP disposal rooms necessitates multiplying my best estimates in Table 2 by a factor of 50:

$$50 \cdot 0.10 \text{ moles/m}^2 = 5 \text{ moles/(m}^2 \cdot \text{yr)}; \quad (9a)$$

$$50 \cdot 0.60 \text{ moles/(drum} \cdot \text{yr)} = 30 \text{ moles/(drum} \cdot \text{yr)}; \quad (9b)$$

$$50 \cdot 1 \ \mu\text{m/yr} = 50 \ \mu\text{m/yr}. \quad (9c)$$

If acidification is caused by CO_2 or, perhaps, H_2S (see below), the increase in rates described above may only be temporary due to passivation of steels by $FeCO_3$ or, perhaps, FeS_2. However, organic acids produced by microbial degradation of cellulosics in the waste (below) could also acidify the brines in WIPP disposal rooms. These acids may not result in passivation of steels. The effects of basic conditions on anoxic corrosion need not be considered here because, although they decrease these rates, my minimum estimates are already 0 moles of H_2 per m^2 of steel per year or 0 moles of H_2 per drum of CH TRU waste per year and 0 μm of steel per year because of passivation (see above).

Based on the results of 6-month experiments, Telander and Westerman (in prep.) reported that an N_2 partial pressure of 73 atm increased the average corrosion rate of steels by about a factor of two from that observed at an N_2 partial pressure of 10 atm. Because 73 atm is about half of lithostatic pressure at the depth of the WIPP underground workings, I assume that total pressure (the effects of which should be equivalent to those of high N_2 partial pressure) could increase the H_2-production and corrosion rates for steels and other Fe-base alloys by as much as a factor of four. Therefore, the effect of lithostatic pressure on the rates estimated for the lowest pH expected in the repository necessitates multiplying the rates obtained from Equations

9a, 9b, and 9c by a factor of four:

$$4 \cdot 5 \text{ moles/m}^2 = 20 \text{ moles/(m}^2 \cdot \text{yr)}; \quad (10a)$$

$$4 \cdot 30 \text{ moles/(drum} \cdot \text{yr)} = 120 \text{ moles/(drum} \cdot \text{yr)}; \quad (10b)$$

$$4 \cdot 50 \ \mu\text{m/yr} = 200 \ \mu\text{m/yr}. \quad (10c)$$

High CO_2 and H_2S partial pressures should increase the H_2-production and corrosion rates for anoxic corrosion of steels and other Fe-base alloys under inundated conditions, at least prior to passivation, because the solubilities of these gases in aqueous solutions are proportional to their partial pressures and they form the weak, diprotic acids H_2CO_3 and H_2S after dissolution. Although weak, these acids do deprotonate to some extent, thus acidifying solutions in contact with these gases. However, I have already included the effects acidification on anoxic corrosion (see above).

The results of 6- and 12-month experiments carried out by Telander and Westerman (in prep.) suggest that H_2 partial pressures of 35, 69, and 70 atm decreased the average corrosion rate of steels by about a factor of five from that observed at the H_2 partial pressures in the low-pressure runs. High H_2 partial pressures have the opposite effect of high N_2 partial pressures (or total pressure) because H_2 is a product of Reactions 6a, 6b, 7, 8a, and 8b. The effects of high H_2 partial pressures on anoxic corrosion need not be addressed further because, although they decrease these rates, my minimum estimates are already 0 moles of H_2 per m^2 of steel per year or 0 moles of H_2 per drum of CH TRU waste per year and 0 μm of steel per year because of passivation.

Telander and Westerman (in prep.) have carried out all of their laboratory studies of anoxic corrosion at 30 ± 5°C. I assume that the temperature during their experiments was normally distributed about a value of 30°C. Therefore, their average rates pertain to this temperature. I also assume a temperature of 30 ± 3°C in WIPP disposal rooms after filling and sealing. This is slightly above the in situ temperature of 27°C at a subsurface depth of 2,150 feet because of the small amount of heat produced by RH TRU waste and, to a much lesser extent, by CH TRU waste. Finally, I assume that a 10°C increase in temperature would increase the rates of Reactions 6a, 6b, 7, 8a, and 8b by a factor of two. Therefore, the effect of a temperature of 33°C on the rates estimated for the lowest pH and highest total pressure expected in the repository, based on experiments carried out at 30 ± 5°C, requires multiplying the rates obtained from Equations 10a, 10b, and 10c by a factor of 1.23 (obtained from $2^{((33 - 30)/10)}$):

$$1.23 \cdot 20 \text{ moles}/(\text{m}^2 \cdot \text{yr}) = 20 \text{ moles}/(\text{m}^2 \cdot \text{yr}); \quad (11a)$$

$$1.23 \cdot 120 \text{ moles}/(\text{drum} \cdot \text{yr}) = 100 \text{ moles}/(\text{drum} \cdot \text{yr}); \quad (11b)$$

$$1.23 \cdot 200 \ \mu\text{m/yr} = 200 \ \mu\text{m/yr}. \quad (11c)$$

These are my maximum estimates, rounded to one significant figure, of these rates under inundated conditions (Table 2). They are significantly higher than those provided for the 1991 and 1992 PA calculations (Brush, 1991), 0.4 moles of H_2 per m^2 of steel per year or 2 moles of H_2 per drum of CH TRU waste per year and 3 μm of steel per year, because the combined effects of pH, high N_2 partial pressure or total pressure, and temperature have a much greater effect on these rates than high N_2 partial pressure, the only factor I included in my previous estimates of the maximum rates under inundated conditions.

My best estimates of H_2-production and corrosion rates for anoxic corrosion of steels and other Fe-base alloys under humid conditions are 0 moles of H_2 per m^2 of steel per year or 0 moles of H_2 per drum of CH TRU waste per year and 0 μm of steel per year (Table 3). These rates are less than those provided for the 1991 and 1992 PA calculations (Brush, 1991), 0.02 moles of H_2 per m^2 of steel per year or 0.1 moles of H_2 per drum of CH TRU waste per year and 0.2 μm of steel per year, which I arbitrarily assumed were one tenth of the best estimates provided at that time for inundated conditions. As of 1991, no H_2 production or corrosion had occurred in 3- and 6-month humid, low-pressure experiments with initially pure N_2 or CO_2, except for very limited H_2 production due to corrosion of some of the bottom 10% of the specimens splashed with brine during pretest preparation procedures. Since then, Telander and Westerman (in prep.) have obtained identical results from 6- and 12-month runs. These results confirm and extend the results of the 3- and 6-month runs. Therefore, I have reduced my best estimates as described above.

My minimum estimates of H_2-production and corrosion rates for anoxic corrosion of steels and other Fe-base alloys under humid conditions are also 0 moles of H_2 per m^2 of steel per year or 0 moles of H_2 per drum of CH TRU waste per year and 0 μm of steel per year (Table 3). These minimum estimates are identical to those provided for the 1991 and 1992 PA calculations (Brush, 1991).

My arbitrary maximum estimates of H_2-production and corrosion rates for anoxic corrosion of steels and other Fe-base alloys under humid conditions are 0.01 moles of H_2 per m^2 of steel per year or 0.06 moles of H_2 per drum of CH TRU waste per year and 0.1 μm of steel per year (Table 3). I arbitrarily assume that these rates are one tenth of my current best estimates for anoxic corrosion under inundated conditions. My maximum estimates for humid conditions are less than those provided for the 1991 and 1992 PA calculations (Brush, 1991), 0.2 moles of H_2

per m^2 of steel per year, 1 mole of H_2 per drum of CH TRU waste per year, and 2 μm of steel per year, which I arbitrarily assumed were identical to the best estimates provided at that time for inundated conditions.

If anoxic-corrosion rates under humid conditions significantly affect the behavior of the repository, additional laboratory studies will be necessary to replace these arbitrary estimates with actual experimental results.

MICROBIAL ACTIVITY

Microbial degradation of cellulosics and, perhaps, plastics and rubbers in the waste to be emplaced in WIPP disposal rooms may, if sufficient brine or H_2O vapor, nutrients, and viable microorganisms are present, produce or consume significant quantities of various gases and produce or consume significant quantities of H_2O (Lappin et al., 1989; Brush, 1990). The gases produced could include CO_2, CH_4, H_2S, N_2, and NH_3; the gases consumed could include CO_2, H_2 and O_2.

Brush (1990) applied the conceptual model of sequential usage of electron acceptors by microorganisms in natural environments (see, for example, Froelich et al., 1979; Berner, 1980) to WIPP disposal rooms. In natural environments, the observed sequence is aerobic respiration, NO_3^- reduction, reduction of Mn(IV) oxides and and hydroxides, reduction of Fe(III) oxides and and hydroxides, SO_4^{2-} reduction, and methanogenesis. Alternatively, reduction of Mn(IV) oxides and hydroxides may precede NO_3^- reduction. Based on which potential electron acceptors will be present in significant quantities in the repository after filling and sealing, I concluded that denitrification, SO_4^{2-} reduction, fermentation, and methanogenesis are potentially significant microbial processes (see Brush, 1990).

A. J. Francis and J. B. Gillow of Brookhaven National Laboratory (BNL) are carrying out laboratory studies of microbial gas production for the WIPP Project. Currently, they are conducting short- and long-term (up to 24-month) studies of microbial degradation of papers under inundated conditions with and without addition of electron acceptors and bentonite, amendment with nutrients, and inoculation with halophilic microorganisms from the WIPP Site and vicinity. They are also planning similar experiments under humid conditions and experiments with other potential substrates such as irradiated and unirradiated plastics and rubbers.

Aerobic Microbial Activity

I concluded that aerobic microbial activity will not affect the gas and H_2O budgets of WIPP disposal rooms directly (see Brush, 1990). However, this process could affect the O_2 budget of the repository significantly. The O_2 budget will in turn affect the chemical behavior

of the repository (see Oxic Corrosion above). Furthermore, Francis and Gillow (in prep.) have observed significant aerobic microbial activity. Therefore, Garner and I have added it to the reaction-path gas-generation model.

During aerobic microbial activity (or any other microbial process) the degradation of organic matter is complex and involves several intermediate steps usually mediated by different microorganisms. Geochemists have described microbial processes by writing simplified overall equations. Berner (1980) used the following equation to represent aerobic microbial activity:

$$CH_2O + O_2 = H_2O + CO_2. \qquad (12)$$

This equation uses the formula CH_2O (a simplified formula for glucose) to represent the substrate (mainly papers and other cellulosics in the case of the WIPP) and does not include the synthesis of cellular material (biomass) by microorganisms. These approximations are certainly adequate for the average-stoichiometry gas-generation model, but may not be for the reaction-path model.

Anaerobic Microbial Activity

I also concluded that microbial denitrification could significantly affect the gas and H_2O budgets of WIPP disposal rooms (see Brush, 1990). Furthermore, Francis and Gillow (in prep.) have observed production of significant quantities of N_2O, a precursor of N_2 and an indicator of denitrification. According to Berner (1980), the overall equation for denitrification is:

$$CH_2O + 0.8H^+ + 0.8NO_3^- = 1.4H_2O + CO_2 + 0.4N_2. \qquad (13)$$

Microbial reduction of Fe(III) oxides and hydroxides will not affect on the gas and H_2O budgets of WIPP disposal rooms significantly (Brush, 1990). However, Fe(III) reduction could affect the O_2 budget, which will in turn affect the chemical behavior of the repository (see Oxic Corrosion). Therefore, Garner and I added five possible Fe(III)-reduction reactions to the reaction-path model:

$$CH_2O + 4FeO(OH) + H_2O = 4Fe(OH)_2 + CO_2 \qquad (14a)$$

$$CH_2O + 4FeO(OH) = 1.33Fe_3O_4 + 1.67H_2O + CO_2 + 1.33H_2 \qquad (14b)$$

$$CH_2O + 4FeO(OH) + H_2O + 3CO_2 = 4FeCO_3 + 4H_2O \qquad (14c)$$

$$CH_2O + 4FeO(OH) + 4H_2S = 4FeS + 7H_2O + CO_2 \quad (14d)$$

$$CH_2O + 4FeO(OH) + 8H_2S = 4FeS_2 + 7H_2O + CO_2 + 4H_2 \quad (14e)$$

Finally, microbial SO_4^{2-} reduction could affect the repository gas and H_2O budgets significantly (Brush, 1990). Francis and Gillow (in prep.) have not analyzed for H_2S, a product of SO_4^{2-} reduction. However, they have observed blackening, an indicator of SO_4^{2-} reduction, in some of their experiments. Berner (1980) gave the following overall equation for SO_4^{2-} reduction:

$$CH_2O + H^+ + 0.5SO_4^{2-} = H_2O + CO_2 + 0.5\ H_2S. \quad (15)$$

Finally, Brush (1990) concluded that microbial fermentation and methanogenesis could significantly affect the gas and H_2O budgets of WIPP disposal rooms. Francis and Gillow (in prep.) have not analyzed for CH_4, a product of methanogenesis. However, it would be almost impossible to rule out methanogenesis in the repository if other microbial processes are expected. Berner's (1980) overall equation for methanogenesis is:

$$2CH_2O = CH_4 + CO_2. \quad (16a)$$

However, the simultaneous presence of CO_2 and H_2 in the repository could facilitate the following reaction proposed by Francis and Gillow (in prep.):

$$CO_2 + 4H_2 = CH_4 + 2H_2O. \quad (16b)$$

Garner and I will include both of these equations in the reaction-path model and will probably use Equation 16b whenever both CO_2 and H_2 are present.

Francis and Gillow (in prep.) observed aerobic respiration, denitrification, and SO_4^{2-} reduction in their long-term study of microbial degradation of papers under inundated conditions. So far, the gas-production rates observed in these experiments have all been within the range estimated by Brush (1991) for the 1991 and 1992 PA calculations. There is probably no justification, at least on the basis of the results obtained by Francis and Gillow to date, for reducing the previously-estimated range. On the other hand, there is certainly no justification for extending it. Therefore, I recommend using the previously-provided rates again. My best estimate of the <u>total</u> microbial gas production rates from <u>all</u> of the processes

described in Reactions 12 through 16a (above) under inundated conditions is 0.1 moles of gas (CO_2, CH_4, H_2S and N_2) per kg of cellulosics per year. There are 10 kg of cellulosics per drum of CH TRU waste (Brush, 1990). (These values do not include any cellulosics in RH TRU waste.) Therefore, this rate is equivalent to 1 mole of gas per drum of CH TRU waste per year. My minimum estimate for inundated conditions is 0 moles of gas per kg of cellulosics per year or 0 moles of gas per drum of CH TRU waste per year. My maximum estimate is 0.5 moles of gas per kg of cellulosics per year or 5 moles of gas per drum of CH TRU waste per year.

Methanogenesis by Reaction 16b could consume significant quantities of CO_2 and especially H_2. Francis and Gillow (in prep.) have not observed this reaction yet. However, if it occurs under expected WIPP conditions, this reaction could consume a significant fraction of the CO_2 produced by microbial activity, the H_2 produced by anoxic corrosion, or even both, depending on the ratio of CO_2 to H_2O in the repository and the extent to which it proceeds. I have not estimated rates for this reaction yet. Predictions of the effects of this methanogenic reaction on the gas and H_2O budgets of the repository will require measurements of its rates of gas consumption under expected WIPP conditions and its incorporation in the reaction-path model Garner and I are developing. However, it may be possible to estimate the rate of Reaction 16b from studies carried out for application other than the WIPP Project.

Because Francis and Gillow (in prep.) have not reported any results for humid conditions yet, I recommend using the same microbial gas-production rates provided for the 1991 and 1992 PA calculations (Brush, 1991). My arbitrary best estimate of the total microbial gas production rates from all of the processes described in Reactions 12 through 16a (above) under humid conditions is 0.01 moles of gas per kg of cellulosics per year or 0.1 moles of gas per drum of CH TRU waste per year. My arbitrary minimum estimate for humid conditions is 0 moles of gas per kg of cellulosics per year or 0 moles of gas per drum of CH TRU waste per year. My arbitrary maximum estimate is 0.1 mole of gas per kg of cellulosics per year or 1 mole of gas per drum of CH TRU waste per year. I have not estimated any rates for methanogenesis by Reaction 16b yet.

Francis and Gillow are now carrying out laboratory studies of microbial gas production under conditions at BNL. Results from these studies will eventually replace these arbitrary estimates.

RADIOLYSIS

The rates of gas production from radiolysis of H_2O in brine and sludges in WIPP disposal rooms and radiolysis of cellulosics, plastics and rubbers in the waste will probably be significantly less than those expected from anoxic corrosion or microbial activity (Molecke, 1979;

Brush, 1990). However, even if these radiolytic gas-production rates are low, Garner and I will include radiolysis in the reaction-path gas-generation model we are developing to: (1) determine if, in the event that the rates and quantities of gas produced by anoxic corrosion and microbial activity turn out to be smaller than expected, radiolysis is still a minor gas-production mechanism; (2) predict the O_2 budget of the repository (see Oxic Corrosion above).

D. T. Reed and S. Okajima of Argonne National Laboratory (ANL) have quantified gas production from α radiolysis of WIPP brines as a function of dissolved ^{239}Pu concentration and brine composition. It is possible to use their results to calculate gas-production rates for other Pu isotopes, particulate Pu in contact with brine (colloids suspended in brine, undissolved particles in the waste, and precipitated particles), and other actinide elements dissolved, suspended, or otherwise in contact with brine. However, I did not have time to do so prior to submission of these estimates to PA. Instead, I considered only dissolved ^{239}Pu. I am currently gathering the information required to extend these calculations to include other Pu isotopes, particulate Pu, and important isotopes of other actinide elements. Eventually, Garner and I may include some or all of these other factors in the reaction-path model.

Reed and Okajima (in prep.) have observed H_2 production, but not O_2 production, from brine radiolysis in experiments carried out with ^{239}Pu. Recently, they have observed production of both H_2 and O_2 in runs conducted with ^{238}Pu. These studies and previous laboratory studies reviewed by Reed and Okajima (in prep.) suggest that, given sufficiently high absorbed doses, the O_2 production rate eventually approaches 50% that of H_2 in both pure H_2O and brines. Strictly speaking, O_2 is not a direct product of the radiolytic decomposition of H_2O. Instead, O_2 forms by the breakdown of O-containing intermediate species, such as H_2O_2 in pure H_2O and, possibly, ClO_3^- (chlorate) or ClO_4^- (perchlorate) in brines. On the other hand, it is possible that these intermediate species will react with electron donors (reductants), such as steels, other Fe-base alloys, other metals, or organic matter, before they produce significant O_2. However, to simplify brine radiolysis for the reaction-path model, Garner and I are using the equation:

$$H_2O \rightarrow H_2 + 0.5O_2. \qquad (17)$$

Initially, we will assume that this process produces O_2 immediately. We may include a realistic induction period to account for the necessary build-up of O-containing intermediate species once the laboratory studies under way at ANL quantify the absorbed dose required to initiate O_2 production. We will then be able to calculate the time required to attain this dose as a function of the dissolved and suspended concentrations of radionuclides in WIPP brines. Until these results become available, the reaction-path model may overestimate the

time required for the repository to become anoxic and overestimate the proportion of the waste that remains oxic in microenvironments in which brine radiolysis is the predominant redox-determining process.

Reed and Okajima (in prep.) reported $G(H_2)$ values of 1.1 to 1.4 molecules per 100 eV for Brine A and ERDA-6, two synthetic WIPP brines, and DH-36 and G-Seep, two brines collected from the WIPP underground workings. The observed $G(H_2)$ values are independent of the dissolved ^{239}Pu concentration in these experiments. Garner and I plan to use units of moles of H_2, O_2, or H_2 plus O_2 per m^3 of brine per year in the reaction-path model. Therefore, I converted the results of Reed and Okajima (in prep.) from units of molecules per 100 eV to units of moles per m^3 of brine as follows.

For a dissolved ^{239}Pu concentration of 1 M, there are $2.39 \cdot 10^2$ g of ^{239}Pu per L of brine. The current estimate of the quantity of Pu to be emplaced in WIPP disposal rooms and the quantities of brine expected in the repository imply that there will not be enough Pu present to support an <u>average</u> Pu concentration of 1 M (see below). However, a <u>local</u> Pu concentration of 1 M may be possible in microenvironments in which Pu is highly soluble. Because there are $1 \cdot 10^3$ L of brine per m^3 of brine, the mass of ^{239}Pu per m^3 of brine is:

$$2.39 \cdot 10^2 \text{ g/L} \cdot 1 \cdot 10^3 \text{ L/m}^3 = 2.39 \cdot 10^5 \text{ g/m}^3. \quad (18)$$

(Only two of the figures in this and the following equations are significant, but I did not round off until the end of these calculations.) The activity of ^{239}Pu per m^3 of brine is:

$$2.39 \cdot 10^5 \text{ g/m}^3 \cdot 0.0613 \text{ Ci/g} = 1.46507 \cdot 10^4 \text{ Ci/m}^3). \quad (19)$$

In Equation 19, "0.0613 Ci/g" is the specific activity of ^{239}Pu. The disintegration rate of ^{239}Pu per m^3 of brine is:

$$1.46507 \cdot 10^4 \text{ Ci/m}^3 \cdot 3.7 \cdot 10^{10} \text{ (d/s)/Ci}$$

$$= 5.42076 \cdot 10^{14} \text{ d/(m}^3 \cdot \text{s)}. \quad (20)$$

In Equation 20, "d" is the abbreviation for "disintegrations," not "days!" The energy-deposition rate per m^3 of brine is:

$$5.42076 \cdot 10^{14} \text{ d/(m}^3 \cdot \text{s)} \cdot 5.15 \text{ MeV/d}$$

$$= 2.79169 \cdot 10^{15} \text{ MeV/(m}^3 \cdot \text{s)}. \quad (21)$$

In Equation 21, "5.15 MeV/d" is the average energy of an α particle emitted during the disintegration of ^{239}Pu. Changing units gives:

$$2.79169 \cdot 10^{15}\ \text{MeV}/(\text{m}^3 \cdot \text{s}) \cdot 1 \cdot 10^{6}\ \text{eV/MeV} \cdot 3.15576 \cdot 10^{7}\ \text{s/yr}$$

$$= 8.80991 \cdot 10^{28}\ \text{eV}/(\text{m}^3 \cdot \text{yr}). \qquad (22)$$

I used a value of 1.25 molecules per 100 eV for $G(H_2)$ (the midpoint of the range of 1.1 to 1.4 molecules per 100 eV reported by Reed and Okajima (in prep.) for Brine A, ERDA-6, DH-36, and G-Seep) to calculate the number of molecules of H_2 produced per m^3 of brine per year:

$$8.80991 \cdot 10^{28}\ \text{eV}/(\text{m}^3 \cdot \text{yr}) \cdot 1.25 \cdot 10^{-2}\ \text{molecules/eV}$$

$$= 1.10124 \cdot 10^{27}\ \text{molecules}/(\text{m}^3 \cdot \text{yr}). \qquad (23)$$

The number of moles of H_2 produced per m^3 of brine per year is:

$$1.10124 \cdot 10^{27}\ \text{molecules}/(\text{m}^3 \cdot \text{yr}) \ / \ 6.0225 \cdot 10^{23}\ \text{molecules/mole}$$

$$= 1.8 \cdot 10^{3}\ \text{moles}/(\text{m}^3 \cdot \text{yr}). \qquad (24)$$

In Equation 24, "$6.0225 \cdot 10^{23}$ molecules/mole is Avogadro's number. Of course, "$1.8 \cdot 10^{3}$ moles/($m^3 \cdot$ yr)" is actually the midpoint of a range of 1.6 to $2.0 \cdot 10^{3}$ moles/($m^3 \cdot$ yr).

I repeated these calculations for dissolved ^{239}Pu concentrations of $1 \cdot 10^{-1}$, $1 \cdot 10^{-2}$, $1 \cdot 10^{-3}$, $1 \cdot 10^{-4}$, $1 \cdot 10^{-5}$, $1 \cdot 10^{-6}$, $1 \cdot 10^{-7}$, $1 \cdot 10^{-8}$, and $1 \cdot 10^{-9}$ M (see Table 4). Again, the quantity of Pu to be emplaced in WIPP disposal rooms and the quantities of brine expected in the repository imply that there will not be enough Pu present to support some of these <u>average</u> Pu concentrations (see below). I calculated O_2-production rates for the same dissolved ^{239}Pu concentrations in these brines by assuming a value of 0.625 molecules per 100 eV for $G(O_2)$ (half the midpoint of the observed range for $G(H_2)$) and neglecting the induction period for O_2 production from the breakdown of O-containing intermediate species (Table 4). (Bear in mind that O-containing intermediate species may react with electron donors in WIPP disposal rooms before they produce significant O_2.) Finally, I calculated total radiolytic gas-production rates by adding the H_2- and O_2-production rates (Table 4).

I converted these rates from units of moles of H_2, O_2, and H_2 plus O_2 per m^3 of brine per year to units of H_2, O_2, and H_2 plus O_2 per equivalent drum of CH TRU waste per year to compare them with the rates of gas production from anoxic corrosion and microbial activity. I

multiplied each of the rates in Table 4 by 135, 305, 525, or 815 m^3 of brine per WIPP disposal room to convert them to units of moles of H_2, O_2, and H_2 plus O_2 per room per year. B. M. Butcher used these estimates of the residual gas-accessible void volume in a WIPP disposal room and immediate vicinity for his recent calculations of gas-storage capacities. I then assumed that these volumes could become inundated. Of course, brine volumes less than 135 m^3 are entirely possible. Next, I divided Butcher's volumes by 6,800 drums of CH TRU waste per room to obtain units of moles of H_2, O_2, and H_2 plus O_2 per drum per year. Tables 5, 6, and 7 give these rates for H_2, O_2, and H_2 plus O_2, respectively.

To calculate the maximum <u>average</u> Pu concentrations as a function of brine volume and time (Table 8), I used the quantities of brine required to saturate the residual gas-accessible void volume in a WIPP disposal room (see above) and referred to the PA code DECAY to obtain the initial Pu inventory and decay predictions used for the most recent PA calculations (WIPP Performance Assessment Department, 1992). (PA personnel will also use this inventory for the round of calculations to be presented to the EPA in February 1994.) At each time (0, 100, 200, 500, 1,000, 2,000, 5,000, and 10,000 years), I added the quantities of ^{238}Pu, ^{239}Pu, ^{240}Pu, ^{241}Pu, ^{242}Pu, and ^{244}Pu present in both CH and RH TRU waste in the column labeled "Scaled Inventory" in the output files from the PA code DECAY. "Scaled inventory" refers to the quantity of Pu (or other) isotopes present in one WIPP disposal panel. I then divided these sums by 12.65, the number of equivalent WIPP disposal rooms in one panel. Next, I calculated the percentage of each isotope of Pu present at each time and calculated the average molecular weight of Pu at that time. I assumed that the molecular weight of each isotope has an integral value equal to its mass number. I then divided the total mass of Pu by 135,000, 305,000, 525,000, or 815,000 L, the quantities of brine present in 135, 305, 525, or 815 m^3 of brine, respectively. Finally, I divided the results by the average molecular weight of Pu at that time to obtain the concentrations shown in Table 8.

Clearly, both the dissolved ^{239}Pu and the volume of brine to which this concentration pertain will strongly affect the H_2-, O_2-, and H_2-plus O_2-production rates from brine radiolysis. If the dissolved ^{239}Pu concentration is low enough, these gas-production rates are obviously insignificant (see Tables 5, 6, and 7). On the other hand, if the dissolved ^{239}Pu concentration and the ^{239}Pu inventory are high enough, these gas-production rates can equal or even exceed those of anoxic corrosion and microbial activity, at least locally. Given a range of 135 to 815 m^3 of brine per room, the range of Pu solubilities and the Pu inventory assumed for WIPP disposal rooms will determine the range of radiolytic gas-production rates.

For my best estimates of the rates of gas production from brine radiolysis, I chose $6.0 \cdot 10^{-10}$ M, the midpoint of the range of Pu(V) solubilities estimated by the Radionuclide-Source-Term Expert Panel (Trauth et al., 1992). (The Expert Panel also estimated the same

midpoint for the range of Pu(IV) solubilities.) For ^{239}Pu, this dissolved concentration yields rates of $1.1 \cdot 10^{-6}$ moles of H_2 per m^3 per year, $5.4 \cdot 10^{-7}$ moles of O_2 per m^3 per year, and $1.6 \cdot 10^{-6}$ moles of H_2 plus O_2 per m^3 per year, equivalent to rates of $6.6 \cdot 10^{-8}$ moles of H_2 per drum per year, $3.3 \cdot 10^{-8}$ moles of O_2 per drum per year, and $9.9 \cdot 10^{-8}$ moles of H_2 plus O_2 per drum per year (Table 2). To convert from units of moles per m^3 per year to moles per drum per year, I used the average of the rates for 305 and 525 m^3 of brine per room in Tables 5, 6, and 7.

For my minimum estimates of the rates of gas production from brine radiolysis, I used the lower limit of the range of Pu solubilities estimated by the Expert Panel and 135 m^3, the lower limit of the range of residual gas-accessible void volume expected in a WIPP disposal room. (Of course, there could be less than 135 m^3 of brine in a room.) The Expert Panel estimated that, for expected repository conditions, the lower limit of the range of Pu solubilities is $2.5 \cdot 10^{-17}$ M, the value estimated for Pu(V). For ^{239}Pu, this dissolved concentration yields rates of $4.5 \cdot 10^{-14}$ moles of H_2 per m^3 per year, $2.2 \cdot 10^{-14}$ moles of O_2 per m^3 per year, and $6.7 \cdot 10^{-14}$ moles of H_2 plus O_2 per m^3 per year, equivalent to rates of $8.9 \cdot 10^{-16}$ moles of H_2 per drum per year, $4.5 \cdot 10^{-16}$ moles of O_2 per drum per year, and $1.3 \cdot 10^{-15}$ moles of H_2 plus O_2 per drum per year (Table 2).

It may be more difficult to defend estimates of the maximum rates of gas production from brine radiolysis. The Expert Panel estimated that the upper limit of the range of Pu solubilities is $5.5 \cdot 10^{-4}$ M, the value estimated for Pu(V). Assuming that all of the Pu present is $^{239}Pu(V)$, this estimate and 815 m^3 of brine per room (the upper limit of the range of residual gas-accessible void volume) yield upper limits of $9.9 \cdot 10^{-1}$ moles of H_2 per m^3 of brine per year, $5.0 \cdot 10^{-1}$ moles of O_2 per m^3 per year, and $1.5 \cdot 10^{0}$ moles of H_2 plus O_2 per m^3 per year (Table 2). Again, the current estimate of the quantity of Pu to be emplaced in the repository and 815 m^3 of brine per WIPP disposal room imply that there will not be enough Pu present to support an <u>average</u> Pu concentration of $5.5 \cdot 10^{-4}$ M (see above). These rates are equivalent to $1.2 \cdot 10^{-1}$ moles of H_2 per drum of CH TRU waste per year, $6.0 \cdot 10^{-2}$ moles of O_2 per drum per year, and $1.8 \cdot 10^{-1}$ moles of H_2 plus O_2 per drum per year (Table 2). These are my favorite estimates of the maximum gas-production rates from brine radiolysis. I like them because the Expert Panel is responsible for defending $5.5 \cdot 10^{-4}$ M as the upper limit of the range of Pu solubilities. A reasonable way to estimate the probability distribution for values within the range of gas-production rates from brine radiolysis is to assume the same probability distribution estimated by the Expert Panel for Pu(V) solubilities.

However, I believe that $5.5 \cdot 10^{-4}$ M may not be a defensible upper limit of the range of Pu solubilities. Pu(III) is probably more soluble than Pu(IV) and Pu(V), the only oxidation states for which the Expert Panel estimated solubilities. Furthermore, Pu(VI) could well turn out to be more soluble than Pu(III)! Presumably, the Expert Panel

did not estimate solubilities of Pu(III) and Pu(VI) because it accepted the hypothesis that Pu(III) and Pu(VI) will be unstable with respect to Pu(IV) and Pu(V) in WIPP disposal rooms and that Pu(IV) and Pu(V) will thus control the solubility of Pu. This hypothesis may be impossible to defend given the results of laboratory studies by Reed and Okajima (in prep.) in which Pu(VI) remained stable in WIPP brines for lengthy periods. They observed that Pu(VI) is the predominant form of Pu in Brine A and G Seep during stability experiments carried out for periods of over 300 and 400 days. (Stability runs are necessary to demonstrate that Pu remains in solution during an experiment to quantify gas production by brine radiolysis.) Reed and Okajima (in prep.) observed dissolved Pu(VI) concentrations on the order of 10^{-3} and 10^{-4} M in Brine A and G Seep during 300- and 400-day stability runs. Furthermore, they observed a Pu(VI) concentration of $2 \cdot 10^{-2}$ M in G Seep during an 80- or 90-day stability run. Because these experiments did not contain high concentrations of the inorganic ligand CO_3^{2-}, which could significantly increase both the stability and the solubility of Pu(VI), or any organic ligands, which could also increase the stability and solubility of Pu(VI), the results are clearly not worst-case. Nevertheless, ^{239}Pu concentrations on the order of 10^{-2} M would, if the inventory of ^{239}Pu were high enough, imply upper limits of the ranges of gas-production rates from brine radiolysis on the order of 10^1 moles of H_2, O_2, and H_2 plus O_2 per m^3 of brine per year (see Table 4) or 10^0 moles of H_2, O_2, and H_2 plus O_2 per drum of CH TRU waste per year (Tables 5, 6, and 7). These rates are similar to those expected from anoxic corrosion and microbial activity under inundated conditions.

If a significant fraction of Pu in WIPP disposal rooms is actually present as Pu(VI), its chemical behavior would probably be similar to that of its oxidation-state analog U(VI). G. R. Choppin observed dissolved U(VI) concentrations of about $1 \cdot 10^{-4}$ M in approximately 600-day dissolution experiments in Brine A at a pH of about 8 and $2 \cdot 10^{-3}$ M in 250-day precipitation runs under the same conditions at Florida State University. (Dissolution and precipitation experiments, also referred to as undersaturation and supersaturation runs, bracket the solubility by approaching equilibrium from opposite directions.) These results are similar to those of the ANL stability runs. Even worse, the Expert Panel's estimate of $1.0 \cdot 10^0$ M for the upper limit of the range of the solubility of U(VI) could apply to Pu(VI) as well. This would, if the inventory of ^{239}Pu were high enough, imply upper limits of the ranges of gas-production rates from brine radiolysis on the order of 10^3 moles of H_2, O_2, and H_2 plus O_2 per m^3 of brine per year (Table 4) or 10^2 moles of H_2, O_2, and H_2 plus O_2 per drum of CH TRU waste per year (Tables 5, 6, and 7). These rates are much higher than those expected from anoxic corrosion and microbial activity under inundated conditions.

Similarly, if a significant fraction of Pu is present as Pu(III), the Expert Panel's estimate of $1.4 \cdot 10^0$ M for the upper limit of the range of the solubilities of Am(III) and Cm(III) could apply to Pu(III). This would also imply very high upper limits of the ranges of

gas-production rates from brine radiolysis.

It is important to point out that such high solubilities may not persist indefinitely. For example, H. Nitsche of Lawrence Berkeley Laboratory observed dissolved Pu concentrations between about $1 \cdot 10^{-4}$ and $1 \cdot 10^{-3}$ M for over 1 year in a precipitation experiment started with initially pure Pu(VI) in Brine A at a pH of about 7. However, after about 400 days, the concentration of Pu dropped to between $1 \cdot 10^{-7}$ and $1 \cdot 10^{-6}$ M. This suggests that Pu(VI) may be unstable with respect to other, less soluble oxidation states and that, given enough time, the solubility of Pu will decrease to the ranges estimated by the Expert Panel for Pu(IV) and Pu(V). Therefore, it would probably be difficult at this time to defend upper limits of the ranges of gas-production rates from brine radiolysis based on a dissolved Pu(VI) concentration of $2 \cdot 10^{-2}$ M observed by Reed and Okajima (in prep.) during an 80- or 90-day stability experiment. It might even be difficult to defend upper limits based on Pu(VI) concentrations on the order of 10^{-4} or 10^{-3} M in several-hundred-day solubility or stability runs. These are the maximum average Pu concentrations that can be supported by the current inventory (see Table 8). Furthermore, even if Pu is highly soluble under some combinations of conditions in WIPP disposal rooms, brine radiolysis would, like anoxic corrosion, probably be self-limiting. This is because neither anoxic corrosion nor brine radiolysis seems to occur under humid conditions. Therefore, small quantities of brine in the repository may produce H_2 (in the case of anoxic corrosion) or H_2 and O_2 (in the case of brine radiolysis), increase the pressure, prevent additional brine inflow or even cause brine outflow, and thus prevent or greatly reduce additional gas production, at least by these mechanisms. However, I still feel that it may be difficult to rule out the possibility of very high (relative to anoxic corrosion and microbial activity) upper limits of the ranges of gas-production rates from brine radiolysis, at least in some microenvironments with high Pu solubilities. Furthermore, if the average Pu solubility turns out to be high, increasing the quantity of Pu to be emplaced in WIPP disposal rooms could significantly affect the gas budget of the repository, and perhaps its performance.

I calculated the gas-production potential for radiolysis of H_2O in brine by ^{239}Pu as follows. According to the initial Pu inventory and decay predictions used for the most recent PA calculations (WIPP Performance Assessment Department, 1992), there will be 568,600 g of ^{239}Pu in CH TRU waste and 14,280 g of ^{239}Pu in RH TRU waste per WIPP disposal panel at the time of emplacement. After 10,000 years, there will be 426,300 g of ^{239}Pu in CH TRU waste and 10,710 g of ^{239}Pu in RH TRU waste per panel. The mass of ^{239}Pu in one panel that will decay during the 10,000-year period of performance of the repository is:

$$(568{,}600 \text{ g} + 14{,}280 \text{ g}) - (426{,}300 \text{ g} + 10{,}710 \text{ g}) = 145{,}870 \text{ g}. \quad (25)$$

(I do not know how many of the figures in this and the following

equations are significant, but I suspect not more than one!) The mass of ^{239}Pu in an equivalent drum of CH TRU waste that will decay in 10,000 years is:

$$145{,}870 \text{ g/panel} / 86{,}000 \text{ drums/panel} = 1.69616 \text{ g/drum}. \quad (26)$$

I have included the ^{239}Pu in RH TRU waste in an "equivalent drum of CH TRU waste" for the sake of completeness, but this only increases the mass of ^{239}Pu per drum by about 2.5%! The number of ^{239}Pu disintegrations per drum in 10,000 years will be:

$$1.69616 \text{ g/drum} / 239 \text{ g/mole} \cdot 6.0225 \cdot 10^{23} \text{ d/mole}$$

$$= 4.27411 \cdot 10^{21} \text{ d}. \quad (27)$$

Assuming that all of the Pu in a drum dissolves in brine at the time of emplacement and remains dissolved throughout the 10,000-year period of performance of the repository is the worst-case assumption from the standpoint of radiolytic gas production. This assumption results in initial dissolved total Pu concentrations of $1.60 \cdot 10^{-3}$, $7.09 \cdot 10^{-4}$, $4.12 \cdot 10^{-4}$, or $2.65 \cdot 10^{-4}$, depending on the volume of brine per WIPP disposal room (see Table 8). Half of these values are higher than $5.5 \cdot 10^{-4}$ M, the upper limit of the range of Pu solubilities estimated by the Expert Panel. However, the laboratory studies of radionuclide chemistry described above have yielded dissolved Pu(VI) concentrations higher than $1.60 \cdot 10^{-3}$ M, at least so far. The total quantity of energy deposited in brine by decay of ^{239}Pu in 10,000 years is:

$$4.27411 \cdot 10^{21} \text{ d} \cdot 5.15 \text{ MeV/d} = 2.20117 \cdot 10^{28} \text{ eV}. \quad (28)$$

The number of moles of H_2 formed is:

$$2.20117 \cdot 10^{28} \text{ eV} \cdot 1.25 \text{ molecules/100 eV} /$$

$$6.0225 \cdot 10^{23} \text{ molecules/mole} = 4.57 \cdot 10^{2} \text{ moles/drum}. \quad (29)$$

In Equation 29, "1.25 molecules per 100 eV" is the midpoint of the range of $G(H_2)$ (1.1 to 1.4 molecules per 100 eV) reported by Reed and Okajima (in prep.) for three WIPP brines (see above) and "$6.0225 \cdot 10^{23}$ molecules/mole is Avogadro's number. Therefore, "$4.57 \cdot 10^{2}$ moles/drum" is actually the midpoint of a range of 4.02 to $5.12 \cdot 10^{2}$ moles per drum.

In addition to about 500 moles of H_2 per drum, the O_2-production potential for brine radiolysis by ^{239}Pu could be as high as about 250 moles per drum, depending on the induction period for O_2 production from the breakdown of O-containing intermediate species (above). However, Garner and I believe that oxic corrosion and aerobic microbial activity (above) will rapidly consume any O_2 produced by brine radiolysis. Therefore, we omit O_2 from the discussion that follows.

Although these results includes decay of ^{239}Pu but none of the other radionuclides in TRU waste, they are of the same order of magnitude as the H_2-production potential of 900 moles per drum from anoxic corrosion of steel CH TRU waste containers (drums and boxes) and steels and other Fe-base alloys in CH TRU waste (Brush, 1990). They are also similar to my calculated gas-production potential of 600 moles per drum from microbial degradation 100% of the cellulosics and 50% of the rubbers in CH TRU waste.

However, values of 500 moles of H_2 per drum and 750 moles of H_2 plus O_2 per drum for the gas-production potential from brine radiolysis by ^{239}Pu are probably far larger than what will actually be produced in WIPP disposal rooms. The assumption that all of the energy from decay of ^{239}Pu will be deposited in brine is probably far too pessimistic. It is much more likely that a significant fraction of this decay energy will be deposited in undissolved, particulate, Pu-bearing solids or other solids with which Pu is associated (cellulosics such as paper towels, articles of clothing, rubber gloves, other solids in sludges, etc.)

Preliminary results obtained after adding brine radiolysis to the PA code PANEL also suggest that actual radiolytic gas production will be much smaller than the gas-production potentials calculated above. (The addition of brine radiolysis to PANEL is the first step in the addition of brine radiolysis to the reaction-path gas-generation model.) PANEL calculates the quantities of radionuclides dissolved in brine in WIPP disposal rooms as a function of time. Currently, it uses either an internal analytical model or the two-phase flow code BRAGFLO to predict the quantity of Salado- or Castile-Fm. brine present as a function of time. It then uses Latin hypercube sampling of solubilities estimated by the Expert Panel to predict the solubilities of Pu and other important actinide elements, and uses the initial inventory and decay rates of individual isotopes of these elements to calculate the relative abundance of each dissolved radionuclide as a function of time. Garner added the equations used to calculate the gas-production potential from decay of ^{239}Pu (above) to PANEL and extended them to include other important α-emitting radionuclides in the WIPP inventory. For his preliminary calculations, Garner used predictions of brine inflow and outflow from BRAGFLO runs made for the last round of PA calculations (WIPP Performance Assessment Department, 1992), which included the average-stoichiometry gas-generation model. The brine volume in a panel varied with time in each vector (simulation). However, the gas-generation rates from anoxic corrosion and microbial activity and the dissolved concentration of each

radioactive element did not vary within a given vector, unless brine was completely consumed or the quantity of a radioactive element in the inventory limited its concentration to a value less than the sampled solubility.

The largest quantity of H_2 produced by brine radiolysis during the 10,000-year period of performance of the repository was 90 moles per drum, a value significantly smaller than the 500-mole-per-drum H_2-production potential from decay of ^{239}Pu calculated above. In this vector, the ^{241}Am was the largest contributor to radiolytic H_2 production. Furthermore, 50% of the 70 vectors produced less than 2 moles of H_2 per drum, a value less than 0.5% of the H_2-production potential.

Clearly, the difference between the H_2-production potential and the values calculated using PANEL suggest that gas production in WIPP disposal rooms may actually be far less than the gas-production potentials. The main reasons for this appear to be: (1) calculations of gas-production potentials often include worst-case assumptions; (2) these calculations also neglect interactions between or among processes; these interactions may significantly decrease the amount of gas produced.

CONSUMPTION OF GASES

The compounds $Ca(OH)_2$ (in hydrated cementitious materials and CaO (a potential backfill additive) could consume significant quantities of CO_2 and H_2S by the reactions:

$$Ca(OH)_2 + CO_2 = CaCO_3 + H_2O; \quad (30a)$$

$$Ca(OH)_2 + H_2S = CaS + 2H_2O; \quad (30b)$$

$$CaO + CO_2 = CaCO_3; \quad (31a)$$

$$CaO + H_2S = CaS + H_2O. \quad (31b)$$

In bench-scale laboratory experiments, $Ca(OH)_2$, dissolved in WIPP brines, reacts very rapidly with gaseous CO_2. Dissolved, hydrated CaO, solid $Ca(OH)_2$ and solid CaO would probably also react very rapidly with gaseous CO_2. However, the effects of transport phenomena must be incorporated in predictions of the rates of CO_2 and, perhaps, H_2S uptake by these compounds in WIPP disposal rooms. Furthermore, estimates of the quantities of hydrated cementitious materials and the concentrations of $Ca(OH)_2$ in these materials are necessary for room-

scale predictions. Therefore, I have not estimated rates for these reactions yet.

REFERENCES

Berner, R. A. (1980). Early Diagenesis: A Theoretical Approach. Princeton University Press, Princeton, NJ.

Brush, L. H. (1990). Test Plan for Laboratory and Modeling Studies of Repository and Radionuclide Chemistry for the Waste Isolation Pilot Plant, SAND90-0266, Sandia National Laboratories, Albuquerque, NM.

Brush, L. H. (1991). Current Estimates of Gas Production Rates, Gas Production Potentials, and Expected Chemical Conditions Relevant to Radionuclide Chemistry for the Long-Term WIPP Performance Assessment. In WIPP Performance Assessment Division, Preliminary Comparison with 40 CFR Part 191, Subpart B for the Waste Isolation Pilot Plant, December 1991, SAND91-0893/3, Sandia National Laboratories, Albuquerque, NM, pp. A-27 to A-36.

Brush, L. H., M. A. Molecke, R. E. Westerman, A. J. Francis, J. B. Gillow, R. H. Vreeland, and D. T. Reed (1992). Laboratory Studies of Gas Generation for the Waste Isolation Pilot Plant. Presented at the Materials Research Society's Symposium on the Scientific Basis for Nuclear Waste Management, Boston, Ma., November 30 to December 4, 1992.

Francis, A. J., and J. B. Gillow. Effects of Microbial Processes on Gas Generation under Expected WIPP Conditions: Annual Report through 1992. SAND93-7036, Sandia National Laboratories, Albuquerque, NM, in prep.

Froelich, P. N., G. P. Klinkhammer, M. L. Bender, N. A. Luedtke, G. R. Heath, D. Cullen, P. Dauphin, D. Hammond, B. Hartman, and V. Maynard (1979). Early Oxidation of Organic Matter in Pelagic Sediments of the Eastern Equatorial Atlantic: Suboxic Diagenesis, Geochimica et Cosmochimica Acta, Vol. 43, pp. 1075-1090.

Grauer, R., B. Knecht, P. Kreis, and J. P. Simpson (1991). Hydrogen Evolution from Corrosion of Iron and Steel in Intermediate Level Waste Repositories. In T. A. Abrajano, Jr., and L. H. Johnson, Eds., Scientific Basis for Nuclear Waste Management XIV, Symposium held November 26-29, 1990, Boston, Massachusetts, U.S.A., Materials Research Society Symposia Proceedings, Vol. 44, Materials Research Society, Pittsburgh, PA, pp. 295-302.

Lappin, A. R., R. L. Hunter, D. P. Garber, and P. B. Davies, Eds. (1989). Systems Analysis, Long-Term Radionuclide Transport, and Dose Assessments, Waste Isolation Pilot Plant (WIPP), Southeastern New Mexico; March, 1989. SAND89-0462, Sandia National Laboratories, Albuquerque, NM.

Molecke, M. A. (1979). Gas Generation from Transuranic Waste Degradation: Data Summary and Interpretation. SAND79-1245, Sandia National Laboratories, Albuquerque, NM.

Molecke, M. A. (1983). A Comparison of Brines Relevant to Nuclear Waste Experimentation. SAND83-0516, Sandia National Laboratories, Albuquerque, NM.

Reed, D. T., and S. Okajima. Radiation Effects Studies in Support of the Waste Isolation Pilot Plant: Progress Report for Fiscal Year 1992. SAND??-????, Sandia National Laboratories, Albuquerque, NM, in prep.

Telander, M. R., and R. E. Westerman. Hydrogen Generation by Metal Corrosion in Simulated WIPP Environments: Progress Report for Period November 1989 - December 1992. SAND92-7347, Sandia National Laboratories, Albuquerque, NM, in prep.

Trauth, K. M., S. C. Hora, R. P. Rechard, and D. R. Anderson (1992). The Use of Expert Judgement to Quantify Uncertainty in Solubility and Sorption Parameters for Waste Isolation Plant Performance Assessment, SAND92-0479, Sandia National Laboratories, Albuquerque, NM.

Uhlig, H. H., and R. W. Revie (1963). Corrosion and Corrosion Control: An Introduction to Corrosion Science and Engineering. John Wiley and Sons, New York, NY.

WIPP Performance Assessment Department (1992). Preliminary Performance Assessment for the Waste Isolation Pilot Plant, December 1992. Volume 4: Uncertainty and Sensitivity Analysis for 40 CFR 191, Subpart B. SAND92-0700/4, Sandia National Laboratories, Albuquerque, NM..

TABLE 1. GAS-GENERATION REACTIONS

Reaction	Abbreviation
Oxic corrosion of steels and other Fe-base materials:	
1. $2Fe + H_2O + 1.5O_2 = 2\gamma FeO(OH)$	Fe to $\gamma FeO(OH)$[1]
Anoxic corrosion of steels and other Fe-base materials:	
6a. $Fe + 2H_2O = Fe(OH)_2 + H_2$	Fe to $Fe(OH)_2$[2]
6b. $3Fe + 4H_2O = Fe_3O_4 + 4H_2$	Fe to Fe_3O_4[2]
7. $Fe + H_2O + CO_2 = FeCO_3 + H_2$	Fe to $FeCO_3$[2]
8a. $Fe + 2H_2S = FeS_2 + 2H_2$	Fe to FeS_2[2]
8b. $Fe + H_2S = FeS + H_2$	Fe to FeS[2]
Microbial degradation of cellulosics and, perhaps, plastics and rubbers:	
12. $CH_2O + O_2 = H_2O + CO_2$	Aerobic respiration[1]
13. $CH_2O + 0.8H^+ + 0.8NO_3^- = 1.4H_2O + CO_2 + 0.4N_2$	Denitrification[2]

TABLE 1. GAS-GENERATION REACTIONS (cont.)

Reaction	Abbreviation
Microbial degradation of cellulosics and, perhaps, plastics and rubbers (cont.):	
14a. $CH_2O + 4FeO(OH) + H_2O = 4Fe(OH)_2 + CO_2$	Fe(III) reduction[1]
14b. $CH_2O + 4FeO(OH) = 1.33Fe_3O_4 + 1.67H_2O + CO_2 + 1.33H_2$	Fe(III) reduction[1]
14c. $CH_2O + 4FeO(OH) + H_2O + 3CO_2 = 4FeCO_3 + 4H_2O$	Fe(III) reduction[1]
14d. $CH_2O + 4FeO(OH) + 4H_2S = 4FeS + 7H_2O + CO_2$	Fe(III) reduction[1]
14e. $CH_2O + 4FeO(OH) + 8H_2S = 4FeS_2 + 7H_2O + CO_2 + 4H_2$	Fe(III) reduction[1]
15. $CH_2O + H^+ + 0.5SO_4^{2-} = H_2O + CO_2 + 0.5\ H_2S$	SO_4^{2-} reduction[2]
16a. $2CH_2O = CH_4 + CO_2$	Methanogenesis[2]
16b. $CO_2 + 4H_2 = CH_4 + 2H_2O$	Methanogenesis[2]

TABLE 1. GAS-GENERATION REACTIONS (cont.)

Reaction	Abbreviation
Radiolysis:	
17. $H_2O = H_2 + 0.5O_2$	Radiolysis of brine[1]
Consumption of gases by cementitious materials and backfill additives:	
25a. $Ca(OH)_2 + CO_2 = CaCO_3 + H_2O$	$Ca(OH)_2$ to $CaCO_3$[2]
25b. $Ca(OH)_2 + H_2S = CaS + 2H_2O$	$Ca(OH)_2$ to CaS[2]
26a. $CaO + CO_2 = CaCO_3$	CaO to $CaCO_3$[2]
26b. $CaO + H_2S = CaS + H_2O$	CaO to CaS[12]

1. Probably will not have a significant, direct effect on the gas and H_2O budget of WIPP disposal rooms, but could be important from the standpoint of the O_2 budget of the repository (see text).

2. Could have a significant, direct effect on the gas and H_2O budget of the repository (see text).

TABLE 2. INUNDATED GAS-PRODUCTION RATES

Process	Gas-Production Rate		
	Minimum	Best	Maximum
Oxic corrosion of steels and other Fe-base materials:			
moles O_2/(m^2 steel · yr)	0	- 5	- 8
moles O_2/(drum · yr)	0[1]	- 30[1]	- 50[1]
μm steel/yr	0	50	80
Anoxic corrosion of steels and other Fe-base materials:			
moles H_2/(m^2 steel · yr)	0	0.1	20
moles H_2/(drum · yr)	0[1]	0.6[1]	100[1]
μm steel/yr	0	1	200
Microbial degradation of cellulosics (Reactions 12 through 16b):			
moles gas/(kg cellulose · yr)	0[2]	0.1[2]	0.5[2]
moles gas/(drum · yr)	0[1, 2]	1[1, 2]	5[1, 2]
Microbial degradation of cellulosics (Reaction 16b):			
moles gas/(kg cellulose · yr)	Not est.[3]	Not est.[3]	Not est.[3]
moles gas/(drum · yr)	Not est.[3]	Not est.[3]	Not est.[3]

TABLE 2. INUNDATED GAS-PRODUCTION RATES (cont.)

Reaction	Gas-Production Rate[1]		
	Minimum	Best	Maximum
Radiolysis of brine:			
moles $H_2/(m^3 \cdot yr)$	$4.5 \cdot 10^{-14}$	$1.1 \cdot 10^{-6}$	$9.9 \cdot 10^{-1}$
moles $H_2/(drum \cdot yr)$	$8.9 \cdot 10^{-16}$	$6.6 \cdot 10^{-8}$	$1.2 \cdot 10^{-1}$
moles $O_2/(m^3 \cdot yr)$	$2.2 \cdot 10^{-14}$	$5.4 \cdot 10^{-7}$	$5.0 \cdot 10^{-1}$
moles $O_2/(drum \cdot yr)$	$4.5 \cdot 10^{-16}$	$3.3 \cdot 10^{-8}$	$6.0 \cdot 10^{-2}$
moles $(H_2 + O_2)/(m^3 \cdot yr)$	$6.7 \cdot 10^{-14}$	$1.6 \cdot 10^{-6}$	$1.5 \cdot 10^{0}$
moles $(H_2 + O_2)/(drum \cdot yr)$	$1.3 \cdot 10^{-15}$	$9.9 \cdot 10^{-8}$	$1.8 \cdot 10^{-1}$
Consumption of CO_2 by cementitious materials and backfill additives:			
moles gas/(drum · yr)	Not est.[4]	Not est.[4]	Not est.[4]

1. Estimates do not include steels or other Fe-base alloys associated with RH TRU waste or steels or other Fe-base alloys used for ground support.

2. Gases produced by Reactions 12 through 16a could include CO_2, CH_4, H_2S, N_2, and NH_3 (see text).

3. Not estimated yet, but gases consumed by Reaction 16b could include significant quantities of CO_2 and especially H_2 (see text).

4. Not estimated yet, but gases consumed by $Ca(OH)_2$ and CaO in cementitious materials and backfill additives could include significant quantities of CO_2 and, perhaps, H_2S (see text).

TABLE 3. HUMID GAS-PRODUCTION RATES

Process	Gas-Production Rate		
	Minimum	Best	Maximum
Oxic corrosion of steels and other Fe-base materials:			
moles O_2/(m^2 steel · yr)	0	- 0.5	- 5
moles O_2/(drum · yr)	0[1]	- 3[1]	- 30[1]
μm steel/yr	0	5	50
Anoxic corrosion of steels and other Fe-base materials:			
moles H_2/(m^2 steel · yr)	0	0	0.01
moles H_2/(drum · yr)	0[1]	0[1]	0.06[1]
μm steel/yr	0	0	0.1
Microbial degradation of cellulosics (Reactions 12 through 16b):			
moles gas/(kg cellulose · yr)	0[2]	0.01[2]	0.1[2]
moles gas/(drum · yr)	0[1, 2]	0.1[1, 2]	1[1, 2]
Microbial degradation of cellulosics (Reaction 16b):			
moles gas/(kg cellulose · yr)	Not set.[3]	Not est.[3]	Not est.[3]
moles gas/(drum · yr)	Not est.[3]	Not est.[3]	Not est.[3]

TABLE 3. HUMID GAS-PRODUCTION RATES (cont.)

Process	Gas-Production Rate		
	Minimum	Best	Maximum
Radiolysis of brine:			
moles $H_2/(m^3 \cdot yr)$	0	0	0
moles H_2/(drum · yr)	0	0	0
moles $O_2/(m^3 \cdot yr)$	0	0	0
moles O_2/(drum · yr)	0	0	0
moles $(H_2 + O_2)/(m^3 \cdot yr)$	0	0	0
moles $(H_2 + O_2)$/(drum · yr)	0	0	0
Consumption of gases by cementitious materials and backfill additives:			
moles gas/(drum · yr)	Not est.[4]	Not est.[4]	Not est.[4]

1. Estimates do not include steels or other Fe-base alloys associated with RH TRU waste or steels or other Fe-base alloys used for ground support.

2. Gases produced by Reactions 12 through 16a could include CO_2, CH_4, H_2S, N_2, and NH_3 (see text).

3. Not estimated yet, but gases consumed by Reaction 16b could include significant quantities of CO_2 and especially H_2 (see text).

4. Not estimated yet, but gases consumed by $Ca(OH)_2$ and CaO in cementitious materials and backfill additives could include significant quantities of CO_2 and, perhaps, H_2S (see text).

TABLE 4. RADIOLYTIC GAS-PRODUCTION RATES (mol/m^3 of brine·yr)[1, 2]

Dissolved ^{239}Pu Conc. (M)	Gas-Production Rate		
	H_2	O_2	$H_2 + O_2$
$1 \cdot 10^{0}$	$1.8 \cdot 10^{3}$	$0.9 \cdot 10^{3}$	$2.7 \cdot 10^{3}$
$1 \cdot 10^{-1}$	$1.8 \cdot 10^{2}$	$0.9 \cdot 10^{2}$	$2.7 \cdot 10^{2}$
$1 \cdot 10^{-2}$	$1.8 \cdot 10^{1}$	$0.9 \cdot 10^{1}$	$2.7 \cdot 10^{1}$
$1 \cdot 10^{-3}$	$1.8 \cdot 10^{0}$	$0.9 \cdot 10^{0}$	$2.7 \cdot 10^{0}$
$1 \cdot 10^{-4}$	$1.8 \cdot 10^{-1}$	$0.9 \cdot 10^{-1}$	$2.7 \cdot 10^{-1}$
$1 \cdot 10^{-5}$	$1.8 \cdot 10^{-2}$	$0.9 \cdot 10^{-2}$	$2.7 \cdot 10^{-2}$
$1 \cdot 10^{-6}$	$1.8 \cdot 10^{-3}$	$0.9 \cdot 10^{-3}$	$2.7 \cdot 10^{-3}$
$1 \cdot 10^{-7}$	$1.8 \cdot 10^{-4}$	$0.9 \cdot 10^{-4}$	$2.7 \cdot 10^{-4}$
$1 \cdot 10^{-8}$	$1.8 \cdot 10^{-5}$	$0.9 \cdot 10^{-5}$	$2.7 \cdot 10^{-5}$
$1 \cdot 10^{-9}$	$1.8 \cdot 10^{-6}$	$0.9 \cdot 10^{-6}$	$2.7 \cdot 10^{-6}$

1. Rates in moles per m^3 of brine per year calculated from experimentally measured values of $G(H_2)$ (see text).

2. Values in bold type may exceed the maximum <u>average</u> Pu concentration or <u>average</u> gas-production rate depending on the quantity of brine present and time (see text).

TABLE 5. RADIOLYTIC H_2-PRODUCTION RATES (mol/drum·yr)[1, 2]

Dissolved ^{239}Pu Conc. (M)	Brine Volume (m^3/room)			
	135	305	525	815
$1 \cdot 10^{0}$	$\mathbf{3.6 \cdot 10^{1}}$	$\mathbf{8.1 \cdot 10^{1}}$	$\mathbf{1.4 \cdot 10^{2}}$	$\mathbf{2.2 \cdot 10^{2}}$
$1 \cdot 10^{-1}$	$\mathbf{3.6 \cdot 10^{0}}$	$\mathbf{8.1 \cdot 10^{0}}$	$\mathbf{1.4 \cdot 10^{1}}$	$\mathbf{2.2 \cdot 10^{1}}$
$1 \cdot 10^{-2}$	$\mathbf{3.6 \cdot 10^{-1}}$	$\mathbf{8.1 \cdot 10^{-1}}$	$\mathbf{1.4 \cdot 10^{0}}$	$\mathbf{2.2 \cdot 10^{0}}$
$1 \cdot 10^{-3}$	$3.6 \cdot 10^{-2}$	$\mathbf{8.1 \cdot 10^{-2}}$	$\mathbf{1.4 \cdot 10^{-1}}$	$\mathbf{2.2 \cdot 10^{-1}}$
$1 \cdot 10^{-4}$	$3.6 \cdot 10^{-3}$	$8.1 \cdot 10^{1-3}$	$\mathbf{1.4 \cdot 10^{-2}}$	$2.2 \cdot 10^{-2}$
$1 \cdot 10^{-5}$	$3.6 \cdot 10^{-4}$	$8.1 \cdot 10^{-4}$	$1.4 \cdot 10^{-3}$	$2.2 \cdot 10^{-3}$
$1 \cdot 10^{-6}$	$3.6 \cdot 10^{-5}$	$8.1 \cdot 10^{-5}$	$1.4 \cdot 10^{-4}$	$2.2 \cdot 10^{-4}$
$1 \cdot 10^{-7}$	$3.6 \cdot 10^{-6}$	$8.1 \cdot 10^{-6}$	$1.4 \cdot 10^{-5}$	$2.2 \cdot 10^{-5}$
$1 \cdot 10^{-8}$	$3.6 \cdot 10^{-7}$	$8.1 \cdot 10^{-7}$	$1.4 \cdot 10^{-6}$	$2.2 \cdot 10^{-6}$
$1 \cdot 10^{-9}$	$3.6 \cdot 10^{-8}$	$8.1 \cdot 10^{-8}$	$1.4 \cdot 10^{-7}$	$2.2 \cdot 10^{-7}$

1. Rates in moles per drum per year calculated from values in moles per m^3 of brine per year (see text).

2. Values in bold type may exceed the maximum <u>average</u> H_2-production rate depending on the quantity of brine present and time (see text).

TABLE 6. RADIOLYTIC O_2-PRODUCTION RATES (mol/drum·yr)[1, 2]

Dissolved ^{239}Pu Conc. (M)	Brine Volume (m^3/room)			
	135	305	525	815
$1 \cdot 10^{0}$	**$1.8 \cdot 10^{1}$**	**$4.0 \cdot 10^{1}$**	**$6.9 \cdot 10^{1}$**	**$1.1 \cdot 10^{2}$**
$1 \cdot 10^{-1}$	**$1.8 \cdot 10^{0}$**	**$4.0 \cdot 10^{0}$**	**$6.9 \cdot 10^{0}$**	**$1.1 \cdot 10^{1}$**
$1 \cdot 10^{-2}$	**$1.8 \cdot 10^{-1}$**	**$4.0 \cdot 10^{-1}$**	**$6.9 \cdot 10^{-1}$**	**$1.1 \cdot 10^{0}$**
$1 \cdot 10^{-3}$	**$1.8 \cdot 10^{-2}$**	**$4.0 \cdot 10^{-2}$**	**$6.9 \cdot 10^{-2}$**	**$1.1 \cdot 10^{-1}$**
$1 \cdot 10^{-4}$	$1.8 \cdot 10^{-3}$	$4.0 \cdot 10^{-3}$	$6.9 \cdot 10^{-3}$	$1.1 \cdot 10^{-2}$
$1 \cdot 10^{-5}$	$1.8 \cdot 10^{-4}$	$4.0 \cdot 10^{-4}$	$6.9 \cdot 10^{-4}$	$1.1 \cdot 10^{-3}$
$1 \cdot 10^{-6}$	$1.8 \cdot 10^{-5}$	$4.0 \cdot 10^{-5}$	$6.9 \cdot 10^{-5}$	$1.1 \cdot 10^{-4}$
$1 \cdot 10^{-7}$	$1.8 \cdot 10^{-6}$	$4.0 \cdot 10^{-6}$	$6.9 \cdot 10^{-6}$	$1.1 \cdot 10^{-5}$
$1 \cdot 10^{-8}$	$1.8 \cdot 10^{-7}$	$4.0 \cdot 10^{-7}$	$6.9 \cdot 10^{-7}$	$1.1 \cdot 10^{-6}$
$1 \cdot 10^{-9}$	$1.8 \cdot 10^{-8}$	$4.0 \cdot 10^{-8}$	$6.9 \cdot 10^{-8}$	$1.1 \cdot 10^{-7}$

1. Rates in moles per drum per year calculated from experimentally measured values of $G(H_2)$ (see text).

2. Values in bold type may exceed the maximum <u>average</u> O_2-production rate depending on the quantity of brine present and time (see text).

TABLE 7. RADIOLYTIC GAS- (H_2 + O_2)-PRODUCTION RATES (mol/drum·yr)[1, 2]

Dissolved ^{239}Pu Conc. (M)	Brine Volume (m^3/room)			
	135	305	525	815
$1 \cdot 10^{0}$	$5.4 \cdot 10^{1}$	$1.2 \cdot 10^{2}$	$2.1 \cdot 10^{2}$	$3.2 \cdot 10^{2}$
$1 \cdot 10^{-1}$	$5.4 \cdot 10^{0}$	$1.2 \cdot 10^{1}$	$2.1 \cdot 10^{1}$	$3.2 \cdot 10^{1}$
$1 \cdot 10^{-2}$	$5.4 \cdot 10^{-1}$	$1.2 \cdot 10^{0}$	$2.1 \cdot 10^{0}$	$3.2 \cdot 10^{0}$
$1 \cdot 10^{-3}$	$5.4 \cdot 10^{-2}$	$1.2 \cdot 10^{-1}$	$2.1 \cdot 10^{-1}$	$3.2 \cdot 10^{-1}$
$1 \cdot 10^{-4}$	$5.4 \cdot 10^{-3}$	$1.2 \cdot 10^{-2}$	$2.1 \cdot 10^{-2}$	$3.2 \cdot 10^{-2}$
$1 \cdot 10^{-5}$	$5.4 \cdot 10^{-4}$	$1.2 \cdot 10^{-3}$	$2.1 \cdot 10^{-3}$	$3.2 \cdot 10^{-3}$
$1 \cdot 10^{-6}$	$5.4 \cdot 10^{-5}$	$1.2 \cdot 10^{-4}$	$2.1 \cdot 10^{-4}$	$3.2 \cdot 10^{-4}$
$1 \cdot 10^{-7}$	$5.4 \cdot 10^{-6}$	$1.2 \cdot 10^{-5}$	$2.1 \cdot 10^{-5}$	$3.2 \cdot 10^{-5}$
$1 \cdot 10^{-8}$	$5.4 \cdot 10^{-7}$	$1.2 \cdot 10^{-6}$	$2.1 \cdot 10^{-6}$	$3.2 \cdot 10^{-6}$
$1 \cdot 10^{-9}$	$5.4 \cdot 10^{-8}$	$1.2 \cdot 10^{-7}$	$2.1 \cdot 10^{-7}$	$3.2 \cdot 10^{-7}$

1. Rates in moles per drum per year calculated from experimentally measured values of $G(H_2)$ (see text).

2. Values in bold type may exceed the maximum **average** gas-production rate depending on the quantity of brine present and time (see text).

TABLE 8. MAXIMUM AVERAGE Pu CONCENTRATIONS IN BRINES IN WIPP DISPOSAL ROOMS (M)[1]

	Brine Volume (m^3/room)			
Time (yr)	135	305	525	815
0	$1.60 \cdot 10^{-3}$	$7.09 \cdot 10^{-4}$	$4.12 \cdot 10^{-4}$	$2.65 \cdot 10^{-4}$
100	$1.56 \cdot 10^{-3}$	$6.91 \cdot 10^{-4}$	$4.02 \cdot 10^{-4}$	$2.59 \cdot 10^{-4}$
200	$1.54 \cdot 10^{-3}$	$6.84 \cdot 10^{-4}$	$3.97 \cdot 10^{-4}$	$2.56 \cdot 10^{-4}$
500	$1.52 \cdot 10^{-3}$	$6.73 \cdot 10^{-4}$	$3.91 \cdot 10^{-4}$	$2.52 \cdot 10^{-4}$
1,000	$1.49 \cdot 10^{-3}$	$6.61 \cdot 10^{-4}$	$3.84 \cdot 10^{-4}$	$2.47 \cdot 10^{-4}$
2,000	$1.44 \cdot 10^{-3}$	$6.39 \cdot 10^{-4}$	$3.71 \cdot 10^{-4}$	$2.39 \cdot 10^{-4}$
5,000	$1.31 \cdot 10^{-3}$	$5.78 \cdot 10^{-4}$	$3.36 \cdot 10^{-4}$	$2.16 \cdot 10^{-4}$
10,000	$1.11 \cdot 10^{-3}$	$4.92 \cdot 10^{-4}$	$2.86 \cdot 10^{-4}$	$1.84 \cdot 10^{-4}$

1. Calculations include all isotopes of Pu expected in the repository, not just ^{239}Pu (see text).

Distribution:

J. N. Butler, Harvard University
A. J. Francis, Brookhaven National Laboratory
J. B. Gillow, Brookhaven National Laboratory
D. T. Reed, Argonne National Laboratory
R. H. Vreeland, West Chester University
R. E. Westerman, Pacific Northwest Laboratory
6115 P. B. Davies
6119 F. Gelbard, Acting
6121 J. R. Tillerson
6303 W. D. Weart
6305 S. A. Goldstein
6305 A. R. Lappin
6306 A. L. Stevens
6342 D. R. Anderson
6342 Staff
6343 V. Harper-Slaboszewicz
6345 R. C. Lincoln
6345 Staff
6347 D. R. Schafer
6347 Staff
6348 J. T. Holmes
6348 Staff
6352 SWCF (6): XXXRC, XXXRC/AC, XXXRC/MA, XXXRC/R, XXXRNC, XXXRNC/SOL

Potential-Flow Analysis of Transient Salt Creep Into a Circular Cavity

Prepared by

Mark Reeves
INTERA Inc.
6850 Austin Center Blvd., Suite #300
Austin, Texas 78731
(512) 346-2000

Prepared for

Fluid Flow and Transport Division 6344
Sandia National Laboratories
P.O. Box 5800
Albuquerque, New Mexico 87185

June 18, 1991

105400R129
097B-00G-054D

CONTENTS

FIGURES

TABLES

1.0 REPOSITORY GAS-PRESSURIZATION ISSUE

The centuries immediately following closure will mark a highly transitory period for the WIPP repository. The relatively large initial gradient between the lithostatic stress of the intact salt (approximately 15 MPa) and the near-atmospheric pressure of the repository causes both room closure due to salt creep and brine inflow. Waste emplacement and subsequent backfilling will leave an initial repository porosity. Over time, creep will reduce this porosity, and a portion of the inflowing brine may lodge within the remaining void volume. Some, perhaps most, of the inflowing brine will be consumed by gas generation processes.

Anoxic corrosion of metal drums and microbial degradation of organic waste produce gas in sufficient quantities to cause a significant buildup of gas pressure. The quantity produced depends not only on the amount of brine inflow but also on the amount of initial water in place. When this gas pressure is sufficiently high to overcome the threshold capillary pressure, some gas will escape into nearby interbeds through the fractures in the disturbed rock surrounding the disposal rooms. The relatively low permeabilities (approximately 10^{-19} m^2) limit the resulting pressure relief, and a substantial gas pressure may still develop within the repository. This gas pressure opposes salt creep. It also opposes brine inflow, thereby reducing the gas-generation potential.

The comparative timing of gas production and creep closure is important. Long before repository pressurization to near-lithostatic pressures, the presence of gas will cause a reversal in the direction of creep, and repository rooms will "reinflate" to a limited extent. If a rapidly diminishing rate of brine inflow reduces gas production to an insignificantly small rate prior to the time of creep reversal, then the repository pressure may never exceed lithostatic pressure. The repository pressure will then asymptotically approach lithostatic pressure from below. Gas release to the interbeds may also prevent repository pressure from exceeding lithostatic pressure. Furthermore, even if a significant gas-production potential remains after the time of creep reversal and repository pressure overshoots the lithostatic pressure, the stresses induced thereby may be sufficiently small that they do not cause significant fracturing of the salt.

2.0 POTENTIAL-FLOW APPROXIMATION OF SALT CREEP

To rigorously treat the above-mentioned coupled processes and the geometrical complexity introduced by the presence of interbeds goes beyond the capability of the presently available computer models. Consequently, an approximate approach is sought. Potential flow constitutes one such approximation. This report demonstrates that the kinematics of the radial geometry imply the existence of a velocity potential and argues, based on this conclusion, that potential flow represents an excellent idealization for treating salt creep. Assuming further that the continuity law of Darcy flow is appropriate brings an immediate computational advantage. It places the gas-pressurization problem into the domain of a modeling technology which has been highly developed by the petroleum industry. The model of interest is a three-phase "black oil" model. The Darcy-flow approach identifies brine and gas as two of the phases and hence treats these two fluids rigorously. The essential step is treating salt as a third fluid phase.

2.1 Purpose of the Report

This report assumes that salt rheology is adequately characterized by means of a nonlinear Maxwell constitutive relation (Morgan *et al.*, 1986, p 15). It first develops solutions for a linearized rheology (Section 3) and then extends this work to a nonlinear rheology (Section 4). The ultimate objective of this analytically based study is to develop appropriate submodels for a standard potential-flow simulator. Originally, only an improved viscosity submodel was sought. However, the study reveals the importance of the repository near field, and characterizes its effect on salt flow by means of an inner boundary-condition submodel. Section 5 presents both viscosity and boundary-condition submodels. Section 6 summarizes the study and notes several implications which could lead to further improvements in the method of simulating salt flow.

2.2 Preliminary Results of Darcy-Flow Simulations

To motivate the analytical analyses to follow, we wish to examine some preliminary results. Figures 1 and 2 present results of Brown and Weatherby (1990), which derive from an implementation of the SANCHO code (Stone *et al.*, 1985). For a general

treatment of the salt constitutive relation of Krieg (1984), these calculations couple a limited treatment of the gas by assuming that no gas escapes from the repository to the nearby interbeds. Figures 1 and 2 show both closure and pressurization of a single room for two different gas-generation rates (Case A and Case D). Figures 1 and 2 also present results obtained by INTERA using the black-oil model ECLIPSE.

Two points are noteworthy here. First, except for a slight underprediction of the gas pressure in Case D, the agreement between the results of SANCHO and ECLIPSE is excellent. Nevertheless, more is desired. For the ECLIPSE calculations shown in Figures 1 and 2, the step-viscosity function $\mu(t)$ (Figure 3) is assumed to be spatially constant. The temporal variation of this quantity was obtained by calibration to the results of Brown and Weatherby (1990). With a more rigorously based viscosity model, one would not need parallel runs with ECLIPSE and SANCHO to define the viscosity function. For repository-scale closure calculations involving many rooms, parallel runs become quite cumbersome.

Before proceeding further, it is appropriate to make a point regarding notation. This report distinguishes two different viscosities. One viscosity, designated as η, represents a physical property of salt. For WIPP salt, it has a power-law dependence on shear stress τ. The report identifies η as the Maxwell-flow viscosity. The other viscosity, designated as μ, represents the viscosity submodel used in the Darcy-flow analysis. In general, this quantity depends on both space and time. The report identifies μ as the Darcy-flow viscosity. The report addresses the problem of making these two viscosities equivalent so that they yield the same salt flow into the repository.

As a second noteworthy point, Figure 1 indicates that, at approximately 100 years, a critical gas pressure is attained at which inwardly directed salt flow ends, and, at a very slow rate, outwardly directed salt flow begins. Figure 2 reveals that this critical pressure lies between 5 and 10 MPa, substantially less than lithostatic pressure (15 MPa). As the report will show, this is a natural consequence of near-field elastic effects in combination with a nonlinear viscosity η.

2.3 Introduction to the Darcy-Flow Viscosity

As a simple analog of the repository problem, Davies (1984, Appendix D) considers a radially symmetric system. He assumes a cylindrically shaped room of radius r=a surrounded by an infinite flow field. Since end effects are not considered, the problem is one dimensional. At r=a, he assumes a boundary stress is $\sigma_r = P_o$, and at r=∞, he assumes a lithostatic condition $\sigma_r = P_\infty$.

For a nonlinear salt viscosity, Davies (1984) solves the steady-state Navier-Stokes equations. He obtains the following relation for velocity:

$$v = \frac{1}{2} Aa \left(\frac{2}{3}\right)^{(n-1)/2} \left(\frac{P_\infty - P_o}{n}\right)^n \left(\frac{a}{r}\right) \tag{2-1}$$

Written in terms of viscosity, Equation 2-1 becomes

$$v = \frac{a}{2} \left(\frac{2}{3}\right)^{1/2} A^{-1/(n-1)} \left[\eta\,(a)\right]^{-n/(n-1)} \left(\frac{a}{r}\right) \tag{2-2}$$

where

$$\eta\,(r) = \left(\frac{3}{2}\right)^{(n-2)(n-1)/2n} \left(\frac{1}{A}\right) \left(\frac{n}{P_\infty - P_o}\right)^{n-1} \left(\frac{r}{a}\right)^{2(n-1)/n} \tag{2-3}$$

Here A and n are material constants arising in the constitutive relation for salt, a is the room radius, P_∞ the lithostatic pressure, and P_o is the room pressure.

In contrast to Equation 2-1, a Darcy-flow analysis yields the following relation for the radial velocity:

$$v = \frac{k}{\mu}\left[\frac{P_\infty - P_o}{\ln(r_\infty/a)}\right]\frac{1}{r} \qquad (2\text{-}4)$$

Here k is the permeability and μ the Darcy-flow viscosity.

The radial dependence r^{-1} is the same for both analyses. Thus, to make the two solutions identical, one needs only to define viscosity and permeability appropriately. Instead of Equation 2-3, the Darcy-flow analysis takes

$$\mu(r) = A^{\frac{1}{n-1}}\eta(r)^{\frac{n}{n-1}}(P_\infty - P_o) \qquad (2\text{-}5)$$

with permeability given by

$$k = \left(\frac{2}{3}\right)^{1/2}\ln\left[\frac{r_\infty}{a}\right]\frac{r^2}{2} \qquad (2\text{-}6)$$

This means that, in this case, a Darcy-flow model will exactly reproduce the steady-state flow, as derived from a general implementation of momentum and constitutive relations.

Fitting the Brown and Weatherby (1990) results with a potential-flow model requires that the value of viscosity μ be smaller at early times when closure is the most rapid than at later times (*c.f.*, Figure 3). A comparison of Equations 2-5 and 2-3 gives the dependence of the Darcy-flow viscosity upon room pressure, *i.e.*, $\mu \sim (P_\infty - P_o)^{(n-1)}$. This relationship indicates that, as a minimum, the potential-flow viscosity must characterize the temporal variation in room pressure. As room pressures increase, the viscosity μ also increases in order to achieve fits to the results of Brown and Weatherby (1990) (Figures 1 and 2).

Figure 3 presents the fitted viscosity-room-pressure relation corresponding to Figures 1 and 2. Here, for simplicity, a spatially constant viscosity function is assumed. It indicates that a room-pressure change from zero to 7.5 MPa necessitates an increase in the Darcy-flow viscosity by a factor of about 6.5. Assuming $n=4.9$, which is appropriate for WIPP salt (Mendenhall, 1991), the steady-state theoretical relationship $\mu \sim (p_- - p_o)^{-(n-1)}$ indicates that the viscosity would change by a factor of about 15. The fitted changes in viscosity lag the theoretical relationship by only a factor of about two. This indicates that, during closure, the WIPP salt appears to be reasonably close to a steady state for room pressures less than about 7.5 MPa.

For room pressures greater than 7.5 MPa, the agreement between the steady-state and fitted viscosities becomes progressively worse. The disagreement becomes particularly noteworthy for room pressures greater than about 10 MPa. Contrary to the steady-state relation of Equation 2-4, the fitted values of μ reach a plateau (Figure 3). This effect is correlated with the reversal in the closure curve (Figure 1).

The steady-state viscosity model ignores the effects of elastic shear which occur in the repository near field. To include such effects, Sections 5 and 6 recommend changes in the steady-state viscosity model considered above, and these sections recommend the addition of a boundary-condition model at $r=a$. The recommended viscosity model would arrest the inwardly directed salt flow at approximately 10 MPa with an infinite value of viscosity, and, with a finite viscosity, it would permit only outwardly directed flow thereafter during the period of gas generation in the repository.

3.0 GOVERNING EQUATIONS FOR MAXWELL FLOW

To focus the theoretical work, this study adopts a relatively simple conceptual model. It is implicitly assumed that the results obtained will have strong implications for a generalized flow geometry. Like Davies (1984), this study considers the radially symmetric salt-flow problem. Davies' work is generalized (1) by assuming a transient boundary condition $\sigma_r = P_o(t)$ at the room boundary $r = a$ and (2) by generalizing his nonlinear viscosity model to the nonlinear Maxwell constitutive relation employed by Morgan *et al.* (1986). For a transient analysis, the Maxwell relation is an appropriate generalization of the nonlinear viscosity model.

3.1 Equations of Change

The general equations of change (Bird *et al.*, 1960, Chapter 3) comprise three relations: an equation of continuity, an equation of motion, and a constitutive relation. The continuity equation expresses the conservation of mass:

$$\frac{\dot{\xi}}{K} = -\frac{1}{r}\frac{\partial}{\partial r}(rv) \tag{3-1}$$

where K symbolizes the bulk modulus, a dot above a variable indicates differentiation with respect to time, and $\xi = -(\sigma_r + \sigma_\theta)/2$ is the negative mean of radial (σ_r) and circumferential (σ_θ) stresses. Expressed in terms of the radial velocity v, the right-hand side denotes a sum of the two strain rates $\dot{\epsilon}_r = \partial v/\partial r$ and $\dot{\epsilon}_\theta = v/r$.

The equation of motion expresses the conservation of momentum:

$$\frac{\partial \xi}{\partial r} + \rho \dot{v} = r^{-2}\frac{\partial}{\partial r}(r^2 \tau) \tag{3-2}$$

where ρ is the density and τ is the shear stress.

To characterize the behavior of salt, the constitutive relation provides a relation between shear stress τ and shear strain Γ. Following Morgan *et al.* (1986), we assume the nonlinear Maxwell relation:

$$\frac{\dot{\tau}}{2G} + \frac{\tau}{\eta(\tau)} = \dot{\Gamma} \tag{3-3}$$

where G is the elastic shear modulus.

Viscosity η is defined in terms of shear stress:

$$\eta(\tau) = |\tau|^{1-n}/A \tag{3-4}$$

where A and n represent material constants. Equations 3-3 and 3-4 apply to the octahedral plane (Jaeger and Cook, 1979, pp. 23,24). On this plane, shear stress τ and shear strain Γ relate to the principal polar components according to the transformations $\tau=(\sigma_r-\sigma_\theta)/2$ and $\Gamma=(\epsilon_r-\epsilon_\theta)/2$.

Two relations result from the dependence of the polar strain components on velocity ($\dot{\epsilon}_r=\partial v/\partial r$ and $\dot{\epsilon}_\theta=v/r$). They are:

$$\dot{\Gamma} = \frac{1}{2}\left(\frac{\partial v}{\partial r} - \frac{v}{r}\right) = \frac{1}{2}\left(\frac{1}{r}\frac{\partial}{\partial r}(rv)\right) - \left(\frac{v}{r}\right) \tag{3-5}$$

and

$$r^{-2}\frac{\partial}{\partial r}\left(r^2\dot{\Gamma}\right) = \frac{1}{2}\frac{\partial}{\partial r}\left[\left[\frac{1}{r}\right]\frac{\partial}{\partial r}(rv)\right] \tag{3-6}$$

These relations will be used by the next section.

Davies (1984) presents a steady-state solution of Equations 3-1 to 3-4. It consists of the following three equations:

$$\xi_o = -P_\infty - (P_\infty - P_o)\left(\frac{1}{n} - 1\right)\left(\frac{a}{r}\right)^{\frac{2}{n}} \tag{3-7}$$

$$\tau_o = -(P_\infty - P_o)\left(\frac{1}{n}\right)\left(\frac{a}{r}\right)^{\frac{2}{n}} \tag{3-8}$$

and

$$v_o = \frac{1}{2}Aa^2\left(\frac{2}{3}\right)^{\frac{n-1}{2}}\left(\frac{P_\infty - P_o}{n}\right)^n \frac{1}{r} \tag{3-9}$$

For a system initially at steady state, the dependent variables may be expressed as $\xi = \xi_o + \Delta\xi$, $\tau = \tau_o + \Delta\tau$, and $v = v_o + \Delta v$, and Equations 3-1 and 3-2 become:

$$\frac{\Delta\dot{\xi}}{K} = -\frac{1}{r}\frac{\partial}{\partial r}(r\,\Delta v) \tag{3-10}$$

and

$$\frac{\partial \Delta p}{\partial r} + \rho\,\Delta\dot{v} = r^{-2}\frac{\partial}{\partial r}(r^2\,\Delta\tau) \tag{3-11}$$

For a linear salt rheology (n=1), Equation 3-3 becomes

$$\left(\frac{\Delta \dot{\tau}}{2G}\right) + \frac{\Delta \tau}{\eta} = \dot{\Gamma} \qquad (3\text{-}12)$$

where viscosity η is constant.

3.2 The Maxwell Flow Potential

In order for a velocity potential to exist, the flow must be irrotational (see, for example, Bird *et al.*, 1960, pp. 133 ff.). Physically, this means that the net flow around a closed loop must vanish. Mathematically, a flow is irrotational if and only if the curl of the velocity is zero ($\nabla \times \mathbf{v} = 0$). In order for the curl of a vector to be nonzero, it must have nonzero spatial derivatives in at least two directions. For radially symmetric flow, velocity varies only in the radial direction. Thus, irrotationality results from the geometry of the flow field. This means that

$$v = -\beta \frac{\partial \Phi}{\partial r} \qquad (3\text{-}13)$$

In the work to follow, we set the proportionality constant $\beta = 1$, and we identify Φ as the Maxwell flow potential. It should be noted that the existence of Φ is not conditioned on linearity. The Maxwell potential exists even for nonlinear salt rheologies.

4.0 SOLUTION OF THE MAXWELL-FLOW EQUATIONS FOR A LINEAR RHEOLOGY

4.1 General Solution

For a linear salt rheology, Laplace transformation (Carslaw and Jaeger, 1959, Chapter XII) facilitates solution. Equations 3-10 to 3-12 transform in a straightforward manner, giving

$$\left(\frac{s}{K}\right)\Delta\bar{\xi} = -\frac{1}{r}\frac{\partial}{\partial r}\left(r\Delta\bar{v}\right) \tag{4-1}$$

$$\frac{\partial\Delta\bar{\xi}}{\partial r} + \rho s\Delta\bar{v} = r^{-2}\frac{\partial}{\partial r}\left(r^2\Delta\bar{\tau}\right) \tag{4-2}$$

and

$$\left(\frac{s}{2G}\right)\Delta\bar{\tau} + \frac{\Delta\bar{\tau}}{\eta} = \bar{\Gamma} \tag{4-3}$$

Here s is the Laplace variable, and a transformed variable is indicated notationally by an overbar.

Using the identity given in Equation 3-6, Equations 4-1 to 4-3 combine to give

$$\frac{\partial}{\partial r}\left[\left(\frac{1}{r}\right)\frac{\partial}{\partial r}\left(r\Delta\bar{v}\right)\right] = q^2\Delta\bar{v} \tag{4-4}$$

where

$$q^2 = \frac{st_a}{a^2}\,\frac{1+st_{\eta G}}{1+s(t_{\eta K}+t_{\eta G})} \qquad (4\text{-}5)$$

Quantity q influences the time variation of the solution, and may be inferred by its dependence on three different time constants:

$$t_a = \frac{a}{(K/\rho)^{1/2}} \qquad (4\text{-}6)$$

$$t_{\eta K} = \eta / 2K \qquad (4\text{-}7)$$

and

$$t_{\eta G} = \eta / 2G \qquad (4\text{-}8)$$

Time constant t_a gives the time required for a sound wave to move a distance r=a within the salt. For ρ = 2300 kg/m^3, K = 1.656E9 Pa (Mendenhall, 1991), and a = 1 m, it has the value t_a = 1.2E-3 s. Time constants $t_{\eta k}$ and $t_{\eta G}$ give relaxation times corresponding to a series coupling of spring and dashpot (Jaeger and Cook, 1979, p. 315). McTigue (1989) estimates that salt viscosity may range from 9E15 to 4E20 Pa·s, depending on the value of shear stress. With G = 9.92E8 Pa (Mendenhall, 1991), this gives 31 d $\le t_{\eta K} \le$ 3,800 y and 52 d $\le t_{\eta G} \le$ 6,400 y. Unlike t_a, these time constants fall within the time period of interest in evaluating repository post-closure gas pressurization.

One may recognize the solution of Equation 4-4 most easily by re-expressing it in terms of the Maxwell potential. Combining Equation 3-13 with Equation 4-4 and integrating once with respect to r gives

$$\left[\frac{1}{r}\right]\frac{\partial}{\partial r}\left(r\Delta\bar{\Phi}\right) = q^2\Delta\bar{\Phi} \qquad (4\text{-}9)$$

The form of Equation 4-9 is identical to that of Darcy flow (see, for example, Matthews and Russell, 1967, Equation A-12). The difference lies in the definition of q. Rather than Equation 4-5, one obtains $q^2=s/D$ for Darcy flow, where $D=k/\mu\phi c$, the hydraulic diffusivity, is defined in terms of porosity ϕ, total compressibility c, viscosity μ, and permeability k.

Consideration of the boundary condition $\Delta P_{-}=0$ at $r=\infty$ eliminates the I_o Bessel function, giving the solution

$$\Delta\bar{\Phi} = BK_o(qr) \qquad (4\text{-}10)$$

Differentiation then gives the desired solution for velocity:

$$\Delta\bar{v} = BqK_1(qr) \qquad (4\text{-}11)$$

We are not interested in tracking processes which occur at the speed of sound. Since $t\sim s^{-1}$, this means that $st_a << 1$. Thus, the Bessel function assumes its small-argument approximation $K_1(qr)=(qr)^{-1}$, and Equation 4-11 becomes

$$\Delta\bar{v} = \frac{B}{r} \qquad (4\text{-}12)$$

where the value of constant B depends on the inner boundary condition.

4.2 Application of Inner Boundary Condition

To apply the inner boundary condition

$$\Delta \bar{\sigma}_r \approx \Delta \bar{P}_o \tag{4-13}$$

we note the definition of radial stress: $\Delta\sigma_r = -\Delta\xi + \Delta\tau$. Equation 4-12 indicates that, since $v \sim r^{-1}$, the negative mean stress is zero, thus reducing the defining expression to $\Delta\sigma_r = \Delta\tau$.

Equations 3-5 and 4-3 provide a relation between shear stress and velocity:

$$\Delta \bar{\tau} = -\left(\frac{\eta}{1+St_{\eta G}}\right)\frac{\Delta \bar{v}}{r} \tag{4-14}$$

Since $\Delta\sigma_r = \Delta\tau$, Equations 4-13 and 4-14 give

$$\frac{\Delta \bar{v}}{a} = -\frac{1}{\eta}\left(1+St_{\eta G}\right)\Delta \bar{P}_o \tag{4-15}$$

This represents a Type-3 boundary condition since it relates velocity and radial stress (pressure). Rather than this condition, one might expect, based on a Darcy-flow analogy, that the gas pressure within the room would introduce a Type-1 condition on the Maxwell potential $\Delta\Phi$. Equation 4-15 indicates, however, that a change in room gas pressure alters the circumferential strain rate $\Delta\dot{\epsilon} = \Delta v/a$ at the boundary.

When combined with Equation 4-12, Equation 4-15 gives the desired expressions for constant B and for radial velocity $\Delta\bar{v}$:

$$B = -\frac{a^2 \Delta \bar{P}_o}{\eta}\left(1 + st_{\eta G}\right) \tag{4-16}$$

and

$$\Delta \bar{v} = -\frac{a^2 \Delta \bar{P}_o}{\eta}\left(1 + st_{\eta G}\right)\frac{1}{r} \tag{4-17}$$

This is the Laplace-space solution. With an expression for the time-dependent room pressure $\Delta P_o(t)$, it may be transformed to real time space.

4.3 Interpretation of the Solution

To understand the result given in Equation 4-17, it is useful first to consider the deformation Δr resulting from an instantaneous step increase in the room pressure, *i.e.*, $\Delta \bar{P}_o = \Delta \bar{P}_o / s$. Considering the relation $\Delta \bar{v} = s\Delta \bar{r}$ and the definition of $t_{\eta G}$ given in Equation 4-8, Equation 4-17 becomes

$$\Delta \bar{r} = -a^2 \Delta \bar{P}_o \left[\left(\frac{1}{\eta}\right)\frac{1}{s^2} + \left(\frac{1}{2G}\right)\frac{1}{s}\right]\left(\frac{1}{r}\right) \tag{4-18}$$

An inverse Laplace transformation then gives

$$\Delta r = -a^2 \Delta P_o \left(\frac{t}{\eta} + \frac{1}{2G}\right)\frac{1}{r} \tag{4-19}$$

The latter equation indicates that the net deformation results from two separate effects. Immediately after a pressure increase ΔP_o, elastic shear stresses cause a deformation - $a^2\Delta P_o t_{\eta G}/\eta r = -a^2\Delta P_o/2Gr$. This effect radiates outward at the speed of sound. Like elastic shear, viscous shear stresses cause an outward displacement in response to a pressure increase. And the magnitude of the effect decreases like 1/r with increasing radial distance.

Focusing on the room boundary condition provides further insight. Assume that, rather than a constant step increase, room pressure increases linearly with time: $\Delta P_o = \alpha_1 t$ and $\Delta \bar{P}_o = \alpha_1/s^2$. The significance of this assumption derives from the fact that a piece-wise linear function could be used to approximate a general expression for $\Delta P_o(t)$. With a linear assumption, incremental velocity (Equation 4-17) becomes

$$\Delta \bar{V} = -\frac{a^2\alpha_1}{\eta}\left(\frac{1}{s^2} + \frac{t_{\eta G}}{s}\right)\frac{1}{r} \qquad (4\text{-}20)$$

An inverse Laplace transformation then gives

$$\Delta V = -\frac{a^2}{\eta}\left[\Delta P_o(t) + \Delta P_o(t_{\eta G})\right]\frac{1}{r} \qquad (4\text{-}21)$$

This equation expresses incremental velocity as the sum of viscous and elastic components. The viscous component varies directly with the value of boundary pressure $\Delta P_o(t)$. The elastic component, however, assumes a constant value proportional to $\Delta P_o(t_{\eta G})$, *i.e.*, the value of the boundary pressure at a time equal to the relaxation time for elastic shear.

One may distinguish three distinct periods with the division among them determined by the value of viscosity. There are: (1) a period dominated by the elastic velocity component, (2) an intermediate period, and (3) a period dominated by the viscous velocity component. If the linear viscosity η has a value appropriate for early times in

the room-closure history, then Period 1 is relatively small and the viscous component dominates during most of the times of interest. If, on the other hand, the linear viscosity η assumes a value appropriate for intermediate times in the room-closure history, for example η(10 years), then Periods 1 and 2 are relatively large and the elastic component plays an important role.

5.0 CONSIDERATION OF A NONLINEAR RHEOLOGY

The behavior of the linear flow system provides a key to understanding the behavior of the nonlinear flow system. For room pressures less than about 7.5 MPa, corresponding to times less than about 100 years, the empirical Darcy viscosity dependence on room pressure in Figure 3 follows that of Equation 2-5. This indicates that viscous effects dominate at these pressures and viscosities. We infer that although both viscosity $\eta(r)$ and $t_{\eta G}(r)$ vary with distance from the room, their values near the room should be sufficiently small that elastic effects are negligible and the system can pass effectively to a pseudo-steady state. Here, Equations 3-7 to 3-9 characterize the dependent variables with room pressure $P_o(t)$. Time lags required to establish steady state are sufficiently small that room pressure may be specified as a function of the current time t.

For room pressures greater than about 7.5 MPa, corresponding to times greater than 100 years, approximately, elastic shear effects begin to assume a more dominant role. This is indicated in Figure 3 by a significant departure of the empirical Darcy viscosity from its steady-state pressure dependence (Equation 2-5). Here, the empirical Darcy viscosity was reduced below the steady-state theoretical values in order to produce additional viscous flow to match the elastic flow of Brown and Weatherby (1990).

5.1 Perturbation Analysis

Here, we assume an initial steady state corresponding to the WIPP system at about t_o = 100 years. Since elastic shear is perceived to be the dominant effect at that time, we employ a perturbation approach which, to zero order, neglects all viscous terms. Thus, the incremental velocity of Equation 4-17 becomes:

$$\Delta \bar{v}^{(0)} = -\Delta \bar{P}_o \frac{sa}{2G}\left(\frac{a}{r}\right) \qquad (5\text{-}1)$$

This equation uses both the definition of $t_{\eta G}$ (Equation 4-8) and the transform of a constant pressure jump $\Delta\bar{P}_o = \Delta P_o/s$.

Similarly, the incremental shear stress of Equation 4-14 becomes

$$\Delta \bar{\tau}^{(0)} = -\frac{2G}{s}\frac{\Delta \bar{v}^{(0)}}{r} \tag{5-2}$$

Equations 5-1 and 5-2 combine to yield

$$\Delta \bar{\tau}^{(0)} = \Delta \bar{P}_{\circ}\left(\frac{a}{r}\right)^{2} \tag{5-3}$$

which transforms to

$$\Delta \tau^{(0)} = \Delta P_{\circ}\left(\frac{a}{r}\right)^{2} \tag{5-4}$$

It is expected that the magnitude of the shear stress will decrease as the room pressure approaches lithostatic pressure, and indeed this is the case. According to Equation 3-8, a negative shear stress is initially present throughout the system. Thus, the positive incremental change of Equation 5-4, when combined with Equation 3-8, gives a net reduction in the magnitude of the shear stress:

$$\tau^{(0)} = -\left(P_{\infty} - \gamma P_{\circ}\right)\left(\frac{1}{n}\right)\left(\frac{a}{r}\right)^{\frac{2}{n}} \tag{5-5}$$

Here the superscript of $\tau^{(0)}$ denotes the order of approximation, and function $\gamma(r)$ is defined as follows:

$$\gamma = 1 + n\left(\frac{a}{r}\right)^{2\left(\frac{n-1}{n}\right)}\frac{\Delta P_o}{P_o} \qquad (5\text{-}6)$$

The first term on the right-hand side of Equation 5-6 represents the steady-state stress, while the second represents the elastically induced reduction in that stress. The extent to which γ exceeds unity indicates the relative importance of the elastic shear process.

Proceeding to a first-order solution consists of first updating the viscosity with Equation 3-4 to form $\eta^{(0)}(r)$ and reforming the solution, this time with the updated viscosity terms included as functions of radius. It is clear that viscosity $\eta^{(0)}$ will be increased, perhaps substantially, in the region most influenced by the elastically altered stress field.

5.2 Velocity Reversal

The interpretation of stress field $\tau^{(0)}(r)$ is quite interesting. The elastically induced reduction of the steady-state field is limited to a relatively small region surrounding the room. For WIPP salt, Mendenhall (1991) reports that $n=4.9$, and Table 1 gives corresponding values of the elastic component of $\gamma(r)$. At radial distances less than one, as measured in units of the room radius, the elastic term is much greater than unity, meaning that elastic shear effects dominate. At radial distances greater than ten, elastic effects are negligible.

In addition, it is apparent that, near the room, the net shear stress will reach zero before room pressures reach lithostatic levels. Setting $r=a$, Equations 5-5 and 5.6 simplify, yielding

$$\tau^{(0)}(r=a) = -\left(\frac{1}{n}\right)\left(P_- - P_o\right) + \Delta P_o \qquad (5\text{-}7)$$

Further setting $\tau^{(0)}=0$ gives

$$\Delta P_o(t) = \left(\frac{1}{n}\right)\left[P_- - P_o(t_o)\right] \qquad (5\text{-}8)$$

In these equations, P_- denotes lithostatic pressure, $P_o(t_o)$ represents the room pressure at time t_o, and $P_o(t_o)+\Delta P_o(t)$ is the room pressure at time $t>t_o$. The significance of t_o may be expressed as follows. After this time, viscous effects can no longer "keep up" with pressure changes within the room. Time constant $t_{\eta G}$, characterizing viscous shear effects, is then much longer than the time constant characterizing pressure changes within the room.

If, for example, P_- = 15 MPa and $P_o(t_o)$ = 7.5 MPa, then Equation 5-8 gives ΔP_o = 1.5 MPa, where n=4.9 is a material constant characterizing WIPP salt (Mendenhall, 1991). This indicates that shear stresses reach zero at P_o = 9 MPa. At that point, an infinite viscosity (*c.f.*, Equation 3-4) halts all viscous flows at the boundary. For pressures P_o > 9 MPa, viscosity drops to finite values, and outwardly driven elastic and viscous flows can then occur at the room boundary. Thus, even though far-field stress fields favor inwardly directed flow, the elastic alteration of the near field forces outwardly directed flow.

5.3 Repository Boundary-Condition Model

Near-field elastic shear effects enter most acutely at the repository boundary and affect salt flow. We note from Equation 5-1 that $\Delta v^{(0)} \sim r^{-1}$. This means that $\Delta\xi = 0$ (Equation 3-10), $\Delta\sigma_r(a) = \Delta\tau(a) = \Delta P_o$ (Equation 4-11), and $\Delta\dot{\Gamma}(a) = -\Delta v^{(0)}/a$ (Equation 3-5). Thus, Equation 3-3 becomes

$$\frac{\Delta \dot{P}_o}{2G} + \frac{\Delta P_o}{\eta^{(0)}(t)} + f_\eta^{(0)}(t) = \frac{\Delta V^{(0)}}{a} \qquad (5\text{-}9)$$

where

$$f_{\eta}^{(0)}(t) = \tau_{o}\left[\eta(t)^{-1} - \eta(t_{o})^{-1}\right] \qquad (5\text{-}10)$$

Expressing Equation 3-3 in terms of incremental changes, causes the appearance of the function $f_{\eta}^{(0)}(t)$. Viscosity $\eta^{(0)}(a,t)$ derives from substituting the time-dependent boundary shear stress (Equation 5-7) into the expression for viscosity given in Equation 3-4. Equation 5-9 gives the boundary velocity at any given time t as a time integral of the room pressure for prior times t' where $t_{o} \leq t' \leq t$. It represents the extension of Equation 4-15 from a linear to a nonlinear rheology.

5.4 Darcy-Flow Viscosity Model

In contrast to the far field, the near field lends itself to linear transient analysis. This is indeed fortunate, since the near field appears to be the dominant participant in the processes controlling the maximum repository pressure. In Section 5.3, the velocity-reversal mechanism is incorporated into the boundary-condition model through a zero-order analysis. Here, we incorporate that mechanism into the viscosity model in a similar manner.

The model computes viscosity $\eta^{(0)}$ using the zero-order estimate of near-field shear stress (Equations 5-5 and 5-6). For the near field, the model is rigorous. Empiricism enters in the far field. There, we follow Equation 5-5 by assuming a relic steady-state stress field. The relic stress field, we assume, dates back several multiples of the appropriate time constant, say, $\alpha t_{\eta G}$ where α equals two or three.

Algorithmically, the viscosity model may be stated in the following manner. Assuming that computations have been performed at discrete times 1,2,...,k-1, t_{k} is the current time. Focusing on the relic portion of the stress field, the algorithm first computes viscosity η using the following equation:

$$\eta(a,t_{ok}) = \left(\frac{3}{2}\right)^{(n-2)(n-1)/2n} \left(\frac{1}{A}\right) \left(\frac{n}{P_{\infty} - P_{o}(t_{ok})}\right)^{n-1} \qquad (5\text{-}11)$$

It then determines a time constant $t_{\eta G}=\eta/2G$ and estimates lag time $\alpha t_{\eta G}$ with $\alpha=2$. (Parameter α may require empirical "trial-and-error" estimation.). To estimate the retarded time, the algorithm uses both a prediction $t_{ok}=t_k-\alpha t_{\eta G}$ and a correction $t_{ok}=\max(t_{ok},t_{o,k-1})$. The latter ensures that the sequence of retarded times $t_{o1},t_{o2},\ldots t_{ok}$ increases monotonically.

With the relic value of repository pressure $P_o(t_{ok})$, the relic steady-state stress field $\tau_o(t_{ok})$ may be determined using Equation 3-8. With the current value of repository pressure $P_o(t_k)$, the elastically induced near-field stress component $\Delta\tau^{(o)}(t_k)$ may be determined using Equation 5-4. Adding the two gives

$$\tau^{(o)}(t_k) = \tau_o(t_{ok}) + \Delta\tau^{(o)} \qquad (5\text{-}12)$$

The relation $\eta=|\tau|^{1-n}/A$ then gives viscosity $\eta^{(o)}(t_k,t_{ok})$ and Equation 2-5 gives the equivalent Darcy-flow viscosity μ.

Near the time of velocity reversal, shear-stress values at the room boundary r=a will pass through zero, going from negative to positive values. As discussed in Section 5.2, this process occurs for room boundary pressures which are significantly below the lithostatic pressure. The process is aided by the nonlinearity of the salt, *i.e,* by large values of *n*. This has the effect of halting inwardly directed viscous flows and then permitting small outwardly directed elastic and viscous flows. The viscosity model includes these mechanisms.

6.0 CONCLUSION

This report has served an important function. It has clarified the physics of repository closure in several respects. For example, it is apparent that elastic shear plays an important role. When repository pressure changes, rapidly changing stresses move radially outward at the speed of sound. For a linear rheology and for the extremely large viscosity values for salt, a steady-state mode of behavior also moves radially outward at the speed of sound. For a nonlinear rheology, the dominant effect of elastic shear appears only within the near field of the repository, extending outward only to a distance equal to several repository radii.

A major objective of this work was to develop an enhanced viscosity model for implementation in a Darcy-flow simulator. That has been accomplished. However, the boundary effect was not anticipated. Based on experience with Darcy-flow analyses, one might expect that the repository pressure would impose a type-one pressure condition at the salt interface. This is not the case. Instead, repository pressure relates to both velocity and shear stress, and as a result, it enters as a type-three condition. This condition, which incorporates the elastic shear effect within the near field, causes a reversal in the direction of flow at less-than-lithostatic repository pressures.

To date, all Darcy-flow simulations have employed the type-one condition at the repository boundary. Rather than introduce a flow reversal *via* a boundary condition, these simulations have relied solely upon an empirically based viscosity which is sufficiently small so as to produce a transient potential distribution within the interior of the salt. In some cases, the quality of the fits to SANCHO (Stone *et al.*, 1985) void-volume and pressure profiles have been poor in the region of the velocity reversal. Undoubtedly transient effects do occur, but for times of approximately 100 years, or greater, they may be confined to the near field.

Geometry determines the validity of a potential-flow model. That constitutes another unanticipated conclusion of this study. For one-dimensional creep, a velocity potential exists, even for a nonlinear rheology. For a repository, consisting of many rooms, the flow should be dominantly one-dimensional except for the near field and for end effects. When viewed radially rather than linearly, end effects may be reasonably one-dimensional.

Several findings of this report may be suitable for further research. In addition to the approximate boundary and viscosity submodels proposed above, a fully nonlinear implementation of the potential-flow concept may be advantageous. However, nonlinearity may still be a significant obstacle to efficient simulation, even in a potential-flow approach. A theoretical study would be needed to establish feasibility and to fix algorithms. Perhaps more important, however, is the treatment of the near field. Generally, flow processes slow considerably as repository pressures rise. However, this is not true for the repository near field. Since elastic shear dominantly controls this region, it remains highly transient throughout the closure period. For a repository consisting of many rooms and pillars, the geometry of the near field may be complex, and a potential-flow implementation may not be possible. Nevertheless, the dominantly linear processes of the near field should lend themselves to efficient solution techniques.

To close, we offer the following specific recommendations for the calculations currently in progress. They are given in the recommended order of implementation:

- Current calculations use a fitted viscosibility function. This function, left in its current form insofar as possible, should be altered with the near-field correction discussed above.

- After current deadlines are satisfied and a more substantial development is possible, then the repository boundary condition should be implemented and tested.

- Shortly thereafter, the viscosibility function should be replaced by the relic steady-state viscosity field discussed above. During the testing, one should keep open the option of introducing more empiricism here. The region just outside the near field may need some adjustment for viscous transient effects.

- In preparation for a full repository simulation, one would then want to design a near-field algorithm. It should take full advantage of the dominantly linear elastic-shear process there to achieve maximum efficiency.

- It would be prudent to formulate nonlinear potential-flow algorithms for the transient far-field simulation.

- To clinch the argument regarding the applicability of potential flow to a rectangular geometry and to identify magnitudes of the expected small errors, one may wish to consider a detailed comparison of potential-flow solutions with direct solutions of the Navier-Stokes equations. A relatively straightforward code like NAVIER might be most appropriate for such a comparison.

With regard to next to the last bullet, it is hoped that the Darcy-flow simulator will prove sufficiently reliable that it may be extended from room to repository scale. In terms of its efficiency, this approach should be the one most likely to succeed. However, if the nonlinearity obstacle is overcome, the nonlinear potential-flow approach may be attractive.

7.0 REFERENCES

Bird, R.B., W.E. Stewart, and E.N. Lightfoot, 1960. Transport Phenomena, John Wiley & Sons, New York.

Brown, W.T. and J.R. Weatherby, 1990. Influence of Gas Generation Potential and Gas Generation Rate on the Performance of CH-TRU Disposal Rooms, memo to B.M. Butcher and F.T. Mendenhall, 6345, September 17.

Carslaw, H.S. and J.C. Jaeger, 1959. Conduction of Heat in Solids, Oxford University Press, Great Britain.

Davies, P.B., 1984. "Deep-Seated Dissolution and Subsidence in Bedded Salt Deposits." Ph.D. dissertation. Applied Earth Sciences Dept, Stanford University.

Jaeger, J.C. and N.G.W. Cook, 1979. Fundamentals of Rock Mechanics, Chapman and Hall, New York.

Krieg, R.D., 1984. Reference Stratigraphy and Rock Properties for the Waste Isolation Pilot Plant (WIPP) Project. Sandia National Laboratories, SAND83-1908.

Matthews, C.S., and D.G. Russell, 1967. Pressure Buildup and Flow Tests in Wells, Society of Petroleum Engineers of AIME, New York.

McTigue, D.F., 1989. Observations of Brine Flow Mechanisms in WIPP Repository Salt Based on Data from a Room D Borehole, internal Sandia memo, March 15, 1989.

Mendenhall, F.T., 1991. Preliminary Calculations on Pre-existing Crack Opening Caused by WIPP Disposal Room Gas Pressurization and Interbed Gas Migration, internal Sandia memo, February 22, 1991.

Morgan, H.S., C.M. Stone, and R.D. Krieg, 1986. An Evaluation of WIPP Structural Modeling Capabilities Based on Comparisons With South Drift Data, Sandia National Laboratories, SAND85-0323.

Stone, C.M., R.D. Krieg, and Z.E. Beisinger, 1985. SANCHO, A Finite Element Computer Program for the Quasistatic, Large Deformation, Inelastic Response of Two-Dimensional Solids. Sandia National Laboratories, SAND84-2618.

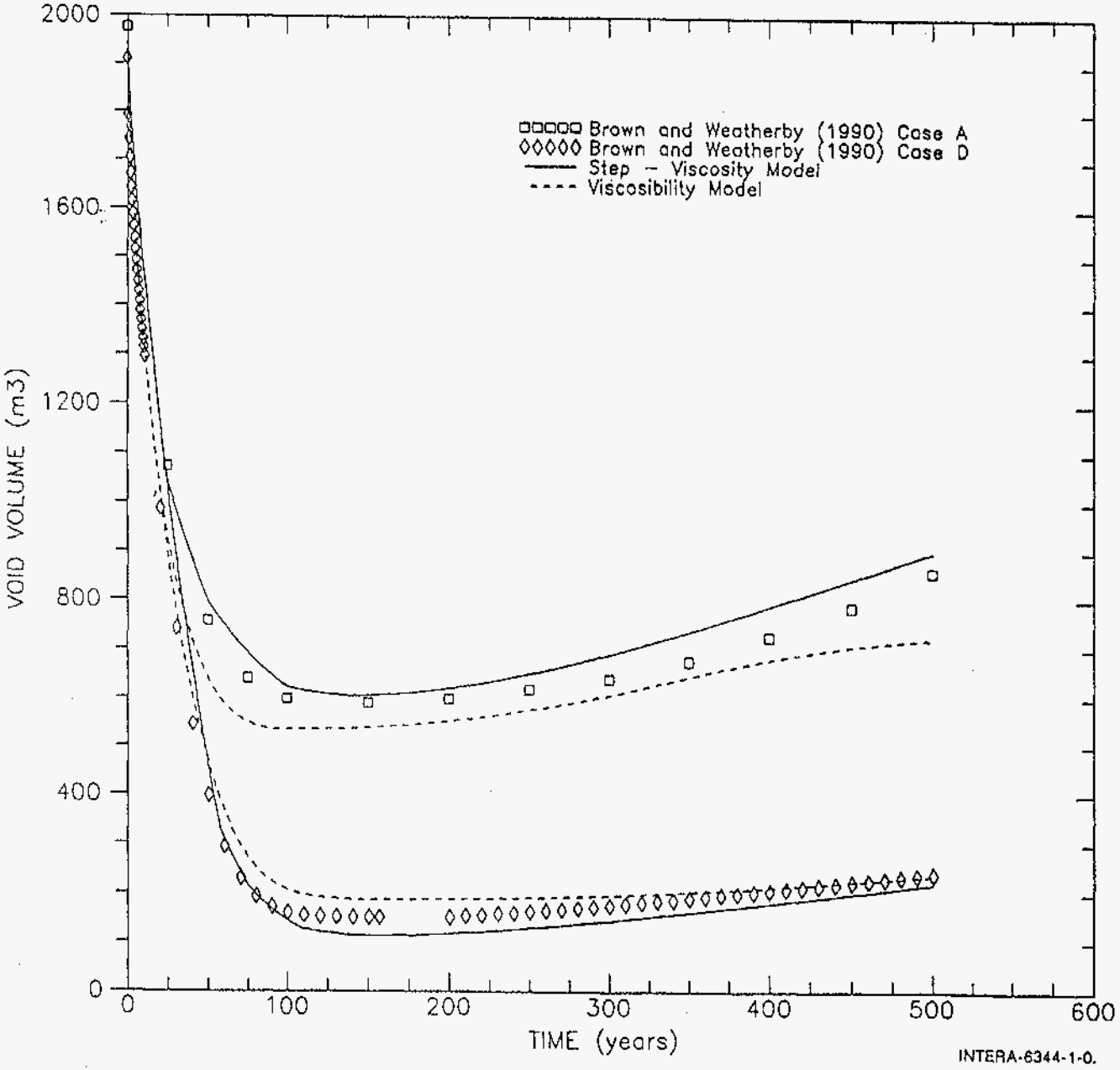

Figure 1. Room Void Volume as a Function of Time (Cases A & D)

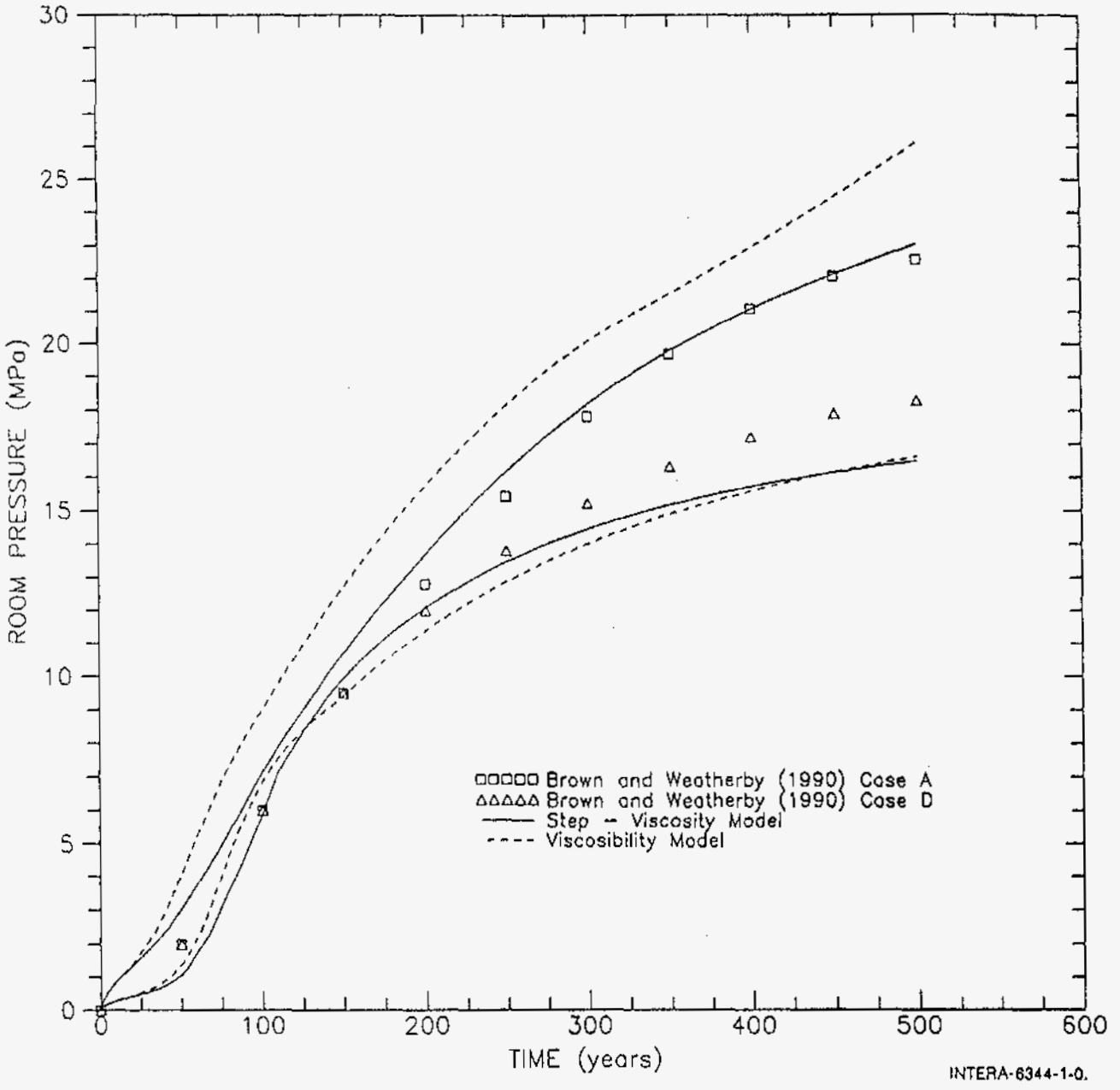

Figure 2. Room Pressure as a Function of Time (Cases A & D)

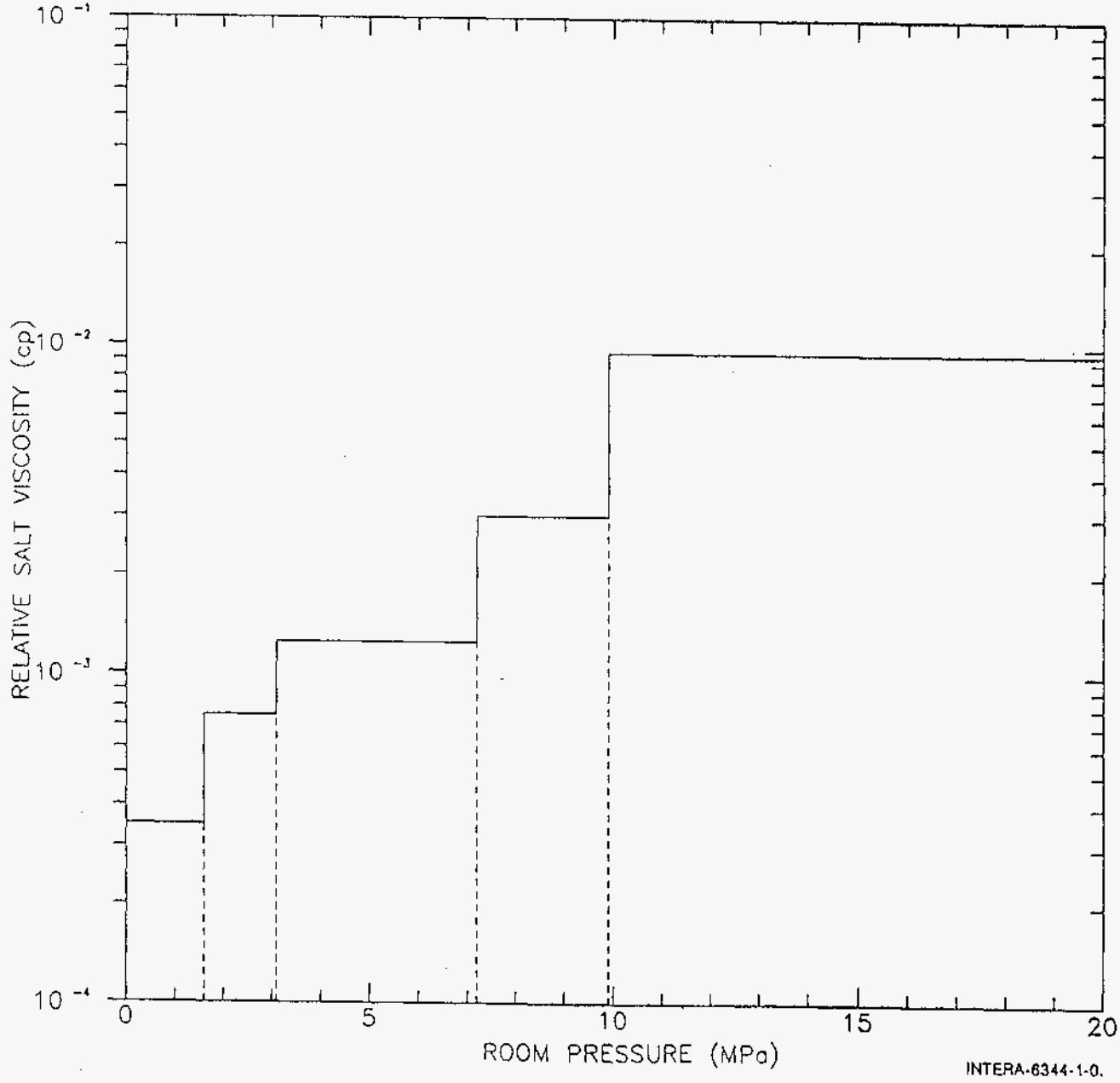

Figure 3. Salt Viscosity Expressed as a Function of Room Pressure (Cases A & D)

Table 1. Elastic Shear Component of $\gamma(r)$*

(r/a)	$n(a/r)^{2(n-1/n)}$
1	4.90
2	1.63
3	0.853
5	0.378
10	0.125

* $\gamma = 4.9$

Sandia National Laboratories

Albuquerque, New Mexico 87185

date: October 6, 1992

to: B. M. Butcher, 6345

Charles M. Stone

from: Charles M. Stone, 1561

subject: Creep Closure Behavior of Waste Disposal Rooms in Bedded Salt Due to Gas Generation Produced by Several Alternatives of the Engineered Alternatives Task Force

Executive Summary

Creep closure analyses of WIPP disposal rooms have been performed for the Baseline and for several alternatives specified by the Engineered Alternatives Task Force (EATF). The analyses, which were carried out to a simulation time of 2000 years, provided information regarding the response of the disposal room and, in particular, information regarding the porosity of the waste and of the backfill as a function of time. Curves of room void volume as a function of time and curves of gas generation rate were provided to produce a three-dimensional porosity surface which can be used in the WIPP Performance Assessment model.

Introduction

The United States Department of Energy (DOE) established the Engineered Alternatives Task Force (EATF) to identify potential engineering modifications to the current design of WIPP and/or to the present waste forms in order to enhance repository performance. The studies completed by the EATF have identified a number of different performance parameters [1], but the relative importance of each specific parameter in demonstrating respository compliance with EPA Standard 40 CFR Part 191 has not been determined. The determination of repository compliance with the EPA standard is the responsibility of the WIPP Performance Assessment organization. This group is responsible for the development of the performance assessment model which is to be used to demonstrate whether the repository is in compliance with the EPA standard. A part of this overall repository model is the Disposal Room model which provides information regarding the response of the disposal room and, in particular, information about the porosity of the waste and the backfill at any time. Porosity is important to study because it gives estimates of how much brine could be available within the disposal room for transporting radionuclides from the repository and their rate of transport.

This memorandum documents the disposal room mechanical creep closure analyses performed in support of the engineered alternatives effort for the EATF Baseline case,

Alternative 2, and Alternative 6. The information required from these analyses are curves of room void volume as a function of time for various values of the gas generation rate. The generated curves can then be combined to produce a porosity surface for use in the repository Performance Assessment model. The next section of this memo describes the three EATF alternatives analyzed. The third section describes the numerical model used for the analyses, and the fourth section discusses the results of the analyses. The last section summarizes the results from the study.

Description of the Engineered Alternatives

EATF Baseline Case

The engineered alternatives considered for the mechanical creep closure analyses of the waste disposal rooms are defined in [2] and [3]. Each of the disposal rooms is 3.96 m high by 10.06 m wide by 91.44 m in length resulting in an initial room volume of 3644 m^3. The Baseline configuration calls for 6804 drums of uniformly distributed unprocessed waste in a disposal room. The corresponding volume occupied by the waste and the drums is 1663 m^3. With the required 0.71 m headspace between the waste and the roof, the total volume of crushed salt backfill necessary to seal the disposal room is found to be approximately 1328 m^3. The Baseline transuranic waste form is a combination of solid organics, solid inorganics and sludges. Solid organics account for 40 percent of the drums, solid inorganics account for 40 percent, and sludges account for the remaining 20 percent. Table 1 summarizes the data available to characterize the baseline waste. The gas generation

Table 1: Waste Form Characterization for the EATF Baseline Case [2]

Waste Form	Drum Count	Drum Weight (Kg)	Density (Kg/m^3)	Porosity
Solid Organics	2722	77	380	0.8
Solid Inorganics	2722	102	900	0.8
Sludges	1360	211	1200	0.5

potential and gas production rate corresponding to the Baseline case are composed of gas from two sources: anoxic corrosion and microbial activity. Reference [2] reports that the estimated gas production potential from anoxic corrosion will be 1050 *moles/drum* with a production rate of 1 *mole/drum/year*. The gas production potential from microbial activity is estimated to be at 550 *moles/drum* with a production rate of 1 *mole/drum/year*. This means that microbial activity ceases at 550 years while anoxic corrosion will continue until 1050 years after emplacement.

Alternative 2 of the EATF

Alternative 2 calls for 6680 drums per equivalent room with the waste and drums occupying 1633 m^3. With the required headspace of 0.71 m, the resulting volume of crushed salt backfill is 1358 m^3. The waste form consists of sludges, solid organics, and solid inorganic waste. The sludges are predominately inorganic solidified wastes combined with some form of cement-based material. The solid organics are considered combustible and include waste such as paper, plastics, etc. The solid inorganic waste consists of metals, glass and a small percentage of other non-combustible materials. For Alternative 2, the

Table 2: Waste Form Characterization for EATF Alternative 2 [3]

Waste Form	Drum Count	Drum Weight (Kg)	Density (Kg/m^3)	Porosity
Cemented Combustibles	2660	430.1	2510	0.3
Cemented Metallics	2660	490.6	3000	0.3
Cemented Sludges	1360	430.1	2510	0.3

sludges are cemented, the solid organics and the solid inorganics are shredded and cemented. After cementing takes place, the volume occupied by the cementing material constitutes approximately 80 percent of the total drum volume. Table 2 is a summary of the waste forms for Alternative 2. The cementing material is assumed to be Portland cement with a Youngs modulus, $E = 3.3 \times 10^{10}$ Pa, and a shear modulus, $\mu = 1.3 \times 10^{10}$ Pa. The gas generation potential and generation rates are defined in [3]. The potential for anoxic corrosion is 1050 *moles/drum* and for microbial activity the potential is 550 *moles/drum.* The gas production rates are dependent upon the degradation of the encapsulating cement. From the time of emplacement to 100 years, gas generation due to anoxic corrosion has a rate of 0.7 *mole/drum/year* with no gas generation due to microbial activity. After 100 years, both anoxic corrosion and microbial activity generate gas at a rate of 1 *mole/drum/ year*. The contribution of the microbial activity begins at 100 years and continues for 550 years or until 650 years after emplacement. The anoxic corrosion potential is reduced by 70 moles/drum during the first 100 years with the remainder of the gas generation potential reduced to zero in 980 years or the year 1080 after emplacement.

Table 3: Waste Form Characterization for EATF Alternative 6 [3]

Waste Form	Drum Count	Drum Weight (Kg)	Density (Kg/m^3	Porosity
Vitrified Combustibles	210	528.0	2162	N/A
Metal Ingots	1449	453.0	2930	0.4
Vitrified Sludges	149	454.3	1858	N/A

Alternative 6 of the EATF

For EATF 6, the sludges are vitrified; the solid organics (combustibles) are incinerated and vitrified; glasses are melted and the metals are separated out, melted and disposed of as ingots. The number of drums per equivalent room for this alternative is 1808. The total volume of the waste and drums is 442 m^3. Again, with the required headspace of 0.71 m, the required volume of crushed salt backfill material is 2549 m^3. Table 3 summarizes the various waste forms for Alternative 6. The gas generation potential and gas generation rate are based on anoxic corrosion and microbial activity of the waste. The gas potential for this alternative is based solely on anoxic corrosion since the waste form is metal ingots. The corrosion potential is 1050 *moles/drum* at a rate of 0.7 *moles/drum/year* which results in a time of gas generation of 1500 years.

The total amount of gas generated in a disposal room for the Baseline case and for Alternatives 2 and 6 was specified to be based on 6804 unprocessed waste drums. A comparison of the total gas potentials for the three cases described here are plotted in Figure 1. The finite element code SANCHO [4] was modified to compute the room

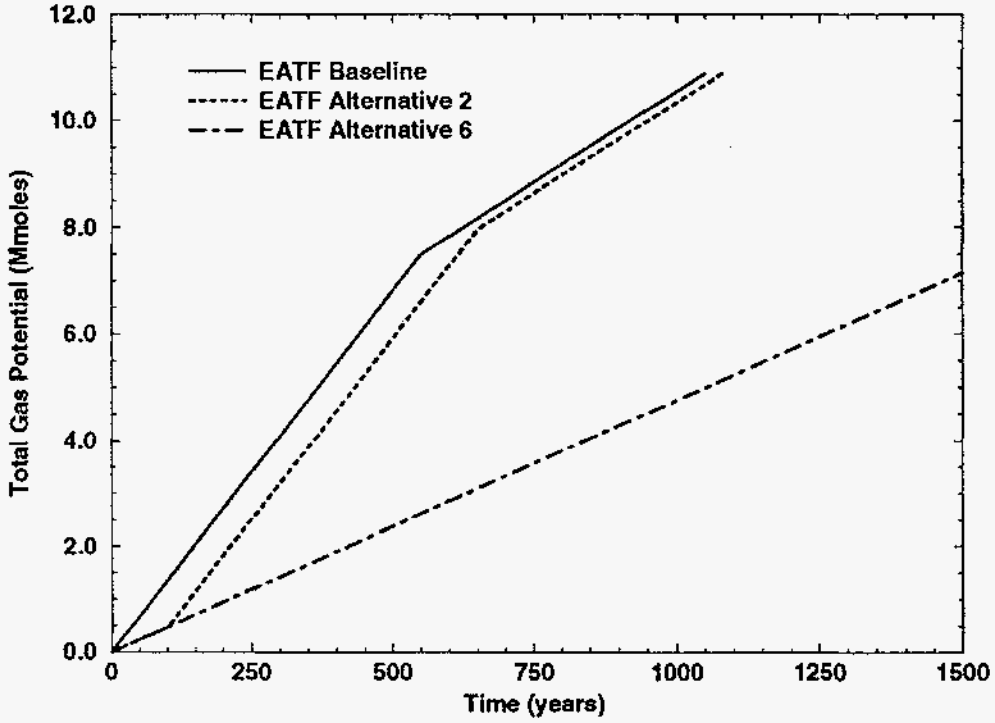

Figure 1. Comparison of Total Gas Potentials for EATF Baseline, EATF Alternative 2, and EATF Alternative 6

pressure and to apply the resulting forces to nodes on the room boundary. The gas pressure was computed from the ideal gas law based on the current free volume in the room (i.e., the volume not occupied by solids) and the total amount of gas potential available in the room. Specifically, the gas pressure p_g was computed from the relationship:

$$p_g = f\frac{NRT}{V - V_s} \qquad \text{(EQ 1)}$$

where N, R, and T are the mass of gas in g-moles, the universal gas constant, and the absolute temperature in $°K$, respectively. The variables V and V_s are the current volume of the disposal room and the volume of solids in the disposal room, respectively. After each iteration in the analysis, the current room volume was calculated based on the locations of the nodes on the boundary of the storage room. The variable f is a multiplier used in the current study to scale the pressure by varying the amount of gas generation. A value of $f = 1.0$ corresponds to an analysis with full gas generation while a value of $f = 0.0$ corresponds to no internal pressure increase due to gas generation.

Description of Numerical Model

The two-dimensional, plane strain disposal room model utilized for the EATF analyses is shown in Figure 2. It closely follows the previous disposal room models[5,6]. The model considers the room to be one of an infinite array of disposal rooms located at the repository horizon with symmetry boundary conditions between rooms. With the additional assumption that gravitational forces do not greatly affect the material response near the

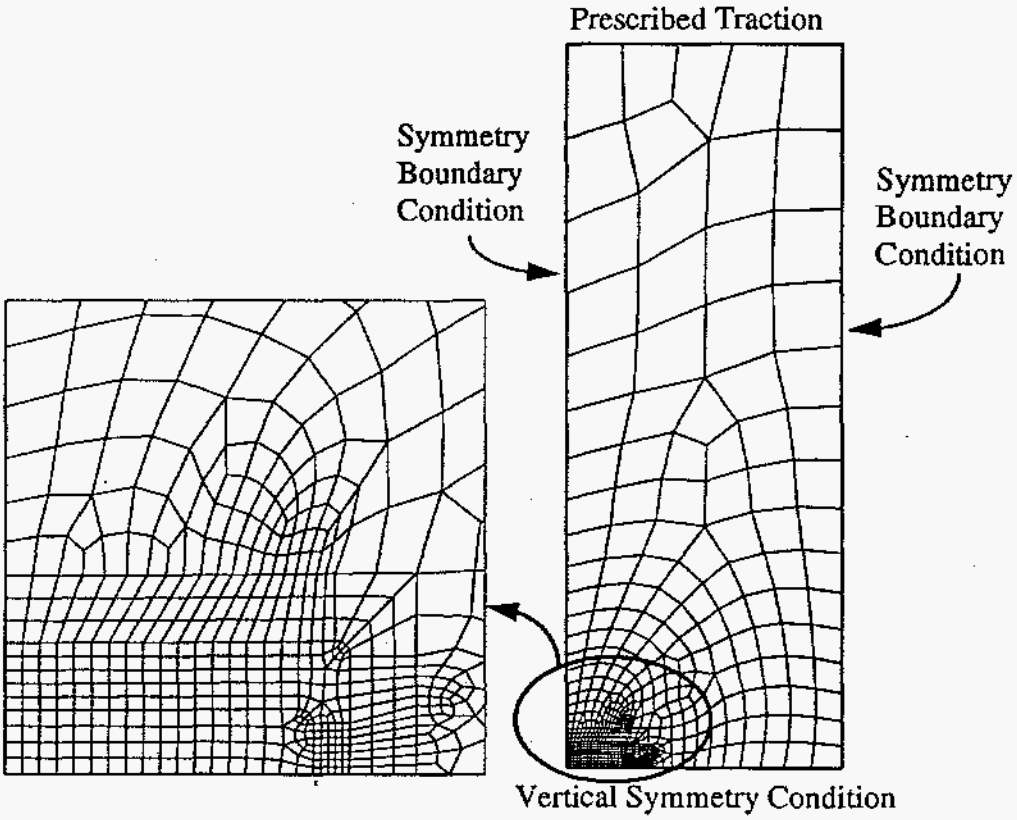

Figure 2. Mesh Discretization and Boundary Conditions Used for the Plane Strain EATF Analyses

room [7] and the use of an all salt stratigraphy, we can employ vertical symmetry boundary conditions to reach the final quarter-symmetry model shown in the figure. The quarter-symmetry model contains 618 four-node quadrilateral elements. Both the left and right vertical boundaries of the mesh were fixed against horizontal motion, and the lower boundary of the mesh was fixed against vertical motion. A prescribed normal traction of 14.8 MPa corresponding to the overburden load at the repository horizon was applied to the upper boundary of the mesh. The intact salt was given an initial hydrostatic stress field of $\sigma_x = \sigma_y = \sigma_z = -14.8$ MPa where σ_x, σ_y, and σ_z are the stresses in the horizontal, vertical, and out-of-plane directions, respectively. The vertical extent of the mesh extends 54 m from the disposal room centerline, and the horizontal mesh dimension is 20.27 m.

The room itself is composed of material representing the waste, the crushed salt backfill, and the headspace. The various dimensions of these materials depends on the particular EATF case being analyzed. The basic quarter-symmetry room dimension is 1.98 m high by 5.03 m wide. For the Baseline Case, the volume of the waste and drums is 1663 m^3 distributed along the 91.44 m length of the drift. This results in a nominal cross-section area of waste equal to 18.19 m^2. We assume a width of waste storage corresponding to 9 m which results in a height of waste of 2.02 m. For the quarter-symmetry room these dimensions become a height of 1.01 m and a width of 4.5 m. The remainder of the disposal room volume was filled with crushed salt backfill which has a porosity of 0.4. The disposal room volume corresponding to the headspace, 653 m^3, was discretized as though it was crushed salt and special capabilities were added to SANCHO to model this region and its response. The crushed salt material representing the headspace was modeled as a very low modulus, elastic material until the disposal room volume had decreased by 653 m^3. At that point, the crushed salt backfill model was invoked for the remainder of the calculation, thus, replacing the elastic material response.

For EATF 2, the waste volume was 1633 m^3 distributed along the length of the drift. The nominal cross-section area of waste is 17.86 m^2 which results in a height of 1.98 m for a width of 9 m of waste storage. For the quarter-symmetry room these dimensions are 0.99 m high by 4.5 m in width. The remainder of the volume was assumed to be crushed salt backfill. As for the Baseline case, the headspace was treated as a low modulus elastic material until the room volume had decreased by 653 m^3 when the crushed salt backfill model was invoked.

EATF 6 has a waste volume of 442 m^3 distributed along the length of the drift. This results in a nominal waste area cross-section of 4.83 m^2. For the assumed width of 9 m, the resulting height of waste is 0.54 m. The quarter-symmetry model assumes a width of 4.5 m and a height of 0.27 m. It was felt that the minimal dimensions of this waste form would not be significant in the calculation of EATF 6 so the entire cross-section of the disposal room was assumed to be filled with crushed salt.

The elastic-secondary creep constitutive model described by Krieg [8] was used for the intact salt. The model can be decomposed into an elastic volumetric part, Equation 2, and a deviatoric part, which is defined in Equation 3. In Equation 3, s_{ij} is the deviatoric stress defined as $s_{ij} = \sigma_{ij} - \frac{\sigma_{kk}}{3}$ and e_{ij} is the deviatoric strain defined by $e_{ij} = \varepsilon_{ij} - \frac{\varepsilon_{kk}}{3}$. The material parameters K,G, A, n, Q, R, T appearing in Equations 2 and 3 are bulk modulus, shear modulus, material creep constant, creep exponent, activation energy, universal gas

$$\varepsilon_{kk} = -\frac{\sigma_{kk}}{3K} \qquad \text{(EQ 2)}$$

$$\dot{s}_{ij} = 2G\dot{e}_{ij} - 2GA\exp\left(\frac{Q}{RT}\right)\left(s_{kl}s_{kl}\right)^{\frac{(n-1)}{2}} s_{ij} \qquad \text{(EQ 3)}$$

constant, and absolute temperature in ^{o}K, respectively. The values of the shear and bulk moduli used in the current work were obtained by dividing the values given by Krieg [8] by a factor of 12.5. This artificial reduction in the moduli has been shown to produce good agreement between computed and in-situ closures [9] when an all salt stratigraphy is used to model the salt formation. The material constants are shown in Table 4.

Table 4: Material Constants Used With the Elastic/Secondary Creep Model

PARAMETER	VALUE
G	992. MPa
K	1656 MPa
A	5.79×10^{-36} $Pa^{-4.9}sec^{-1}$
n	4.9
$Q/(RT)$	20.13

The material models and constants used for the waste and crushed salt backfill were identical to those used in earlier studies [5,6]. The crushed salt backfill model was developed by Sjaardema and Krieg [10] based on data from creep-consolidation experiments on crushed salt. In this material model, creep is included in both the volumetric and the deviatoric response. The form of the model, shown in Equations 4 through 7, is such that the mechanical response of the crushed salt becomes identical to that of the intact salt as the density of the backfill approaches the density of the intact salt. The variables in Equations 4 through 7 not previously defined are material constants B_0 and B_1 obtained

$$G = G_0 \exp\left(G_1 \rho\right) \qquad \text{(EQ 4)}$$

$$K = K_0 \exp\left(K_1 \rho\right) \qquad \text{(EQ 5)}$$

$$\dot{s}_{ij} = 2G\dot{e}_{ij} - 2GA\,(\rho_{intact}/\rho)^{n} exp\left(\frac{Q}{RT}\right)(s_{kl}s_{kl})^{\frac{(n-1)}{2}} s_{ij} \qquad \text{(EQ 6)}$$

$$\dot{\rho}_{creep} = B_0\,(exp\,(B_1 p) - 1)\,exp\,(A\rho) \qquad \text{(EQ 7)}$$

from the creep consolidation experiments and the density ρ computed from the equation:

$$\rho = \rho_0 exp\left(\int_{t_0}^{t} \dot{e}_v dt\right) \qquad \text{(EQ 8)}$$

where ρ_0 is the density at time t_0. The intact density of the salt appears in Equation 6 as ρ_{intact}. The elastic moduli are assumed to depend on the density of the backfill through the relationships shown in Equations 4 and 5. The constants K_0 and K_1 were determined by using the least squares method to fit the modulus data to the function in Equation 4. In the fit, the function was constrained so that the bulk modulus of the crushed salt was equal to the bulk modulus of the intact salt when the crushed salt was fully compacted. No

Table 5: Material Constants Used With the Crushed Salt Backfill Model

PARAMETER	VALUE
G_0	864 Pa
G_1	6.53×10^{-3} m^3/kg
K_0	1.41×10^{3} Pa
K_1	6.53×10^{-3} m^3/kg
A_c	5.79×10^{-36} Pa$^{-4.9}$sec^{-1}
n	4.9
Q/RT	20.13
A	-17.3×10^{-3} m^3/kg
B_0	1.3×10^{8} kg (m^3 sec)$^{-1}$
B_1	0.82×10^{-6} Pa^{-1}

experiments have been conducted to determine how the shear modulus varies with density, so the shear modulus was assumed to vary according to the same exponential form as the bulk modulus. The constant G_0 was selected so that the shear modulus for the crushed salt was equal to that of the intact salt when the crushed salt was fully consolidated, and the constant G_1 was assumed to be the same as K_1. Because the shear and bulk moduli of the

intact salt were divided by 12.5, G_0 and K_0 were divided by the same factor. Table 5 lists the values of the creep constants and elastic constants used for the backfill material.

The stress-strain behavior of the waste was represented by a volumetric plasticity model [4] with a piecewise linear function defining the relationship between the mean stress and the volumetric strain. Compaction experiments on simulated waste were used to develop this relationship. The deviatoric response of the waste material has not been characterized. It is anticipated that when a drum filled with loosely compacted waste is compressed axially, the drum will not undergo significant lateral expansion until most of the void space inside the drum has been eliminated.

For the volumetric plasticity model, the yield surface in principal stress space is a surface of revolution with its axis centered about the hydrostat and the open end pointing into the compression direction. The open end is capped with a plane which is at right angles to the hydrostat. The deviatoric part is elastic-perfectly plastic so the surface of revolution is stationary in stress space. The volumetric part has variable strain hardening so the end plane moves outward during volumetric yielding. The volumetric hardening is defined by a set of pressure-volumetric strain relations. A flow rule is used such that deviatoric strains produce no volume change (associated flow). The model is best broken into volumetric and deviatoric parts with the deviatoric part resembling conventional plasticity. The volumetric yield function is a product of two functions describing the surface of revolution and the plane normal to the pressure axis. These are given by

$$\phi_s = \frac{1}{2} s_{ij} s_{ij} - (a_0 + a_1 p + a_2 p^2) \qquad \text{(EQ 9)}$$

$$\phi_p = p - g(e_v) \qquad \text{(EQ 10)}$$

where a_0, a_1, a_2 are constants defining the yield surface, p is the pressure, and e_v is the volume strain. The form of g is defined in this problem by a set of piecewise linear segments relating pressure-volume strain. Table 6 lists the pressure-volumetric strain data

Table 6: Pressure-Volumetric Strain Data Used in the Volumetric Plasticity Model for the Waste Drums

PRESSURE (MPa)	$\ln(\rho/\rho_0)$
0.028	0.032
0.733	0.741
1.133	0.898
1.667	1.029
2.800	1.180
10.17	1.536

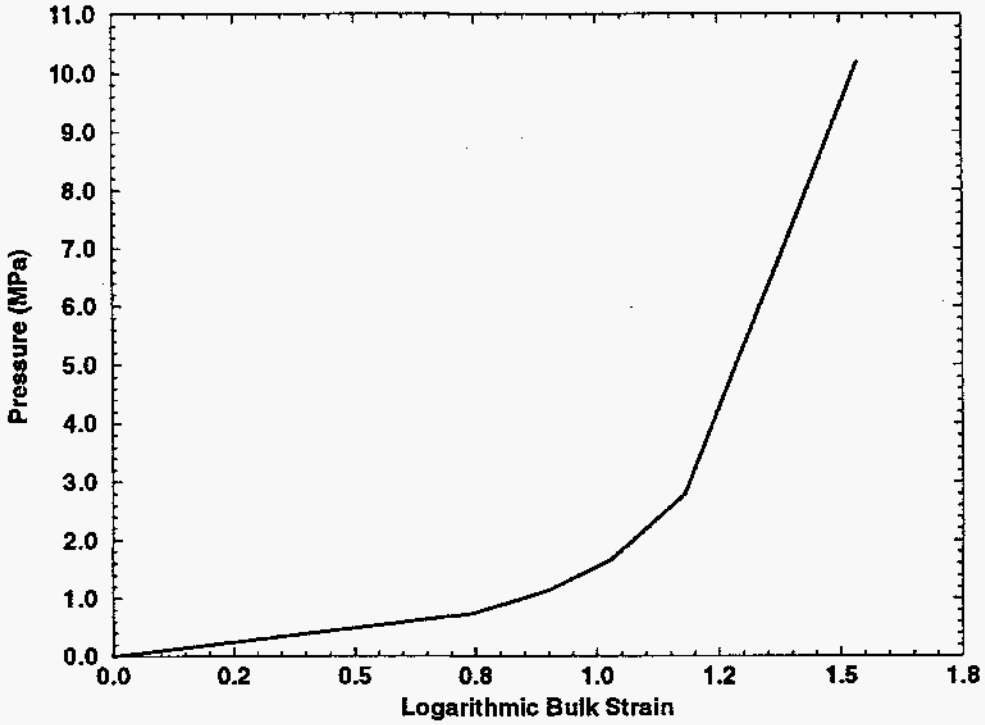

Figure 3. Curve of the Pressure-Bulk Strain Input to the Volumetric Plasticity Model Used to Model the Waste Drums

used for the waste drum model and the data is plotted in Figure 3. The elastic material parameters and constants defining the yield surface are given in Table 7.

Table 7: Material Constants Used With the Volumetric Plasticity Model for the Waste

PARAMETER	VALUE
G	333 MPa
K	222 MPa
a_0	0.
a_1	0.
a_2	3.

The calculations were run for a simulation period of 2000 years following excavation with a time step of 0.025 years. During the analysis it was necessary to monitor the room volumetric behavior and assess whether the waste and backfill within the room should be deleted from the problem. Because of the gas pressure, closure of the room stops and the room volume begins to increase with increasing gas pressure. In the event of room expansion, it is believed that the walls of the room would separate from the room contents. At the point in time when the room begins to expand, the elements representing the waste

and backfill were deleted so that they would not resist expansion of the room. The process of deleting the room contents was found to be a sensitive modeling parameter. If the room contents were deleted too early, then the room would experience a sudden decrease in void volume, but if the contents were deleted too late, then the final void volume could be in error. Several computer runs were generally required for each EATF Alternative to establish the appropriate deletion time. However, some effects of deletion time were still observed in the porosity surfaces. These will be discussed in the results section.

Results of the Analyses

EATF Baseline Case

The initial effective porosity of the disposal room can be determined from the volume of solids associated with the waste and the crushed salt. The initial porosity of the crushed salt is defined to be 0.4 [5] while the porosity of the waste can be calculated from a drum weighted average involving the solid organics (2722 drums, porosity = 0.8), the solid inorganics (2722 drums, porosity = 0.8), and the sludge (1360 drums, porosity = 0.5) which results in a waste porosity of 0.74. Combining the volume of crushed salt (1328 m^3) with the volume of waste and drums (1663 m^3) and their respective porosities results in a solid volume of 1229 m^3. From the solid volume of 1229 m^3 and the total room volume of 3644 m^3, an effective room porosity of 0.6626 can be calculated. This initial porosity value can be seen as the starting point in Figure 4 which is a plot of room porosity as a function of time for various rates of gas generation. Recall that the variable f is a multiplier applied to the ideal gas law as defined in Equation 1. The room porosity is seen to decrease from the initial value until the gas generation rate has produced enough gas and, therefore, internal pressure to reduce the room closure rate and begin to increase the room volume. The minimum room porosity is reached by 200 years. The limiting $f = 0.0$ case results in a minimum porosity value of 0.22. For all values of the multiplier, a steady state porosity value has been achieved by 2000 years.

Figure 5 and Figure 6 show the vertical and horizontal closures, respectively, for the disposal room. These closure values are nodal displacement values from the quarter symmetry model multiplied by a factor of 2.0 to reflect estimates of the total closure for the room. These plots clearly show the perturbations in the solution generated by deleting the waste and backfill material. These disturbances are local to the time of material deletion and quickly damp out. Effects on the long term solution have been determined to be minimal. It is interesting to note that the horizontal and vertical closure curves are similar in shape and magnitude for each value of f. No decrease in room closure is observed for values of f below 0.2. Figure 7 shows the magnitude of gas pressure produced for each value of f. The lithostatic stress level is 14.8 MPa, and this level is exceeded for values of f above 0.4.

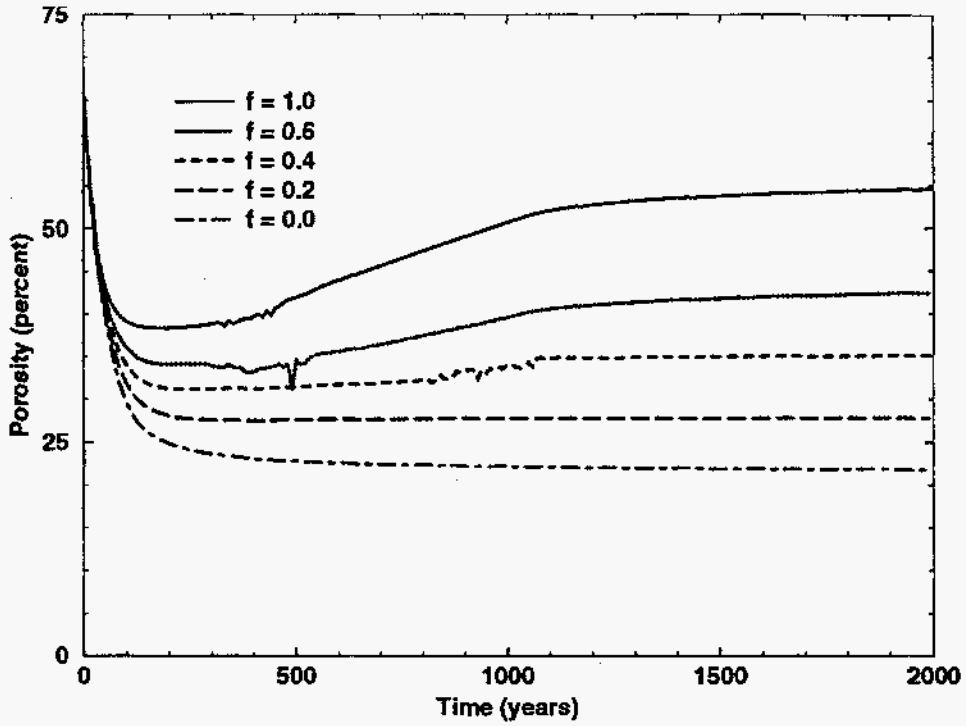

Figure 4. Disposal Room Porosity History for the EATF Baseline Case. Each Curve Represents a Different Gas Generation Rate Through the Multiplier *f*.

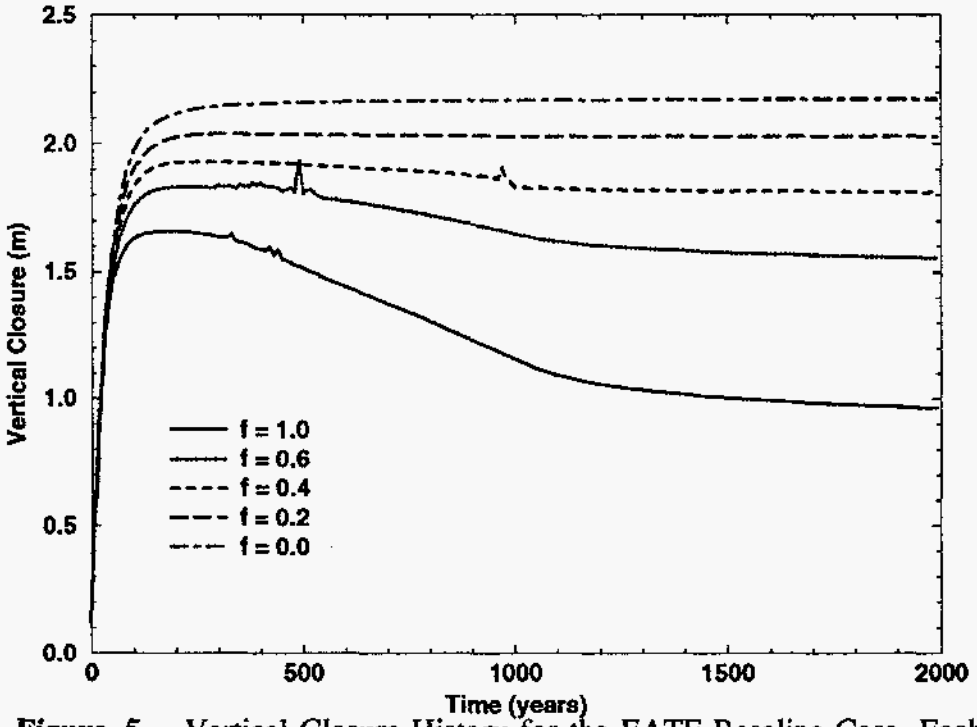

Figure 5. Vertical Closure History for the EATF Baseline Case. Each Curve Represents a Different Gas Generation Rate Through the Multiplier *f*.

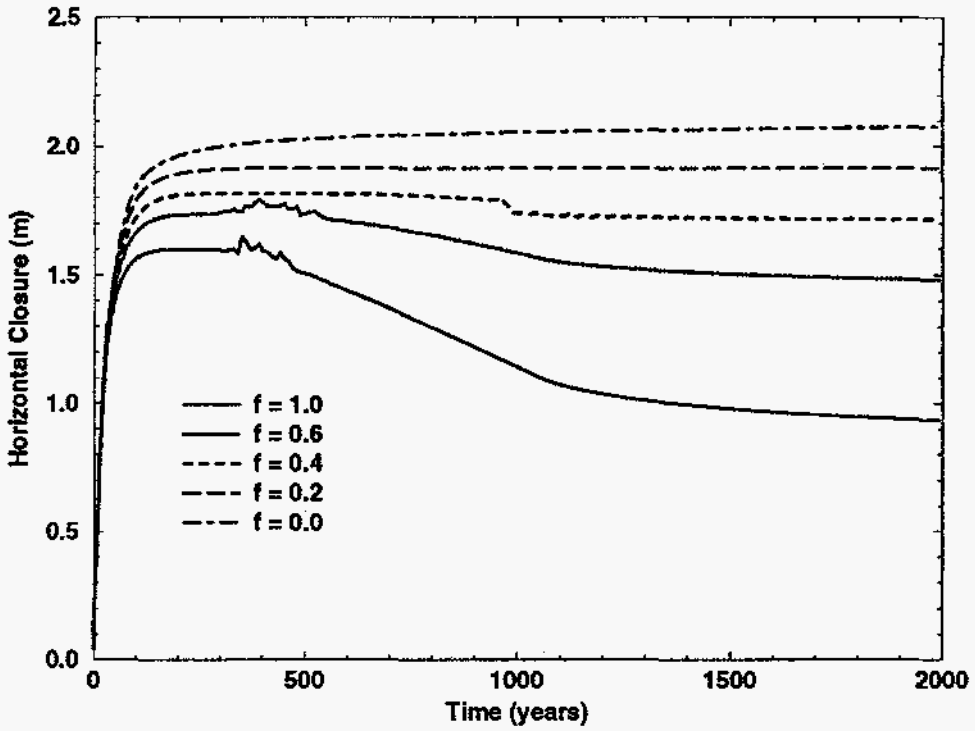

Figure 6. Horizontal Closure History for the EATF Baseline Case. Each Curve Represents a Different Gas Generation Rate Through the Multiplier *f*.

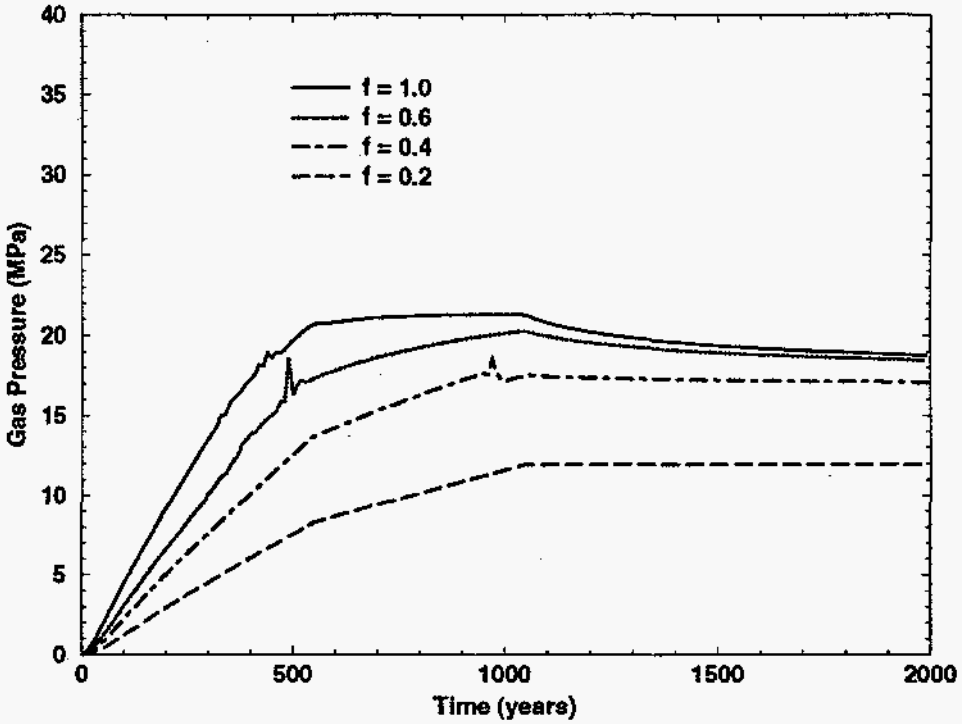

Figure 7. Disposal Room Gas Pressure History for the EATF Baseline Case. Each Curve Represents a Different Gas Generation Rate Through the Multiplier *f*.

EATF Alternative 2 Case

Recall that for EATF Alternative 2 that the waste is cemented, and therefore there is a limiting value of room porosity which is related to the porosity of the cemented material. Figure 8 shows the porosity as a function of time for various values of *f*. The initial effective

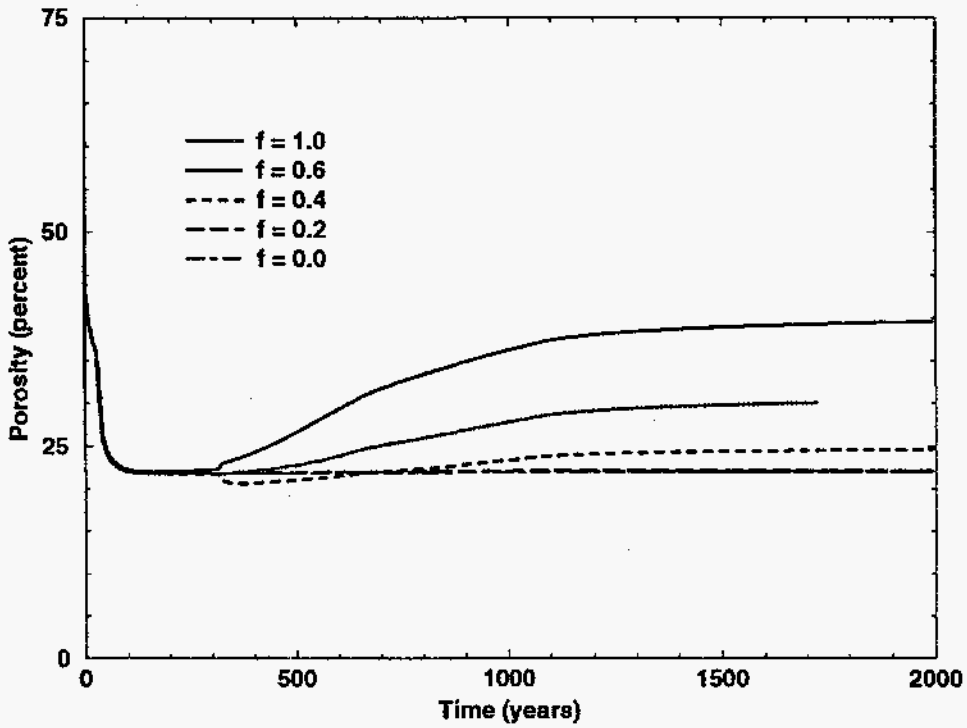

Figure 8. Disposal Room Porosity History for the EATF Alternative 2. Each Curve Represents a Different Gas Generation Rate Through the Multiplier *f*.

porosity has been calculated to be 0.4627, and that value is seen to be the starting point for each calculation. The figure clearly shows that for lower values of *f*, the room porosity reaches a minimum value and does not increase for the duration of the analysis. For values of *f* greater than or equal to 0.4, the porosity begins to increase during the period between 200 and 300 years. A minimum porosity of 0.22 is achieved. Plots of vertical and horizontal closure histories are shown in Figure 9 and Figure 10, respectively. A maximum limit on the closures is observed due to the presence of the rigid cemented block of waste. As in the Baseline analysis, the effects of the material deletion can be seen in the plotted results. Closure histories are clearly affected by the increasing gas pressure. The vertical closure *f* = 1.0 case shows that the room expands back to its original dimension due to the gas pressure. The gas pressure histories are shown in Figure 11. Breakpoints which were used for defining the various gas generation rates can be clearly seen.

EATF Alternative 6 Case

In Alternative 6, the combustible waste is burned, and the metals are separated and stored as ingots. The volume of waste for this case is small, and the model assumed that the

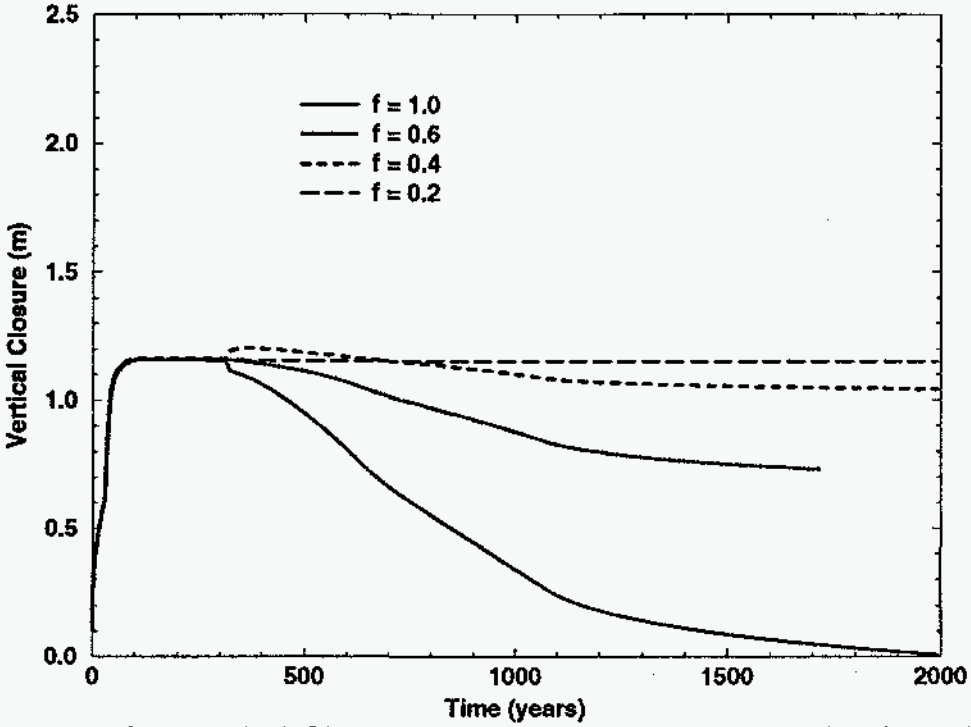

Figure 9. Vertical Closure History for the EATF Alternative 2. Each Curve Represents a Different Gas Generation Rate Through the Multiplier *f*.

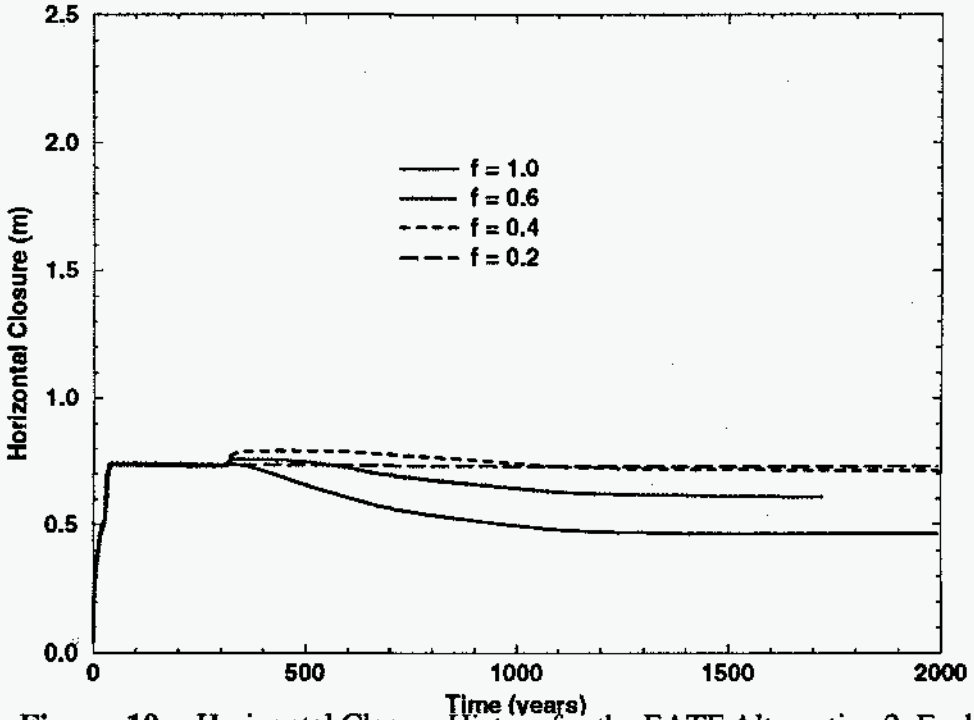

Figure 10. Horizontal Closure History for the EATF Alternative 2. Each Curve Represents a Different Gas Generation Rate Through the Multiplier *f*.

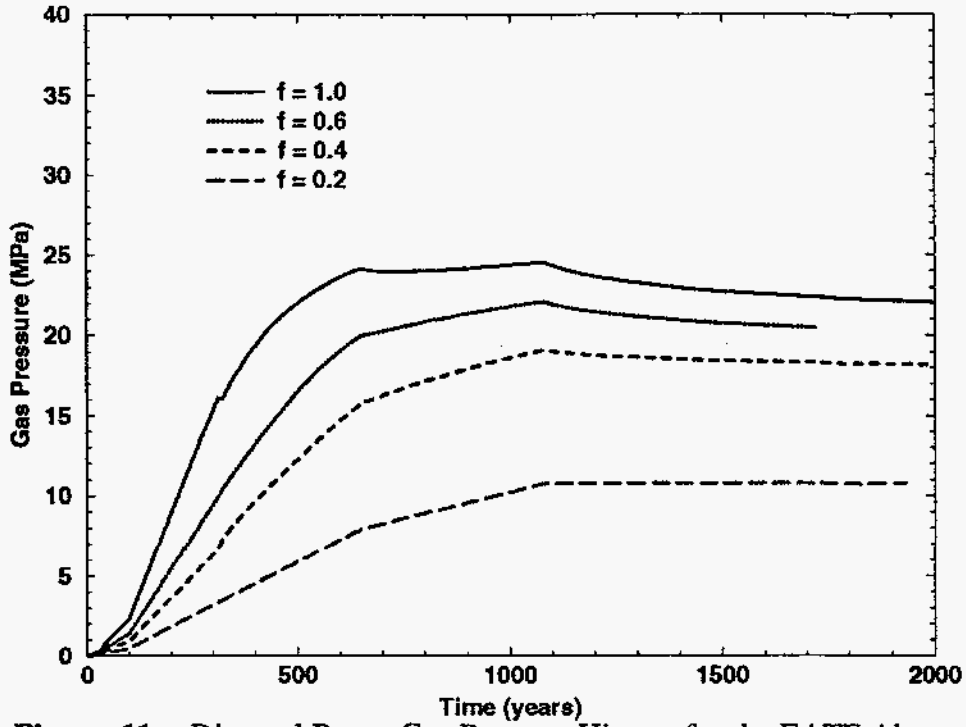

Figure 11. Disposal Room Gas Pressure History for the EATF Alternative 2. Each Curve Represents a Different Gas Generation Rate Through the Multiplier *f*.

disposal room volume was filled completely with crushed salt except for the headspace. The initial effective porosity has been calculated to be 0.5075, and that value is seen to be the starting point for each calculation. Figure 12 shows the porosity histories for the various gas generation rates. When there is no gas generation, the crushed salt compacts to a very low porosity within 100 years. The crushed salt waste does compact to a low porosity (below 0.10) for all of the gas generation rates analyzed. Some increase in porosity is observed for all of the non-zero multiplier values with a steady state value reached by 2000 years. The vertical and horizontal closure histories, shown in Figure 13 and Figure 14, respectively, show maximum closure associated with the analyses with lower gas pressures. Reopening of the disposal room occurs to some extent for all of the non-zero pressure values. The largest effect of reopening occurs for the maximum pressure case (f = 1.0). Figure 15 shows the plotted gas pressure histories. The peak pressure is reached at 1500 years when the maximum gas potential is reached. The room pressure drops due to the increased volume associated with reopening of the disposal room.

Summary of Results

Calculations of the mechanical creep closure response of the Baseline and Alternatives 2 and 6 of the EATF have been performed to allow three-dimensional porosity surfaces of the disposal room to be constructed for WIPP Performance Assessment activities. Data supplied to F. T. Mendenhall consisted of porosity histories for various gas generation rates for a period of 2000 years following excavation. Closure results from the calculations show

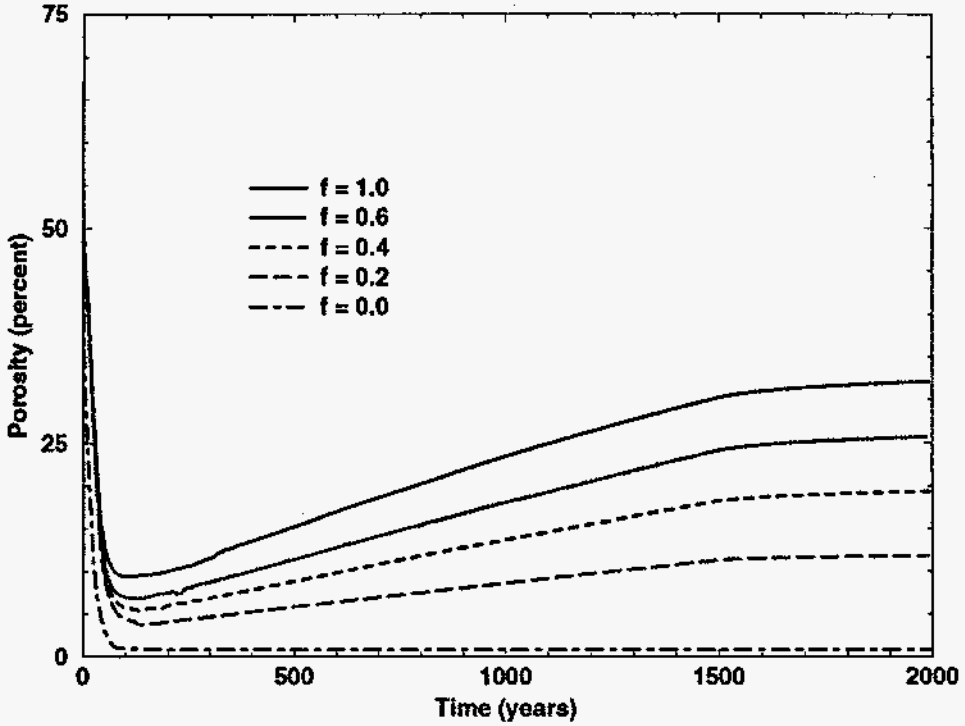

Figure 12. Disposal Room Porosity History for the EATF Alternative 6. Each Curve Represents a Different Gas Generation Rate Through the Multiplier *f*.

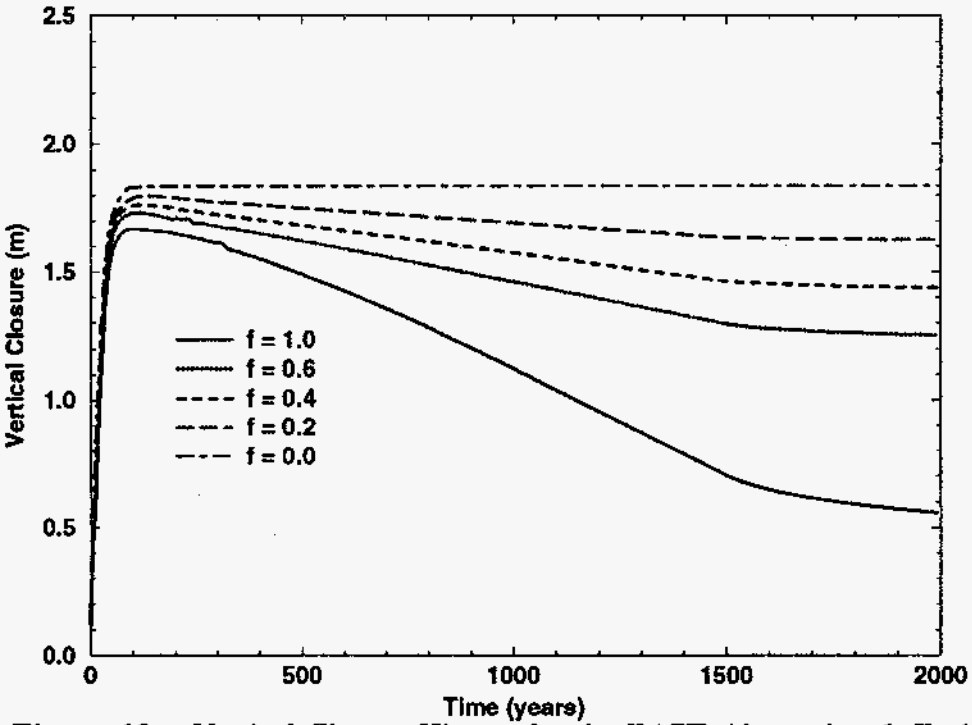

Figure 13. Vertical Closure History for the EATF Alternative 6. Each Curve Represents a Different Gas Generation Rate Through the Multiplier *f*.

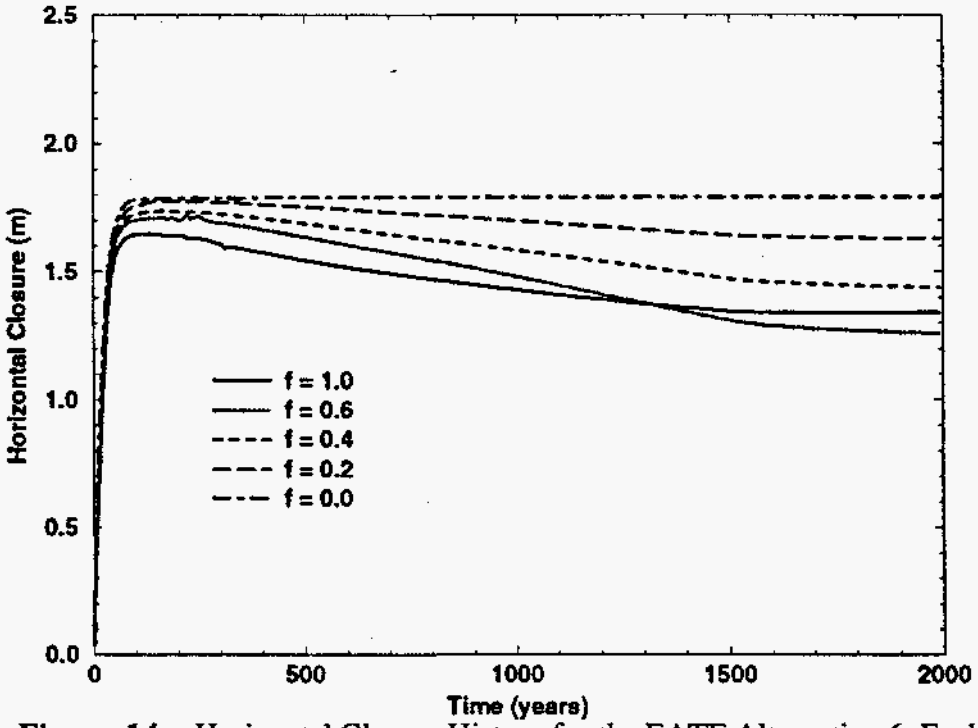

Figure 14. Horizontal Closure History for the EATF Alternative 6. Each Curve Represents a Different Gas Generation Rate Through the Multiplier *f*.

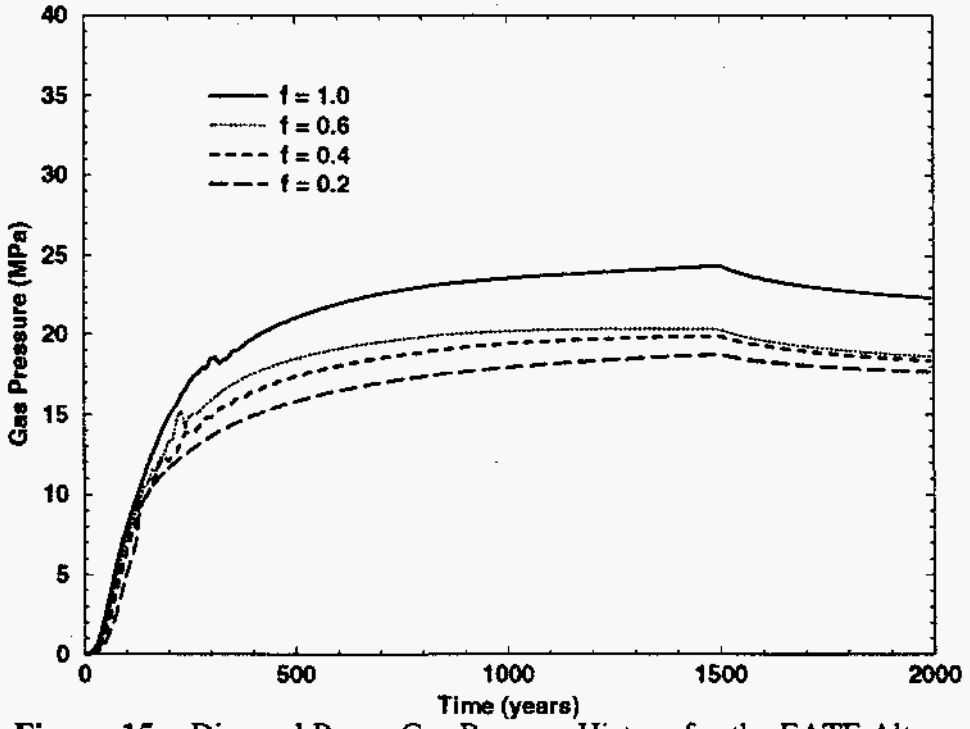

Figure 15. Disposal Room Gas Pressure History for the EATF Alternative 6. Each Curve represents a Different Gas Generation Rate Through the Multiplier *f*.

rapid closure of the disposal room occurring during the first 100 years following excavation. Depending upon the gas generation rate, the disposal room would then begin to experience an increase in porosity due to the action of the internally generated pressure acting on the room boundaries. In almost all cases, steady state response was achieved within 2000 years.

References

1. Marietta, M. G., S. G. Bertram-Howery, D. R. Anderson, K. F. Brinster, R. V. Guzowski, H. Lussolino, and R. P. Rechard, "Performance Assessment Methodology Demonstration: Methodology Development for Evaluating Compliance With EPA 40 CFR 191 Subpart B for the Waste Isolation Pilot Plant," SAND89-2027, Sandia National Laboratories, Albuquerque, New Mexico, December, 1989.

2. Beraun, R. and P. B. Davies, "Baseline Design Input Data Base to be Used During Calculations Effort to be Performed by Division 1514 in Determining the Mechanical Creep Closure Behavior of Waste Disposal Rooms in Bedded Salt," Memorandum to Distribution, Sandia National Laboratories, Albuquerque, New Mexico, September 12, 1991.

3. Beraun, R., F. T. Mendenhall, and R. P. Rechard, "Compilation of Input Data for Alternatives 2 and 6 of the EATF to be Used During Calculations Effort to be Performed by Division 1514 in Determining the Mechanical Creep Closure Behavior of Waste Disposal Rooms in Bedded Salt," Memorandum to Distribution, Sandia National Laboratories, Albuquerque, New Mexico, September 6, 1991.

4. Stone, C. M., R. D. Krieg, and Z. E. Beisinger, "SANCHO - A Finite Element Computer Program for the Quasistatic, Large Deformation, Inelastic Response of Two-Dimensional Solids," SAND84-2618, Sandia National Laboratories, Albuquerque, New Mexico, April, 1985.

5. Weatherby, J. R., J. G. Arguello, B. M. Butcher, and C. M. Stone, "The structural response of a WIPP disposal room with internal gas generation," Proceedings of the 32nd U. S. Rock Mechanics Symposium, Norman, OK, July, 1991.

6. Weatherby, J. R., W. T. Brown, and B. M. Butcher, "The closure of WIPP disposal rooms filled with various waste and backfill combinations," Proceedings of the 32nd U. S. Rock Mechanics Symposium, Norman, OK, July, 1991.

7. Arguello, J. G., "Use of Midheight Symmetry Plane to Compute Disposal Room Closure," Memorandum to Distribution, Sandia National Laboratories, Albuquerque, NM, January 1990.

8. Krieg, R. D., "Reference Stratigraphy and Rock Properties for the Waste Isolation Pilot Plant (WIPP) Project," SAND83-1908, Sandia National Laboratories, Albuquerque, New Mexico, 1984.

9. Morgan, H. S. and R. D. Krieg, "A Comparison of Unified Creep-Plasticity and Conventional Creep Models for Rock Salt Based on Predictions of Creep Behavior Measured in Several *In Situ* and Bench-Scale Experiments," SAND87-1867, Sandia National Laboratories, Albuquerque, NM, 1988.

10. Sjaardena, G. D. and R. D. Krieg, "A Constitutive Model for the Consolidation of WIPP Crushed Salt and Its Use in Analyses of Backfilled Shaft and Drift Configurations," SAND87-1977, Sandia National Laboratories, Albuquerque, New Mexico, 1987.

Distribution

1425 J. H. Biffle

1434 D. R. Martinez

1500 D. J. McCloskey

1561 H. S. Morgan

1561 J. G. Arguello

1561 E. L. Hoffman

1561 J. R. Weatherby

1562 R. K. Thomas

6121 J. R. Tillerson

6121 R. E. Finley

6121 D. E. Munson

6345 R. C. Lincoln

6345 F. T. Mendenhall

1561 C. M. Stone

Sandia National Laboratories

Albuquerque, New Mexico 87185

date: March 31, 1993

to: B. M. Butcher, 6345

Charles M. Stone

from: Charles M. Stone, 1561

subject: Application of SANTOS to Waste Disposal Room Problems Including a Demonstration of Coupled Structural/Porous Flow Capability

Executive Summary

Creep closure analyses of a WIPP disposal room have been performed, using the finite element code SANTOS, for comparison to earlier calculations using SANCHO. SANTOS, which is currently being developed in Department 1561 for WIPP disposal room applications, contains state-of-the-art finite element technology and makes extensive use of vector processing on the CRAY computer to achieve large increases in speed over conventional finite element codes. SANTOS should eventually replace SANCHO for performing disposal room calculations and therefore, it must be demonstrated that SANTOS meets all of the code qualification criteria. The Baseline disposal room design analyzed previously served as the benchmark for these comparisons. The additional physics and modeling capabilities built into SANTOS allow the analyst to make fewer assumptions regarding the disposal room model than in the earlier SANCHO calculations. An additional capability to model single phase, fully saturated, porous flow in a deforming medium has been incorporated within SANTOS to allow for coupled structural/porous flow solutions. This capability is also demonstrated using the Baseline disposal room configuration.

Introduction

This memorandum documents predicted mechanical creep closure of a WIPP disposal room containing waste, in the form of drums, and salt backfill material using the SANTOS [1] finite element code. The waste drums and backfill material compact due to creep closure of the room, but the rate of room closure is slowed by the resistance of the compacting room contents. Over time, the waste and waste drums stored in the room are assumed to decompose and generate gas which acts upon the surfaces of the room and affects the rate of room closure. These effects are all part of the disposal room model which is being used to assist in demonstrating repository compliance with all federal and state regulations.The disposal room analyses presented here correspond to the Baseline room model [2] with internal gas generation. Typical information required from disposal room analyses are curves of room void volume as a function of time for specific fractions (f) of the gas

generation rate. The generated curves will be used to compare with, or to generate results for defining, a porosity surface used for the repository performance assessment model.

The finite element code SANTOS is being developed to extend our ability to analyze complex disposal room problems. The code employs state-of-the-art large strain, finite element technology coupled with extensive code vectorization to achieve large increases in speed over conventional finite element codes. The code is based on the transient dynamic code PRONTO2D [3] and employs a self-adaptive, dynamic relaxation solution scheme to achieve quasistatic solutions. The code has been previously benchmarked for use in WIPP drift analyses [4]. Since that time it has been used as an analysis tool for other WIPP applications [5] and it is currently being proposed that SANTOS replace SANCHO as the code of choice for disposal room calculations. The code has an improved contact surface detection algorithm which is necessary for performing disposal room analyses. This is an enhancement in capability over the contact detection algorithm found in SANCHO[6]. It allows the gap between the crushed salt backfill and the roof to be explicitly modeled rather than being lumped into the crushed salt backfill model. Perhaps the most distinguishing feature of SANTOS is the unique capability to perform coupled structural/hydrological analyses for single phase, fully saturated, porous flow. The coupling of the solutions is through the compression/dilatation of the salt due to changes in the mean stress and through the large geometry changes in the salt surrounding the disposal room.This capability allows the analyst to monitor the amount of brine inflow into the disposal room over time.

In this memo several different analyses are presented to document the capabilities of SANTOS for addressing disposal room problems. A direct comparison with SANCHO results will serve to qualify SANTOS for performing disposal room calculations. Several additional calculations are presented which look at modeling of the gap between the crushed salt and roof and how the final room porosity changes with the modeling assumptions. A final analysis is presented which addresses the question of brine inflow into the disposal room.

The next section of this memo describes the Baseline design analyzed. The third section describes the numerical models used for the analyses, and the fourth section discusses the results of the analyses and compares them to previous solutions obtained with SANCHO. The last section summarizes the results from the study.

Description of the Baseline Design

The Baseline design, defined in [2], calls for 6804 drums of uniformly distributed unprocessed waste to be stored in a disposal room. Each of the rectangular disposal rooms is 3.96 m high by 10.06 m wide by 91.44 m in length resulting in an initial room volume of 3644 m^3. The corresponding volume occupied by the waste and the drums is 1663 m^3. With the required 0.71 m headspace between the waste and the roof, the total volume of crushed salt backfill necessary to fill the disposal room is approximately 1328 m^3. The Baseline transuranic waste form is a combination of solid organics, solid inorganics, and sludges.

Solid organics account for 40 percent of the drums, solid inorganics account for 40 percent, and sludges account for the remaining 20 percent. Table 1 summarizes the data available to characterize the baseline waste. The gas generation potential and gas production rate corresponding to the Baseline case are composed of gas from two sources: anoxic corrosion and microbial activity. Reference [2] reports that the estimated gas production potential from anoxic corrosion will be 1050 *moles/drum* with a production rate of 1 *mole/drum/year*. The gas production potential from microbial activity is estimated to be 550 *moles/drum* with a production rate of 1 *mole/drum/year*. This means that microbial activity ceases at 550 years while anoxic corrosion will continue until 1050 years after emplacement.

Table 1: Waste Form Characterization for the Baseline Design [2]

Waste Form	Drum Count	Drum Weight (Kg)	Density (Kg/m^3)	Porosity
Solid Organics	2722	77	380	0.8
Solid Inorganics	2722	102	900	0.8
Sludges	1360	211	1200	0.5

The total amount of gas generated in a disposal room for the Baseline case was specified to be based on 6804 unprocessed waste drums per room. The total gas potential for the Baseline case described here is plotted in Figure 1. The finite element code is able to compute the room pressure and to apply the resulting forces to nodes on the room boundary.

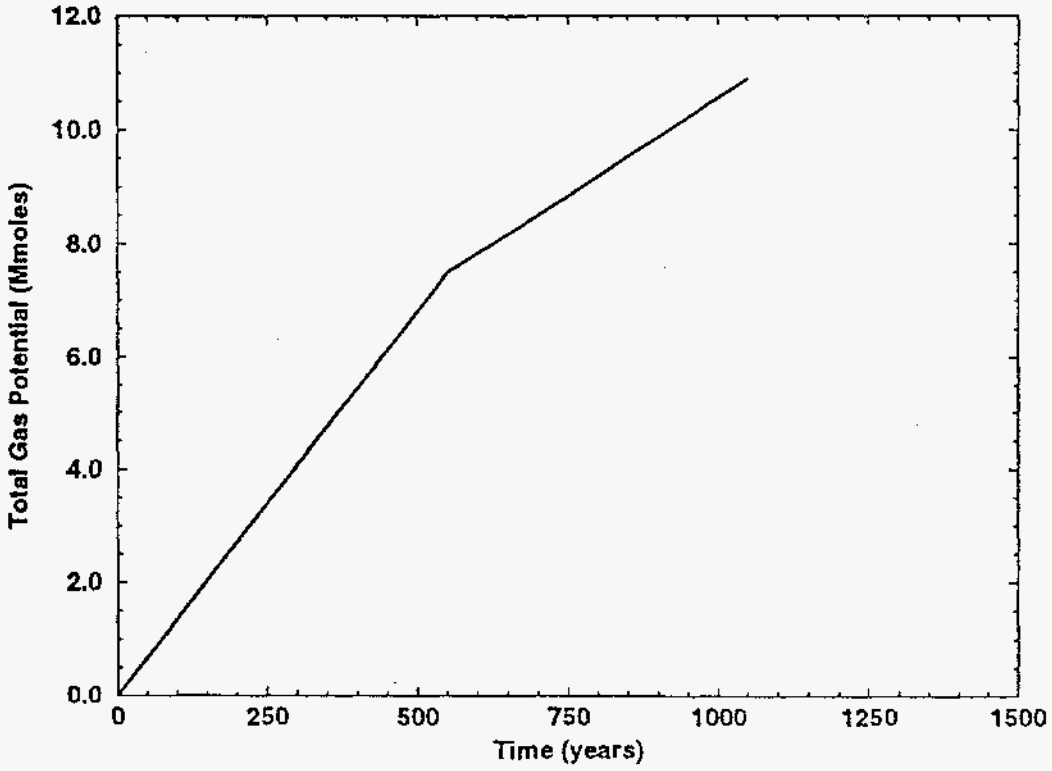

Figure 1. History of the Total Gas Potential for the Baseline Design (f = 1.0).

The gas pressure was computed from the ideal gas law based on the current free volume in the room (i.e., the volume not occupied by solids) and the total amount of gas potential available in the room. Specifically, the gas pressure p_g was computed from the relationship:

$$p_g = f\frac{NRT}{V - V_s} \qquad \text{(EQ 1)}$$

where N, R, and T are the mass of gas in g-moles, the universal gas constant, and the absolute temperature in $°K$, respectively. The variables V and V_s are the current volume of the disposal room and the volume of solids in the disposal room, respectively. After each step in the analysis, the current room volume was calculated based on the locations of the nodes on the boundary of the disposal room. The variable f is a multiplier used to scale the pressure by varying the amount of gas generation. A value of $f = 1.0$ corresponds to an analysis with full gas generation while a value of $f = 0.0$ corresponds to no internal pressure increase due to gas generation. All subsequent gas generation and pressure calculations were based on this gas potential.

Description of Numerical Models

Four two-dimensional, plane strain disposal room models were utilized for the series of Baseline analyses described in this memo. The first model, called the Reference Model, is the same model used with SANCHO to perform the analyses described in [7]. The second model is the Reference Model With Contact Surfaces which is similar to the Reference Model, but introduces frictionless contact surfaces between the crushed salt backfill and the disposal room surfaces. The third model is called the Revised Model With Contact Surfaces. This model explicitly models the headspace or air gap between the crushed salt backfill and the roof. Frictionless contact surfaces are used between the crushed salt backfill and the disposal room surfaces. The final model is the Coupled Structural/Porous Flow Model which is identical to the Revised Model With Contact Surfaces and includes brine inflow and gas generation in the disposal room.

The models are patterned after previous disposal room models[8,9]. Each model considers the room to be one of an infinite array of disposal rooms located at the repository horizon with symmetry boundary conditions between rooms. With the additional assumption that gravitational forces do not greatly affect the material response near the room [10] and the use of an all salt stratigraphy, vertical symmetry boundary conditions can be used to obtain the final quarter-symmetry model shown in Figure 2. Both the left and right vertical boundaries of the mesh are fixed against horizontal motion, and the lower boundary of the mesh is fixed against vertical motion. A prescribed normal traction of 14.8 MPa corresponding to the overburden load at the repository horizon was applied to the upper boundary of the mesh. The intact salt is given an initial hydrostatic stress field of $\sigma_x = \sigma_y = \sigma_z = -14.8$ MPa where σ_x, σ_y, and σ_z are the stresses in the horizontal,

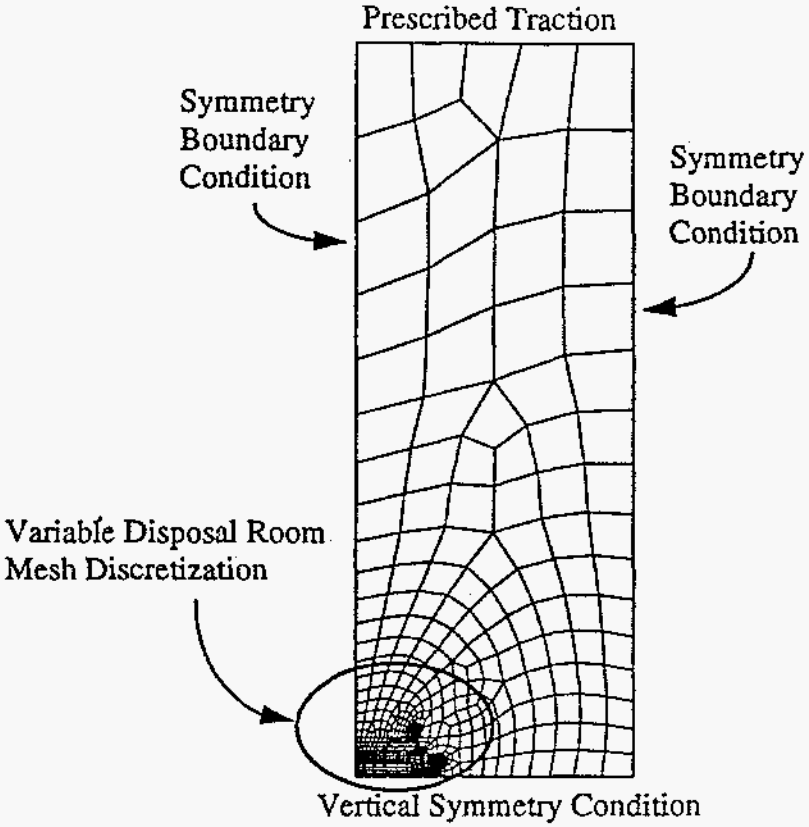

Figure 2. Geometry and Boundary Conditions Used for the Plane Strain Baseline Analyses

vertical, and out-of-plane directions, respectively. The vertical extent of the mesh extends 54 m from the disposal room centerline, and the horizontal mesh dimension is 20.27 m.

The mesh discretization of the disposal room and surrounding salt is different for each model. The Reference Model, with the disposal room discretization shown in Figure 3, contains 664 nodes and 618 four node quadrilateral elements. The Reference Model With Contact Surfaces, shown in Figure 4, contains 1194 nodes and 1093 elements. The Revised Model With Contact Surfaces and the Coupled Structural/Porous Flow model both contain 1048 nodes and 952 elements. The mesh discretization of the disposal room contents and surrounding salt for these models is shown in Figure 5.

The room itself is composed of material representing the waste, the crushed salt backfill, and for some models, the gap or headspace between the crushed salt and roof. The basic quarter-symmetry room dimensions are 1.98 m high by 5.03 m wide. For the Baseline case, the volume of the waste and drums is 1663 m^3 distributed along the 91.44 m length of the drift. This results in a nominal cross-section area of waste equal to 18.19 m^2. We assume a width of waste storage corresponding to 9 m which results in a height of waste of 2.02 m. For the quarter-symmetry room these dimensions become a height of 1.01 m and a width of 4.5 m. The remainder of the disposal room volume was filled with crushed salt backfill, which has a porosity of 0.4, within 0.35m of the roof. The disposal room volume

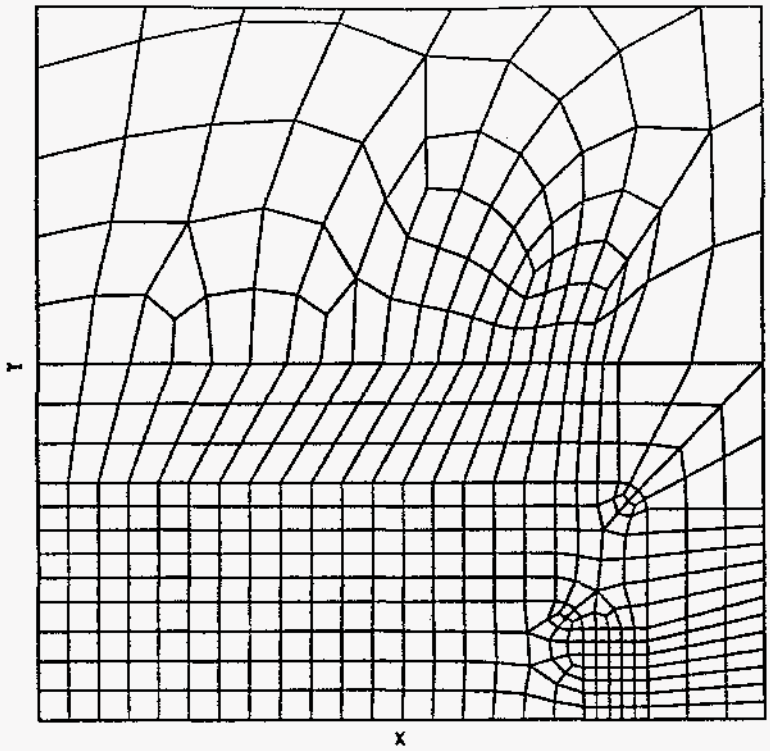

Figure 3. Local Discretization in the Vicinity of the Disposal Room for the Reference Model

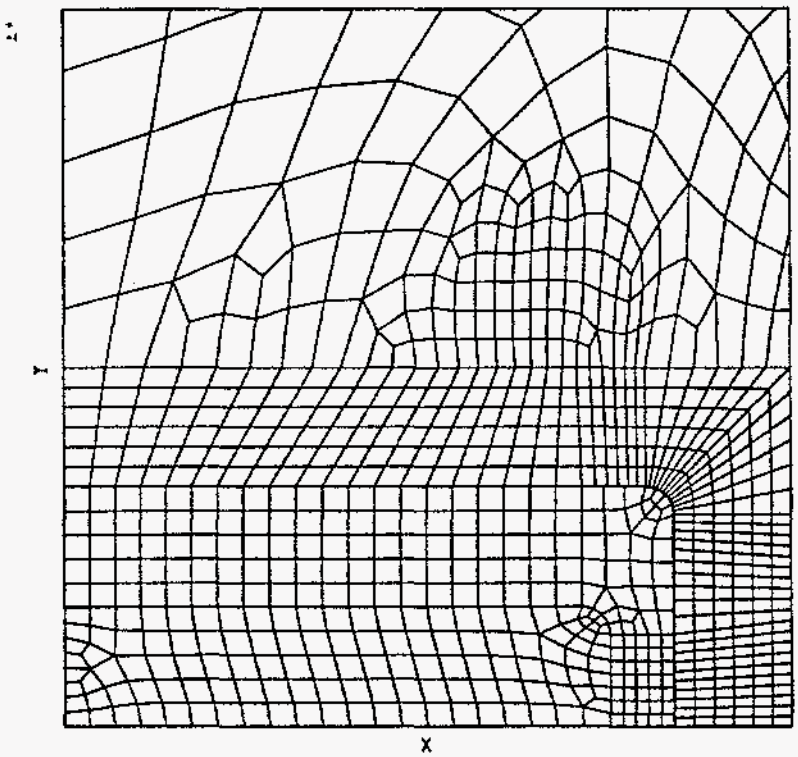

Figure 4. Local Discretization in the Vicinity of the Disposal Room for the Reference Model With Contact Surfaces

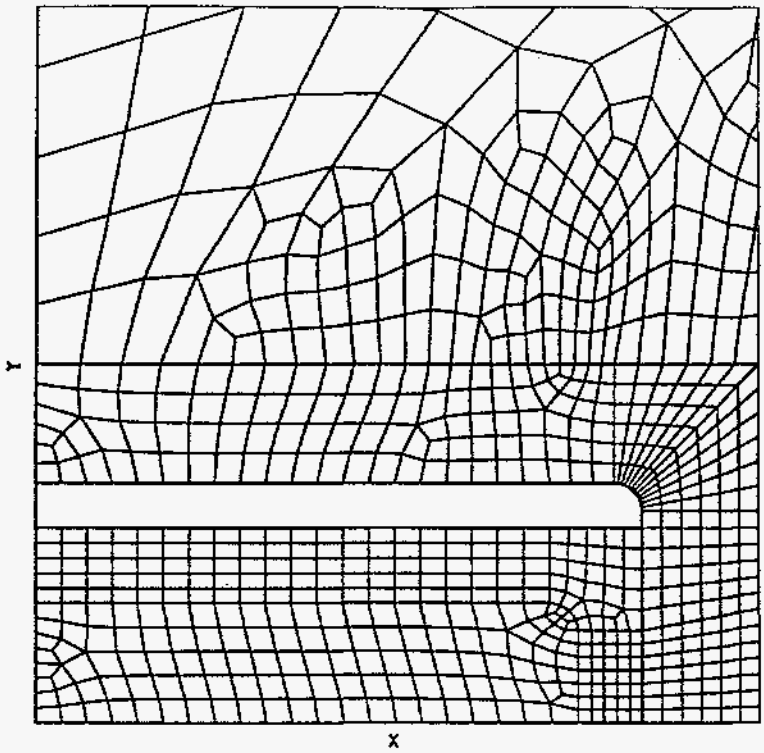

Figure 5. Local Discretization in the Vicinity of the Disposal Room for the Revised Model With Contact Surfaces

corresponding to the headspace gap (653 m^3) was discretized as though it were crushed salt for the Reference Model analyses. These calculations assume that the headspace was a part of the crushed salt backfill which means that the crushed salt begins to compact from the first time step. There is no low modulus elastic response as in some previous calculations[7] to simulate the behavior of the headspace. The Revised Model and the Coupled Structural/ Porous Flow model both explicitly model the headspace gap. Contact surfaces are assumed to exist between the crushed salt backfill and the surfaces of the disposal room. The contact surface allows frictionless sliding between the roof and crushed salt and it allows the roof and sidewall to separate from the crushed salt if the generated gas pressure is sufficient.

The elastic-secondary creep constitutive model described by Krieg [11] was used for the intact salt. The model can be decomposed into an elastic volumetric part, defined in Equation 2, and a deviatoric part, which is defined in Equation 3. In Equation 3, s_{ij} is the deviatoric stress defined as $s_{ij} = \sigma_{ij} - \frac{\sigma_{kk}}{3}$, and e_{ij} is the deviatoric strain defined by $e_{ij} = \varepsilon_{ij} - \frac{\varepsilon_{kk}}{3}$. The material parameters K,G, A, n, Q, R, and T appearing in Equations 2 and 3 are the bulk modulus, shear modulus, material creep constant, creep exponent, activation energy, universal gas

$$\varepsilon_{kk} = -\frac{\sigma_{kk}}{3K} \qquad \text{(EQ 2)}$$

$$\dot{s}_{ij} = 2G\dot{e}_{ij} - 2GA\exp\left(\frac{Q}{RT}\right)\left(s_{kl}s_{kl}\right)^{\frac{(n-1)}{2}} s_{ij} \qquad \text{(EQ 3)}$$

constant, and absolute temperature in ^{o}K, respectively. The values of the shear and bulk moduli used in the current work were obtained by dividing the values given by Krieg [11] by a factor of 12.5. This artificial reduction in the moduli has been shown to produce good agreement between computed and in-situ closures [12] when an all salt stratigraphy is used to model the salt formation. The material constants are listed in Table 2.

Table 2: Material Constants Used With the Elastic/Secondary Creep Model

PARAMETER	VALUE
G	992. MPa
K	1656 MPa
A	5.79×10^{-36} $Pa^{-4.9}sec^{-1}$
n	4.9
$Q/(RT)$	20.13

The material models and constants used for the waste and crushed salt backfill were identical to those used in earlier studies [8,9]. The crushed salt backfill model was developed by Sjaardema and Krieg [13] based on data from creep-consolidation experiments on crushed salt. In this material model, creep is included in both the volumetric and the deviatoric response. The form of the model, shown in Equations 4 through 7, is such that the mechanical response of the crushed salt becomes identical to that of the intact salt as the density of the backfill approaches the density of the intact salt. The variables in Equations 4 through 7 not previously defined are material constants B_0 and B_1 obtained

$$G = G_0\exp\left(G_1\rho\right) \qquad \text{(EQ 4)}$$

$$K = K_0\exp\left(K_1\rho\right) \qquad \text{(EQ 5)}$$

$$\dot{s}_{ij} = 2G\dot{e}_{ij} - 2GA\left(\rho_{intact}/\rho\right)^{n}\exp\left(\frac{Q}{RT}\right)\left(s_{kl}s_{kl}\right)^{\frac{(n-1)}{2}} s_{ij} \qquad \text{(EQ 6)}$$

$$\dot{\rho}_{creep} = B_0\left(\exp\left(B_1 p\right) - 1\right)\exp\left(A\rho\right) \qquad \text{(EQ 7)}$$

from the creep consolidation experiments and the density ρ computed from the equation:

$$\rho = \rho_0\exp\left(\int_{t_0}^{t}\dot{e}_v dt\right) \qquad \text{(EQ 8)}$$

where ρ_0 is the density at time t_0. The intact density of the salt appears in Equation 6 as ρ_{intact}. The elastic moduli are assumed to depend on the density of the backfill through the relationships shown in Equations 4 and 5. The constants K_0 and K_1 were determined by using the least squares method to fit the modulus data to the function in Equation 4. In the fit, the function was constrained so that the bulk modulus of the crushed salt was equal to the bulk modulus of the intact salt when the crushed salt was fully compacted. No experiments have been conducted to determine how the shear modulus varies with density, so the shear modulus was assumed to vary according to the same exponential form as the bulk modulus. The constant G_0 was selected so that the shear modulus for the crushed salt was equal to that of the intact salt when the crushed salt was fully consolidated, and the constant G_1 was assumed to be the same as K_1. Because the shear and bulk moduli of the intact salt were divided by 12.5, G_0 and K_0 were divided by the same factor. Table 3 lists the values of the creep constants and elastic constants used for the backfill material.

The stress-strain behavior of the waste was represented by a volumetric plasticity model [6] with a piecewise linear function defining the relationship between the mean stress and the volumetric strain. Compaction experiments on simulated waste were used to develop this relationship. The deviatoric response of the waste material has not been characterized. It is anticipated that when a drum filled with loosely compacted waste is compressed axially, the drum will not undergo significant lateral expansion until most of the void space inside the drum has been eliminated.

Table 3: Material Constants Used With the Crushed Salt Backfill Model

PARAMETER	VALUE
G_0	848 Pa
G_1	6.53×10^{-3} m^3/kg
K_0	1.408×10^{5} Pa
K_1	6.53×10^{-3} m^3/kg
A_c	5.79×10^{-36} $Pa^{-4.9}sec^{-1}$
n	4.9
Q/RT	20.13
A	-17.3×10^{-3} m^3/kg
B_0	1.3×10^{8} kg $(m^3\ sec)^{-1}$
B_1	0.82×10^{-6} Pa^{-1}

For the volumetric plasticity model, the yield surface in principal stress space is a surface of revolution with its axis centered about the hydrostat and the open end pointing into the compression direction. The open end is capped with a plane which is at right angles to the

hydrostat. The deviatoric part is elastic-perfectly plastic so the surface of revolution is stationary in stress space. The volumetric part has variable strain hardening so the end plane moves outward during volumetric yielding. The volumetric hardening is defined by a set of pressure-volumetric strain relations. A flow rule is used such that deviatoric strains produce no volume change (associated flow). The model is best broken into volumetric and deviatoric parts with the deviatoric part resembling conventional plasticity. The volumetric yield function is a product of two functions, ϕ_s and ϕ_p, describing the surface of revolution and the plane normal to the pressure axis, respectively. These are given by

$$\phi_s = \bar{\sigma} - (a_0 + a_1 p + a_2 p^2) \qquad \text{(EQ 9)}$$

$$\phi_p = p - g(e_v) \qquad \text{(EQ 10)}$$

where a_0, a_1, a_2 are constants defining the deviatoric yield surface, p is the pressure, and e_v is the volume strain. The effective stress, $\bar{\sigma}$, is defined as $\sqrt{\frac{3}{2} s_{ij} s_{ij}}$ where s_{ij} has been defined previously as the deviatoric stress. This definition of the yield function is different from the definition used in SANCHO which used $\frac{1}{2} s_{ij} s_{ij}$ instead of $\bar{\sigma}$. This change in definition results in a change in the values of the constants a_0, a_1, and a_2. The form of g is defined in this problem by a set of piecewise linear segments relating pressure-volume strain. Table 4 lists the pressure-volumetric strain data used for the waste drum model and the data is plotted in Figure 6. The elastic material parameters and constants defining the yield surface are given in Table 5.

Table 4: Pressure-Volumetric Strain Data Used in the Volumetric Plasticity Model for the Waste Drums

PRESSURE (MPa)	$\ln(\rho/\rho_0)$
0.028	0.032
0.733	0.741
1.133	0.898
1.667	1.029
2.800	1.180
10.17	1.536

The fundamental equation governing the coupling between the structural response of the salt and the flow of brine in a fully-saturated porous medium is given in Equation (11). The coupling is primarily through the compression/dilatation rate of the salt but the formulation does include the effects of changing geometry associated with the deforming salt medium surrounding the disposal room.

$$C\frac{dp}{dt} - \nabla\bullet\left(\frac{\kappa}{\mu}\nabla p\right) = -B\frac{d\sigma}{dt} \qquad \text{(EQ 11)}$$

The time derivative of the pressure in the classical, linear theory is replaced in the more general model with the convected derivative, following the motion of the solid material. This is critical in order to compute the brine flux relative to the creep of the salt and is convenient in the Lagrangian scheme employed in SANTOS. The complete development of this equation for a single phase, fluid saturated, porous medium is discussed in [14].

The variable C is the capacitance defined by

$$C = \frac{1}{K}\left(1 - \frac{K}{K_s}\right) + \frac{\phi}{K_f}\left(1 - \frac{K_f}{K_s}\right) \qquad \text{(EQ 12)}$$

where K, K_s, K_f are the drained bulk modulus, the solid bulk modulus, and the fluid bulk modulus, respectively. The variables ϕ , p, κ, and μ are the porosity, pore pressure, permeability, and fluid viscosity, respectively. The term on the right-hand-side (RHS) of Equation (11) is the forcing term where the coefficient B is defined by

$$B = \frac{1}{K}\left(1 - \frac{K}{K_s}\right) \qquad \text{(EQ 13)}$$

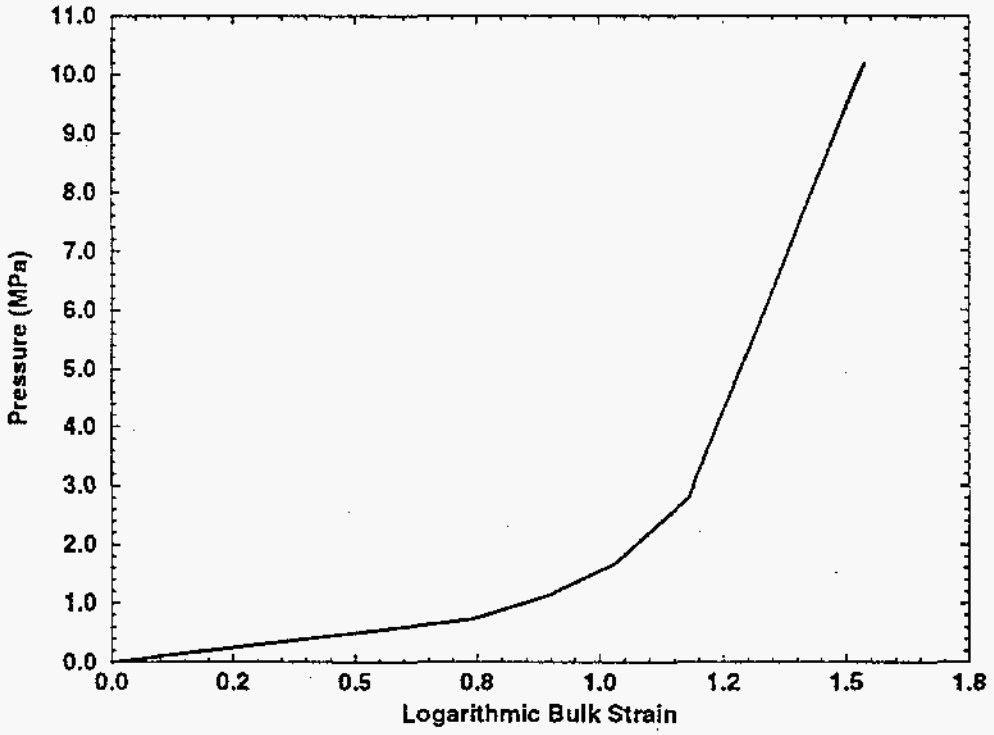

Figure 6. Curve of the Pressure-Bulk Strain Input to the Volumetric Plasticity Model Used to Model the Waste Drums

and the variable σ is defined as $\sigma_{kk}/3$. The RHS term is a source/sink term which reflects changes in the mean stress rate. For example, if the mean stress rate is relaxing (*i.e.*, compression decreasing in magnitude), $-\frac{d}{dt}(\sigma) < 0$, the salt tends to dilate, creating a sink for the fluid pressure. It should be emphasized that the form of Equation (11) is very much dependent upon the particular choice of constitutive model for the volumetric deformation of the salt. The constitutive model presented here describes a material that responds volumetrically as a linearly elastic solid.

Table 5: SANTOS Material Constants Used With the Volumetric Plasticity Model for the Waste

PARAMETER	VALUE
G	333 MPa
K	222 MPa
a_0	1.0 MPa
a_1	3.
a_2	0.

The coupled structural/porous flow problem definition and geometry are similar to the Baseline design calculation except for the location of the top boundary 200 m from the disposal room to represent far field behavior. Any additional differences lie with the specification of the fluid flow portion of the problem. The initial pore pressure distribution is calculated from the expression

$$p(x_i, t) = -B\frac{\sigma_{kk}}{3}(x_i, t) \qquad \text{(EQ 14)}$$

where the mean stress is evaluated from the initial elastic response upon introducing the disposal room. It is based on the fact that upon mining, the state of stress changes immediately but the change in fluid content is initially zero. The boundary conditions on pore pressure are simply to match the pressure at the room boundary to the gas pressure produced in the room. Symmetry boundary conditions along the periphery are satisfied through the natural boundary condition of a zero pore flux. The initial value of the pore pressure was determined from Equation (14) to be 6.0 MPa. The fluid properties used in the calculation are given in Table 6.

Two methods are available for coupling the structural and porous flow equations. The first involves a fully coupled, simultaneous solution of the discretized equations. The second, which is chosen for the current implementation, allows the solutions to be staggered, *i.e.*, the structural solution is determined first with the resulting stresses and displacements used in the porous flow solution. The computed pore pressures are then available to the structural code for use in computing effective stress quantities in the constitutive routines. The porous

flow equation is solved using a preconditioned conjugate gradient method which is robust, efficient, and lends itself well to vectorization on the CRAY computer.

Table 6: Estimated Porous Flow Material Properties for WIPP Salt[15]

Property	Value
Drained Bulk Modulus, K	20.7 GPa
Solid Bulk Modulus, K_s	23.5 GPa
Fluid Bulk Modulus, K_f	3.7 GPa
Salt Porosity, ϕ	0.01
Permeability, κ	1.0×10^{-21} m^2
Fluid Viscosity, μ	1.6×10^{-3} Pa s

The calculations were run for a simulation period of 2000 years following excavation with a time step of 0.025 years. From a structural point of view, the size of the time step should be small enough to accurately capture the physical response of the disposal room system. However, the fluid flow equations have a size requirement on the integration over the time step. The selection of too large a time step can result in the loss of the transient response and the generation of a steady state solution. An inappropriately small time step may produce nonphysical spatial oscillations in the early time pore pressure field due to the limited resolution ability (for pore pressure gradients) of the finite element mesh. We have employed a method described in [16] to estimate the minimum time step to capture the phenomena of interest. The time step of 0.025 years meets the requirements of capturing the transient response and of reducing the pore pressure gradient. A listing of the SANTOS input commands for the Coupled Structural/Porous Flow analysis is given in the Appendix.

Results of the Analyses

The primary outputs obtained from prior SANCHO disposal room calculations are porosity histories, gas pressure and displacement histories.The initial effective porosity of the disposal room can be determined from the volume of solids associated with the waste and the crushed salt. The initial porosity of the crushed salt is defined to be 0.4 [8] while the porosity of the waste can be calculated from a drum weighted average involving the solid organics (2722 drums, porosity = 0.8), the solid inorganics (2722 drums, porosity = 0.8), and the sludge (1360 drums, porosity = 0.5) which results in a waste porosity of 0.74. Combining the volume of crushed salt (1328 m^3) with the volume of waste and drums (1663 m^3), their respective porosities result in a solid volume of 1229 m^3. From the solid volume of 1229 m^3 and the total room volume of 3644 m^3, an effective room porosity of 0.6626 can be calculated. This initial porosity value can be viewed as the starting point for the porosity curves.

Reference Model

A comparison of the disposal room porosity history computed with SANCHO and SANTOS for the $f = 0.0$ case is shown in Figure 7. The figure shows that both calculations start at the correct effective room porosity and track each other for the 2000 year simulation period, finally reaching a nearly constant porosity of 27 percent. Figure 8 shows the deformed shape of the disposal room and contents computed by SANTOS at various times during the 2000 year simulation period. The key feature of this figure is the shape of the disposal room corner and the fact that it maintains its integrity during the 2000 year simulation period. Early calculations with SANCHO exhibited difficulties associated with the behavior of the crushed salt in the room corner. The uniform strain element in SANTOS does not show any spurious behavior. Figure 9 and Figure 10 show the vertical and horizontal displacement histories, respectively, for node points on the disposal room surface. The computed nodal displacement values have been doubled to reflect *total* displacement values for the room. The agreement with the SANCHO results is excellent and shows that the large deformation kinematics and the material models used in the SANTOS calculation have been implemented correctly. The degree of agreement demonstrated in this calculation should serve to qualify SANTOS for application to future disposal room calculations.

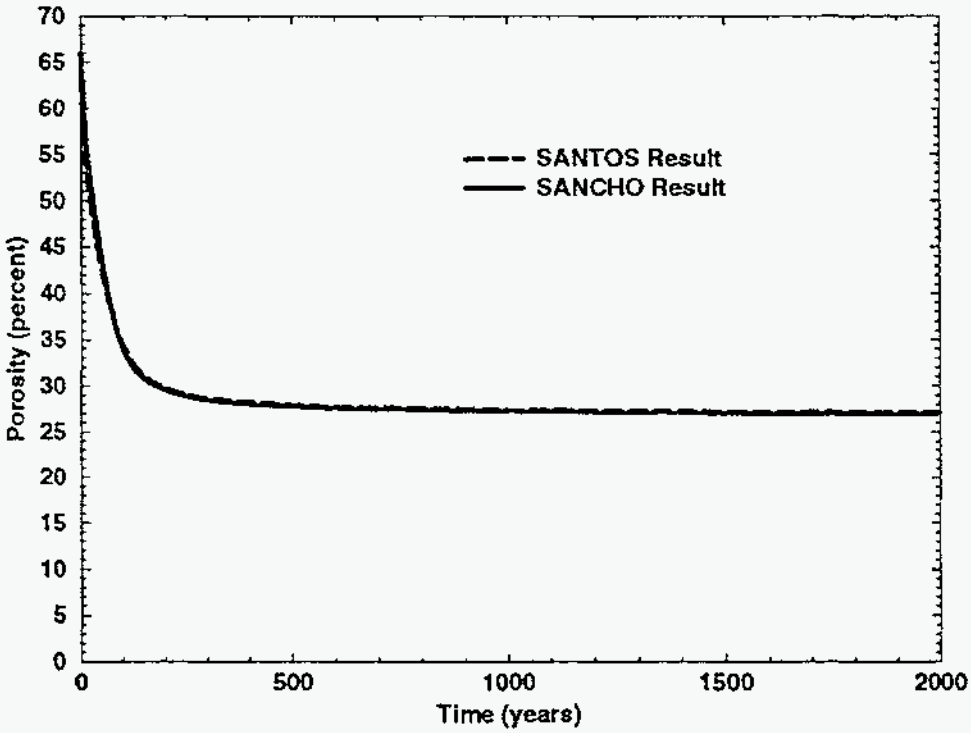

Figure 7. Comparison of Porosity Histories Between SANTOS and SANCHO for the Reference Model Calculation.

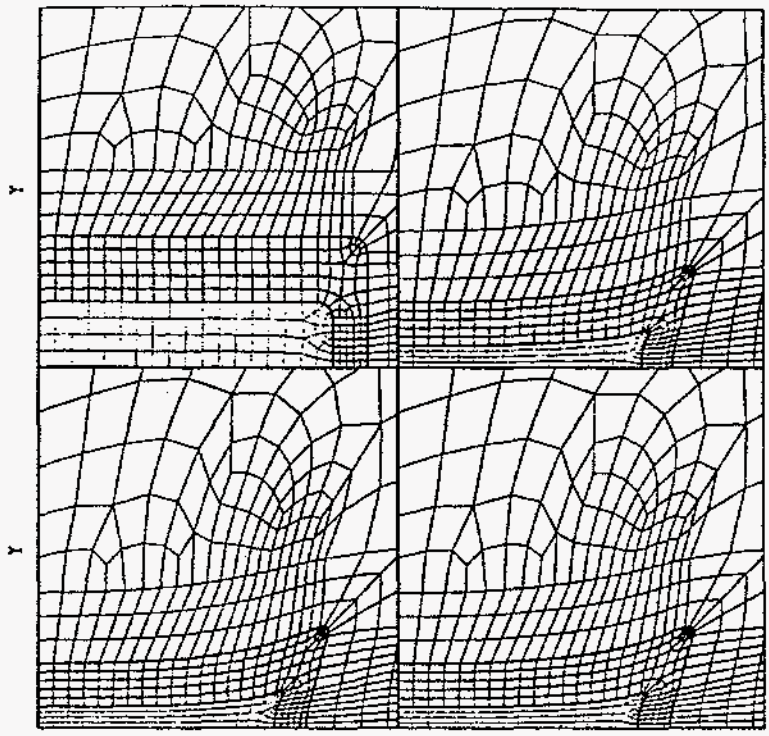

Figure 8. Deformed Shape of Disposal Room and Contents at Various Times During the Simulation. Times Beginning at Top Left and Proceeding Clockwise Are 0., 250., 500., and 1000. Years.

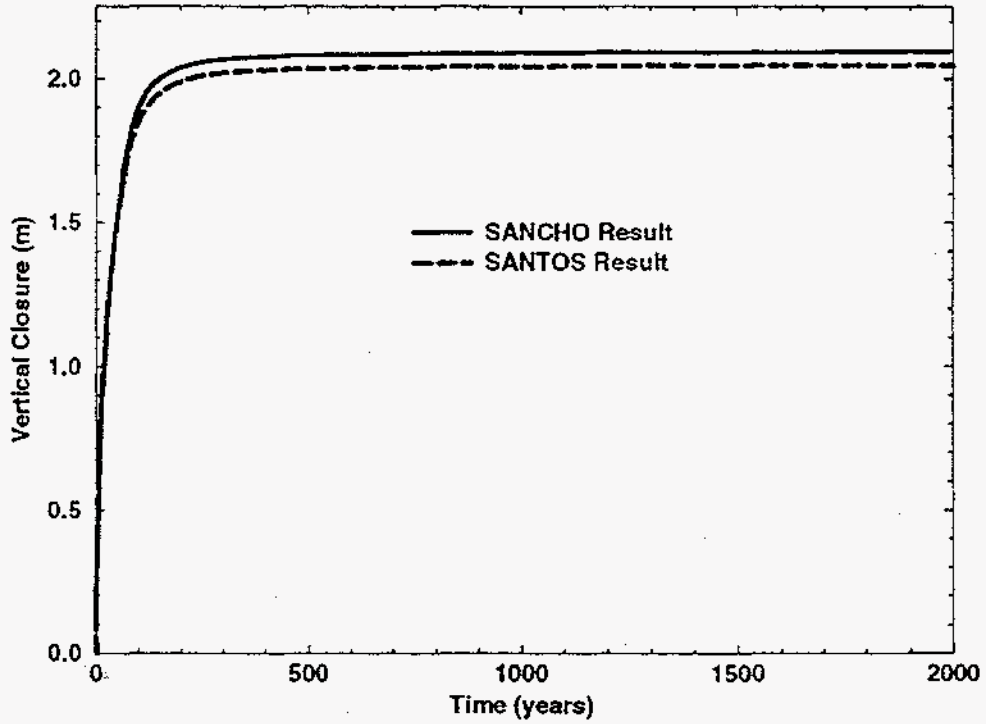

Figure 9. Comparison of the Disposal Room Vertical Closure Results Between SANTOS and SANCHO for the Reference Model Calculation.

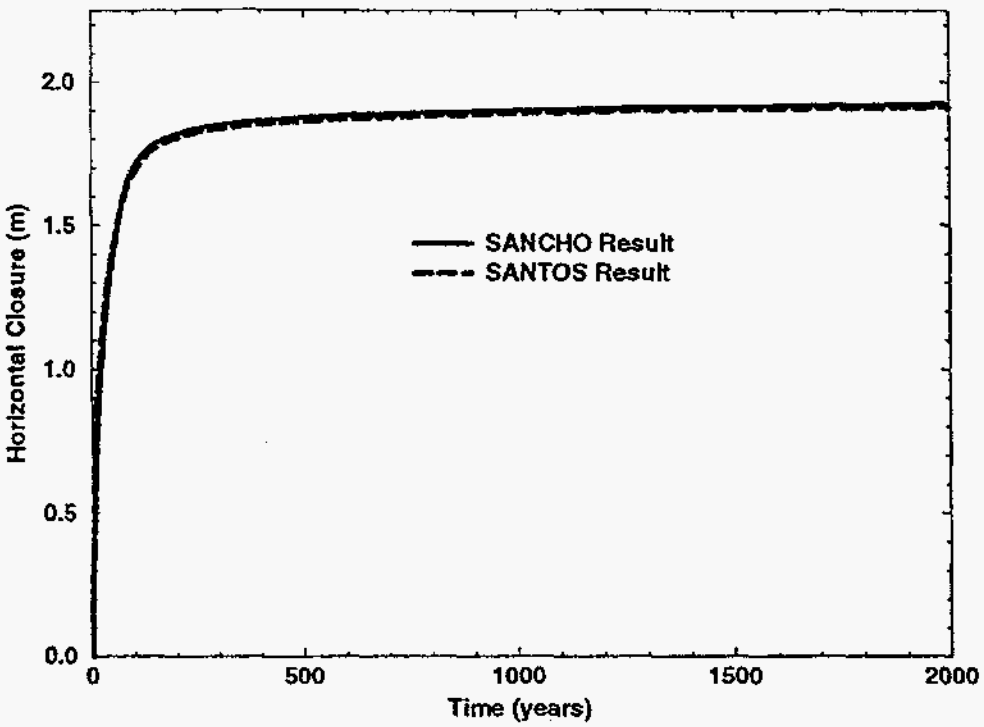

Figure 10. Comparison of the Disposal Room Horizontal Closure Results Between SANTOS and SANCHO for the Reference Model Calculation.

Reference Model With Contact Surfaces

In a demonstration calculation, contact surfaces were placed along the boundary between the room contents and the disposal room surfaces. This calculation evaluates the modeling of the waste/room interaction using contact surfaces and its effect on the effective room porosities. Comparison of disposal room porosity histories for the Reference Model (f = 0.0) with and without contact surfaces is shown in Figure 11. The results show very little difference in porosity between the two models. Figure 12 shows the deformed shape of the room contents and disposal room at various times during the simulation. The deformed shape shows that the room contents are effectively compacted by the salt deformation at the corner of the room. The room actually accomplishes compaction of the crushed salt by squeezing at the corner. The resulting contact of the roof with the side walls can be seen in the figure as well as the sliding that occurs between the crushed salt and the disposal room surfaces. Note the differences in the deformed disposal room compared with the Reference Model deformed shape shown in Figure 8.

Revised Model With Contact Surfaces

In the Revised Model With Contact Surfaces, the headspace or air gap is explicitly modeled. Contact surfaces are defined between the room contents and the roof/sidewalls with a sliding coefficient of friction of zero. In this calculation gas generation was assumed with a value of f = 1.0. With gas generation defined, the room reopens due to the effect of gas pressure acting on the walls of the disposal room. This reopening begins to occur after the internal gas pressure has reached approximately 10 MPa. The use of contact surfaces

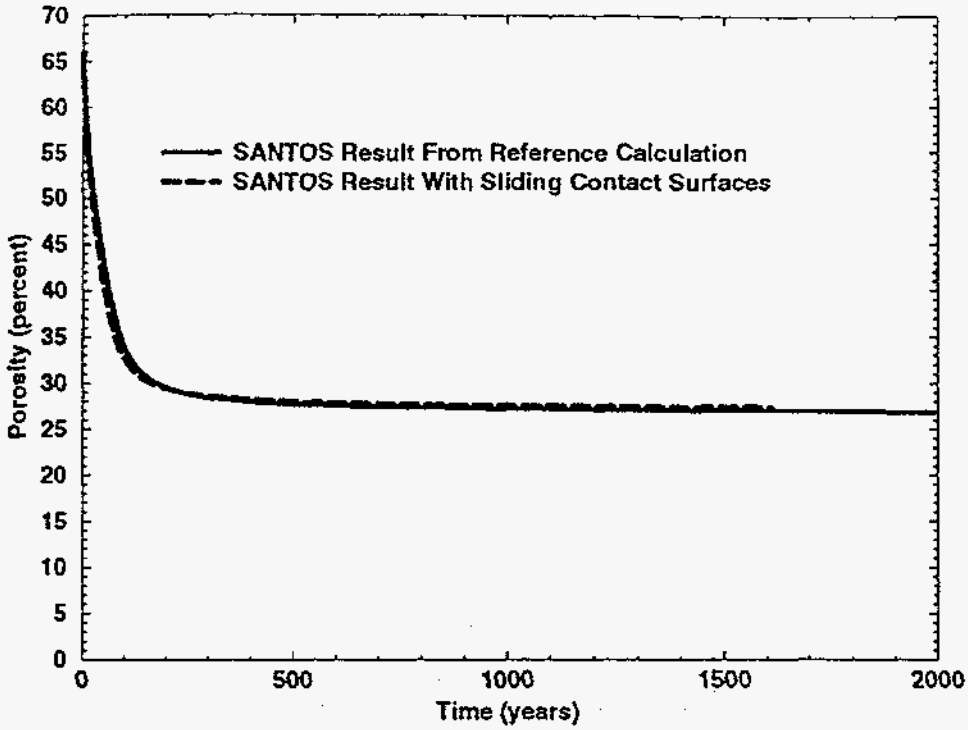

Figure 11. Comparison of the Effective Room Porosity History for the Reference Model With and Without Contact Surfaces. Both Calculations Were Performed With SANTOS.

allows the room to reopen without deleting the contents as in the SANCHO calculations which results in a more stable calculation. Figure 13 shows the effective room porosity from the Revised Model compared to the comparable SANCHO calculation with $f = 1.0$. It is clear from this calculation that the way that the headspace or air gap is modeled makes a difference in the computed porosities. Instead of reaching a minimum porosity of 38 percent, the disposal room only reaches a minimum porosity of 43 percent. The higher porosity results from the method of loading the crushed salt and waste. The SANCHO calculation used a reduced elastic stiffness for the air gap. This stiffness is small but some additional compaction does occur at early times. The use of the contact surfaces allows the air gap to close without some precompaction of the waste. The disposal room reopening is also observed to be more gradual with the air gap. No initial calculation was required to determine the appropriate time to delete the room contents upon reopening. The use of contact surfaces would easily allow for recompaction of the room contents such as might occur during a human intrusion event.

Both solutions reach the same approximate porosity at 2000 years. This process is controlled by equilibrium between the gas pressure with the overburden load. Figure 14 shows the disposal room deformed shape for various times during the simulation. The figure shows the contact and subsequent reopening of the disposal room. Reopening occurs both along the top and the side of the crushed salt and waste. It is interesting to note the deformed shape of the room with $f = 1.0$ compared to $f = 0.0$ in Figure 12. The biggest difference in the deformed shapes appears to be the behavior of the corner due to the fact that it remains more open in this calculation due to the gas pressure.

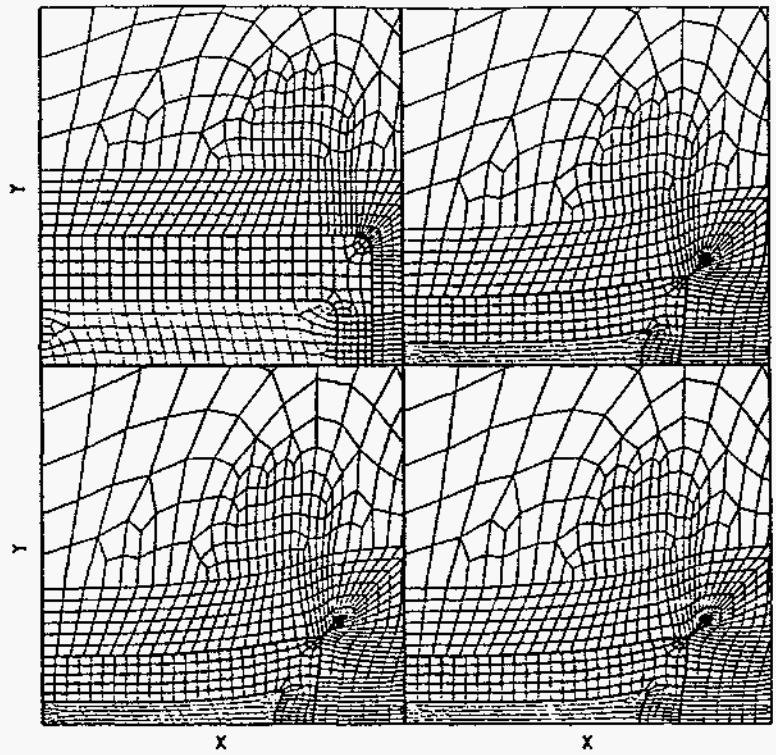

Figure 12. Deformed Shape of the Disposal Room and Contents at Various Times During the Simulation. Times Beginning at Top Left and Proceeding Clockwise are 0., 250., 500. and 1000. Years.

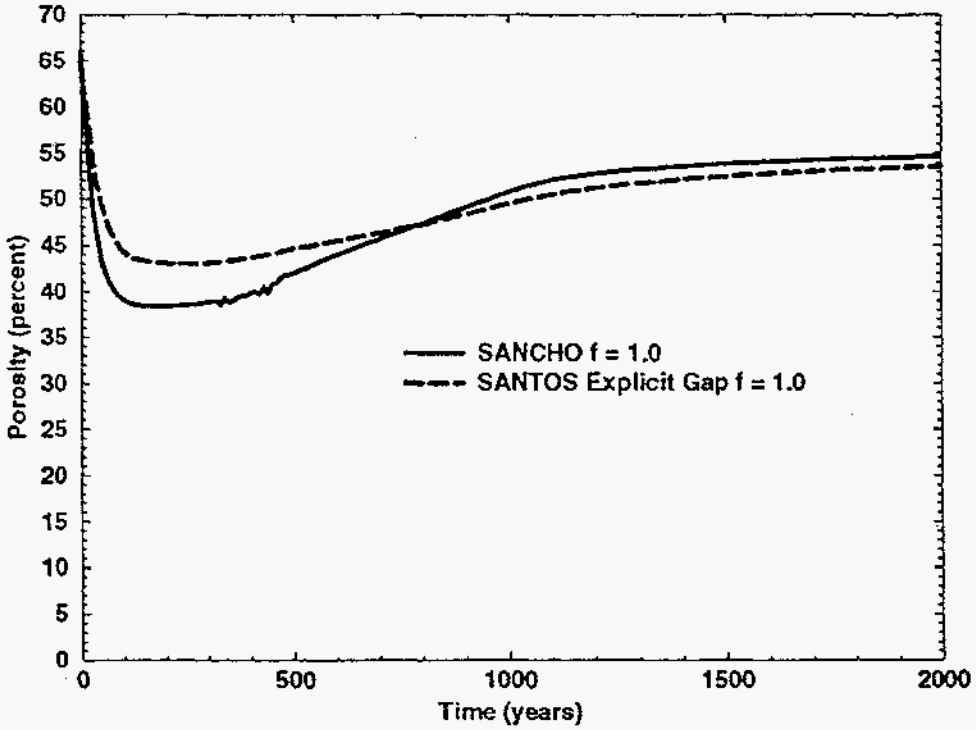

Figure 13. Comparison of Effective Disposal Room Porosity Calculations Between a Reference Model Analysis With SANCHO and SANTOS With the Headspace Explicitly Modeled.

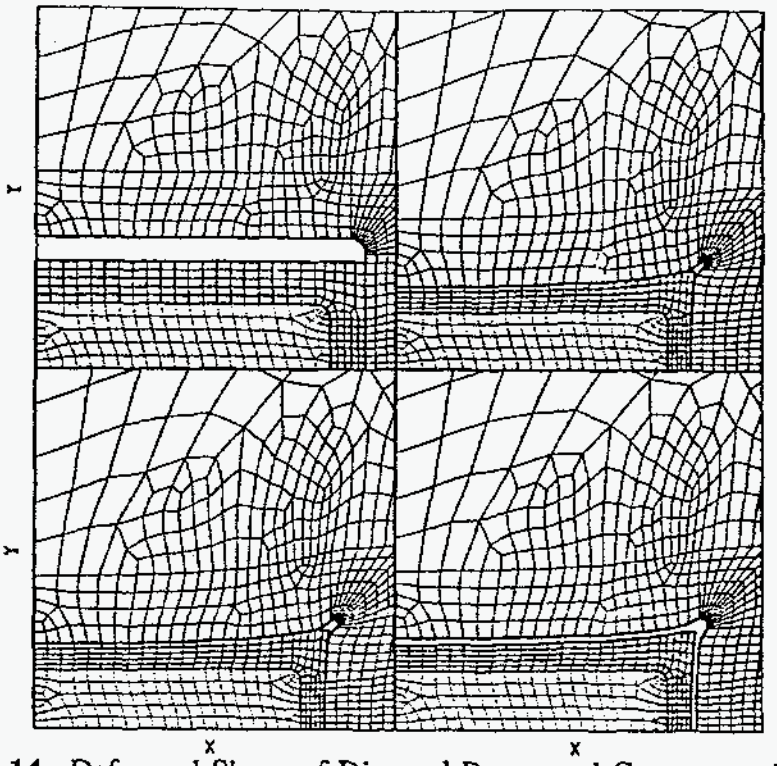

Figure 14. Deformed Shape of Disposal Room and Contents at Various Times During the Simulation. Times Beginning at Top Left and Proceeding Clockwise Are 0., 250., 500., and 1000. Years.

Coupled Structural/Porous Flow Model

The structural solution of the Coupled Structural/Porous Flow problem is the same as presented for the Revised Model With Contact Surfaces. The quantities of interest for the porous flow calculation are the gas pressure and the total brine inflow into the disposal room. The computed gas pressure is shown in Figure 15. The maximum disposal room pressure reaches approximately 22.0 Mpa at 1050 years after emplacement. This pressure acts as an adaptive pore pressure boundary condition on the boundary of the disposal room. The resulting brine inflow for a single disposal room is shown in Figure 16. The brine accumulation reaches a peak value at approximately 120 years, after which time the gas pressure begins to reverse the flow of brine. The amount of brine inflow is affected by the deformation of the salt and by the magnitude of the gas pressure. Figure 16 shows the brine accumulation reaching zero after approximately 270 years. Beyond that time the flow is outward into the formation and dominated by the internal gas pressure. Figure 17 shows a contour plot of pore pressure at 1000 years after waste emplacement. It is easy to observe the effect of gas pressure on the pore pressure field. The entire model is at a pore pressure level greater than the initial pore pressure of 6.0 MPa. As expected, the contours of pore pressure near the disposal room reflect the magnitude of the gas pressure within the room. The coupled structural/porous flow calculation using SANTOS took approximately one hour on the CRAY. This should be compared to run times of 20 hours for structural calculations only using SANCHO.

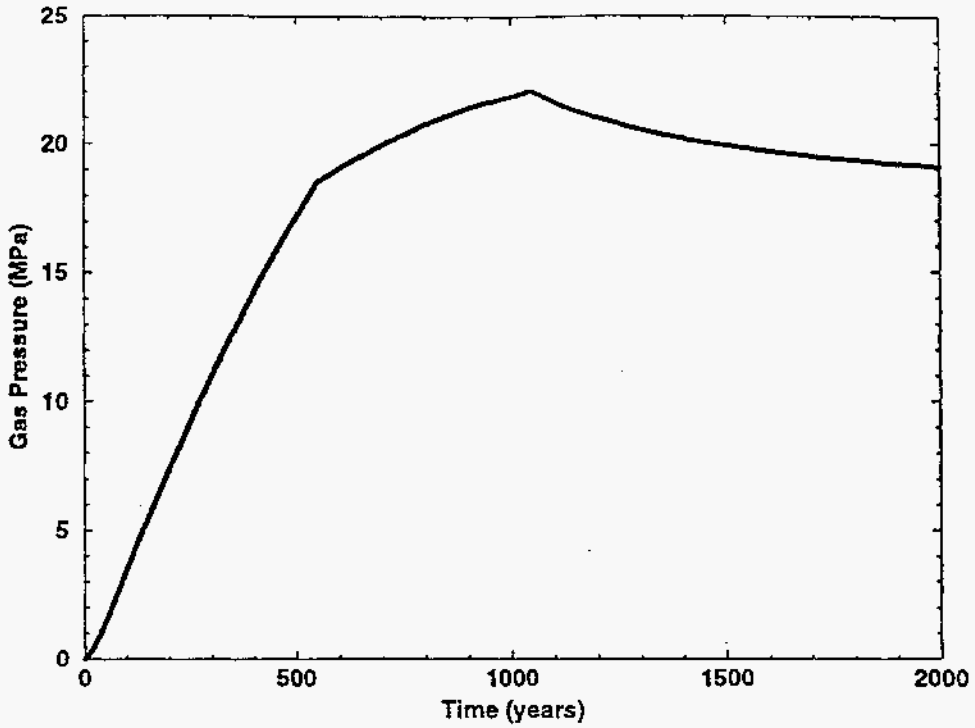

Figure 15. Computed Gas Pressure From Coupled Structural/Porous Flow Calculation Using SANTOS.

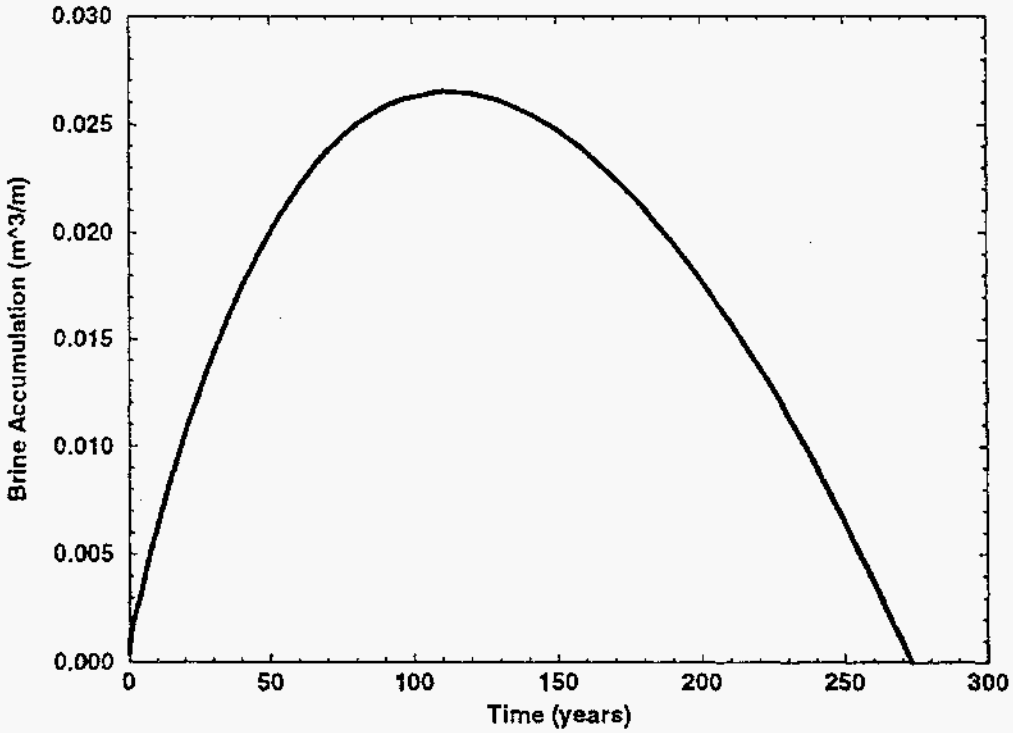

Figure 16. Brine Accumulation in the Disposal Room Determined By a Coupled Structural/Porous Flow Calculation With SANTOS.

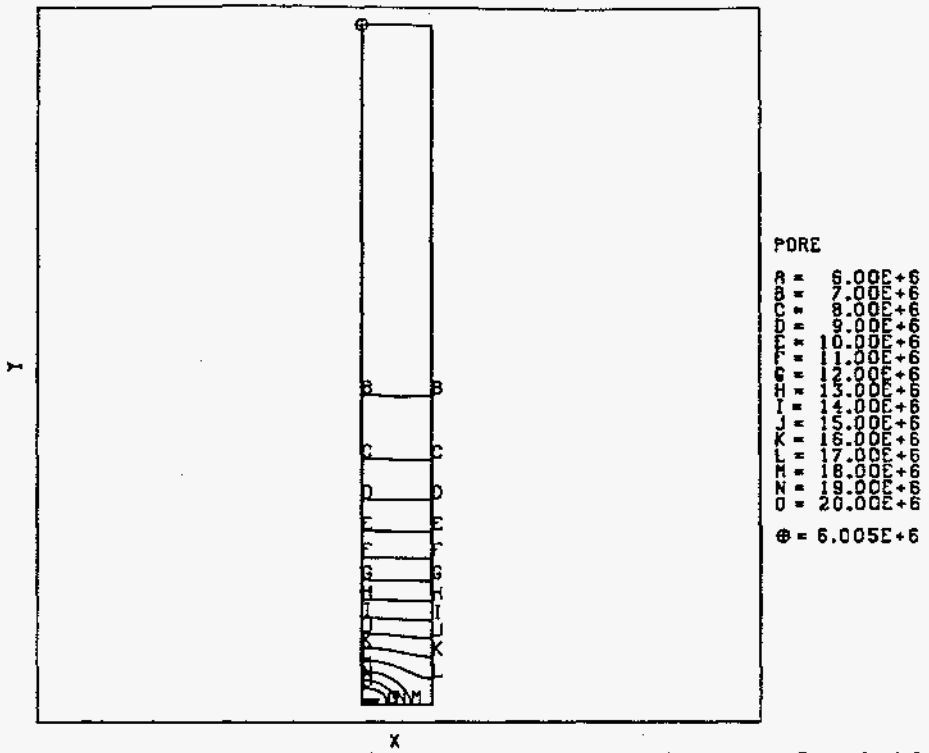

Figure 17. Contour Plot of Pore Pressure Results From the Coupled Structural/ Porous Flow Calculation. Contours Are Plotted at 1000 Years After Waste Emplacement.

Summary of Results

Calculations of the mechanical creep closure response of the Baseline disposal room design have been performed with SANTOS for comparison with results obtained using SANCHO. The comparisons of porosity histories and room displacements for the Reference Model with $f = 0.0$ showed excellent agreement between the two codes. The level of agreement provides confidence that SANTOS is qualified to perform future disposal room calculations. A demonstration calculation, the Reference Model With Contact Surfaces, was also presented which used contact surfaces between the room contents and the disposal room surfaces. A comparison with the Reference Model was made which showed that the effective room porosity was unaffected by the modeling change. A third disposal room analysis, the Revised Model With Contact Surfaces which explicitly modeled the headspace or air gap, was performed with internal gas generation ($f = 1.0$). The analysis showed that the effective porosity of the disposal room was higher at early times (< 200 years) than the porosity calculated using SANCHO with an approximate method of modeling the headspace. The effective porosities calculated with the two codes did converge to the same value at 2000 years. This result suggests that the headspace or air gap must be modeled correctly for the determination of the correct porosity value, especially at early times. A coupled structural/porous flow calculation was performed which determined the amount of brine inflow into the disposal room. The calculation, for a single phase, fully saturated, deforming porous medium, coupled the brine flow to the changes in mean stress in the salt. The gas generation within the disposal room provided a pore pressure boundary

condition at the disposal room boundary. The maximum brine accumulation occurred at 120 years after waste emplacement, and the brine volume was reduced to zero by 270 years due to the gas generation within the room. The gas pressure affected the pore pressure within the salt medium by raising the pore pressure to values greater than the initial condition.

References

1. Stone, Charles M., "SANTOS - A Two-Dimensional Finite Element Program for the Quasistatic, Large Deformation, Inelastic Response of Solids," SAND90-0543, Sandia National Laboratories, Albuquerque, NM, in preparation.

2. Beraun, R. and P. B. Davies, "Baseline Design Input Data Base to be Used During Calculations Effort to be Performed by Division 1514 in Determining the Mechanical Creep Closure Behavior of Waste Disposal Rooms in Bedded Salt," Memorandum to Distribution, Sandia National Laboratories, Albuquerque, New Mexico, September 12, 1991.

3. Taylor, L. M. and D. P. Flanagan, "PRONTO 2D - A Two-Dimensional Transient Solid Dynamics Program," SAND86-0594, Sandia National Laboratories, Albuquerque, NM, March 1987.

4. Stone, C. M., "Qualification of the finite element code SANTOS for performing large scale thermal/structural analyses of a salt repository," memo to Distribution, Sandia National Laboratories, Albuquerque, NM, September 5, 1989.

5. Stone, C. M. and J. G. Arguello, "Panel Scale Calculations for the Waste Isolation Pilot Plant (WIPP)," memo to F. T. Mendenhall, 6345, Sandia National Laboratories, Albuquerque, NM, December 17, 1991.

6. Stone, C. M., R. D. Krieg, and Z. E. Beisinger, "SANCHO - A Finite Element Computer Program for the Quasistatic, Large Deformation, Inelastic Response of Two-Dimensional Solids," SAND84-2618, Sandia National Laboratories, Albuquerque, New Mexico, April, 1985.

7. Stone, C. M., "Creep Closure Behavior of Waste Disposal Rooms in Bedded Salt Due to Gas Generation Produced by Several Alternatives of the Engineered Alternatives Task Force," memo to B. M. Butcher, 6345, Sandia National Laboratories, Albuquerque, NM, October 6, 1992.

8. Weatherby, J. R., J. G. Arguello, B. M. Butcher, and C. M. Stone, "The structural response of a WIPP disposal room with internal gas generation," Proceedings of the 32nd U. S. Rock Mechanics Symposium, Norman, Ok, July, 1991.

9. Weatherby, J. R., W. T. Brown, and B. M. Butcher, "The closure of WIPP disposal rooms filled with various waste and backfill combinations," Proceedings of the 32nd U. S. Rock Mechanics Symposium, Norman, Ok, July, 1991.

10. Arguello, J. G., "Use of a Midheight Symmetry Plane to Compute Disposal Room Closure," Memorandum to Distribution, Sandia National Laboratories, Albuquerque, NM, January 1990.

11. Krieg, R. D., "Reference Stratigraphy and Rock Properties for the Waste Isolation Pilot Plant (WIPP) Project," SAND83-1908, Sandia National Laboratories, Albuquerque, New Mexico, 1984.

12. Morgan, H. S. and R. D. Krieg, "A Comparison of Unified Creep-Plasticity and Conventional Creep Models for Rock Salt Based on Predictions of Creep Behavior Measured in Several *In Situ* and Bench-Scale Experiments," SAND87-1867, Sandia National Laboratories, Albuquerque, NM, 1988.

13. Sjaardema, G. D. and R. D. Krieg, "A Constitutive Model for the Consolidation of WIPP Crushed Salt and Its Use in Analyses of Backfilled Shaft and Drift Configurations," SAND87-1977, Sandia National Laboratories, Albuquerque, New Mexico, 1987.

14. Stone, C. M. and D. F. McTigue, "Coupled Salt Deformation and Brine Flow," memo to Distribution, Sandia National Laboratories, Albuquerque, NM, January 12, 1993.

15. McTigue, D. F. "Coupled Rock Deformation and Pore Fluid Flow for Salt Based on Linear Poroelasticity," memo to Distribution, Sandia National Laboratories, Albuquerque, NM, March 2, 1990.

16. Gartling, D. K., "COYOTE - A Finite Element Computer Program for Nonlinear Heat Conduction Problems," SAND77-1332, Sandia National Laboratories, Albuquerque, NM, June 1978.

Appendix - SANTOS Input

```
TITLE
PRESSURIZED ROOM CALCULATION - COUPLED DISPOSAL ROOM MODEL
PLANE STRAIN
INITIAL STRESS = USER
PLOT ELEMENT, STRESS, STRAIN, VONMISES, PRESSURE
PLOT NODAL, DISPLACEMENT
PLOT,STATE, EQCS, DENSITY, EV
RESIDUAL TOLERANCE = .5
MAXIMUM ITERATIONS = 500
MAXIMUM TOLERANCE = 100.
INTERMEDIATE PRINT = 10
PREDICTOR SCALE FACTOR = 0.0
ELASTIC SOLUTION
STEP CONTROL
  20   3.1536E7
 1980  3.1536E9
38000  6.3072E10
END
OUTPUT TIME
  10   3.1536E7
 100   3.15E6E9
 950   6.3072E10
END
PLOT TIME
  1   3.15E6E7
  100 3.1536E9
  200 6.3072E10
END
MATERIAL, 1, POWER LAW CREEP, 1.
TWO MU = 1.984E9
BULK MODULUS = 1.656E9
CREEP CONSTANT = 5.79E-36
STRESS EXPONENT = 4.9
THERMAL CONSTANT = 20.13
END
MATERIAL, 2, VOLUMETRIC CREEP, 1.
```

TWO MU = 1696.
BULK MODULUS = 1408.
CREEP CONSTANT = 5.79E-36
STRESS EXPONENT = 4.9
THERMAL CONSTANT = 20.13
SHEAR EXPONENT = 6.53E-3
BULK EXPONENT = 6.53E-3
B0 = 1.3e8
B1 = .82E-6
A1 = -17.3E-3
INTACT DENSITY = 2140
INITIAL DENSITY = 1300
END
MATERIAL, 3, SOIL N FOAMS, 1.
TWO MU = 3.333E8
BULK MODULUS = 2.223E8
A0 = 1.0E6
A1 = 3.
A2 = 0.
PRESSURE CUTOFF = 0.
FUNCTION ID = 2
END
NO DISPLACEMENT X = 1
NO DISPLACEMENT Y = 2
PRESSURE, 200, 1, 14.8E6
ADAPTIVE PRESSURE, 300, 0., 1.E-6
CONTACT SURFACE 400 500 0. 1.E-2, 1.
CONTACT SURFACE 600 500 0. 1.E-2, 1.
CONTACT SURFACE 400 600 0. 1.E-2, 1.
FUNCTION,1 $ FUNCTION TO DEFINE PRESCRIBED PRESSURE
0., 1.
6.3072E10, 1.
END
FUNCTION,2
0., 0.
.0323, .02833E6
.741, .733E6
.898, 1.1333E6

1.029, 1.667E6
1.18, 2.8E6
1.536, 10.167E6
END
XBEGIN,DIABLOS
POROUS FLOW INTEGRAL = 300
ADAPTIVE PORE PRESSURE, 10, 300
FUNCTION = 1
0., 1.
1.E11, 1.
END
MATERIAL, 1, POROUS
PERMEABILITY = 1.E-21
VISCOSITY = 1.6E-3
STORATIVITY = 8.E-12
FLUID DENSITY = 0.0
COMPRESSIBILITY = 0.0
STRESS COUPLING = 5.76E-12
END
MATERIAL, 2, POROUS
PERMEABILITY = 1.E-21
VISCOSITY = 1.6E-3
STORATIVITY = 8.E-12
FLUID DENSITY = 0.0
COMPRESSIBILITY = 0.0
STRESS COUPLING = 0.0
END
MATERIAL, 3, POROUS
PERMEABILITY = 1.E-21
VISCOSITY = 1.6E-3
STORATIVITY = 8.E-12
FLUID DENSITY = 0.0
COMPRESSIBILITY = 0.0
STRESS COUPLING = 0.0
END
MAXIMUM ITERATIONS = 1000
RESIDUAL TOLERANCE = 1.E-8
INITIAL PORE PRESSURE = CONSTANT = 6.E6

WIPP
UC721 - DISTRIBUTION LIST

Federal Agencies

US Department of Energy (6)
Office of Civilian Radioactive Waste Mgmt.
Attn: Deputy Director, RW-2
Associate Director, RW-10/50
Office of Prog. & Resources Mgmt.
Office of Contract Business Mgmt.
Director, RW-22
Analysis & Verification Division
Associate Director, RW-30
Office of Systems & Compliance
Associate Director, RW-40
Office of Storage & Transportation
Director, RW-4/5
Office of Strategic Planning and International Programs
Office of External Relations
Forrestal Building
Washington, DC 20585

US Department of Energy
Albuquerque Operations Office
Attn: National Atomic Museum Library
P.O. Box 5400
Albuquerque, NM 87185-5400

US Department of Energy
Research & Waste Management Division
Attn: Director
P.O. Box E
Oak Ridge, TN 37831

US Department of Energy (5)
Carlsbad Area Office
Attn: G. Dials
M. McFadden
R. Lark
D. Galbraith
J. A. Mewhinney
P.O. Box 3090
Carlsbad, NM 88221-3090

US Department of Energy
Attn: E. Young
Room E-178
GAO/RCED/GTN
Washington, DC 20545

US Department of Energy
Office of Environmental Restoration and Waste Management
Attn: J. Lytle, EM-30
Forrestal Building
Washington, DC 20585-0002

US Department of Energy (3)
Office of Environmental Restoration and Waste Management
Attn: M. Frei, EM-34, Trevion II
Washington, DC 20585-0002

US Department of Energy
Office of Environmental Restoration and Waste Management
Attn: S. Schneider, EM-342, Trevion II
Washington, DC 20585-0002

US Department of Energy (2)
Office of Environment, Safety & Health
Attn: C. Borgstrom, EH-25
R. Pelletier, EH-231
Washington, DC 20585

US Department of Energy (2)
Idaho Operations Office
Fuel Processing & Waste Mgmt. Division
785 DOE Place
Idaho Falls, ID 83402

US Environmental Protection Agency (2)
Radiation Protection Programs
Attn: M. Oge
ANR-460
Washington, DC 20460

Boards

Defense Nuclear Facilities Safety Board
Attn: D. Winters
625 Indiana Ave. NW, Suite 700
Washington, DC 20004

Nuclear Waste Technical Review Board (2)
Attn: Chairman
S. J. S. Parry
1100 Wilson Blvd., Suite 910
Arlington, VA 22209-2297

State Agencies

Attorney General of New Mexico
P.O. Drawer 1508
Santa Fe, NM 87504-1508

Environmental Evaluation Group (3)
Attn: Library
7007 Wyoming NE
Suite F-2
Albuquerque, NM 87109

NM Energy, Minerals, and Natural
Resources Department
Attn: Library
2040 S. Pacheco
Santa Fe, NM 87505

NM Environment Department (3)
Secretary of the Environment
Attn: Mark Weidler
1190 St. Francis Drive
Santa Fe, NM 87503-0968

NM Bureau of Mines & Mineral Resources
Socorro, NM 87801

NM Environment Department
WIPP Project Site
Attn: P. McCasland
P.O. Box 3090
Carlsbad, NM 88221

Laboratories/Corporations

Battelle Pacific Northwest Laboratories
Attn: R. E. Westerman, MSIN P8-44
Battelle Blvd.
Richland, WA 99352

INTERA, Inc. (10)
Attn: G. A. Freeze
1650 University Blvd. NE, Suite 300
Albuquerque, NM 87102

INTERA, Inc. (5)
Attn: J. F. Pickens
6850 Austin Center Blvd., Suite 300
Austin, TX 78731

INTERA, Inc.
Attn: S. Mishra
101 Convention Center Drive
MS 423
Las Vegas, NV 89109

INTERA, Inc.
Attn: W. Stensrud
P.O. Box 2123
Carlsbad, NM 88221

Los Alamos National Laboratory
Attn: B. Erdal, INC-12
P.O. Box 1663
Los Alamos, NM 87544

RE/SPEC, Inc
Attn: Angus Robb
4775 Indian School NE, Suite 300
Albuquerque, NM 87110-3927

RE/SPEC, Inc
Attn: J. L. Ratigan
P.O. Box 725
Rapid City, SD 57709

Southwest Research Institute (2)
Center for Nuclear Waste Regulatory Analysis
Attn: P. K. Nair
6220 Culebra Road
San Antonio, TX 78228-0510

Tech Reps, Inc. (4)
Attn: J. Chapman (2)
T. Peterson (2)
5000 Marble NE, Suite 222
Albuquerque, NM 87110

Lawrence Berkeley Laboratory (2)
Attn: K. Pruess
G. Moridis
Earth Sciences Division
MS 50E
Berkeley, CA 94720

Westinghouse Electric Corporation (5)
Attn: Library
J. Epstein
J. Lee
B. A. Howard
R. Kehrman
P.O. Box 2078
Carlsbad, NM 88221

S. Cohen & Associates
Attn: Bill Thurber
1355 Beverly Road
McLean, VA 22101

National Academy of Sciences, WIPP Panel

Howard Adler
Oxyrase, Incorporated
7327 Oak Ridge Highway
Knoxville, TN 37931

Ina Alterman
Board of Radioactive Waste Management
GF456
2101 Constitution Ave.
Washington, DC 20418

Rodney C. Ewing
Department of Geology
University of New Mexico
Albuquerque, NM 87131

Charles Fairhurst
Department of Civil and Mineral Engineering
University of Minnesota
500 Pillsbury Dr. SE
Minneapolis, MN 55455-0220

B. John Garrick
PLG Incorporated
4590 MacArthur Blvd., Suite 400
Newport Beach, CA 92660-2027

Leonard F. Konikow
US Geological Survey
431 National Center
Reston, VA 22092

Carl A. Anderson, Director
Board of Radioactive Waste Management
National Research Council
HA 456
2101 Constitution Ave. NW
Washington, DC 20418

Christopher G. Whipple
ICF Kaiser Engineers
1800 Harrison St., 7th Floor
Oakland, CA 94612-3430

John O. Blomeke
720 Clubhouse Way
Knoxville, TN 37909

Sue B. Clark
University of Georgia
Savannah River Ecology Lab
P.O. Drawer E
Aiken, SC 29802

Konrad B. Krauskopf
Department of Geology
Stanford University
Stanford, CA 94305-2115

Della Roy
Pennsylvania State University
217 Materials Research Lab
Hastings Road
University Park, PA 16802

David A. Waite
CH_2 M Hill
P.O. Box 91500
Bellevue, WA 98009-2050

Thomas A. Zordon
Zordan Associates, Inc.
3807 Edinburg Drive
Murrysville, PA 15668

Universities

University of New Mexico
Geology Department
Attn: Library
141 Northrop Hall
Albuquerque, NM 87131

University of Washington
College of Ocean & Fishery Sciences
Attn: G. R. Heath
583 Henderson Hall, HN-15
Seattle, WA 98195

Libraries

Thomas Brannigan Library
Attn: D. Dresp
106 W. Hadley St.
Las Cruces, NM 88001

Government Publications Department
Zimmerman Library
University of New Mexico
Albuquerque, NM 87131

New Mexico Junior College
Pannell Library
Attn: R. Hill
Lovington Highway
Hobbs, NM 88240

New Mexico State Library
Attn: N. McCallan
325 Don Gaspar
Santa Fe, NM 87503

New Mexico Tech
Martin Speere Memorial Library
Campus Street
Socorro, NM 87810

WIPP Public Reading Room
Carlsbad Public Library
101 S. Halagueno St.
Carlsbad, NM 88220

Foreign Addresses

Studiecentrum Voor Kernenergie
Centre d'Energie Nucleaire
Attn: A. Bonne
SCK/CEN Boeretang 200
B-2400 Mol, BELGIUM

Atomic Energy of Canada, Ltd.
Whiteshell Laboratories
Attn: B. Goodwin
Pinawa, Manitoba, CANADA R0E 1L0

Francois Chenevier (2)
ANDRA
Route de Panorama Robert Schumann
B. P. 38
92266 Fontenay-aux-Roses, Cedex
FRANCE

Claude Sombret
Centre d'Etudes Nucleaires de la Vallee Rhone
CEN/VALRHO
S.D.H.A. B.P. 171
30205 Bagnols-Sur-Ceze, FRANCE

Commissariat a L'Energie Atomique
Attn: D. Alexandre
Centre d'Etudes de Cadarache
13108 Saint Paul Lez Durance Cedex
FRANCE

Bundesanstalt fur Geowissenschaften und
Rohstoffe
Attn: M. Langer
Postfach 510 153
D-30631 Hannover, GERMANY

Bundesministerium fur Forschung und
Technologie
Postfach 200 706
5300 Bonn 2, GERMANY

Institut fur Tieflagerung
Attn: K. Kuhn
Theodor-Heuss-Strasse 4
D-3300 Braunschweig, GERMANY

Gesellschaft fur Anlagen und Reaktorsicherheit
(GRS)
Attn: B. Baltes
Schwertnergasse 1
D-50667 Cologne, GERMANY

Physikalisch-Technische Bundesanstalt
Attn: P. Brenneke
Postfach 3345
D-3300 Braunschweig, GERMANY

Shingo Tashiro
Japan Atomic Energy Research Institute
Tokai-Mura, Ibaraki-Ken, 319-11
JAPAN

Netherlands Energy Research Foundation ECN
Attn: L. H. Vons
3 Westerduinweg
P.O. Box 1
1755 ZG Petten
THE NETHERLANDS

Svensk Karnbransleforsorjning AB
Attn: F. Karlsson
Project KBS (Karnbranslesakerhet)
Box 5864
S-102 48 Stockholm
SWEDEN

Nationale Genossenschaft fur die Lagerung
Radioaktiver Abfalle (2)
Attn: S. Vomvoris
P. Zuidema
Hardstrasse 73
CH-5430 Wettingen
SWITZERLAND

AEA Technology
Attn: J. H. Rees
D5W/29 Culham Laboratory
Abington, Oxfordshire OX14 3DB
UNITED KINGDOM

AEA Technology
Attn: W. R. Rodwell
044/A31 Winfrith Technical Centre
Dorchester, Dorset DT2 8DH
UNITED KINGDOM

AEA Technology
Attn: J. E. Tinson
B4244 Harwell Laboratory
Didcot, Oxfordshire OX11 ORA
UNITED KINGDOM

D. R. Knowles
British Nuclear Fuels, plc
Risley, Warrington, Cheshire WA3 6AS
1002607 UNITED KINGDOM

INTERA Switzerland (3)
Attn: R. Senger
Mellingerstrasse 207
CH-5405 Baden
SWITZERLAND

Internal

MS	Org.	
0827	1502	P. J. Hommert
1324	6115	P. B. Davies (6)
1324	6115	S. W. Webb
1324	6115	A. R. Lappin
1324	6115	T. Christian-Frear
1320	6119	E. J. Nowak
1332	6121	J. R. Tillerson
1395	6700	P. Brewer
1335	6705	M. Chu
1395	6707	M. Marietta
1335	6303	W. Weart
1395	6701	L. Shephard
1341	6706	A. L. Stevens
1395	6701	L. Shephard
1341	6747	K. W. Larson (6)
1341	6748	B. M. Butcher
1328	6749	D. R. Anderson
1328	6749	P. Vaughn
1395	6743	V. H. Slaboszewicz
1341	6747	D. R. Schafer
1341	6748	J. T. Holmes
1328	6741	H. N. Jow
1330	6352	C. B. Michaels (2)
1330	6352	NWM Library (20)
9018	8523-2	Central Technical Files
0899	4414	Technical Library (5)
0619	12613	Print Media
0100	7613-2	Document Processing (2) for DOE/OSTI

* U.S. GOVERNMENT PRINTING OFFICE 1995-774-030/20010